UNIVERSITY OF COPENHAGEN
NIELS BOHR INSTITUTE, FACULTY OF SCIENCE

Ice flow signatures on small and big scales

Combining radio-echo sounding and ice core data to characterize the flow dynamics in the Northeast Greenland Ice Stream

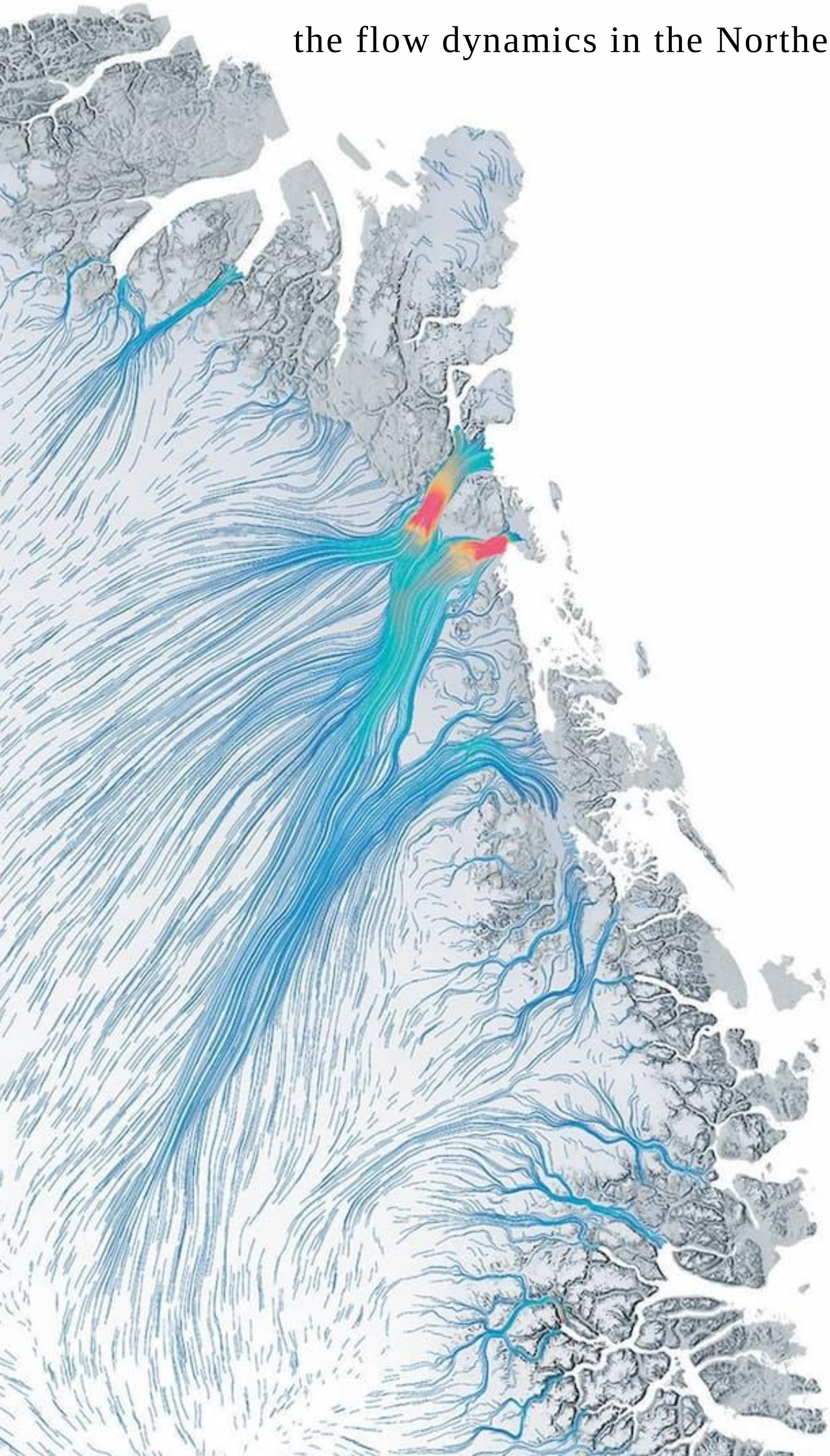

PhD Thesis

Tamara Annina Gerber

Supervisors
Dorthe Dahl-Jensen
Sune Olander Rasmussen

May 31st, 2022

This thesis has been submitted to the
PhD School of the Faculty of Science,
University of Copenhagen.

Preface

The work presented in this thesis is original and was conducted by Tamara Annina Gerber during the PhD enrollment period from 2019–2022. The project was supervised by Dorthe Dahl-Jensen and Sune Olander Rasmussen. This PhD has been financially supported by the Villum Investigator Project IceFlow (grant no. 16572) and the Project HPC-EUROPA3 (INFRAIA-2016-1-730897), with the support of the EC Research Innovation Action under the H2020 Programme.

Part of this thesis has been published in the following scientific article:
T. A. Gerber et al. (2021). "Upstream flow effects revealed in the EastGRIP ice core using Monte Carlo inversion of a two-dimensional ice-flow model". In: *The Cryosphere* 15.8, pp. 3655–3679. DOI: `10.5194/tc-15-3655-2021`

Published work and the help of others have been acknowledged, and relevant sources have been provided.

The image on the title page was taken from the following source: J. Cheshire (2021). *Atlas of the Invisible education resources*. URL: `https://jcheshire.com/` (visited on 05/24/2022)

“We need the tonic of wildness...At the same time that we are earnest to explore and learn all things, we require that all things be mysterious and unexplorable, that land and sea be indefinitely wild, unsurveyed and unfathomed by us because unfathomable. We can never have enough of nature. ”

Henry David Thoreau, *Walden; Or, Life in the Woods*

UNIVERSITY OF COPENHAGEN

Abstract

Faculty of Science
Niels Bohr Institute

Doctor of Philosophy

Ice flow signatures on small and big scales

Combining radio-echo sounding and ice core data to characterize flow dynamics in the Northeast Greenland Ice Stream

by Tamara Annina GERBER

Ice streams transport large amounts of ice from the ice sheet interior to the coast and are responsible for the primary dynamic mass loss in Greenland and Antarctica. The future stability of ice sheets and their contribution to sea-level rise strongly depends on the response of ice streams to a warming climate. Yet, the physical processes that govern rapid ice flow are still not entirely understood, and prognostic ice-sheet models cannot accurately reproduce these highly dynamic areas. The Northeast Greenland Ice Stream (NEGIS) is Greenland's largest active ice stream and extends from the ice-sheet center over more than 700 km to the northeastern coast. A deep ice core, the East Greenland Ice-core Project (EastGRIP), is drilled in its onset region and can provide unique, detailed information about past climatic conditions and ice-flow history, as well as the physical properties affecting present-day ice flow. However, observations from ice cores at single point locations might not be representative of the conditions over broader spatial scales, and climatic interpretations in fast-flowing areas are therefore affected by upstream flow effects. Radio-echo-sounding (RES) can provide complementing information on larger spatial scales through the efficient mapping of in-situ properties of ice sheets using electromagnetic waves. However, an unambiguous interpretation of radargrams is difficult without additional information on the physical properties of the subsurface.

This thesis aims to combine the information from the EastGRIP ice core with an extensive set of RES images recorded in the NEGIS onset region in order to link the small scales of direct observations with the larger scales required for ice flow models and a complete understanding of ice stream dynamics. My studies specifically focus on the internal stratigraphy that causes radar reflections due to contrasts in dielectric properties. By simulating the movement of internal layers with a simple ice-flow model, I determined the upstream flow effects affecting some of the chemical properties measured in the EastGRIP ice core. Travel time differences in the signal reflections between different antenna polarizations further provide information about the ice crystal orientation fabric. In combination with other methods, this approach allowed me to obtain a map of the spatial distribution of the crystal fabric anisotropy, as well as determining its potential effects on the ice viscosity and hence flow dynamics. Finally, I investigated the reflection properties of the internal stratigraphy near EastGRIP by numerical modeling of synthetic radargrams with the dielectric record of the EastGRIP ice core, allowing me to study the effects of small-scale folds and layer roughness on the received signal.

The results obtained in this thesis thus have wide implications for reducing ambiguities in the interpretation of radargrams and ice core measurements, thereby hoping to contribute towards an improved and more holistic understanding of the dynamic processes governing the NEGIS.

KØBENHAVNS UNIVERSITET

Résumé

Det Natur- og Biovidenskabelige Fakultet
Niels Bohr Institutet

Doktor i filosofi

Isstrømsignaturer på lille og stor skala

En kombination af radio-ekkolodning og iskernedata med henblik på at karakterisere bevægelsesdynamikker i den Nordøstgrønlandske Isstrøm

af Tamara Annina GERBER

Isstrømme transporterer store mængder is fra iskappens indre til kysten, og er den primære årsag til det dynamiske tab af ismasse fra Grønland og Antarktis. Den fremtidige stabilitet af iskapperne samt deres bidrag til havniveaustigningen afhænger stærkt af, hvordan isstrømme vil respondere på et varmere klima. De styrende processer bag hurtige strømninger af is er dog stadig ikke forstået til fulde, og prognostiske iskappemodeller er fortsat ikke i stand til at reproducere disse højdynamiske områder nøjagtigt. Den Nordøstgrønlanske Isstrøm (NEGIS) er Grønlands største aktive isstrøm, og strækker sig over mere end 700 km fra kysten til isdeleren. Boringen af en dyb iskerne, kaldet 'the East Greenland Ice-core Project' (EastGRIP), pågår ved isstrømmens udspring, og af denne iskerne kan der udledes detaljeret information omkring tidligere klimatiske betingelser, og isstrømmes historiske bevægelser, samt de fysiske egenskaber som påvirker isstrømme i dag. Observationer fra iskerner er dog ikke nødvendigvis repræsentative på større længdeskala, og klimatiske tolkninger af iskerner i områder med hurtig isflydning påvirkes af dynamiske effekter opstrømsk. Radio-ekkolodning (RES) kan biddrage med komplementerende viden på større længdeskala gennem effektiv kortlægning af iskapper ved brug af elektromagnetiske bølger. En utvetydig tolkning af RES radargrammer er dog imidlertid betinget af en god forståelse af isens dielektriske egenskaber.

Arbejdet præsenteret i denne afhandling tilstræber at kombinere information fra EastGRIP-iskernen med et omfattende sæt af RES-billeder optaget i NEGIS-udspringsregionen. Afhandlingen har særligt et henblik på at forbinde direkte observationer mellem små og store længdeskalaer, som er nødvendig for at forbedre numeriske modeller af isstrømme, samt at skabe en dybere forstålse af den isdynamik, der tillader istrømme at opstå. Mine studier fokuserer specifikt på den interne stratigrafi, som forårsager radarreflektioner på grund af kontraster i dielektriske egenskaber. Ved at simulere flydningen af interne lag med en simpel isstrømsmodel, bestemte jeg, hvordan dynamiske effekter opstrømsk har påvirket en række af egenskaberne målt i EastGRIP iskernen. Forskelle i udbredelseshastigheder af reflekterede bølger mellem forskellige antennepolariseringer giver derudover information omkring orienteringen af iskrystaller. Kombineret med andre metoder har denne tilgang gjort det muligt for mig at udarbejde et kort over den rumlige fordeling af isanisotropien, samt at bestemme dens effekt på isens viskositet og derigennem bevægelsesdynamik. Til sidst undersøgte jeg den interne stratigrafis refleksionsegenskaber ved numerisk modellering af syntetiske radargrammer med dielektriske optegnelser taget fra EastGRIP iskernen, for, således, at studerer effekterne af småskalafoldninger og lagenes ruhed på det indgående signal.

Samlet set hjælper resultaterne opnået i denne afhandling med at reducere uklarheder i tolkningen af radargrammer og iskernemålinger, og bidrager dermed til en bedre forståelse af de styrende dynamiske processer i NEGIS.

UNIVERSTITÄT KOPENHAGEN

Zusammenfassung

Natur- und Biowissenschaftliche Fakultät
Niels Bohr Institut

Doktor der Philosophie

Eisflusssignaturen auf kleinen und grossen Skalen

Kombinierte Analyse von Radarmessungen und Eiskerndaten zur Charakterisierung der Eisdynamik im Nordostgrönländischen Eisstrom

von Tamara Annina GERBER

Eisströme transportieren große Mengen an Eis vom Inneren der Eisschilde in Richtung Küste und sind hauptverantwortlich für den dynamischen Eisverlust in Grönland und der Antarktis. Die Stabilität von Eisschilden, sowie deren Beitrag zum Meeresspiegelanstieg, hängt stark davon ab, wie Eisströme auf Klimaveränderungen reagieren. Die Prozesse, welche den Eisfluss kontrollieren, sind jedoch noch nicht vollständig verstanden. Dies führt zu grossen Unsicherheiten in Prognosen der zukünftigen Entwicklung der Eisschilde in Grönland und der Antarktis. Der Nordostgrönländische Eisstrom (NEGIS) ist der grösste aktive Eisstrom in Grönland und erstreckt sich vom Eisschildzentrum über mehr als 700 km an die nordöstliche Küste. In seiner Ursprungsregion wird derzeit ein Eiskern gebohrt. Dieser Eiskern des sogenannten 'East Greenland Ice-core Project' (EastGRIP) liefert wertvolle Informationen über die klimatischen Bedingungen in der Vergangenheit und bietet zudem Einsicht in die physikalischen Eigenschaften, welche heute die Fliessdynamik beeinflussen. Beobachtungen in Eisbohrkernen sind zwar detailliert, jedoch nicht unbedingt flächendeckend repräsentativ. Klimatische Interpretationen werden von sogenannten Fliesseffekten beeinflusst, da das Eis ursprünglich weiter stromaufwärts abgelagert wurde. Georadar-Methoden (RES) nutzen elektromagnetische Wellen, um Strukturen im Untergrund abzubilden und liefern damit ergänzende, flächendeckende Informationen. Allerdings ist die Interpretation von Radargrammen ohne zusätzliche Erkenntnisse über die physikalischen Eigenschaften von Eis nicht eindeutig.

Diese Dissertation umfasst eine kombinierte Analyse von Eiskern- und Radardaten aus der NEGIS Entstehungsregion. Das Ziel dabei ist es, die kleinen Skalen direkter Beobachtungen mit grösseren Massstäben zu verknüpfen, welche für Eisflussmodelle, sowie für ein vollumfängliches Verständnis der Eisstromdynamik erforderlich sind. Meine Untersuchungen konzentrieren sich dabei insbesondere auf die interne Stratigraphie von Eisschichten, anhand denen ich den Ort und die glaziologischen Gegebenheiten rekonstruierte, unter welchen das Eis im EastGRIP Eiskern ursprünglich abgelagert wurde. Laufzeitunterschiede zwischen reflektierten Signalen mit unterschiedlichen Polarisierungen geben zudem Aufschluss über die Orientierung der Eiskristalle. In Kombination mit weiteren Methoden erstellte ich eine Karte über die räumliche Verteilung der Kristall-Anisotropie sowie dessen Auswirkung auf die Fliesseigenschaften von Eis. Schliesslich untersuchte ich mit Hilfe von numerischen Modellierungen, wie sich bestimmte Eigenschaften von internen Schichten auf Radarsignale auswirken, wobei ich mich auf Beobachtungen und Messungen am EastGRIP Eiskern stützte.

Die in dieser Arbeit präsentierten Ergebnisse helfen Mehrdeutigkeiten bei der Interpretation von Radargrammen und Eiskernmessungen zu reduzieren und tragen zum besseren Verständnis der dynamischen Prozesse im NEGIS bei.

Acknowledgements

First and foremost, I would like to express my gratitude to my supervisor **Dorthe Dahl-Jensen** for creating a comfortable working atmosphere and for making me feel welcome as part of the PICE family. Thank you for giving me the freedom to develop my own ideas, for connecting me with the right people at the right time, and for the good times we've spent at the fireplace in your garden, where you and **Jørgen Peder Steffensen** shared the inspiring stories of your experiences in Greenland. Second, I would like to thank my co-supervisor **Sune Olander Rasmussen** for his helpful advice and moral support along the way, for sharing anecdotes from the field, and for his great sense of humor that reminded me to take things not too seriously. I also want to offer special thanks to my evaluation committee **Anders Svensson**, **Knut Christianson**, and **Marie Cavitte** for taking the time to read and evaluate my work.

I further want to thank you, **Christine Hvidberg**, for organizing our weekly meetings and activities in our group, and for your advice on scientific and personal matters. Thank you, **Julien Westhoff**, for your friendship, for reminding me when it is time to stop working and drink a beer with you, and for the great memories, I share with you from our trips to Greenland, Japan, and Scandinavia. Thank you, **Nicholas Rathmann**, for your patience in answering my countless questions, for organizing our writing retreats and for the dances that helped me cope with stressful times. Thank you, **Giulia Sinnl** and **Jia-Mei Lin**, for your friendship and company in the office, for reminding me of my deadlines, proofreading my manuscripts, laughing about my jokes, and cheering me up every day. Thank you, **Aslak Grinsted**, for your useful input and contribution to our discussions, and thank you, **David Lilien**, for your invaluable help in proofreading and for asking the critical questions that made me do better.

Moreover, I want to express my gratitude to you, **Olaf Eisen**, for your guidance and for sharing your ideas at the beginning of my PhD, for your friendly reminders of taking enough breaks, and for your efforts in connecting me with others to combine the individual scientific pieces in order to understand the big picture. Thank you, **Steven Franke**, for our countless virtual discussions, for sharing your excellent skills in figure-making with me, and for your company during your stay in Copenhagen. Thank you, **Ilka Weikusat**, **Daniela Jansen**, **Angelika Humbert**, **Nicolas Stoll**, and **Ole Zeising**, for your feedback and critical thoughts on my work and for letting me learn from your expertise. Furthermore, I want to thank **Craig Warren** and **Antonis Giannopoulos** for hosting me during my stay abroad in Newcastle and Edinburgh, for connecting me to the glaciology groups, and for sharing their insights and modeling experience from an engineering perspective.

I am grateful to my housemates **Mads**, **Christine**, **Qing**, and **Jesus**, who made me feel at home in Copenhagen right from the start. Thank you for sharing your meals, bottles of wine, and good times with me, thank you for building me up when I was down and coping with me when I was stressed. I am grateful to my friends and shipmates, **Dominic** and **George**, for reminding me of the sweet parts of life and the good times we spent on our sailboat that gave me the energy and motivation to carry on. Thank you, my dear friends **Jacqueline** and **Katharina**, for giving me the feeling that I can always count on you, no matter how far the distance between us or how long since we last saw each other. I am grateful to my sister, **Aline**, for her physiotherapist advice, for reminding me of the importance of getting enough sleep and recovery, and for her ability to make me laugh even from far away. I also want to thank my brother, **Fabian**, for inspiring me to travel the unpaved roads, for driving more than 1000 km to supply me with Swiss food and drinks, and for his great care and love. Finally, I want to express my deep gratitude to my parents **Esther** and **Christoph**. Thank you for raising me to be strong and independent, for sparing no efforts in supporting me in all possible ways, and thank you, for passing on to me your curiosity and passion for natural sciences and adventures. You have taught me so much about snow and ice on our countless ski tours in the Swiss Alps long before I even knew what the word *glaciology* meant.

Contents

List of Figures

List of Tables

List of Abbreviations

AC	**A**lternating **C**urrent
AMOC	**A**tlantic **M**eridional **O**verturning **C**irculation
AWI	**A**lfred **W**egener **I**nstitute
b2k	**b**efore the year **2000**
COF	**C**rystal **O**rientation **F**abric
CReSIS	**C**enter for **Re**mote **S**ensing of **I**ce **S**heets
DC	**D**irect **C**urrent
DEP	**D**i-Electric **P**rofiling
D-O-event	**D**ansgaard-**O**eschger **event**
EastGRIP[1]	**East GR**eenland **I**ce core **P**roject
ECM	**E**lectrical **C**onductivity **M**easurement
EDML	**E**PICA **D**ronning **M**aud **L**and
ELA	**E**quilibrium **L**ine **A**ltitude
EPICA	**E**uropean **P**roject for **I**ce **C**oring in **A**ntarctica
FDTD	**F**inite **D**ifference **T**ime **D**omain
GICC05	**G**reenland **I**ce-**C**ore **C**hronology 20**05**
GISP2	**G**reenland **I**ce-**S**heet **P**roject **2**
GRIP	**GR**eenland **I**ce-core **P**roject
GrIS	**Gr**eenland **I**ce **S**heet
IRH	**I**nternal **R**eflection **H**orizon
LGM	**L**ast **G**lacial **M**aximum
MCE	**M**aximum **C**ounting **E**rror
NEEM	**N**orth Greenland **EEM**ian Ice Drilling
NEGIS	**N**orth **E**ast **G**reenland **I**ce **S**tream
NorthGRIP	**North GR**eenland **I**ce-core **P**roject
ODF	**O**rientation **D**istribution **F**unction
pRES	**p**hase-sensitive **R**adio **E**cho **S**ounding
RES	**R**adio **E**cho **S**ounding
SAR	**S**ynthetic **A**perture **R**adar
UHF	**U**ltra **H**igh **F**requency
UWB	**U**ltra **W**ide **B**and

---

[1] sometimes also EGRIP

to my parents

Chapter 1

Aim and structure of this thesis

Ice cores provide the most direct and detailed information about the physical and chemical properties of ice and the prevailing conditions at a certain point in the ice sheet. The logistical costs, technical challenges, particularly in fast-flowing ice and shear margins, difficulty in reconstructing the absolute orientation of the core, and their limitation of being a point measurement, however, make ice cores impractical for a spatially extensive understanding of the ice characteristics. Yet, a large-scale description of material properties and processes relevant for ice flow is necessary for obtaining conclusive prognoses of ice-sheet evolution and sea-level rise by numerical models.

Geophysical methods, in particular Radio-Echo Sounding (RES), are more efficient in mapping basal and internal structures on large spatial scales and provide essential information for ice-sheet models. For example, the thickness and deformation of internal layers offers information about past accumulation rates in the source area and the ice-flow history. Moreover, the reflected signal depends on the geometrical structure of the reflector and is simultaneously affected by the physical properties of the ice column above. Hence, RES bears the potential of acquiring information on past flow dynamics as well as the physical properties affecting ice-flow processes today. The work presented in this thesis aims to combine observations from the East Greenland Ice-core Project (EastGRIP) deep ice core with RES data recorded in the Northeast Greenland Ice Stream (NEGIS) onset to bridge between the small-scale detailed ice-core information and the larger scales required for a thorough understanding of ice-flow dynamics in the NEGIS and ice streams in general.

The thesis is structured as follows:

- Chapter 2 aims to introduce the reader to the characteristics of ice sheets and the processes by which they interact with its surrounding. A brief overview is given about the role ice sheets played in the climate system in the past providing the context to current developments. This chapter also gives an introduction to the ice-sheet dynamics and the processes which are relevant for ice flow. Finally, the reader is introduced to the characteristics of the NEGIS and the survey area of its onset region.
- Chapter 3 gives an overview and theoretical background on the scientific methods used in this thesis. These include ice-core analysis, Radio-Echo-Sounding and ice-flow modeling. I thereby focus particularly on the ice-core measurements which can provide information about past climate and flow, and which are relevant for the work presented in this thesis. I elaborate on some technical aspects of the RES method and introduce the reader to the EGRIP-NOR-2018 survey which provides much of the data used in my studies. Finally, a brief overview is provided on ice-flow models and the information which is necessary to overcome some of their shortcomings and improve their reliability in prognostic simulations of future ice-sheet evolution.
- Chapter 4 presents my efforts in determining the source area and upstream effects in the EastGRIP ice core by simulating the propagation of internal reflections observed in radargrams. The work presented in this chapter has been published in *'The Cryosphere'*:

Gerber, T. A., Hvidberg, C. S., Rasmussen, S. O., Franke, S., Sinnl, G., Grinsted, A., Jansen, D., and Dahl-Jensen, D. (2021). "Upstream flow effects revealed in the EastGRIP ice core using Monte Carlo inversion of a two-dimensional ice-flow model", In: *The Cryosphere*, 15, pp. 3655–3679, https://doi.org/10.5194/tc-15-3655-2021.

- **Chapter 5** focuses on determining the crystal orientation fabric in the NEGIS onset region with a combination of methods. Radar-based analyses provide insight into the horizontal fabric anisotropy and are compared to ice-core observations and numerical modeling of fabric evolution. By calculating directional enhancement factors, the impact of the fabric on ice viscosity is estimated and discussed in terms of its effect on the ice-stream dynamics. This chapter is a manuscript which will soon be submitted to '*Nature Geoscience*'.
- **Chapter 6** demonstrates my studies on theoretical concepts of radar wave propagation using numerical modeling with GprMax. Here, I used measurements of the EastGRIP ice core to determine the nature of internal reflections and to investigate the effects of anisotropy from directional layer roughness. I further discuss the strengths and limitations of GprMax for glaciological applications. This chapter is a draft version of a manuscript that could be published in a similar form in the future.
- **Chapter 7** gives a brief overview of my contributions as a co-author in publications which are related to the work presented in this thesis.
- **Chapter 8** summarizes the work achieved during my PhD and discusses the implications of my findings in a wider glaciological context. This chapter also provides an outlook on how some of the numerous, still remaining questions concerning ice-stream dynamics could be addressed in the future, and ends with a few concluding remarks.

Chapter 2

General introduction

The Earth's climate is a significant factor controlling living conditions on our planet, and the climate history has considerably shaped the world we know today. Triggered by external forcing such as solar activity and changes in the Earth's orbit or by interactions within various components of the Earth system, the global climate has naturally changed many times in the past. While some of these changes occurred slowly and steadily, leaving time for adaption and migration of living organisms, others happened on much shorter time scales, leading to mass extinction, the formation of new ecosystems, and eventually the evolution of new species (Bennett, 1990).

Human activities of the recent past have noticeably increased the greenhouse gas concentration in the atmosphere, which has already led to an increase in the global mean surface temperature of 0.84–1.10°C since 1850–1900 (IPCC, 2021). In 2019, the CO_2 concentration in the atmosphere has likely been higher than at any time in the past 2 Million years (IPCC, 2021). The pace at which we are currently altering the climate is unprecedented over many thousands of years and has a direct impact on our lives and living resources all over the world. One consequence of climate change is the increased frequency of extreme weather events such as heavy precipitation, hurricanes, hot extremes, droughts, and wildfires (IPCC, 2014a). The second type of impact includes slower, more extensive, and long-lasting changes to the Earth system: Rising sea level causes higher risks of floodings and threatens coastal areas and islands to drown; the acidification of the oceans endangers sensitive marine ecosystems and food security of thousands of people; and changes in wind, ocean circulation, and precipitation patterns lead to an overall shift of climate zones towards the poles. These developments bring vast social, economic, and environmental problems that will be amplified in the years to come. Understanding the complexity of the climate system, the ongoing changes in its components and the interaction between them is thus crucial to predict and prepare for the current and future challenges related to the climate crisis.

The individual components of the climate system react at different time scales, and many of the ongoing developments will continue even in the absence of further emissions. Some of these processes can trigger positive feedback mechanisms and cascade effects, and might be irreversible in the foreseeable future (Brovkin et al., 2021). One of these so-called tipping points is the collapse of the polar ice sheets of Greenland and West Antarctica: Once a critical temperature is held for sufficiently long, the ice sheets will shrink inexorably due to self-amplifying effects until they disappear entirely (Ridley et al., 2010). When tipping points are passed, decreasing temperatures to the pre-industrial level will not be enough to stabilize the ice sheets, and the re-growth of similar-sized ice bodies would require a much colder climate for tens of thousands of years (Alley et al., 2010). While the exact position of tipping points is not precisely known, it is unmistakably clear that a world without glaciers and ice sheets would be a very different one.

2.1 Ice sheets and their role in the Earth system

Ice sheets stand in direct and constant interaction with the ocean, the atmosphere, and the solid Earth. Together with glaciers, ice caps, sea ice, snow, and permafrost, they form the cryosphere and constitute part of the complex and interwoven climate system. Changes in one of its components can have far-reaching, direct, or indirect effects on other elements of the Earth system. Because of this interconnection, ice sheets not only react passively to changes in temperature and precipitation but influence the climate directly through feedback mechanisms on local, regional, and global scales.

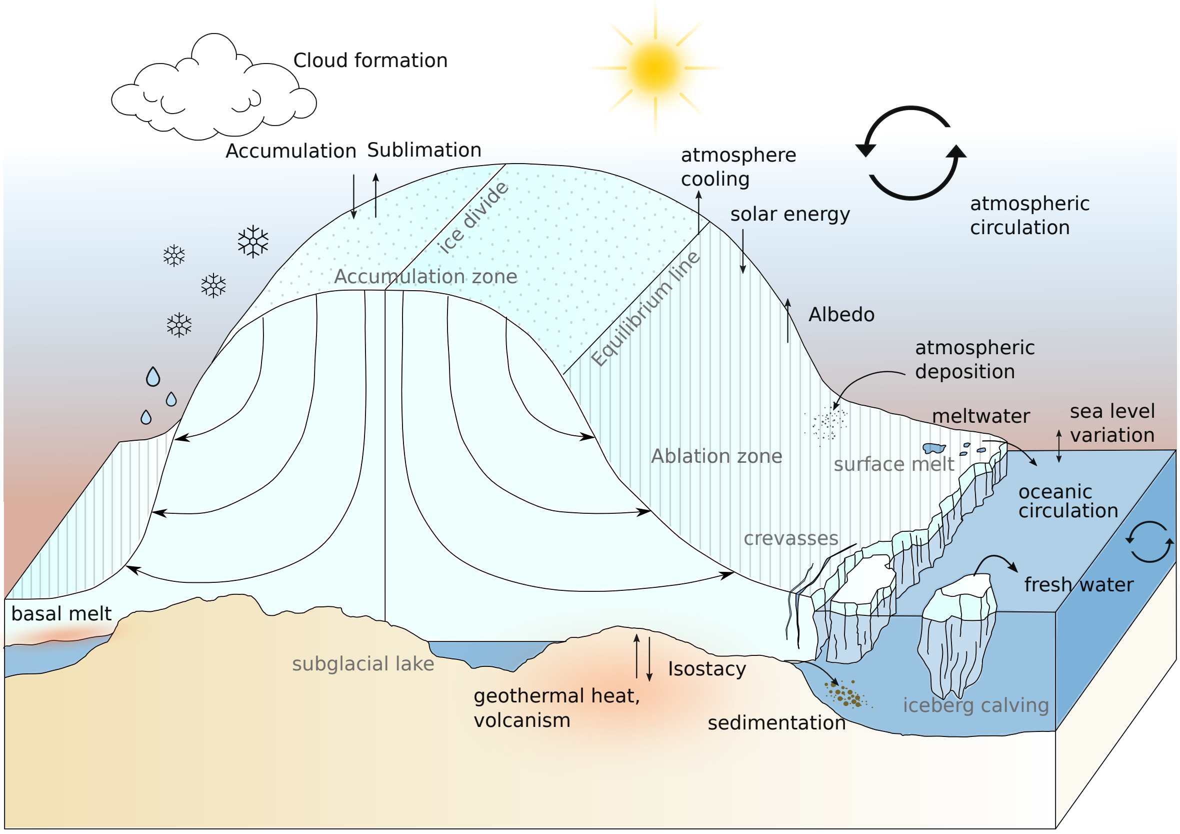

FIGURE 2.1: Illustration of interaction processes between a typical ice sheet and the atmosphere, the ocean, and the solid Earth. Interactions are two-sided; Ice sheets not only react to changes in its surrounding, but also influence the environment directly. Figure modified from Ahlenius (2016).

Figure 2.1 illustrates the most important components of a typical ice sheet and the interactions with its direct surrounding. Ice sheets usually are thickest in their center, reaching heights of 3-4 km above the bed (e.g. Bamber et al., 2001; Fretwell et al., 2013). Temperatures at these elevations normally are cold enough so that precipitation falls as snow all year round and surface melt is rare. The ice body thins out towards the edges, and the surface is located in warmer atmospheric layers at lower elevations. The temperatures there can be warm enough so that ice melts and precipitation falls as rain during the summer months. The ice-sheet margin is also typically where mass loss exceeds mass gain and where the ablation zone is located. The equilibrium line separates this area from its counterpart, the accumulation zone, where the mass accumulation is larger than mass loss. In steady-state, ice sheets keep their shape by transporting mass from the accumulation zone to the ablation zone, mainly due to internal deformation and sliding over the bed (e.g. Budd and Jacka, 1989). Mass accumulation occurs primarily through snowfall, whereas melt, sublimation, and iceberg calving are the main processes responsible for mass loss. The ice-sheet mass balance determines whether ice sheets grow or shrink: if the total mass loss exceeds the mass gain, the mass balance is negative, and the ice sheet shrinks, while a positive mass balance leads to ice-sheet growth.

Atmospheric circulation transports moisture and heat, and is essentially responsible for the climate on regional scales, affecting, for instance, the amount of snowfall. In return, the presence of ice sheets influences the atmosphere through their topography and cold surface that affect winds and the formation of clouds (e.g. Vizcaino et al., 2008). Another important positive feedback mechanism is the reflectivity of the Earth's surface or *albedo*. Due to its brightness, snow reflects a tremendous amount of the sunlight, so snow-covered glaciers, ice sheets, sea ice, and landscapes have a cooling effect (Box et al., 2012). As the extent of the cryosphere decreases, more solar energy is absorbed by the darker ocean and snow-free surfaces which reinforces the warming trend. The albedo of ice sheets can also decrease when its surface color changes, for example, by atmospheric deposition of natural and industrial particles or the presence of surface meltwater (Gardner and Sharp, 2010). At depth, ice sheets interact with the solid Earth too. Geothermal heat can lead to basal melt and facilitate ice flow through the presence of water (e.g. Pollard et al., 2005). On the other hand causes the weight of ice sheets a depression in the underlying lithosphere and asthenosphere and leads to a post-glacial rebound after its removal. The weight re-distribution by fluctuating ice sheets can affect geological processes on longer time scales than climatic oscillations. This is why a continental uplift can be observed among other places in Scandinavia today, long after the ice sheet has disappeared (Emery and Aubrey, 1985). Post-glacial rebound affects the landscape through changes in sedimentation and erosion processes and can also facilitate melt formation in the asthenosphere due to mantle decompression, stimulating volcanic activity (Stevens et al., 2016).

Ultimately, ice-sheet fluctuations affect the global sea level and oceanic current systems. When ice sheets shrink, meltwater flows into the ocean and changes the salinity and temperature gradients (e.g. Vizcaino et al., 2008; Swingedouw et al., 2009; Ivanovic et al., 2018). These are the main factors controlling the thermohaline conveyor belt, a global oceanic current system that transports heat and nutrients and is, among other things, responsible for the mild climate in Europe. Perturbations of ocean currents related to freshwater input can have consequences reaching global scales and constitute another tipping point in the climate system (Stocker and Wright, 1991).

Today's ice sheets sit near the poles, but during the cold phases of the Quaternary, larger areas were covered by continental bodies of ice. Since the beginning of the Pleistocene 2.58 Ma ago, the Earth's climate experienced numerous cycles of extensive glaciation, interrupted by warmer interglacial periods such as the current Holocene. The occurrence of past ice ages was dictated by astronomical cycles with periodicities of 23,000, 41,000, and 100,000 years (Broecker, 1966). Geological archives (Fig. 2.2) show that high levels of CO_2 in the atmosphere and warm temperatures during the interglacials correlate with high sea levels (Alley et al., 2005; Berends et al., 2021) governed by the advance and retreat of glaciers and ice sheets. The transition between glacial and interglacial periods is initiated by favorable parameters of the Earth's orbit, leading to an increase in global temperature and atmospheric CO_2 concentrations released by a warmer ocean (Sigman et al., 2010). Acting as a greenhouse gas, CO_2 amplifies the warming effect to which glaciers and ice sheets respond by shrinking, and the mass transfer from land to the ocean leads to higher sea levels during warmer periods. The transition into cold phases can be understood in a similar, reversed fashion.

During the last glacial maximum (LGM), 21,000 years ago, the total ice volume was about twice as large as today, burying broad areas of North and South America, Scandinavia, parts of Asia and New Zealand under kilometer-thick ice (Clark and Mix, 2002; Hulton et al., 2002). Only the ice sheets of Greenland and Antarctica survived the subsequent phase of deglaciation leading up to the current interglacial period. At least twice during the past 20,000 years, the

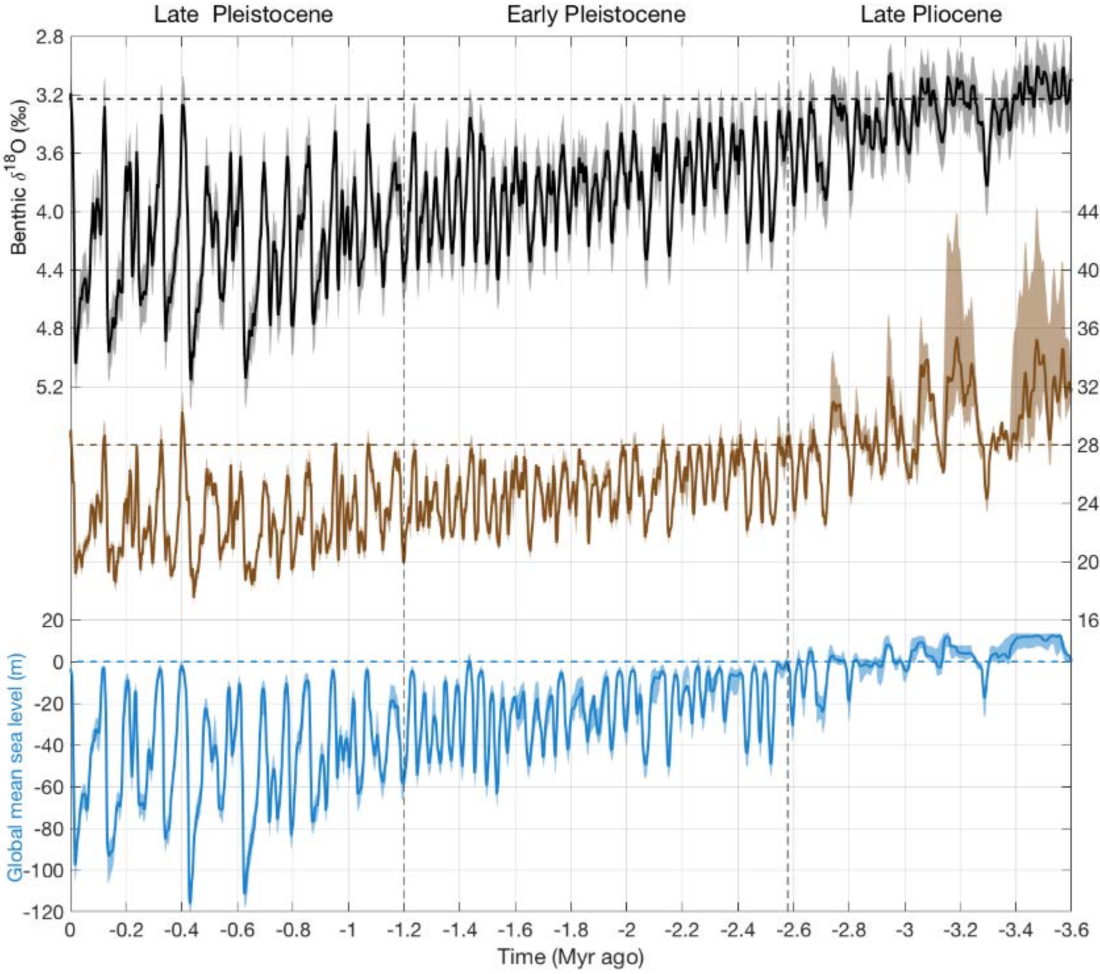

FIGURE 2.2: Climate variability during the Pleistocene (Berends et al., 2021): The $\delta^{18}O$ record acts as a proxy for temperature and correlates with high atmospheric CO_2 concentrations and global sea level. A general trend of decreasing temperatures is superimposed by cyclic climate variations of 41,000 years in the early Pleistocene. At the Mid-Pleistocene transition, 1.2 Myr ago, the ice age periodicity shifted to a cycle length of 100,000 years, which dominated the climate during the late Pleistocene.

collapse of ancient ice sheets released enormous amounts of freshwater into the ocean, corresponding to 1.5–3 times the water equivalent of the Greenland ice sheet, and raised the global sea level by approximately 24–28 m within a few centuries (Fairbanks, 1989). Today, the ice sheets of Greenland and Antarctica store 99 % of all ice on Earth, accommodating approximately 68 % of our freshwater resources (Gleick, 1993). Greenland contains enough ice to raise the global sea level by 7.4 m (Morlighem et al., 2017), while the ice volume of Antarctica corresponds to an additional 58 m sea-level rise equivalent (Fretwell et al., 2013). Yet, a global sea level rise of only a few meters would be enough to pose a severe threat to the human population and crucial infrastructure concentrated in coastal areas. Thousands of islands, coral reefs, and vulnerable ecosystems would be endangered to drown in rising seas, and storms would have a greater potential to cause damage by flooding. During the past century, the global sea level has risen by ∼0.19 m (IPCC, 2014b), partially due to the thermal expansion of water under higher temperatures but primarily due to the melting of land ice. Currently, an acceleration of sea level rise is observed (Dangendorf et al., 2019). How this trend evolves in the 21st century and beyond will strongly impact the lives of future generations, but predictions are complicated, and uncertainties are large. Future sea level scenarios depend mainly on the contribution from the

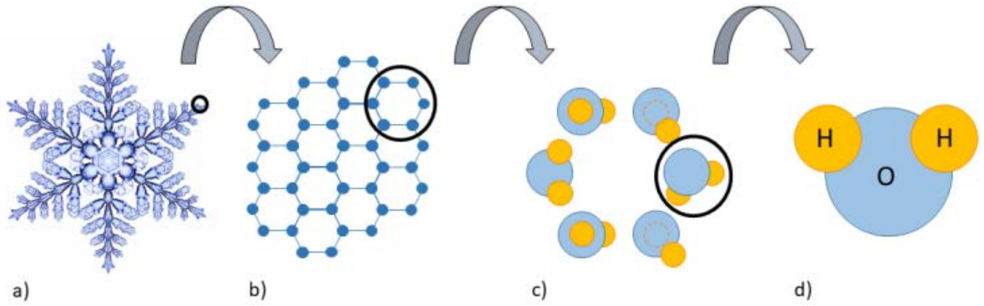

FIGURE 2.3: The hexagonal properties of an ice crystal **a)** results from its molecular structure **b)**. It consists of hexagonal rings **c)** which are created by the alignment of the individual H_2O molecules **d)** due to electrostatic forces. Figure adapted from (Nelson, 2011).

cryosphere. However, many gaps remain in our understanding of how and how fast glaciers and ice sheets respond to climate change. One of the most considerable uncertainties arises from our insufficient understanding of processes related to ice flow and dynamic mass loss of ice sheets.

2.2 Ice-sheet dynamics

Ice sheets form through the accumulation of snow over tens of thousands of years: Each year, a new snow layer is added to the surface, and the accumulated load compresses the underlying snowpack. Gradually, the older snow is transformed into firn and eventually into ice. Glacier ice behaves like a viscous fluid deforming under its own weight and is constantly moving. The slow and continuous ice deformation is known as creep and strongly depends on the grain-scale structure and physical properties of the ice. In addition to the internal deformation of ice, basal sliding and deformation of basal material contributes to ice flow which re-distributes mass withing glaciers and ice sheets. A brief overview of the relevant processes is given in the following.

2.2.1 Structure and deformation of glacier ice

When water freezes under conditions prevailing on the Earth's surface, H_2O molecules bind to layers of hexagonal rings (Fig. 2.3). The hexagonal crystal structure arises from electrostatic forces acting between positively charged hydrogen atoms and negatively charged ion pairs (Pauling, 1935; Petrenko and Whitworth, 2006). Like a deck of cards, a single ice crystal consists of several layers stacked on top of one another. The plane of the ring layers is termed the *basal plane*, while the direction perpendicular to it is called the *c-axis*. The deformation of single ice crystals occurs through *dislocation glide* along crystallographic planes (e.g. Weiss and Grasso, 1997; Montagnat et al., 2006), i.e. small defects in the crystal lattice that facilitate the movement of atoms past one another. This mechanism is several orders of magnitude easier along the basal plane than in any other direction (Duval et al., 1983), so ice crystals are mechanically anisotropic.

Glacier ice consists of billions of ice crystals. The crystal orientation fabric (COF), or simply *fabric*, describes the orientation of the individual crystal axes in polycrystalline ice. In freshly deposited snow, along with firn and ice which has not yet experienced strong deformation, ice crystals usually are oriented randomly, so the bulk mechanical properties are isotropic

(Fig. 2.4b). When ice deforms, the alignment of atoms in the crystal lattice and the location of grain boundaries change through processes generally summarized as *recrystallization*. These deformation mechanisms initiate the apparent rotation of crystals to minimize the lattice strain energy, so the c-axes tend to point in the direction of dominant compression (e.g. Gow and Williamson, 1976; Azuma and Higashi, 1985). Fabrics with a preferred c-axis orientation, also called anisotropic COF, lead to anisotropic bulk mechanical properties (Fig. 2.4c) and have significant effects on ice flow, as ice becomes stiffer in the preferred c-axis direction while softening for shear strain along the basal planes.

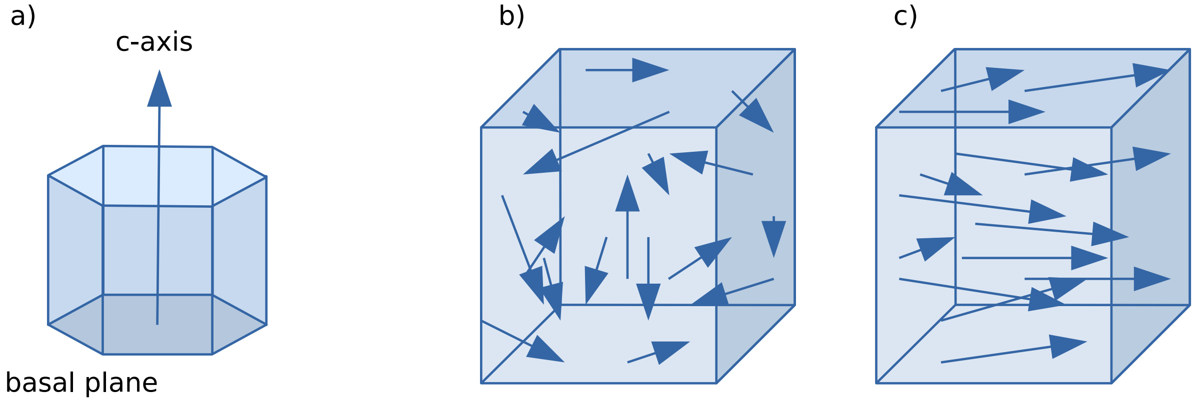

FIGURE 2.4: **a)** The susceptibility to shear deformation of single ice crystals is several orders of magnitude larger along the basal plane in comparison to the c-axis or other directions. **b)** The effect of this anisotropy is not noticeable in the bulk mechanical properties of polycrystalline glacier ice if the crystals are randomly oriented. **c)** In case of a preferred alignment of the c-axis, however, the ice viscosity strongly depends on the applied strain relative to the COF.

The crystal orientation is not the only factor controlling the ice viscosity. In contrast to the COF however, other factors, namely temperature, water and air content, grain size, and impurities, affect the ice deformation equally in all directions. The creep relation, or flow law, connects the strain rate, $\dot{\epsilon}$, to deviatoric stresses, τ, and for isotropic ice it can be written in a simplified form (Glen, 1958) :

$$\dot{\epsilon} = A\tau^n. \tag{2.1}$$

Experiments have shown that the creep exponent n assumes values between 1.5 and 4.2 (Weertman, 1983), but n = 3 is assumed in most glacier models, although the justification of this common assumption is still under discussion (e.g Bons et al., 2018) . The empirical flow parameter A accounts for the ice viscosity and is primarily dominated by temperature. Warm ice becomes softer through increased dislocation mobility and wider grain boundaries (Barnes et al., 1971). In temperate ice, the presence of water can further decrease the viscosity as it supports geometrical adjustments of neighboring grains by facilitating grain-boundary sliding or melting and refreezing (Barnes et al., 1971; Duval, 1977). The flow parameter A is also a function of density, as in presence of air bubbles, ice becomes porous and more susceptible to deformation (Budd and Jacka, 1989). However, this is only relevant in the uppermost part of the ice sheet. Bubbles are abundant in glacier ice and make up 10 % of the volume at the firn–ice transition, but the bubble size decreases as a function of depth, as the air is compressed by the increasing surrounding ice pressure. The gas pressure within the bubbles increases too until gas molecules form *clathrate hydrates* and air bubbles disappear (Miller, 1969).

The role of grain size is not yet entirely understood but experiments indicate that the susceptibility to deformation increases with decreasing grain size, at least for fine-grained ice under low stresses (Baker, 1978; Duval and Gac, 1980). It is, however, difficult to study the relation between crystal size and deformation rate independently because they both affect one another. The direct effect of impurities on the viscosity is not entirely understood either: Impurities can appear as particles, liquids and gases. Some of them can substitute for molecules in the H_2O lattice, and decrease the ice viscosity by creating additional dislocations. Most impurities, however, accumulate at the grain boundaries and, while not altering the viscosity directly, they indirectly play a role through their effect on fabric evolution, grain size and dislocation density (Song et al., 2006). Ice with a high impurity content, e.g. from cold periods, tends to have smaller crystals and deforms more readily compared to purer ice from warmer times (Herron and Langway, 1982; Fisher and Koerner, 1986; Dahl-Jensen and Gundestrup, 1987; Durand et al., 2006).

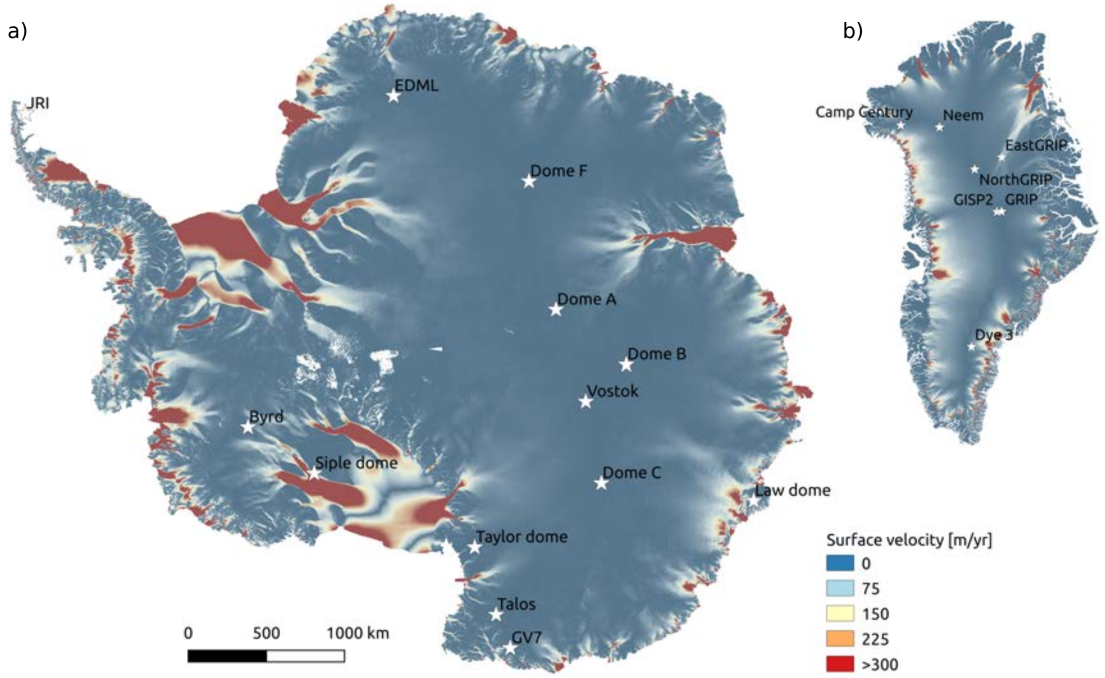

FIGURE 2.5: Surface velocities of **a)** the Antarctic and **b)** the Greenland ice sheets, inferred from satellite measurements (Rignot et al., 2011; Mouginot et al., 2012; Joughin et al., 2018) and locations of deep ice-core drilling projects.

2.2.2 Ice flow mechanics

The stunning landscapes of subarctic and alpine regions with fjords, U-shaped valleys, moraines, and planes with fruitful soil are the result of ancient glaciers and ice sheets flowing through the area. Ice flow re-distributes mass from topographic highs to lows and is the key factor determining the shape of glaciers and ice sheets. Ice flow is also directly linked to dynamic discharge trough iceberg calving and is thus an important contribution to the mass balance of glaciers and ice sheets (Shepherd et al., 2020). Understanding the mechanisms governing ice flow is therefore crucial for prognostic models that are used to simulate the ice-sheet evolution in the future. Figure 2.5 shows the surface velocities obtained from satellite measurements in Greenland and Antarctica (Rignot et al., 2011; Mouginot et al., 2012; Joughin et al., 2018). In the ice-sheet center, particularly near topographic domes and ice divides, the surface velocities are small. Ice flow generally speeds up towards the ice-sheet margins and reach the highest velocities when the flow is channeled in ice streams and glaciers, which eventually discharge into the ocean by feeding floating ice shelves or calving icebergs. The observed surface velocities arise from a combination of internal creep, sliding over the bed and the deformation of basal material. The main driving stress is gravity acting on the ice mass and exercises a force in the direction of

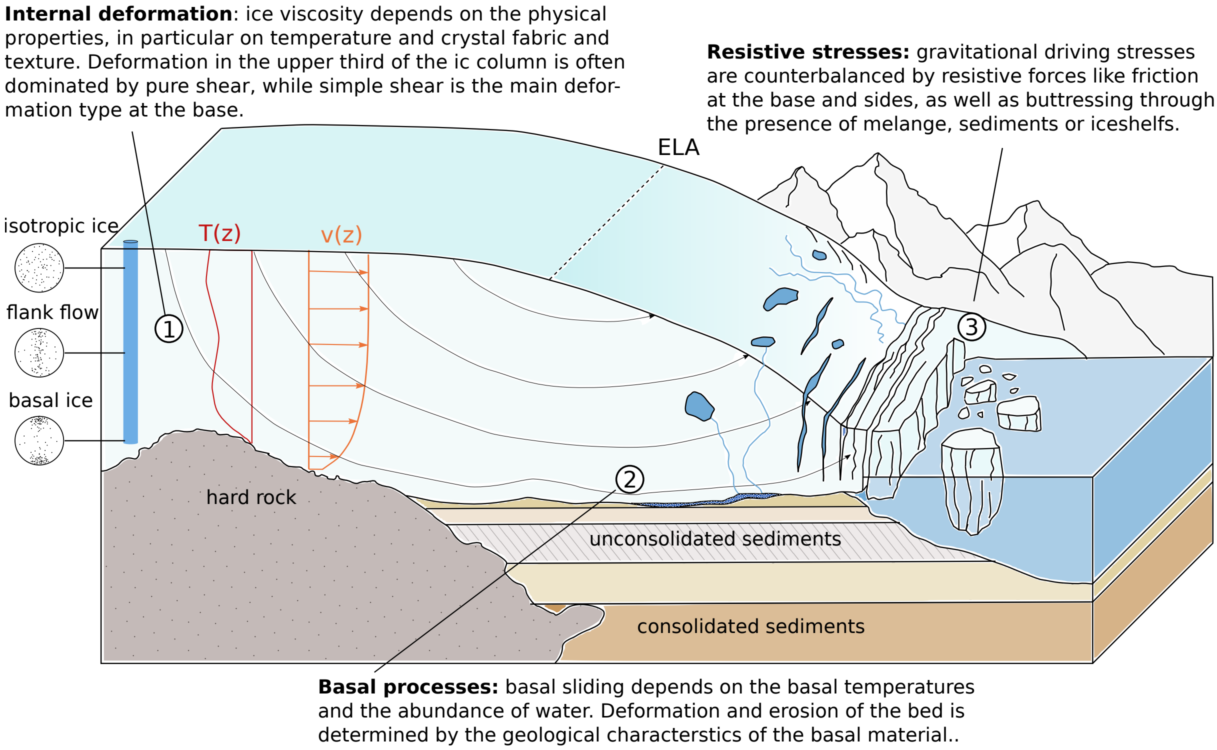

Internal deformation: ice viscosity depends on the physical properties, in particular on temperature and crystal fabric and texture. Deformation in the upper third of the ic column is often dominated by pure shear, while simple shear is the main deformation type at the base.

Resistive stresses: gravitational driving stresses are counterbalanced by resistive forces like friction at the base and sides, as well as buttressing through the presence of melange, sediments or iceshelfs.

Basal processes: basal sliding depends on the basal temperatures and the abundance of water. Deformation and erosion of the bed is determined by the geological characterstics of the basal material..

FIGURE 2.6: Illustration summarizing the key processes relevant for ice flow. **1)** Part of the ice movement originates from the internal deformation of ice and depends on its physical characteristics such as temperature, crystal fabric and impurities. **2)** The other important contribution to ice flow is basal sliding and deformation of basal material. **3)** Buttressing from ice shelves, melange and friction at the bed or at mountain flanks provides resistance counterbalancing the gravitational force.

decreasing surface slope. This is counter-balanced by resisting forces within the ice and at its boundaries at the bed, mountain flanks and glacier terminals (Fig. 2.6). The most important resisting force is exercised at the bed. The magnitude of basal resistance depends on the type of rock and sediment, the ice temperature and the availability of melt water. Beds can consist of rigid rock or softer, easily deformable sediments. Temperatures close to the melting point and the presence of water can facilitate rapid deformation when the water pressure is close to the weight of the overlying ice (Budd and Jacka, 1989). However, direct observation of basal processes are restricted to the few locations where boreholes reach the bed and, therefore, basal properties remain one of the largest uncertainties in ice-sheet models (Babaniyi et al., 2021).

Ice typically flows fastest at the surface and the velocity remains nearly constant in the upper third of the ice sheet (Paterson, 1983), where the major deformation mechanism is pure shear. With further depth, the velocity decreases until it reaches the magnitude of basal motion or becomes zero if the bed is frozen. Here deformation occurs primarily through simple shear. Within the ice column the deformation mechanism is a mixture of these two end-members. Ice flow not only leaves traces at the bed through erosion and sediment deposition but also induces signatures in the internal stratigraphy (e.g. NEEM Community members et al., 2013; Franke et al., 2022a). Initially homogeneously deposited layers are compressed and stretched, folded and overturned as a consequence of ice flow. Folded layers and physical properties of ice, in particular the fabric, can act as tracers of past ice flow activities (e.g. Bons et al., 2016; Jansen et al., 2016; Lilien et al., 2021).

Ice streams are areas where the ice flows particularly fast in a channeled manner, and is efficiently transported from the ice-sheet interior towards outlet glaciers, typically calving into the ocean or flowing into floating ice shelves. Ice streams play a central role in the ice-sheet mass balance and stability (Alley and Bindschadler, 2001). About 90 % of the Antarctic (Bentley and Giovinetto, 1991) and 50 % of the Greenland (Rignot and Kanagaratnam, 2006) ice mass is lost through ice streams and outlet glaciers. Some ice streams are constrained by the bed topography where ice flow is channeled and accelerated due to a number of reasons: Enhanced ice thickness over topographic lows can lead to larger basal driving stresses and basal temperatures, and lubricating meltwater is more likely to exist in topographic lows (Bennett, 2003). Other ice streams, however, lack those topographic boundaries, and different processes, e.g. ice rheology or basal sliding must be responsible for the rapid ice flow.

2.3 Regional overview

The research presented in this thesis mostly focuses on the onset region of the North East Greenland Ice Stream (NEGIS, Fig. 2.7), although the results also have implications for other areas. The NEGIS is the largest active ice stream of the Greenland ice sheet and efficiently drains a considerable part of northeastern Greenland (Khan et al., 2014). The ice stream initiates around 50 km from the central ice divide and spans over more than 700 km towards the northeastern coast, where it discharges ice through the three marine outlet glaciers Nioghalvfjerdsfjorden glacier, Zachariae isbræ and Storstrømmen glacier.

Unlike most other ice streams in Greenland, the NEGIS is not constrained by an extensive overdeepened bed (Joughin et al., 2001; Franke et al., 2020), but is separated from the slow-moving ice by well-defined shear margins. While increasing amount of ice is dragged into the ice stream along flow, the ice flow accelerates and the ice stream symmetrically widens with downstream distance (Fahnestock et al., 2001b). The East GReenland Ice-core Project (EastGRIP) is the first deep ice core being retrieved in a fast-flowing ice stream. The drill site is located in the ice-stream center where surface velocities of around 55 ma^{-1} are measured (Hvidberg et al., 2020). The drilling project started in 2015 and by 2019, a depth of 2122 m was reached, almost 80 % of the expected ice thickness of 2680 m (Franke et al., 2020). Due to the Covid-19 pandemic, the project has been put on halt for two subsequent years, but drilling activities are resumed in 2022.

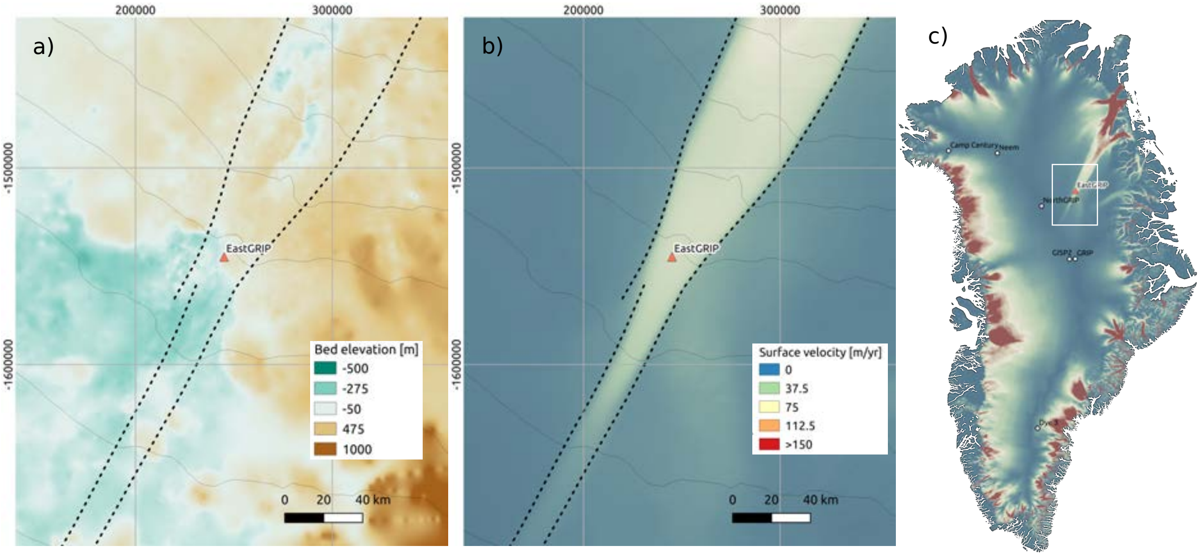

FIGURE 2.7: **a)** Bed topography (Franke et al., 2020) and **b)** surface velocities (Joughin et al., 2018) of the NEGIS, located in the northeastern part of **c)** the Greenland Ice Sheet. The EastGRIP ice-core site is located in the ice-stream center of the NEGIS onset, just before a remarkable step in the bed topography.

The ice core and the large number of associated surface-based scientific projects are an important contribution towards understanding the mechanisms governing ice flow in the NEGIS and ice streams in general. In the past decade, a number of studies have been published that provide pieces of information contributing to a better comprehension of the ice dynamics in the region and ultimately improve our ability of reproducing ice streams in ice-flow models. Basal analyses by Franke et al. (2020) showed that the basal morphology upstream of EastGRIP is smooth with elongated flow-parallel structures. In the vicinity of EastGRIP, the bed elevation increases from below sea level to ∼200 m above sea level. The basal topography on this plateau is more rough and variable, and the ice stream seems to be topographically constrained by a valley that arises ∼135 km downstream of EastGRIP. Christianson et al. (2014) analyzed data from a radar survey conducted in 2014 and identified the basal material to be porous, water-saturated till that is easy to deform and might facilitate fast ice-flow. The same data also suggests that the basal hydrology plays a dominant role in confining the NEGIS in the upstream part (Keisling et al., 2014). The presence of considerable amount of meltwater was also suggested by Fahnestock et al. (2001b) and Zeising and Humbert (2021) who found evidence of high basal melt rates. An exceptionally high geothermal heat flux is also required by some modeling efforts in order to reproduce the high surface velocities (Smith-Johnsen et al., 2020b). However, Bons et al. (2021) called attention to the fact that a geothermal heat flux of 970 $\mathrm{mWm^{-2}}$ often discussed would be higher than anywhere else in the world, including highly volcanic areas like Iceland or Yellowstone. This is in contradiction to any known geological processes and suggests that basal heat alone cannot explain the presence and current state of the NEGIS. Analyses of RES and seismic data by Riverman et al. (2019) revealed higher firn-densification rates in the shear margins related to high along-flow stresses. They suggest that the resulting surface troughs affect the hydropotential which currently stabilizes the position of the NEGIS shear margins. The role of the shear margins was also studied by Holschuh et al. (2019a) who found evidence that they could be between 3–6°C warmer than the surrounding ice, and that ice flow is partially facilitated by temperature-controlled shear-margin softening. Yet, many questions remain to be answered to understand the processes related to the formation, maintenance and future evolution of the NEGIS.

References

Ahlenius, H. (2016). *Ice sheets, schematic illustration for Greenland and Antarctica*. URL: https://www.grida.no/resources/5222 (visited on 05/18/2022).

Alley, R. B. and Bindschadler, R. A. (2001). “The West Antarctic ice sheet and sea-level change”. In: *The West Antarctic ice sheet: behavior and environment* 77, pp. 1–11. DOI: 10.1029/AR077p0001.

Alley, R. B., Clark, P. U., Huybrechts, P., and Joughin, I. (2005). “Ice-sheet and sea-level changes”. In: *science* 310.5747, pp. 456–460. DOI: 10.1126/science.1114613.

Alley, R. B., Andrews, J., Brigham-Grette, J., Clarke, G., Cuffey, K., Fitzpatrick, J., Funder, S., Marshall, S., Miller, G., Mitrovica, J., Muhs, D., Otto-Bliesner, B., Polyak, L., and White, J. (2010). “History of the Greenland Ice Sheet: paleoclimatic insights”. In: *Quaternary Science Reviews* 29.15-16, pp. 1728–1756. DOI: 10.1016/j.quascirev.2010.02.007.

Azuma, N. and Higashi, A. (1985). “Formation processes of ice fabric pattern in ice sheets”. In: *Annals of Glaciology* 6, pp. 130–134. DOI: 10.3189/1985AoG6-1-130-134.

Babaniyi, O., Nicholson, R., Villa, U., and Petra, N. (2021). “Inferring the basal sliding coefficient field for the Stokes ice sheet model under rheological uncertainty”. In: *The Cryosphere* 15.4, pp. 1731–1750. DOI: 10.5194/tc-15-1731-2021.

Baker, R. W. (1978). “The Influence of Ice-Crystal Size on Creep”. In: *Journal of Glaciology* 21.85, pp. 485–500. DOI: 10.3189/S0022143000033633.

Bamber, J. L., Layberry, R. L., and Gogineni, S. (2001). “A new ice thickness and bed data set for the Greenland ice sheet: 1. Measurement, data reduction, and errors”. In: *Journal of Geophysical Research: Atmospheres* 106.D24, pp. 33773–33780. DOI: 10.1029/2001JD900054.

Barnes, P., Tabor, D., and Walker, J. (1971). “The friction and creep of polycrystalline ice”. In: *Proceedings of the Royal Society of London. A. Mathematical and Physical Sciences* 324.1557, pp. 127–155. DOI: 10.1098/rspa.1971.0132.

Bennett, K. D. (1990). “Milankovitch cycles and their effects on species in ecological and evolutionary time”. In: *Paleobiology* 16.1, pp. 11–21. DOI: 10.1017/S0094837300009684.

Bennett, M. R. (2003). “Ice streams as the arteries of an ice sheet: their mechanics, stability and significance”. In: *Earth-Science Reviews* 61.3-4, pp. 309–339. DOI: 10.1016/S0012-8252(02)00130-7.

Bentley, C. R. and Giovinetto, M. (1991). “Mass balance of Antarctica and sea level change”. In: *International Conference on the Role of the Polar Regions in Global Change* 2, pp. 481–488.

Berends, C. J., De Boer, B., and Van De Wal, R. S. (2021). “Reconstructing the evolution of ice sheets, sea level, and atmospheric CO_2 during the past 3.6 million years”. In: *Climate of the Past* 17.1, pp. 361–377. DOI: 10.5194/cp-17-361-2021.

Bons, P. D., Riese, T. de, Franke, S., Llorens, M.-G., Sachau, T., Stoll, N., Weikusat, I., Westhoff, J., and Zhang, Y. (2021). “Comment on “Exceptionally high heat flux needed to sustain the Northeast Greenland Ice Stream” by Smith-Johnsen et al.(2020)”. In: *The Cryosphere* 15.5, pp. 2251–2254. DOI: 10.5194/tc-15-2251-2021.

Bons, P. D., Jansen, D., Mundel, F., Bauer, C. C., Binder, T., Eisen, O., Jessell, M. W., Llorens, M.-G., Steinbach, F., Steinhage, D., and Weikusat, I. (2016). “Converging flow and anisotropy cause large-scale folding in Greenland’s ice sheet”. In: *Nature communications* 7.1, pp. 1–6. DOI: 10.1038/ncomms11427.

Bons, P. D., Kleiner, T., Llorens, M.-G., Prior, D. J., Sachau, T., Weikusat, I., and Jansen, D. (2018). “Greenland Ice Sheet: Higher nonlinearity of ice flow significantly reduces estimated basal motion”. In: *Geophysical Research Letters* 45.13, pp. 6542–6548. DOI: 10.1029/2018GL078356.

Box, J., Fettweis, X., Stroeve, J., Tedesco, M., Hall, D., and Steffen, K. (2012). “Greenland ice sheet albedo feedback: thermodynamics and atmospheric drivers”. In: *The Cryosphere* 6.4, pp. 821–839. DOI: 10.5194/tc-6-821-2012.

Broecker, W. S. (1966). “Absolute Dating and the Astronomical Theory of Glaciation: Changes in climate occur in response to periodic variations in the earth’s tilt and precession.” In: *Science* 151.3708, pp. 299–304. DOI: 10.1126/science.151.3708.299.

Brovkin, V., Brook, E., Williams, J. W., Bathiany, S., Lenton, T. M., Barton, M., DeConto, R. M., Donges, J. F., Ganopolski, A., McManus, J., Praetorius, S., Vernal, A. de, Ab-Ouchi, A., Cheng, H., Claussen, M., Crucifix, M., Gallopin, G., Iglesias, V., Kaufman, D. S., Kleinen, T., Lambert, F., Leeuw, S. van der, Liddy, H., Loutre, M.-F., McGee, D., Rehfeld, K., Rhodes, R., Seddon, A. W., Trauth, M. H., Vanderveken, L., and Yu, Z. (2021). “Past abrupt changes, tipping points and cascading impacts in the Earth system”. In: *Nature Geoscience* 14.8, pp. 550–558. DOI: 10.1038/s41561-021-00790-5.

Budd, W. F. and Jacka, T. (1989). “A review of ice rheology for ice sheet modelling”. In: *Cold Regions Science and Technology* 16.2, pp. 107–144. DOI: 10.1016/0165-232X(89)90014-1.

Christianson, K., Peters, L. E., Alley, R. B., Anandakrishnan, S., Jacobel, R. W., Riverman, K. L., Muto, A., and Keisling, B. A. (2014). “Dilatant till facilitates ice-stream flow in northeast Greenland”. In: *Earth and Planetary Science Letters* 401, pp. 57–69. DOI: 10.1016/j.epsl.2014.05.060.

Clark, P. U. and Mix, A. C. (2002). “Ice sheets and sea level of the Last Glacial Maximum”. In: *Quaternary Science Reviews* 21.1-3, pp. 1–7. DOI: 10.1016/S0277-3791(01)00118-4.

Dahl-Jensen, D. and Gundestrup, N. (1987). “Constitutive properties of ice at Dye 3, Greenland”. In: *International Association of Hydrological Sciences Publication* 170, pp. 31–43.

Dangendorf, S., Hay, C., Calafat, F. M., Marcos, M., Piecuch, C. G., Berk, K., and Jensen, J. (2019). “Persistent acceleration in global sea-level rise since the 1960s”. In: *Nature Climate Change* 9.9, pp. 705–710. DOI: 10.1038/s41558-019-0531-8.

Durand, G., Gagliardini, O., Thorsteinsson, T., Svensson, A., Kipfstuhl, S., and Dahl-Jensen, D. (2006). “Ice microstructure and fabric: an up-to-date approach for measuring textures”. In: *Journal of Glaciology* 52.179, pp. 619–630. DOI: 10.3189/172756506781828377.

Duval, P. (1977). “The role of the water content on the creep rate of polycrystalline ice”. In: *IAHS Publ* 118, pp. 29–33.

Duval, P., Ashby, M., and Anderman, I. (1983). “Rate-controlling processes in the creep of polycrystalline ice”. In: *The Journal of Physical Chemistry* 87.21, pp. 4066–4074. DOI: 10.1021/j100244a014.

Duval, P. and Gac, H. L. (1980). “Does the Permanent Creep-Rate of Polycrystalline Ice Increase with Crystal Size?” In: *Journal of Glaciology* 25.91, pp. 151–158. DOI: 10/hwsk.

Emery, K. and Aubrey, D. (1985). “Glacial rebound and relative sea levels in Europe from tide-gauge records”. In: *Tectonophysics* 120.3-4, pp. 239–255. DOI: 10.1016/0040-1951(85)90053-8.

Fahnestock, M., Abdalati, W., Joughin, I., Brozena, J., and Gogineni, P. (2001b). “High geothermal heat flow, basal melt, and the origin of rapid ice flow in central Greenland”. In: *Science* 294.5550, pp. 2338–2342. DOI: 10.1126/science.1065370.

Fairbanks, R. G. (1989). “A 17,000-year glacio-eustatic sea level record: influence of glacial melting rates on the Younger Dryas event and deep-ocean circulation”. In: *Nature* 342.6250, pp. 637–642. DOI: 10.1038/342637a0.

Fisher, D. A. and Koerner, R. M. (1986). “On the special rheological properties of ancient microparticle-laden Northern Hemisphere ice as derived from bore-hole and core measurements”. In: *Journal of Glaciology* 32.112, pp. 501–510. DOI: 10.3189/S0022143000012211.

Franke, S., Jansen, D., Binder, T., Paden, J. D., Dörr, N., Gerber, T. A., Miller, H., Dahl-Jensen, D., Helm, V., Steinhage, D., Weikusat, I., Wilhelms, F., and Eisen, O. (2022a). “Airborne ultra-wideband radar sounding over the shear margins and along flow lines at the onset region of the Northeast Greenland Ice Stream”. In: *Earth System Science Data* 14.2, pp. 763–779. DOI: 10.5194/essd-14-763-2022.

Franke, S., Jansen, D., Binder, T., Dörr, N., Helm, V., Paden, J., Steinhage, D., and Eisen, O. (2020). "Bed topography and subglacial landforms in the onset region of the Northeast Greenland Ice Stream". In: *Annals of Glaciology* 61.81, pp. 143–153. DOI: `10.1017/aog.2020.12`.

Fretwell, P. et al. (2013). "Bedmap2: improved ice bed, surface and thickness datasets for Antarctica". In: *The Cryosphere* 7.1, pp. 375–393. DOI: `10.5194/tc-7-375-2013`.

Gardner, A. S. and Sharp, M. J. (2010). "A review of snow and ice albedo and the development of a new physically based broadband albedo parameterization". In: *Journal of Geophysical Research: Earth Surface* 115.F1. DOI: `10.1029/2009JF001444`.

Gleick, P. H. (1993). "Water in crisis". In: *Pacific Institute for Studies in Dev., Environment & Security. Stockholm Env. Institute, Oxford Univ. Press. 473p* 9, pp. 1051–0761.

Glen, J. (1958). "The flow law of ice: A discussion of the assumptions made in glacier theory, their experimental foundations and consequences". In: *IASH Publ* 47.171, e183.

Gow, A. J. and Williamson, T. (1976). "Rheological implications of the internal structure and crystal fabrics of the West Antarctic ice sheet as revealed by deep core drilling at Byrd Station". In: *Geological Society of America Bulletin* 87.12, pp. 1665–1677. DOI: `10.1130/0016-7606(1976)87<1665:RIOTIS>2.0.CO;2`.

Herron, S. L. and Langway, C. C. (1982). "A comparison of ice fabrics and textures at Camp Century, Greenland and Byrd Station, Antarctica". In: *Annals of glaciology* 3, pp. 118–124. DOI: `10.3189/S0260305500002639`.

Holschuh, N., Lilien, D. A., and Christianson, K. (2019a). "Thermal Weakening, Convergent Flow, and Vertical Heat Transport in the Northeast Greenland Ice Stream Shear Margins". In: *Geophysical Research Letters* 46.14, pp. 8184–8193. DOI: `10.1029/2019GL083436`.

Hulton, N. R., Purves, R., McCulloch, R., Sugden, D. E., and Bentley, M. J. (2002). "The last glacial maximum and deglaciation in southern South America". In: *Quaternary Science Reviews* 21.1-3, pp. 233–241. DOI: `10.1016/S0277-3791(01)00103-2`.

Hvidberg, C. S., Grinsted, A., Dahl-Jensen, D., Khan, S. A., Kusk, A., Andersen, J. K., Neckel, N., Solgaard, A., Karlsson, N. B., Kjær, H. A., and Vallelonga, P. (2020). "Surface velocity of the Northeast Greenland Ice Stream (NEGIS): assessment of interior velocities derived from satellite data by GPS". In: *The Cryosphere* 14.10, pp. 3487–3502. DOI: `10.5194/tc-14-3487-2020`.

IPCC (2014a). "Climate change 2013: the physical science basis: Working Group I contribution to the Fifth assessment report of the Intergovernmental Panel on Climate Change". In: *Climate Change 2021: The Physical Science Basis. Contribution of Working Group I to the Sixth Assessment Report of the Intergovernmental Panel on Climate Change*. Cambridge, United Kingdom and New York, NY, USA: Cambridge University Press.

IPCC (2014b). *Climate Change 2014: Synthesis Report. Contribution of Working Groups I, II and III to the Fifth Assessment Report of the Intergovernmental Panel on Climate Change*. Cambridge, United Kingdom and New York, NY, USA: Cambridge University Press.

IPCC (2021). "Summary for Policymakers". In: *Climate Change 2021: The Physical Science Basis. Contribution of Working Group I to the Sixth Assessment Report of the Intergovernmental Panel on Climate Change*. Cambridge, United Kingdom and New York, NY, USA: Cambridge University Press.

Ivanovic, R. F., Gregoire, L. J., Burke, A., Wickert, A. D., Valdes, P. J., Ng, H. C., Robinson, L. F., McManus, J. F., Mitrovica, J. X., Lee, L., and Dentith, J. E. (2018). "Acceleration of Northern Ice Sheet Melt Induces AMOC Slowdown and Northern Cooling in Simulations of the Early Last Deglaciation". In: *Paleoceanography and Paleoclimatology* 33.7, pp. 807–824. DOI: `10.1029/2017PA003308`.

Jansen, D., Llorens, M.-G., Westhoff, J., Steinbach, F., Kipfstuhl, S., Bons, P. D., Griera, A., and Weikusat, I. (2016). "Small-scale disturbances in the stratigraphy of the NEEM ice core:

observations and numerical model simulations". In: *The Cryosphere* 10.1, pp. 359–370. DOI: `10.5194/tc-10-359-2016`.

Joughin, I., Fahnestock, M., MacAyeal, D., Bamber, J. L., and Gogineni, P. (2001). "Observation and analysis of ice flow in the largest Greenland ice stream". In: *Journal of Geophysical Research: Atmospheres* 106.D24, pp. 34021–34034. DOI: `10.1029/2001JD900087`.

Joughin, I., Smith, B. E., and Howat, I. M. (2018). "A complete map of Greenland ice velocity derived from satellite data collected over 20 years". In: *Journal of Glaciology* 64.243, pp. 1–11. DOI: `10.1017/jog.2017.73`.

Keisling, B. A., Christianson, K., Alley, R. B., Peters, L. E., Christian, J. E., Anandakrishnan, S., Riverman, K. L., Muto, A., and Jacobel, R. W. (2014). "Basal conditions and ice dynamics inferred from radar-derived internal stratigraphy of the northeast Greenland ice stream". In: *Annals of Glaciology* 55.67, pp. 127–137. DOI: `10.3189/2014AoG67A090`.

Khan, S. A., Kjær, K. H., Bevis, M., Bamber, J. L., Wahr, J., Kjeldsen, K. K., Bjørk, A. A., Korsgaard, N. J., Stearns, L. A., Van Den Broeke, M. R., Liu, L., Larsen, N. K., and Muresan, I. S. (2014). "Sustained mass loss of the northeast Greenland ice sheet triggered by regional warming". In: *Nature Climate Change* 4.4, pp. 292–299. DOI: `10.1038/nclimate2161`.

Lilien, D. A., Rathmann, N. M., Hvidberg, C. S., and Dahl-Jensen, D. (2021). "Modeling Ice-Crystal Fabric as a Proxy for Ice-Stream Stability". In: *Journal of Geophysical Research: Earth Surface* 126.9, e2021JF006306. DOI: `10.1029/2021JF006306`.

Miller, S. L. (1969). "Clathrate hydrates of air in Antarctic ice". In: *Science* 165.3892, pp. 489–490. DOI: `10.1126/science.165.3892.489`.

Montagnat, M., Weiss, J., Chevy, J., Duval, P., Brunjail, H., Bastie, P., and Gil Sevillano, J. (2006). "The heterogeneous nature of slip in ice single crystals deformed under torsion". In: *Philosophical Magazine* 86.27, pp. 4259–4270. DOI: `10.1080/14786430500452602`.

Morlighem, M., Williams, C. N., Rignot, E., An, L., Arndt, J. E., Bamber, J. L., Catania, G., Chauché, N., Dowdeswell, J. A., Dorschel, B., Fenty, I., Hogan, K., Howat, I., Hubbard, A., Jakobsson, M., Jordan, T. M., Kjeldsen, K. K., Millan, R., Mayer, L., Mouginot, J., Noël, B. P. Y., O'Cofaigh, C., Palmer, S., Rysgaard, S., Seroussi, H., Siegert, M. J., Slabon, P., Straneo, F., Broeke, M. R. van den, Weinrebe, W., Wood, M., and Zinglersen, K. B. (2017). "BedMachine v3: Complete Bed Topography and Ocean Bathymetry Mapping of Greenland From Multibeam Echo Sounding Combined With Mass Conservation". In: *Geophysical Research Letters* 44.21, pp. 11, 051–11, 061. DOI: `10.1002/2017GL074954`.

Mouginot, J., Scheuchl, B., and Rignot, E. (2012). "Mapping of ice motion in Antarctica using synthetic-aperture radar data". In: *Remote Sensing* 4.9, pp. 2753–2767. DOI: `10.3390/rs4092753`.

NEEM Community members et al. (2013). "Eemian interglacial reconstructed from a Greenland folded ice core". In: *Nature* 493.7433, pp. 489–494. DOI: `10.1038/nature11789`.

Nelson, J. (2011). *Story of snow*. Accessed: 2022-05-01. URL: `http://www.storyofsnow.com/media/blogs/a/Why6fig%201%20for%20blog.jpg`.

Paterson, W. (1983). "Deformation within polar ice sheets: an analysis of the Byrd Station and Camp Century borehole-tilting measurements". In: *Cold Regions Science and Technology* 8.2, pp. 165–179. DOI: `10.1016/0165-232X(83)90007-1`.

Pauling, L. (1935). "The structure and entropy of ice and of other crystals with some randomness of atomic arrangement". In: *Journal of the American Chemical Society* 57.12, pp. 2680–2684. DOI: `10.1021/ja01315a102`.

Petrenko, V. and Whitworth, R. (2006). *Physics of Ice. NY*.

Pollard, D., DeConto, R. M., and Nyblade, A. A. (2005). "Sensitivity of Cenozoic Antarctic ice sheet variations to geothermal heat flux". In: *Global and Planetary Change* 49.1-2, pp. 63–74. DOI: `10.1016/j.gloplacha.2005.05.003`.

Ridley, J., Gregory, J. M., Huybrechts, P., and Lowe, J. (2010). "Thresholds for irreversible decline of the Greenland ice sheet". In: *Climate Dynamics* 35.6, pp. 1049–1057. DOI: `10.1007/s00382-009-0646-0`.

Rignot, E. and Kanagaratnam, P. (2006). "Changes in the velocity structure of the Greenland Ice Sheet". In: *Science* 311.5763, pp. 986–990. DOI: `10.1126/science.1121381`.

Rignot, E., Mouginot, J., and Scheuchl, B. (2011). "Ice flow of the Antarctic ice sheet". In: *Science* 333.6048, pp. 1427–1430. DOI: `10.1126/science.1208336`.

Riverman, K. L., Alley, R. B., Anandakrishnan, S., Christianson, K., Holschuh, N. D., Medley, B., Muto, A., and Peters, L. E. (2019). "Enhanced Firn Densification in High-Accumulation Shear Margins of the NE Greenland Ice Stream". In: *Journal of Geophysical Research: Earth Surface* 124.2, pp. 365–382. DOI: `10.1029/2017JF004604`.

Shepherd, A. et al. (2020). "Mass balance of the Greenland Ice Sheet from 1992 to 2018". In: *Nature* 579.7798, pp. 233–239. DOI: `10.1038/s41586-019-1855-2`.

Sigman, D. M., Hain, M. P., and Haug, G. H. (2010). "The polar ocean and glacial cycles in atmospheric CO2 concentration". In: *Nature* 466.7302, pp. 47–55. DOI: `10.1038/nature09149`.

Smith-Johnsen, S., De Fleurian, B., Schlegel, N., Seroussi, H., and Nisancioglu, K. (2020b). "Exceptionally high heat flux needed to sustain the Northeast Greenland Ice Stream". In: *The Cryosphere* 14.3, pp. 841–854. DOI: `10.5194/tc-14-841-2020`.

Song, M., Cole, D. M., and Baker, I. (2006). "An investigation of the effects of particles on creep of polycrystalline ice". In: *Scripta materialia* 55.1, pp. 91–94. DOI: `10.1016/j.scriptamat.2006.03.029`.

Stevens, N. T., Parizek, B. R., and Alley, R. B. (2016). "Enhancement of volcanism and geothermal heat flux by ice-age cycling: A stress modeling study of Greenland". In: *Journal of Geophysical Research: Earth Surface* 121.8, pp. 1456–1471. DOI: `10.1002/2016JF003855`.

Stocker, T. F. and Wright, D. G. (1991). "Rapid transitions of the oceans deep circulation induced by changes in surface water fluxes". In: *Nature* 351.6329, pp. 729–732. DOI: `10.1038/351729a0`.

Swingedouw, D., Fichefet, T., Goosse, H., and Loutre, M.-F. (2009). "Impact of transient freshwater releases in the Southern Ocean on the AMOC and climate". In: *Climate Dynamics* 33.2, pp. 365–381. DOI: `10.1007/s00382-008-0496-1`.

Vizcaino, M., Mikolajewicz, U., Gröger, M., Maier-Reimer, E., Schurgers, G., and Winguth, A. M. (2008). "Long-term ice sheet–climate interactions under anthropogenic greenhouse forcing simulated with a complex Earth System Model". In: *Climate dynamics* 31.6, pp. 665–690. DOI: `10.1007/s00382-008-0369-7`.

Weertman, J. (1983). "Creep deformation of ice". In: *Annual Review of Earth and Planetary Sciences* 11.1, pp. 215–240. DOI: `10.1146/annurev.ea.11.050183.001243`.

Weiss, J. and Grasso, J.-R. (1997). "Acoustic emission in single crystals of ice". In: *The Journal of Physical Chemistry B* 101.32, pp. 6113–6117. DOI: `10.1021/jp963157f`.

Zeising, O. and Humbert, A. (2021). "Indication of high basal melting at the EastGRIP drill site on the Northeast Greenland Ice Stream". In: *The Cryosphere* 15.7, pp. 3119–3128. DOI: `10.5194/tc-15-3119-2021`.

Chapter 3

Scientific methods

The investigation of the polar ice sheets started at the end of the 19th century by early explorers who documented their observations, collected material or made simple measurements on their routes. Over time, the expeditions became more sophisticated, logistically more expensive, and involved larger groups and collaborations between several nations. Along with a growing scientific interest new techniques developed, sometimes by accident, sometimes out of necessity. Three methods in particular revolutionized the field of glaciology: The recognition that information about the past climate can be obtained from ice cores, the mapping of the current state of glaciers and ice sheets with RES, and the power of computer simulations to understand past, present and future processes that are spatially and temporally too extensive to be reproduced in laboratories. In this chapter, I elaborate on these three scientific approaches and their particularities that are relevant for this thesis.

3.1 Ice cores

The characteristics of polar ice reflect the environmental conditions during the time of snowfall and its transformation into ice (Alley et al., 1993; Petit et al., 1999; Andersen et al., 2004; Marcott et al., 2014). Because ice sheets are formed and maintained by the incremental buildup of new snow layers at the surface, the age of the ice, in general, increases with depth. The stratigraphy of polar ice contains chemical signals which are generally well preserved, and ice cores are, therefore, an excellent paleoclimatic archive.

This was recognized for the first time by the Danish scientist Willi Dansgaard, who discovered the relation between the isotopic composition of rainwater and the temperature during its formation (Dansgaard, 1964). His visit in the American military base, Camp Century, resulted in the systematic measurement of isotopes along the 1390 m long Camp Century ice core, showing not only a paleoclimatic reconstruction of past temperatures, but also that the climate changed repeatedly and abruptly during the past 100’000 years (Dansgaard et al., 1969). The first climate-research motivated deep ice-core drilling followed in 1979 in southern Greenland (Dye 3) and marked the beginning of a new era in climate science (Steffensen, 2012). Since then, six deep ice cores reaching the bed have successfully been drilled in Greenland alone, complemented by about a dozen Antarctic deep cores (Fig. 2.5) and several shallower cores recovered from ice sheets, glaciers and ice caps around the world (e.g. Gow et al., 1968; Dansgaard et al., 1969; Dansgaard et al., 1982; Lorius et al., 1985; Andersen et al., 2004; Barbante et al., 2006; Fudge et al., 2013; NEEM Community members et al., 2013).

The isotopic composition of snow is by far not the only measure for reconstructing the environment, under which the ice was originally formed; Ancient air trapped in bubbles, for example, provides insight into past atmospheric compositions (e.g. Blunier et al., 1995; Bender et al., 1997; Rhodes et al., 2013), and impurities act as proxies for natural processes like volcanic eruptions, wild fires, the abundance of storms, lightening, microbial processes, or solar activity (e.g. Raisbeck et al., 2007; Alley et al., 2010; Kellerhals et al., 2010; Delaygue and Bard, 2011; Steinhilber et al., 2012; Rasmussen et al., 2013; Erhardt et al., 2022). Measuring these properties

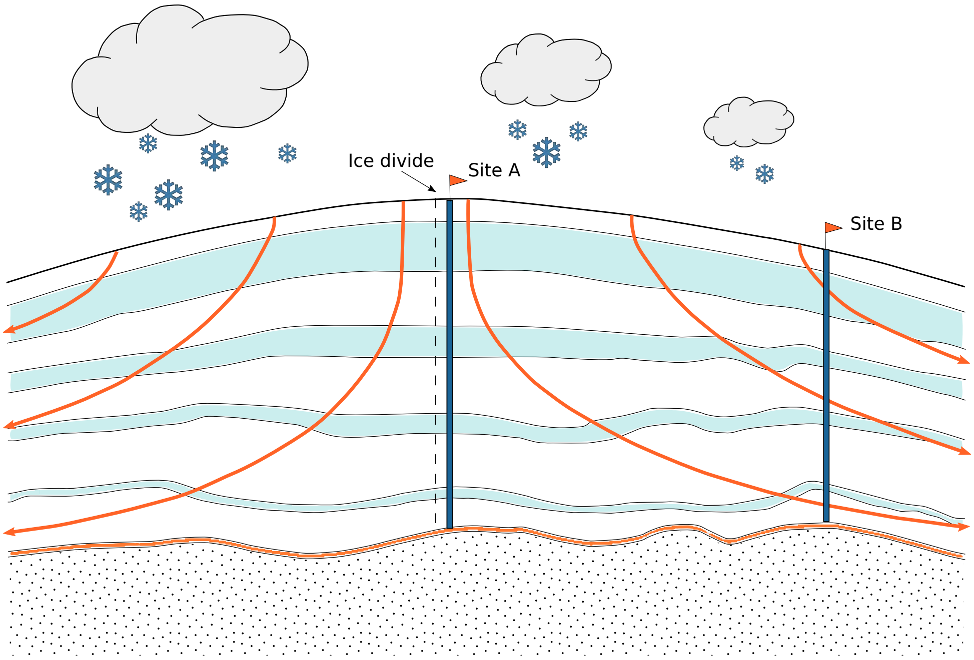

FIGURE 3.1: Ice-sheet cross-section and internal stratigraphy. Isochronous layers deposited at the ice-sheet surface experience vertical thinning and deformation as a result of vertical compression and ice flow. Ice cores drilled at the ice-sheet center (close to the ice divide, Site A) have a good chance to find undisturbed internal stratigraphy due to smaller ice-flow velocities. On the ice-sheet flanks (Site B), the ice-core record is subject to upstream effects, as the ice originates from further upstream, and the internal stratigraphy is more likely to show signs of ice flow such as folds or overturned stratigraphy. Figure adapted from Cuffey and Paterson (2010).

is valuable not only for reconstructing the climate of the past, but also for understanding how different processes are related to one another.

In comparison to other paleoarchives, ice cores particularly excel through their high temporal resolution and complete chronology (Andersen et al., 2004). Annual layers can be identified by the changing isotopic composition of the precipitation throughout the year (Ekaykin et al., 2002; Hastings et al., 2004), as well as by impurities which peak in different seasons (Beer et al., 1991; Whitlow et al., 1992; Legrand and Mayewski, 1997). Annual layer counting is a robust way of establishing time scales (e.g. Vinther et al., 2006; Winstrup et al., 2012; Sigl et al., 2016). Difficulties can occur at depth where layers become thinner as a result of vertical compression and horizontal extension because of ice flow, so individual years sometimes become hard to distinguish. At depths where individual annual layers become unrecognizable, the ice-core dating is, therefore, often supported by ice-flow modeling (e.g. Ruth et al., 2007; Parrenin et al., 2007). Volcanic ash layers can additionally support time scales through tephra dating (Abbott and Davies, 2012; Svensson et al., 2020). Together with other records such as cosmogenic isotopes, volcanic particles can link ice cores to other paleoclimatic archives (Parrenin et al., 2012; Lowe et al., 2015). In doing so, the timing of major climatic changes and short-time anomalies can be determined with high accuracy, and the linkage between different locations provides valuable insights into the spatio-temporal climate variability.

In central Greenland, roughly the upper half of the ice sheet constitutes of ice that was deposited during the Holocene, the current interglacial period which started around 11.7 ka before the year 2000 (b2k) (Rasmussen et al., 2014). The climate during that time was unusually stable with only a few short temperature fluctuations like the 8.2 ka b2k cooling event (Thomas et al., 2007), the 3.3 ka b2k Minoan warming (Easterbrook, 2016) or the more recent little ice age that lasted from 1570–1850 CE (common era) (Fischer et al., 1998). In the lower half of the central Greenland ice sheet, the ice stems from the Last Glacial Period, where temperatures were on average about 10°C colder than today (Kindler et al., 2014). The Last Glacial Period is characterized by abrupt climatic changes unrelated to the orbital characteristics which otherwise dominated the periodicity of glacial–interglacial cycles (Broecker, 1966). These so-called Dansgaard–Oeschger (D-O) events (Dansgaard et al., 1993) are climatic anomalies where temperatures rapidly increased by several degrees within a few decades and returned more slowly back to colder conditions (Kindler et al., 2014). The episodes of enhanced temperatures within the glacial period are referred to as *interstadials*, and the cold phases are termed *stadials* (Rasmussen et al., 2014). In order to compare the climatic records from different sources, the D-O events were numbered starting from the most recent event, the Younger Dryas cold phase (Greenland Stadial 1 (GS-1), Alley, 2000) and the warm phase of the Bølling-Allerød (Greenland Interstadial 1 (GI-1), Friedrich et al., 2001). In paleoclimatic archives from the southern hemisphere, lower-amplitude climate oscillations are recorded with anti-phase characteristics, i.e. indication of colder climate is found in the South when it was warm in the North and vice versa (e.g. Blunier et al., 1998; White and Steig, 1998). The cause of D-O events has been subject to extensive discussions in the past but the most accepted explanations today are attributed to jumps between quasi-stable states of the Atlantic Meridional Overturning Circulation (AMOC) (e.g. Peltier and Vettoretti, 2014; Li and Born, 2019). A recent study by Vettoretti et al. (2022) suggests, that the atmospheric CO_2 concentration might be the critical factor controlling the stability of the climate system, as it can flip stochastically between the two states if the CO_2 level remains within a certain window.

In total, 25 D-O events are recorded during the Last Glacial Period which began 115 ka b2k, following the previous interglacial period called *Eemian* (Rasmussen et al., 2014; NEEM Community members et al., 2013). Although the Greenland ice sheet has existed since approximately one million years (Schaefer et al., 2016), the oldest stratigraphy from Greenland ice cores only reaches back into the Eemian where temperatures were similar as today. Antarctica has likely been ice covered for more than five million years (Shakun et al., 2018), and because of the lower accumulation rate, the stratigraphy from Antarctic ice cores reaches back to 800’000 years (Jouzel et al., 2007). One of the big goals in ice-core drilling is to provide stratigraphic records as far back in time as possible and great effort is put into finding the right spots for ice-core drilling with the prospect of extending the current time scales (Dahl-Jensen, 2018).

The choice of ice-core drill sites primarily depends on the scientific questions that should be addressed; the best climatic resolution is typically obtained in areas of high accumulation rates, large ice thickness and slow ice movement, where annual layers can be expected to be thick and undisturbed (e.g. Andersen et al., 2004). Long climatic records require undisturbed stratigraphy, low accumulation rates and the absence of basal melt (Fischer et al., 2013; Dahl-Jensen, 2018), while other sites are chosen due to interesting bed characteristics or specific targets such as subglacial lakes (e.g. Bulat, 2016). Most deep ice cores so far have been drilled in areas with low surface velocities, close to domes or ice divides, which facilitates the logistics and simplifies stratigraphic interpretations. One exception is the EastGRIP ice core, located in the onset region of the NEGIS. It is the first deep ice core that is drilled in an active ice stream, with a surface velocity of 55 ma^{-1} at the drill site (Hvidberg et al., 2020). While most deep ice cores primarily aim to reconstruct the climate of the past, a second focal point of EastGRIP is to study the ice-flow dynamics and processes relevant for ice streams. An ice core which is drilled on the flanks of the ice sheet, like EastGRIP, is affected by upstream effects (Fig. 3.1). That is, the ice retrieved from a certain depth was originally deposited further upstream under conditions which are potentially quite different from the location of the drill site (Site B in Fig. 3.1). Hence, corrections for spatial variations of atmospheric conditions like accumulation rate, temperatures and atmospheric pressure, are necessary for climatic interpretations of such ice cores. In contrast, ice cores drilled near topographic domes (e.g. Site A in Fig. 3.1) ensure that the ice was deposited at almost the same location as it is recovered, and that variations in its measurements solely indicate temporal climatic fluctuations.

After retrieving ice cores, the ice-core processing typically follows a highly organized workflow. A few non-destructive methods, like Dielectric Profiling (DEP), are applied before the core is cut into several pieces. Approximately half of the core is archived, and the rest is divided into a thin physical properties piece and a larger piece from the the central core section for non-destructive Electrical Conductivity Measurement (ECM) and visual stratigraphy (for details on processing see (Westhoff et al., 2021)). Further sectioning of the ice core provides samples for stable water isotope, impurity, gas, and tephra measurements. Here, I will shortly describe three types of ice-core measurements that can indicate signs of ice flow and which are relevant for the studies included in this thesis.

3.1.1 Visual stratigraphy

The amount of impurities like dust or volcanic ash, as well as the number of air bubbles in polar ice depends on the atmospheric conditions during ice formation, and can vary between snowfall events (Beer et al., 1991). Processing with the line scanner makes the stratigraphy of ice visible by generating a gray-scale image indicative of the ice purity (Westhoff et al., 2021). For this measurement, a freshly polished piece of the ice core is illuminated at a certain angle from below, and the light passing through the ice is recorded by a camera from above. Because of the inclined light incidence, the camera only records indirect light that is scattered in the core sample. Hence, pure ice appears dark, while layers containing air bubbles or insoluble impurities appear bright (Svensson et al., 2005). Ice from the Holocene is in general rather transparent, although bright layers can be observed occasionally (Svensson et al., 2005). Ice from the Last Glacial Period contains more impurities, and the stratigraphy is visible through the appearance of so-called *cloudy bands*. These are most pronounced in ice deposited during the stadials, although the stratigraphy also visually exists in ice from interstadials (e.g Svensson et al., 2005; Jansen et al., 2016; Westhoff et al., 2021).

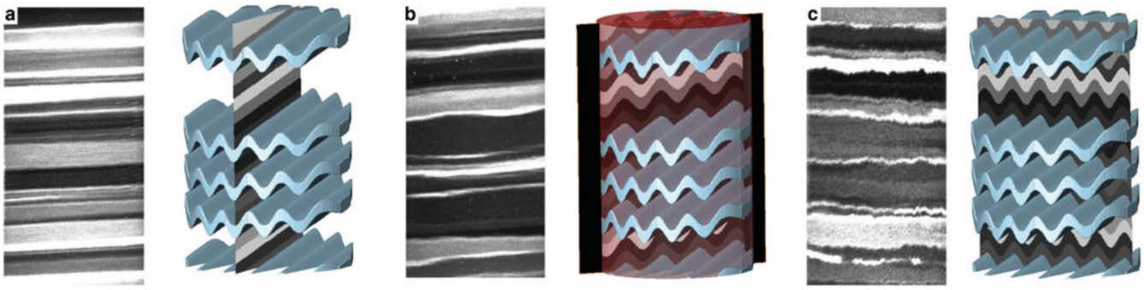

FIGURE 3.2: Deformation features in the EastGRIP ice core which were made visible with the line scanner and oriented relative to the ice-flow direction by Westhoff et al. (2021). Depending on the viewing angle of the linescan image, internal layers are **a)** very smooth, **b)** slightly folded or **c)** considerably folded.

Visual stratigraphy can be used to produce records of e.g. melt layers (Herron and Langway, 1982; Alley and Anandakrishnan, 1995; Westhoff et al., 2022) or wind-blown features (Fegyveresi et al., 2018), and the grayscale-record is a good indication of the general impurity content (Svensson et al., 2005). In contrast to chemical analyses, line scan images show a 2D picture of structures which are excellent to detect folds and small-scale geometrical features (e.g. Thorsteinsson, 1996; Alley et al., 1997; Jansen et al., 2016). In the EastGRIP ice core, the characteristics of the visual stratigraphy images strongly vary among the analyzed samples (Westhoff et al., 2021). During ice-core drilling, the original core orientation is normally not preserved, as the drill is free to rotate within the borehole. Core break matching in general recovers a consecutive ice-core orientation, but prior to cutting the core is rotated once more. Core cutting thus occurs in a random fashion and the photographs are taken from different angles. While some of the linescan images show completely smooth layers, other samples appear considerably folded (Fig. 3.2). Making use of the layer inclination observed in the linescan images, Westhoff et al. (2021) developed a method to orient the EastGRIP ice core and showed that folded layers appear on images transverse to flow, while flow-parallel images show the least deformed stratigraphy.

Due to densification of the snow pack and vertical compression of the ice, the folds observed at EastGRIP and similar structures in other ice cores (e.g. Alley et al., 1997; Waddington et al., 2001) cannot be explained as remnants of surface features like wind-blown Sastrugis (Waddington et al., 2001). It is thus fair to assume that the folds are a consequence of ice flow, and hence indicative of the deformation history. At EastGRIP, the orientation of the folding axes is in agreement with the deformation regime prevailing in the NEGIS onset region, where ice-flow channeling leads to compression perpendicular to the ice flow, while the flow acceleration simultaneously leads to along-flow extension (Joughin et al., 2018). Ice-core diameters are typically limited to approximately 10 cm, so only small-scale structural features are observable, but indication of the existence of larger folds exceeding the core diameter has been observed in several other ice cores (e.g. Taylor et al., 1993; Alley et al., 1995; NEEM Community members et al., 2013; Jansen et al., 2016).

3.1.2 Dielectric properties

The electrical properties of natural ice from the polar regions depend on the amount of impurities, such as marine ions, sulphuric, nitric and organic acids, as well as soluble terrestrial material (e.g Moore et al., 1989; Moore et al., 1994). Electrical stratigraphy of ice cores has become a standard procedure in ice-core processing, and is used as primary tool for identifying volcanic eruptions, counting of annual layers and the matching of ice cores for time-scale establishment (e.g. Hammer et al., 1994; Rasmussen et al., 2013; Mojtabavi et al., 2020b). The methods of ECM and DEP are both electrical methods, but differ mainly in the type of current applied and the resulting sensitivity towards impurities (e.g. Moore et al., 1992). ECM uses a direct current (DC), i.e. the electrical charge only flows in one direction (Hammer, 1980) which limits its sensitivity to acids and makes this method particularly useful to find volcanic reference horizons (Hammer, 1980; Moore et al., 1992; Taylor et al., 1992; Taylor et al., 1997). DEP on the other hand makes use of an alternating current (AC), with a periodical change of charge direction and voltage level (Wilhelms et al., 1998). The DEP conductivity is therefore also sensitive towards the salt content and further allows to determine the dielectric permittivity, but is measured at a lower resolution than ECM (Moore et al., 1989; Mojtabavi et al., 2020c,e). The combined application of these methods helps to resolve ambiguities in identifying chemical factors that regulate the dielectric properties of polar ice (Moore et al., 1992).

The ECM system used at EastGRIP was developed and described by Hammer (1980). Before the measurement is taken, a fresh, flat surface along the ice core is prepared with a microtome knife to avoid falsification of the measurements related to ice-core aging (Maccagnan et al., 1981; Schwander et al., 1983). A high voltage of 1250 V is applied on a pair of brass electrodes which are dragged by the operator along the ice surface, while the DC running between the electrodes is recorded. Despite its name, ECM is not a direct measure of electrical conductivity, but since volume conduction dominates over surface conduction it provides a good approximation (Hammer, 1980; Schwander et al., 1983).

The DC conductivity of ice is mainly bound to the movement of protons associated with the H^+ of strong acids, and is therefore sensitive to the presence of acid layers. The acidity of the ice core depends on the chemical composition of the precipitation, which shows a strong seasonality (Taylor et al., 1992). During warm periods such as the Holocene, Nitrate (NO_3^-)

seems to dominate the ECM signal (Neftel et al., 1985; Taylor et al., 1992). Enhanced NO_3^- due to biological activity during the summer leads to a higher concentration of H^+ in the ice. The seasonal response of ECM therefore shows higher signal levels in the winter and lower levels in the summer. During cold conditions, the atmospheric dust concentration, mainly $CaCO_3$, is higher and strongly alters the acidity of the ice (Wolff et al., 1995). Part of the H^+ in the core is neutralized and the ECM current decreases by a factor of 100 (Taylor et al., 1997). This effect is stronger during the winter, where dust levels are enhanced, such that the ECM signal in general shows peaks during the summer and dips during the winter.

Further events that are unrelated to a specific season, including biomass burning events or volcanic activities, can additionally affect the ECM measurements (Taylor et al., 1997). Volcanoes that emit H_2S and SO_2 increase the concentration of H_2SO_4 in both, atmosphere and precipitation. Similar to the effect of nitrate, an increase in H^+ causes an increased ECM current. This effect can last for several years, as long as the H_2SO_4 aerosols remain in the atmosphere (Taylor et al., 1997). Biomass burning events increase the amount of ammonium (NH_4^+) in the core which neutralizes a part of H^+ and decreases the ECM current, typically lasting for about a week (Taylor et al., 1997).

In contrast to ECM, the DEP technique requires no special ice surface preparation nor a physical contact between the electrodes and the ice. The DEP instrument used at EastGRIP is based on the early developments of e.g. Moore and Paren (1987) and Moore (1993) and was improved by Wilhelms et al. (1998) by fitting the guarded capacitor method to the ice-core geometry. Thereby, the core is placed between two curved electrodes forming a capacitor, with the ice acting as the dielectric. The AC capacitance and conductance are measured at a frequency of 250 kHz. After correcting for the free air capacitance, the ice core's dielectric properties can be calculated directly (Wilhelms et al., 1998). Accordingly, the DEP method not only results in the electrical conductivity but also provides information on the dielectric permittivity. The permittivity of ice depends primarily on the density and the crystal orientation, but the instrument sensitivity is not high enough to detect effects of the latter.

Salts affect the conductivity through so-called *Bjerrum defects* that produce a dielectric AC conductivity, but cannot provide a DC current (for details see Moore et al., 1994). Unlike the ECM method, DEP is therefore also sensitive to the salt content of ice. The seasonality observed in ECM records of interglacial and interstadial ice also prevails in DEP inferred conductivity. However, while most of the ECM signal is lost in alkaline ice, DEP provides a clear, albeit slightly lower-amplitude response which is mainly regulated by ammonium (Moore et al., 1994).

3.1.3 Crystal orientation fabric

Ice crystals are uniaxial birefringent, so the dielectric permittivity along the c-axis is larger than in the direction of the basal plane (e.g. Fujita et al., 1993). The c-axis orientation can be measured using polarized light microscopy of ice-core thin sections. Light traveling through an ice crystal gets dispersed into an ordinary (perpendicular to the c-axis) and an extraordinary (parallel to the c-axis) component. Different refraction indices between the ordinary and extraordinary component lead to a phase shift and interference between these components causes variations in the light intensity. Fabric analyzers make use of these characteristics by measuring the intensity of a polarized monochromatic light beam traveling through ice and passing a polarization filter oriented at 90° relative to the initial wave polarization (Eichler, 2013).

The fabric of the EastGRIP ice core was measured with the automated fabric analyzer described by (Wilson et al., 2003) in discrete samples every 10–15 m (Stoll, 2019). The instrument automatically rotates the polarization directions by eight incremental steps between 0 and 90° in order to provide the azimuth and inclination of the c-axis orientation for each crystal. To obtain a statistical description of the crystal orientation fabric (COF), each individual c-axis orientation is transformed into Cartesian coordinates to determine the second-order orientation tensor (Stoll, 2019). The distribution of the c-axes orientation can so be represented by an ellipsoid whose principal axes are described by the tensor eigenvalues (λ_i) and eigenvectors (a_i). By convention, the eigenvalues are defined as $\lambda_1 + \lambda_2 + \lambda_3 = 1$ and $\lambda_1 < \lambda_2 < \lambda_3$.

Most ice-core records show a development from a close-to-isotropic fabric in the uppermost part of the ice sheet towards an oriented fabric with depth (e.g. Thorsteinsson et al., 1997; Azuma et al., 2000; Fitzpatrick et al., 2014; Montagnat et al., 2014), whereby the fabric type depends on the in-situ strain-rate regime and the deformation history. In order to minimize the free energy of the system, the ice crystals apparently ’rotate’ so that their c-axes point in the direction of dominant compression (Gow et al., 1968; Azuma and Higashi, 1985). At ice domes the vertical compression typically dominates and leads to the transition from near-isotropy at the surface to a vertical single maximum of increasing strength with depth, that is most c-axes are oriented vertically (e.g. Azuma et al., 1999; Diprinzio et al., 2005; Durand et al., 2009; Montagnat et al., 2012). Single maximum also exist in areas of simple shear, for example in shear margins or at the ice-sheet base, whereby the c-axes tend to point perpendicular to the shear plane, i.e. horizontal in shear margins and vertical at the base (e.g. Herron and Langway, 1982; Gow et al., 1997; Gerbi et al., 2021; Monz et al., 2021; Thomas et al., 2021). Ice cores drilled in areas with considerable ice flow typically show the development of a girdle fabric, as horizontal extension exists in addition to vertical compression (e.g. Faria et al., 2014; Fitzpatrick et al., 2014; Montagnat et al., 2014). Similarly, the EastGRIP ice core shows a rapid development from a vertical single-maximum fabric at a depth of 111 m (beginning of the physical properties analyses) to a vertical girdle that is fully developed at around 500 m. Above around 200 m depth, the largest eigenvector points in the vertical direction which changes in larger depths where the horizontal eigenvalue becomes dominant. In that sense, the fabric is not a perfect girdle but is superimposed by a horizontal single maximum in the direction perpendicular to flow. The fabric data of the EastGRIP ice core has not been published yet, but is available to the EastGRIP community and has partially been described by Stoll (2019).

Fabric evolution processes are complex and involve a number of different mechanisms. Most of our current knowledge stems from a combination of ice-core observations, computer simulations and ice deformation tests (e.g. Azuma and Higashi, 1985; Fan et al., 2020; Montagnat et al., 2012; Faria et al., 2002). The process which is considered most important in the evolution of COF under cold, low-stress conditions is lattice rotation (Alley, 1988). This mechanism describes the apparent rotation of crystals due to their mechanical anisotropy (Pimienta et al., 1987) and can explain the most common fabric types observed in ice sheets (Lilien et al., 2021). However, other processes generally summarized as recrystallization can additionally affect the fabric evolution (e.g. Azuma and Higashi, 1985; Alley, 1988), including normal grain growth, rotation recrystallization and migration recrystallization (De La Chapelle et al., 1998). Normal grain growth describes the growth of larger ice crystals at the cost of smaller ones, as atoms escape from one crystal to another in order to reduce the total strain energy of the system (Gow and Williamson, 1976; Montagnat and Duval, 2000). By rotation recrystallization new grain boundaries develop within crystals, a process caused by the alignment of dislocations through bending stresses (Duval and Castelnau, 1995). Similar to normal grain growth, migration recrystallization involves mass transfer from high-energy to low-energy crystals. Crystals which are favorably oriented relative to the strain-rate regime thereby grow at the cost of highly strained ones (Duval and Castelnau, 1995). While normal grain growth doesn’t affect the orientation of crystals, the other two lead to crystal reorientation, although migration recrystallization is much more important than rotation recrystallization (Duval and Castelnau, 1995; Montagnat and Duval, 2000). At temperatures above –10°C, migration recrystallization becomes particularly important with the consequence that fabric is controlled by the in-situ stress, rather the strain history (Duval and Castelnau, 1995).

3.2 Radio-echo sounding

Repeated aircraft accidents over polar regions around the mid-twentieth century led to the recognition that ice is almost transparent for the propagation of radar waves (Turchetti et al., 2008). Radar altimeters used during flights frequently recorded the reflected signal from the bed instead of the ice-sheet surface. The false altitude reading often mislead pilots during landing maneuvers, so airplanes sometimes crashed as a consequence. Initially, radar wave propagation through ice was investigated to increase the safety of pilots, but it soon became interesting to scientists who realized the great potential of measuring the thickness of the ice (Waite and Schmidt, 1962). This insight was followed by the development of RES systems that revolutionized glaciology. Because of the low costs of radar surveys and fast data acquisition in comparison to other geophysical methods, and the possibility of conducting airborne surveys (e.g. Conway et al., 2009; Blindow et al., 2011), RES is widely used in glaciology today.

A RES system consists of a transmitter unit, releasing a pulse of electromagnetic waves, and a receiver unit, which records those waves after traveling through the subsurface and being reflected at dielectric contrasts. The design of the radar strongly depends on the goal of the survey. Early systems operated with short pulses at frequencies of 30–600 MHz for ice-thickness mapping in Greenland and Antarctica. For sounding of temperate glaciers, lower-frequency systems between 1–32 MHz are used because the absorption in warm ice and in presence of water is larger (Gogineni et al., 1998). In the late 70s, the first coherent RES systems were developed (Walford et al., 1977) which considerably improved the azimuth resolution and processing gain by signal stacking (Schroeder et al., 2020). Synthetic Aperture Radar (SAR) processing further reduced ambiguities in resolving reflecting geometries, increasing the along-track resolution (Musil and Doake, 1987). The still remaining cross-track ambiguities were soon overcome by the development of multi-channel systems (e.g. Paden et al., 2010), and multi-polarization radars also allow the imaging of anisotropy (e.g. Dall et al., 2010; Yan et al., 2020).

Most early applications of RES in glaciology focused on the mapping of ice thickness (Gogineni et al., 2001; Bohleber et al., 2017) and basal topography (e.g. Bamber et al., 2013; Fretwell et al., 2013; Christianson et al., 2014; Franke et al., 2020) to estimate the ice volume and provide important input data for ice-sheet modeling. While reflections at the bed are particularly strong due to the sharp dielectric contrast between basal material and ice, reflections also occur within the ice column. The ability of mapping these englacial structures in high resolution has largely improved with the development of more sensitive radar systems. Internal reflections can have various origins, for example layers of liquid water (Bamber, 1987; Davis et al., 1990), density contrasts due to variations in the air content (e.g. Robin et al., 1969; Ackley and Keliher, 1979), and changes in crystal size or orientation (Harrison, 1973; Eisen et al., 2007). Most internal reflections are, however, associated with impurities such as volcanic ash layers and are thus considered isochrones, i.e. horizons of uniform age (Jacobel and Hodge, 1995; Eisen et al., 2006). The revealed internal stratigraphy can therefore be used for connecting ice-core sites for time-scale validation or mapping of the ice volume in the past, and deformed layers can indicate the presence of basal melt or ice-flow dynamics (e.g. Fahnestock et al., 2001b; Oswald and Gogineni, 2011; MacGregor et al., 2015; Bons et al., 2016; Cavitte et al., 2016; Das et al., 2020).

3.2.1 Radar wave propagation

Radar wave propagation is based on electromagnetic theory and governed by the Maxwell's equations which describe the interaction and development of electric and magnetic fields:

$$\nabla \times \mathbf{H} = j + \frac{\partial \mathbf{D}}{\partial t} \tag{3.1}$$

$$\nabla \times \mathbf{E} = -\frac{\partial \mathbf{B}}{\partial t} \tag{3.2}$$

$$\nabla \cdot \mathbf{B} = 0 \tag{3.3}$$

$$\nabla \cdot \mathbf{D} = q \tag{3.4}$$

with the following parameters:

- **H**: magnetic field intensity in $\left[\mathrm{Am}^{-1}\right]$
- **E**: electric field intensity in $\left[\mathrm{Vm}^{-1}\right]$
- **B**: magnetic flux density in $\left[\mathrm{T} = \mathrm{Vsm}^{-2}\right]$
- **D**: electric flux density in $\left[\mathrm{Am}^{-2}\right]$
- **j**: electric current density in $\left[\mathrm{Am}^{-2}\right]$
- q: electric charge density in $\left[\mathrm{Asm}^{-3}\right]$

Equation (3.1) is called Ampère's law and describes the generation of magnetic fields by electric currents. The second Maxwell's equation (Eq. (3.2)) is referred to as Faraday's law which expresses the induction of electric fields resulting from time-varying magnetic fields. The Gauss' law for magnetic (Eq. (3.3)) and electric (Eq. (3.4)) fields state that the magnetic field is solenoidal, meaning that there are no sources nor sinks, while monopoles do exist in electric fields. Constitutive equations relate the material properties to the electromagnetic (EM) fields:

$$\mathbf{B} = \mu \mathbf{H} \tag{3.5}$$

$$\mathbf{D} = \varepsilon \mathbf{E}, \tag{3.6}$$

$$j = \sigma \mathbf{E} \tag{3.7}$$

where μ is the magnetic permeability in $\left[\mathrm{Vs}(\mathrm{Am})^{-1}\right]$, ε is the dielectric permittivity in $\left[\mathrm{As}(\mathrm{Vm})^{-1}\right]$ and σ is the electrical conductivity in $[\mathrm{Sm}^{-1}]$. The evolution of electromagnetic fields depends on the characteristics of the subsurface, and they may propagate either through diffusion or as waves. RES recordings require the propagation as radio waves, which is the case in low-loss materials, where energy dissipation is small compared to energy storage. Since the electrical conductivity σ represents the ability to conduct an electric current, energy dissipates quickly in conductive materials. The dielectric permittivity ε describes the capacity of a material to store an electric charge so that for successful RES surveys, the conductivity of the medium must be small in comparison to its permittivity ($\sigma \ll \varepsilon$) (Hubbard and Glasser, 2005). The differential equations for electric and magnetic fields can be developed by transforming Maxwell's equations and assuming a charge- and current-free media (Brewster, 2010):

$$\nabla^2 \mathbf{E} = \mu\varepsilon \frac{\partial^2 \mathbf{E}}{\partial t^2} \tag{3.8}$$

$$\nabla^2 \mathbf{B} = \mu\varepsilon \frac{\partial^2 \mathbf{B}}{\partial t^2}. \tag{3.9}$$

These equations are equivalent to the wave equation

$$\nabla^2 f = \frac{1}{c^2} \frac{\partial^2 f}{\partial t^2}, \tag{3.10}$$

where f stands for displacement and c is velocity. The formula for the propagation speed of electromagnetic waves consequently is:

$$c = \frac{1}{\sqrt{\mu\varepsilon}}. \tag{3.11}$$

The wave frequencies are determined by antennae characteristics which typically operate at a range of 1 MHz to 1 GHz. In this spectrum, the velocity and attenuation can be considered to be frequency independent (Hubbard and Glasser, 2005).

3.2.2 EGRIP-NOR-2018 UWB data

Most results obtained in this thesis are based on, or compared to the airborne ultra-wideband (UWB) EGRIP-NOR-2018 radar dataset that is described in detail by Franke et al. (2022a). The survey was conducted in 2018 with a multi-channel UWB radar by the Alfred Wegener Institute (AWI), mounted on the Polaris 6 aircraft. The survey region covers an area of $\sim$24,000 km^2 and extends across the shear margins of the NEGIS and approximately 150 km up- and 126 km downstream of EastGRIP. The flight lines are arranged parallel and perpendicular to the ice stream, with an approximate grid spacing of 10 km up- and downstream of EastGRIP and 5 km in the vicinity of the drill site.

The radar system is a Multichannel Coherent Radar Depth Sounder (MCoRDS) with eight antennas that act as both, transmitter and receiver using a transmit-receive switch. During the entire survey, the electrical field component was polarized parallel to the flight direction and the transmitted signal consists of a linear frequency-modulated chirp in the frequency band of 180–210 MHz (center frequency 195 MHz). To improve the dynamic range, three alternating waveforms of different pulse length and receiver gain were used for optimal mapping of the ice surface, internal layers and the bed. Data processing includes pulse compression, synthetic aperture radar (SAR) focusing and array processing (Franke et al., 2022a).

Figure 3.3c shows an example of a radargram recorded across the ice stream around 40 km upstream of EastGRIP. The first reflection corresponds to the ice-sheet surface, the bed reflection is clearly visible at a two-way travel time of around 37 μs. The internal stratigraphy is heavily folded outside the shear margins where no correlation with the bed topography is apparent. Internal layers are drawn down towards the shear margins where the stratigraphy is strongly folded on much smaller wavelengths than the big folds outside the ice stream. Because of steeply inclined layers, the shear margins appear as vertical white stripes that mark signal power loss due to off-nadir scattering. In the ice-stream interior the stratigraphy is relatively undisturbed and undulations mostly follow the bed topography. The dark shadows on the left-hand side of the radargram are a result of birefringence-induced power modulation that arises from a horizontally anisotropic COF.

3.3 Ice-flow models

"All models are wrong, but some of them are useful". This aphorism by George Box is as true for ice-flow models as for any other attempt of describing reality in terms of physical equations. The great advantage in ice-flow models lies in their ability of simulating processes that are taking place on temporal and spatial scales that are too large to be represented by any experimental attempts. The 'wrongness' of models can be decreased by including more detailed processes, decreasing the spatial and temporal resolution, and gathering more information about initial conditions, but comes at the cost of high demands of computing resources. Ultimately, the model complexity depends on the scientific question that intends to be answered. Simple ice-flow models, like the Nye model (Nye, 1963) or the Dansgaard–Johnsen model (Dansgaard and

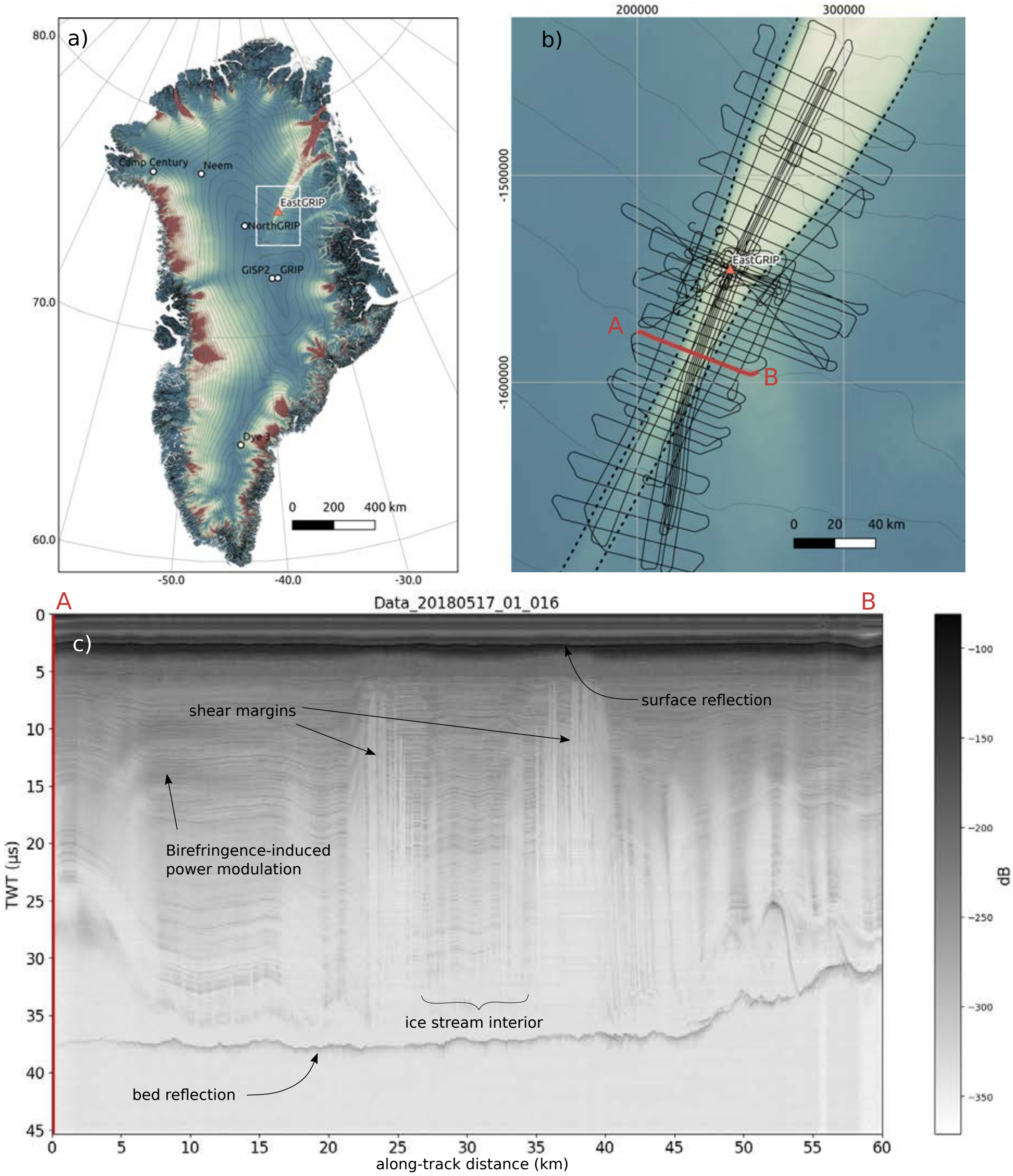

FIGURE 3.3: Location **a)** and survey layout **b)** of the EGRIP-NOR-2018 airborne UWB radar measurements. **c)** Radargrams crossing the ice stream typically show heavily folded internal stratigraphy and resulting loss of radar return power across the shear margins, intact stratigraphy inside the ice stream and large-scale folds outside the NEGIS.

Johnsen, 1969) limit the physical description of ice flow to the bare minimum, but still provide valuable results in terms of internal stratigraphy. Simple models have the advantage of running fast, having fewer parameters to tune and gain a better intuition of how each of them affects the modeling result, and analytical solutions simplify inversion methods.

Some important questions about the past and future behavior of ice sheets, or understanding ice flow in a particular area, however, can only be addressed with numerical models that describe the physics of ice-flow dynamics in higher detail. The most thorough description of ice flow is given by the full-Stokes equations, taking into account that ice is a viscous, incompressible fluid. These equations are, however, computationally expensive to solve and require a high enough spatial resolution, which makes full-Stokes models impractical for studies that include the entire ice sheet or long temporal scales. In that case, computational costs can be minimized by using techniques that approximate the full-Stokes equations at lower costs (e.g. MacAyeal, 1989; Blatter, 1995; Greve, 1997; Schoof and Hewitt, 2013). Such approximations are commonly used and perform reasonably well in the ice-sheet interior, but do not capture the ice dynamics in fast-flowing areas or in regions with strong variability in basal characteristics (Gudmundsson, 2003; Hindmarsh, 2004; Schoof and Hindmarsh, 2010; Rückamp et al., 2022).

Computation time can also be reduced by using a coarser spatio-temporal discretization which, however, decreases the ability to resolve details. Typical grid cells have a side length of 5–20 km (Calov et al., 2015; Fürst et al., 2015; Saito et al., 2016), but higher resolution might be required to capture processes e.g. at the glacier front. Finite element grids allow to decrease the cell size to the level of detail required in a particular area (Seroussi et al., 2013; Schlegel et al., 2015; Schlegel et al., 2016), and adaptive mesh methods adjust the grid with time, allowing for instance to follow grounding-line retreats with high enough resolution (e.g. Cornford et al., 2013).

Boundary conditions play a significant role in the model outcomes, but many of the subsurface properties that are required to describe the initial state of an ice sheet are difficult to observe directly. The geothermal heat flux, for example, and the associated melt-water production affects the basal friction and sliding velocities, but the thermal state of the bed is in most places highly uncertain (MacGregor et al., 2016). Similarly, the basal topography and material properties control the flow speed and basal deformation (Rignot et al., 2016), but accurate mapping of these quantities remains difficult. Many ice-sheet models use assimilation techniques to infer basal friction and sliding velocities from surface velocities and ice thickness. These methods minimize the cost function between observed and modeled surface velocities and often assume that the ice rheology, i.e. temperature, impurity content and crystal orientation, is described by an isotropic Glen's flow law (e.g. MacAyeal, 1993; Joughin et al., 2001; Morlighem et al., 2010; Seroussi et al., 2011). However, the ice rheology is more complicated in reality, as it depends non-linearly on temperature, and crystal fabric introduces anisotropic viscosities. In any case, this type of inverse problem is underconstrained, and many sets of subsurface parameters might equally well reproduce the observed surface velocities (Arthern and Gudmundsson, 2010), but can lead to divergence in prognostic model outcomes (Goelzer et al., 2018).

Overall, predictions of ice-sheet evolution in the future are complex, the associated uncertainties are large and their origin manifold. The mass balance of the polar ice sheets, however, depends strongly on a few dozen ice streams and outlet glaciers (Bentley and Giovinetto, 1991; Rignot and Kanagaratnam, 2006), each with their own characteristics. The accurate representation of these major glaciers in ice-sheet models can thus help to improve the reliability of ice-sheet prognoses, but requires the comprehension of the individual flow dynamics and boundary conditions in the respective areas.

References

Abbott, P. M. and Davies, S. M. (2012). “Volcanism and the Greenland ice-cores: the tephra record”. In: *Earth-Science Reviews* 115.3, pp. 173–191. DOI: `10.1016/j.earscirev.2012.09.001`.

Ackley, S. F. and Keliher, T. E. (1979). “Ice sheet internal radio-echo reflections and associated physical property changes with depth”. In: *Journal of Geophysical Research: Solid Earth* 84.B10, pp. 5675–5680. DOI: `10.1029/JB084iB10p05675`.

Alley, R. B., Meese, D. A., Shuman, C. A., Gow, A. J., Taylor, K. C., Grootes, P. M., White, J. W., Ram, M., Waddington, E. D., Mayewski, P. A., and Zielinski, G. A. (1993). “Abrupt increase in Greenland snow accumulation at the end of the Younger Dryas event”. In: *Nature* 362.6420, pp. 527–529. DOI: `10.1038/362527a0`.

Alley, R., Gow, A., Meese, D., Fitzpatrick, J., Waddington, E., and Bolzan, J. (1997). “Grain-scale processes, folding, and stratigraphic disturbance in the GISP2 ice core”. In: *Journal of Geophysical Research: Oceans* 102.C12, pp. 26819–26830. DOI: `10.1029/96JC03836`.

Alley, R. B. (1988). “Fabrics in polar ice sheets: development and prediction”. In: *Science* 240.4851, pp. 493–495. DOI: `10.1126/science.240.4851.493`.

Alley, R. B. (2000). “The Younger Dryas cold interval as viewed from central Greenland”. In: *Quaternary science reviews* 19.1-5, pp. 213–226. DOI: `10.1016/S0277-3791(99)00062-1`.

Alley, R. B. and Anandakrishnan, S. (1995). “Variations in melt-layer frequency in the GISP2 ice core: implications for Holocene summer temperatures in central Greenland”. In: *Annals of Glaciology* 21, pp. 64–70. DOI: `10.3189/s0260305500015615`.

Alley, R. B., Gow, A., Johnsen, S., Kipfstuhl, J., Meese, D., and Thorsteinsson, T. (1995). “Comparison of deep ice cores”. In: *Nature* 373.6513, pp. 393–393.

Alley, R. B., Andrews, J., Brigham-Grette, J., Clarke, G., Cuffey, K., Fitzpatrick, J., Funder, S., Marshall, S., Miller, G., Mitrovica, J., Muhs, D., Otto-Bliesner, B., Polyak, L., and White, J. (2010). “History of the Greenland Ice Sheet: paleoclimatic insights”. In: *Quaternary Science Reviews* 29.15-16, pp. 1728–1756. DOI: `10.1016/j.quascirev.2010.02.007`.

Andersen, K. K., Azuma, N., Barnola, J. M., Bigler, M., Biscaye, P., Caillon, N., Chappellaz, J., Clausen, H. B., Dahl-Jensen, D., Fischer, H., Flückiger, J., Fritzsche, D., Fujii, Y., Goto-Azuma, K., Grønvold, K., Gundestrup, N. S., Hansson, M., Huber, C., Hvidberg, C. S., Johnsen, S. J., Jonsell, U., Jouzel, J., Kipfstuhl, S., Landais, A., Leuenberger, M., Lorrain, R., Masson-Delmotte, V., Miller, H., Motoyama, H., Narita, H., Popp, T., Rasmussen, S. O., Raynaud, D., Rothlisberger, R., Ruth, U., Samyn, D., Schwander, J., Shoji, H., Siggard-Andersen, M. L., Steffensen, J. P., Stocker, T., Sveinbjörnsdóttir, A. E., Svensson, A., Takata, M., Tison, J. L., Thorsteinsson, T., Watanabe, O., Wilhelms, F., and White, J. W. (2004). “High-resolution record of Northern Hemisphere climate extending into the last interglacial period”. In: *Nature* 431.7005, pp. 147–151. DOI: `10.1038/nature02805`.

Arthern, R. J. and Gudmundsson, G. H. (2010). “Initialization of ice-sheet forecasts viewed as an inverse Robin problem”. In: *Journal of Glaciology* 56.197, pp. 527–533. DOI: `10.3189/002214310792447699`.

Azuma, N. and Higashi, A. (1985). “Formation processes of ice fabric pattern in ice sheets”. In: *Annals of Glaciology* 6, pp. 130–134. DOI: `10.3189/1985AoG6-1-130-134`.

Azuma, N., Wang, Y., Mori, K., Narita, H., Hondoh, T., Shoji, H., and Watanabe, O. (1999). “Textures and fabrics in the Dome F (Antarctica) ice core”. In: *Annals of Glaciology* 29, pp. 163–168. DOI: `10.3189/172756499781821148`.

Azuma, N., Wang, Y., Yoshida, Y., Narita, H., Hondoh, T., Shoji, H., and Watanabe, O. (2000). “Crystallographic analysis of the Dome Fuji ice core”. In: *Physics of Ice Core Records*. Hokkaido University Press, pp. 45–61.

Bamber, J. L., Griggs, J. A., Hurkmans, R. T. W. L., Dowdeswell, J. A., Gogineni, S. P., Howat, I., Mouginot, J., Paden, J., Palmer, S., Rignot, E., and Steinhage, D. (2013). "A new bed elevation dataset for Greenland". In: *The Cryosphere* 7.2, pp. 499–510. DOI: `10.5194/tc-7-499-2013`.

Bamber, J. (1987). "Internal reflecting horizons in Spitsbergen glaciers". In: *Annals of Glaciology* 9, pp. 5–10. DOI: `10.3189/S0260305500200682`.

Barbante, C. et al. (2006). "One-to-one coupling of glacial climate variability in Greenland and Antarctica". In: *Nature* 444.7116, pp. 195–198. DOI: `10.1038/nature05301`.

Beer, J., Finkel, R., Bonani, G., Gäggeler, H., Görlach, U., Jacob, P., Klockow, D., Langway, C., Neftel, A., Oeschger, H., Schotterer, U., Schwander, J., Siegenthaler, U., Suter, M., Wagenbach, D., and Wölfli, W. (1991). "Seasonal variations in the concentration of 10Be, Cl-, NO3-, SO42-, H2O2, 210Pb, 3H, mineral dust, and δ^{18}O in greenland snow". In: *Atmospheric Environment. Part A. General Topics* 25.5-6, pp. 899–904. DOI: `10.1016/0960-1686(91)90131-P`.

Bender, M., Sowers, T., and Brook, E. (1997). "Gases in ice cores". In: *Proceedings of the National Academy of Sciences* 94.16, pp. 8343–8349. DOI: `10.1073/pnas.94.16.8343`.

Bentley, C. R. and Giovinetto, M. (1991). "Mass balance of Antarctica and sea level change". In: *International Conference on the Role of the Polar Regions in Global Change* 2, pp. 481–488.

Blatter, H. (1995). "Velocity and stress fields in grounded glaciers: a simple algorithm for including deviatoric stress gradients". In: *Journal of Glaciology* 41.138, pp. 333–344. DOI: `10.3189/S002214300001621X`.

Blindow, N., Salat, C., Gundelach, V., Buschmann, U., and Kahnt, W. (2011). "Performance and calibration of the helicoper GPR system BGR-P30". In: *2011 6th International Workshop on Advanced Ground Penetrating Radar (IWAGPR)*. IEEE, pp. 1–5. DOI: `10.1109/IWAGPR.2011.5963896`.

Blunier, T., Chappellaz, J., Schwander, J., Stauffer, B., and Raynaud, D. (1995). "Variations in atmospheric methane concentration during the Holocene epoch". In: *Nature* 374.6517, pp. 46–49. DOI: `10.1038/374046a0`.

Blunier, T., Chappellaz, J., Schwander, J., Dällenbach, A., Stauffer, B., Stocker, T., Raynaud, D., Jouzel, J., Clausen, H., Hammer, C., and Johnsen, S. (1998). "Asynchrony of Antarctic and Greenland climate change during the last glacial period". In: *Nature* 394.6695, pp. 739–743. DOI: `10.1038/29447`.

Bohleber, P., Sold, L., Hardy, D. R., Schwikowski, M., Klenk, P., Fischer, A., Sirguey, P., Cullen, N. J., Potocki, M., Hoffmann, H., and Mayewski, P. (2017). "Ground-penetrating radar reveals ice thickness and undisturbed englacial layers at Kilimanjaro's Northern Ice Field". In: *The Cryosphere* 11.1, pp. 469–482. DOI: `10.5194/tc-11-469-2017`.

Bons, P. D., Jansen, D., Mundel, F., Bauer, C. C., Binder, T., Eisen, O., Jessell, M. W., Llorens, M.-G., Steinbach, F., Steinhage, D., and Weikusat, I. (2016). "Converging flow and anisotropy cause large-scale folding in Greenland's ice sheet". In: *Nature communications* 7.1, pp. 1–6. DOI: `10.1038/ncomms11427`.

Brewster, H. D. (2010). *Electromagnetism*. Oxford Book.

Broecker, W. S. (1966). "Absolute Dating and the Astronomical Theory of Glaciation: Changes in climate occur in response to periodic variations in the earth's tilt and precession." In: *Science* 151.3708, pp. 299–304. DOI: `10.1126/science.151.3708.299`.

Bulat, S. A. (2016). "Microbiology of the subglacial Lake Vostok: first results of borehole-frozen lake water analysis and prospects for searching for lake inhabitants". In: *Philosophical Transactions of the Royal Society A: Mathematical, Physical and Engineering Sciences* 374.2059, p. 20140292. DOI: `10.1098/rsta.2014.0292`.

Calov, R., Robinson, A., Perrette, M., and Ganopolski, A. (2015). "Simulating the Greenland ice sheet under present-day and palaeo constraints including a new discharge parameterization". In: *The Cryosphere* 9.1, pp. 179–196. DOI: `10.5194/tc-9-179-2015`.

Cavitte, M. G., Blankenship, D. D., Young, D. A., Schroeder, D. M., Parrenin, F., Lemeur, E., Macgregor, J. A., and Siegert, M. J. (2016). "Deep radiostratigraphy of the East Antarctic plateau: connecting the Dome C and Vostok ice core sites". In: *Journal of Glaciology* 62.232, pp. 323–334. DOI: 10.1017/jog.2016.11.

Christianson, K., Peters, L. E., Alley, R. B., Anandakrishnan, S., Jacobel, R. W., Riverman, K. L., Muto, A., and Keisling, B. A. (2014). "Dilatant till facilitates ice-stream flow in northeast Greenland". In: *Earth and Planetary Science Letters* 401, pp. 57–69. DOI: 10.1016/j.epsl.2014.05.060.

Conway, H., Smith, B., Vaswani, P., Matsuoka, K., Rignot, E., and Claus, P. (2009). "A low-frequency ice-penetrating radar system adapted for use from an airplane: test results from Bering and Malaspina Glaciers, Alaska, USA". In: *Annals of Glaciology* 50.51, pp. 93–97. DOI: 10.3189/172756409789097487.

Cornford, S. L., Martin, D. F., Graves, D. T., Ranken, D. F., Le Brocq, A. M., Gladstone, R. M., Payne, A. J., Ng, E. G., and Lipscomb, W. H. (2013). "Adaptive mesh, finite volume modeling of marine ice sheets". In: *Journal of Computational Physics* 232.1, pp. 529–549. DOI: https://doi.org/10.1016/j.jcp.2012.08.037.

Cuffey, K. M. and Paterson, W. S. B. (2010). *The physics of glaciers*. eng. 4. ed. Amsterdam: Butterworth-Heinemann/Elsevier.

Dahl-Jensen, D. (2018). "Drilling for the oldest ice". In: *Nature Geoscience* 11.10, pp. 703–704. DOI: 10.1038/s41561-018-0241-2.

Dall, J., Kristensen, S. S., Krozer, V., Hernández, C. C., Vidkjær, J., Kusk, A., Balling, J., Skou, N., Søbjærg, S. S., and Christensen, E. L. (2010). "ESA's polarimetric airborne radar ice sounder (POLARIS): Design and first results". In: *IET Radar, Sonar & Navigation* 4.3, pp. 488–496. DOI: 10.1049/iet-rsn.2009.0035.

Dansgaard, W., Clausen, H. B., Gundestrup, N., Hammer, C. U., Johnsen, S. F., Kristinsdottir, P. M., and Reeh, N. (1982). "A new Greenland deep ice core". In: *Science* 218.4579, pp. 1273–1277. DOI: 10.1126/science.218.4579.1273.

Dansgaard, W., Johnsen, S. J., Møller, J., and Langway Jr, C. C. (1969). "One thousand centuries of climatic record from Camp Century on the Greenland ice sheet". In: *Science* 166.3903, pp. 377–381. DOI: 10.1126/science.166.3903.377.

Dansgaard, W. (1964). "Stable isotopes in precipitation". In: *tellus* 16.4, pp. 436–468. DOI: 10.3402/tellusa.v16i4.8993.

Dansgaard, W. and Johnsen, S. J. (1969). "A flow model and a time scale for the ice core from Camp Century, Greenland". In: *Journal of Glaciology* 8.53, pp. 215–223. DOI: 10/hwss.

Dansgaard, W., Johnsen, S. J., Clausen, H. B., Dahl-Jensen, D., Gundestrup, N., Hammer, C., Hvidberg, C., Steffensen, J., Sveinbjörnsdottir, A., Jouzel, J., and Bond, G. (1993). "Evidence for general instability of past climate from a 250-kyr ice-core record". In: *nature* 364.6434, pp. 218–220. DOI: 10.1038/364218a0.

Das, I., Padman, L., Bell, R. E., Fricker, H. A., Tinto, K. J., Hulbe, C. L., Siddoway, C. S., Dhakal, T., Frearson, N. P., Mosbeux, C., Cordero, S. I., and Siegfried, M. R. (2020). "Multidecadal Basal Melt Rates and Structure of the Ross Ice Shelf, Antarctica, Using Airborne Ice Penetrating Radar". In: *Journal of Geophysical Research: Earth Surface* 125.3, e2019JF005241. DOI: 10.1029/2019JF005241.

Davis, C. H., Dean, R. H., and Xin, W. (1990). "Radar reflections from water injected into an Antarctic glacier". In: *IEEE Transactions on Geoscience and Remote Sensing* 28.4, pp. 723–726. DOI: 10.1109/TGRS.1990.572991.

De La Chapelle, S., Castelnau, O., Lipenkov, V., and Duval, P. (1998). "Dynamic recrystallization and texture development in ice as revealed by the study of deep ice cores in Antarctica and Greenland". In: *Journal of Geophysical Research: Solid Earth* 103.B3, pp. 5091–5105. DOI: 10.1029/97JB02621.

Delaygue, G. and Bard, E. (2011). "An Antarctic view of Beryllium-10 and solar activity for the past millennium". In: *Climate Dynamics* 36.11-12, pp. 2201–2218. DOI: 10.1007/s00382-010-0795-1.

Diprinzio, C., Wilen, L., Alley, R., Fitzpatrick, J., Spencer, M., and Gow, A. (2005). “Fabric and texture at Siple Dome, Antarctica”. In: *Journal of Glaciology* 51.173, pp. 281–290. DOI: `10.3189/172756505781829359`.

Durand, G., Svensson, A., Persson, A., Gagliardini, O., Gillet-Chaulet, F., Sjolte, J., Montagnat, M., and Dahl-Jensen, D. (2009). “Evolution of the texture along the EPICA Dome C ice core”. In: *Low Temperature Science* 68.Supplement, pp. 91–105.

Duval, P. and Castelnau, O. (1995). “Dynamic recrystallization of ice in polar ice sheets”. In: *Le Journal de Physique IV* 5.C3, pp. C3–197. DOI: `10.1051/jp4:1995317`.

Easterbrook, D. (2016). “Chapter 8 - Temperature Fluctuations in Greenland and the Arctic”. In: *Evidence-Based Climate Science (Second Edition)*. Ed. by D. J. Easterbrook. Second Edition. Elsevier, pp. 137–160. DOI: `10.1016/B978-0-12-804588-6.00008-2`.

Eichler, J. (2013). “C-Axis analysis of the NEEM ice core–An approach based on digital image processing”. Fachbereich Physik, Freie Universität Berlin.

Eisen, O., Hamann, I., Kipfstuhl, S., Steinhage, D., and Wilhelms, F. (2007). “Direct evidence for continuous radar reflector originating from changes in crystal-orientation fabric”. In: *The Cryosphere* 1.1, pp. 1–10. DOI: `10.5194/tc-1-1-2007`.

Eisen, O., Wilhelms, F., Steinhage, D., and Schwander, J. (2006). “Improved method to determine radio-echo sounding reflector depths from ice-core profiles of permittivity and conductivity”. In: *Journal of Glaciology* 52.177, pp. 299–310. DOI: `10.3189/172756506781828674`.

Ekaykin, A. A., Lipenkov, V. Y., Barkov, N. I., Petit, J. R., and Masson-Delmotte, V. (2002). “Spatial and temporal variability in isotope composition of recent snow in the vicinity of Vostok station, Antarctica: implications for ice-core record interpretation”. In: *Annals of Glaciology* 35, pp. 181–186. DOI: `10.3189/172756402781816726`.

Erhardt, T., Bigler, M., Federer, U., Gfeller, G., Leuenberger, D., Stowasser, O., Röthlisberger, R., Schüpbach, S., Ruth, U., Twarloh, B., Wegner, A., Goto-Azuma, K., Kuramoto, T., Kjær, H. A., Vallelonga, P. T., Siggaard-Andersen, M.-L., Hansson, M. E., Benton, A. K., Fleet, L. G., Mulvaney, R., Thomas, E. R., Abram, N., Stocker, T. F., and Fischer, H. (2022). “High-resolution aerosol concentration data from the Greenland NorthGRIP and NEEM deep ice cores”. In: *Earth System Science Data* 14.3, pp. 1215–1231. DOI: `10.5194/essd-14-1215-2022`.

Fahnestock, M., Abdalati, W., Joughin, I., Brozena, J., and Gogineni, P. (2001b). “High geothermal heat flow, basal melt, and the origin of rapid ice flow in central Greenland”. In: *Science* 294.5550, pp. 2338–2342. DOI: `10.1126/science.1065370`.

Fan, S., Hager, T., Prior, D. J., Cross, A. J., Goldsby, D. L., Qi, C., Negrini, M., and Wheeler, J. (2020). “Temperature and strain controls on ice deformation mechanisms: insights from the microstructures of samples deformed to progressively higher strains at -10, -20 and $-30\,°\mathrm{C}$”. In: *The Cryosphere Discussions* 2020, pp. 1–43. DOI: `10.5194/tc-2020-2`.

Faria, S. H., Weikusat, I., and Azuma, N. (2014). “The microstructure of polar ice. Part I: Highlights from ice core research”. In: *Journal of Structural Geology* 61, pp. 2–20. DOI: `10.1016/j.jsg.2013.09.010`.

Faria, S. H., Ktitarev, D., and Hutter, K. (2002). “Modelling evolution of anisotropy in fabric and texture of polar ice”. In: *Annals of Glaciology* 35, pp. 545–551. DOI: `10/cs42nf`.

Fegyveresi, J. M., Alley, R. B., Muto, A., Orsi, A. J., and Spencer, M. K. (2018). “Surface formation, preservation, and history of low-porosity crusts at the WAIS Divide site, West Antarctica”. In: *The Cryosphere* 12.1, pp. 325–341. DOI: `10.5194/tc-12-325-2018`.

Fischer, H., Severinghaus, J., Brook, E., Wolff, E., Albert, M., Alemany, O., Arthern, R., Bentley, C., Blankenship, D., Chappellaz, J., Creyts, T., Dahl-Jensen, D., Dinn, M., Frezzotti, M., Fujita, S., Gallee, H., Hindmarsh, R., Hudspeth, D., Jugie, G., Kawamura, K., Lipenkov, V., Miller, H., Mulvaney, R., Parrenin, F., Pattyn, F., Ritz, C., Schwander, J., Steinhage, D., Ommen, T. van, and Wilhelms, F. (2013). “Where to find 1.5 million yr old ice for the IPICS "Oldest-Ice" ice core”. In: *Climate of the Past* 9.6, pp. 2489–2505. DOI: `10.5194/cp-9-2489-2013`.

Fischer, H., Werner, M., Wagenbach, D., Schwager, M., Thorsteinnson, T., Wilhelms, F., Kipfstuhl, J., and Sommer, S. (1998). “Little ice age clearly recorded in northern Greenland ice cores”. In: *Geophysical Research Letters* 25.10, pp. 1749–1752. DOI: `10.1029/98GL01177`.

Fitzpatrick, J. J., Voigt, D. E., Fegyveresi, J. M., Stevens, N. T., Spencer, M. K., Cole-Dai, J., Alley, R. B., Jardine, G. E., Cravens, E. D., Wilen, L. A., Fudge, T., and Mcconnell, J. R. (2014). “Physical properties of the WAIS Divide ice core”. In: *Journal of Glaciology* 60.224, pp. 1181–1198. DOI: `10.3189/2014JoG14J100`.

Franke, S., Jansen, D., Binder, T., Paden, J. D., Dörr, N., Gerber, T. A., Miller, H., Dahl-Jensen, D., Helm, V., Steinhage, D., Weikusat, I., Wilhelms, F., and Eisen, O. (2022a). “Airborne ultra-wideband radar sounding over the shear margins and along flow lines at the onset region of the Northeast Greenland Ice Stream”. In: *Earth System Science Data* 14.2, pp. 763–779. DOI: `10.5194/essd-14-763-2022`.

Franke, S., Jansen, D., Binder, T., Dörr, N., Helm, V., Paden, J., Steinhage, D., and Eisen, O. (2020). “Bed topography and subglacial landforms in the onset region of the Northeast Greenland Ice Stream”. In: *Annals of Glaciology* 61.81, pp. 143–153. DOI: `10.1017/aog.2020.12`.

Fretwell, P. et al. (2013). “Bedmap2: improved ice bed, surface and thickness datasets for Antarctica”. In: *The Cryosphere* 7.1, pp. 375–393. DOI: `10.5194/tc-7-375-2013`.

Friedrich, M., Kromer, B., Kaiser, K. F., Spurk, M., Hughen, K. A., and Johnsen, S. J. (2001). “High-resolution climate signals in the Bølling–Allerød Interstadial (Greenland Interstadial 1) as reflected in European tree-ring chronologies compared to marine varves and ice-core records”. In: *Quaternary Science Reviews* 20.11. INTIMATE, pp. 1223–1232. DOI: `10.1016/S0277-3791(00)00148-7`.

Fudge, T. J., Steig, E. J., Markle, B. R., Schoenemann, S. W., Ding, Q., Taylor, K. C., McConnell, J. R., Brook, E. J., Sowers, T., White, J. W., Alley, R. B., Cheng, H., Clow, G. D., Cole-Dai, J., Conway, H., Cuffey, K. M., Edwards, J. S., Lawrence Edwards, R., Edwards, R., Fegyveresi, J. M., Ferris, D., Fitzpatrick, J. J., Johnson, J., Hargreaves, G., Lee, J. E., Maselli, O. J., Mason, W., McGwire, K. C., Mitchell, L. E., Mortensen, N., Neff, P., Orsi, A. J., Popp, T. J., Schauer, A. J., Severinghaus, J. P., Sigl, M., Spencer, M. K., Vaughn, B. H., Voigt, D. E., Waddington, E. D., Wang, X., and Wong, G. J. (2013). “Onset of deglacial warming in West Antarctica driven by local orbital forcing”. In: *Nature* 500.7463, pp. 440–444. DOI: `10.1038/nature12376`.

Fujita, S., Mae, S., and Matsuoka, T. (1993). “Dielectric anisotropy in ice Ih at 9.7 GHz”. In: *Annals of Glaciology* 17, pp. 276–280. DOI: `10.3189/S0260305500012969`.

Fürst, J. J., Goelzer, H., and Huybrechts, P. (2015). “Ice-dynamic projections of the Greenland ice sheet in response to atmospheric and oceanic warming”. In: *The Cryosphere* 9.3, pp. 1039–1062. DOI: `10.5194/tc-9-1039-2015`.

Gerbi, C., Mills, S., Clavette, R., Campbell, S., Bernsen, S., Clemens-Sewall, D., Lee, I., Hawley, R., Kreutz, K., Hruby, K., and al., et (2021). “Microstructures in a shear margin: Jarvis Glacier, Alaska”. In: *Journal of Glaciology* 67.266, pp. 1163–1176. DOI: `10.1017/jog.2021.62`.

Goelzer, H., Nowicki, S., Edwards, T., Beckley, M., Abe-Ouchi, A., Aschwanden, A., Calov, R., Gagliardini, O., Gillet-Chaulet, F., Golledge, N. R., Gregory, J., Greve, R., Humbert, A., Huybrechts, P., Kennedy, J. H., Larour, E., Lipscomb, W. H., Le clec’h, S., Lee, V., Morlighem, M., Pattyn, F., Payne, A. J., Rodehacke, C., Rückamp, M., Saito, F., Schlegel, N., Seroussi, H., Shepherd, A., Sun, S., Wal, R. van de, and Ziemen, F. A. (2018). “Design and results of the ice sheet model initialisation experiments initMIP-Greenland: an ISMIP6 intercomparison”. In: *The Cryosphere* 12.4, pp. 1433–1460. DOI: `10.5194/tc-12-1433-2018`.

Gogineni, S., Tammana, D., Braaten, D., Leuschen, C., Akins, T., Legarsky, J., Kanagaratnam, P., Stiles, J., Allen, C., and Jezek, K. (2001). “Coherent radar ice thickness measurements over the Greenland ice sheet”. In: *Journal of Geophysical Research: Atmospheres* 106.D24, pp. 33761–33772. DOI: `10.1029/2001JD900183`.

Gogineni, S., Chuah, T., Allen, C., Jezek, K., and Moore, R. K. (1998). “An improved coherent radar depth sounder”. In: *Journal of Glaciology* 44.148, pp. 659–669. DOI: `10.3189/S0022143000002161`.

Gow, A., Meese, D., Alley, R., Fitzpatrick, J., Anandakrishnan, S., Woods, G., and Elder, B. (1997). “Physical and structural properties of the Greenland Ice Sheet Project 2 ice core: A review”. In: *Journal of Geophysical Research: Oceans* 102.C12, pp. 26559–26575. DOI: `10.1029/97JC00165`.

Gow, A. J. and Williamson, T. (1976). “Rheological implications of the internal structure and crystal fabrics of the West Antarctic ice sheet as revealed by deep core drilling at Byrd Station”. In: *Geological Society of America Bulletin* 87.12, pp. 1665–1677. DOI: `10.1130/0016-7606(1976)87<1665:RIOTIS>2.0.CO;2`.

Gow, A. J., Ueda, H. T., and Garfield, D. E. (1968). “Antarctic ice sheet: Preliminary results of first core hole to bedrock”. In: *Science* 161.3845, pp. 1011–1013. DOI: `10.1126/science.161.3845.1011`.

Greve, R. (1997). “Application of a polythermal three-dimensional ice sheet model to the Greenland ice sheet: response to steady-state and transient climate scenarios”. In: *Journal of Climate* 10.5, pp. 901–918. DOI: `10.1175/1520-0442(1997)010<0901:AOAPTD>2.0.CO;2`.

Gudmundsson, G. H. (2003). “Transmission of basal variability to a glacier surface”. In: *Journal of Geophysical Research: Solid Earth* 108.B5. DOI: `10.1029/2002JB002107`.

Hammer, C., Clausen, H., and Langway, C. (1994). “Electrical conductivity method (ECM) stratigraphic dating of the Byrd Station ice core, Antarctica”. In: *Annals of Glaciology* 20, pp. 115–120. DOI: `10.3189/1994AoG20-1-115-120`.

Hammer, C. U. (1980). “Acidity of polar ice cores in relation to absolute dating, past volcanism, and radio–echoes”. In: *Journal of Glaciology* 25.93, pp. 359–372. DOI: `10/hwsm`.

Harrison, C. H. (1973). “Radio Echo Sounding of Horizontal Layers in Ice”. In: *Journal of Glaciology* 12.66, pp. 383–397. DOI: `10.3189/s0022143000031804`.

Hastings, M. G., Steig, E. J., and Sigman, D. M. (2004). “Seasonal variations in N and O isotopes of nitrate in snow at Summit, Greenland: Implications for the study of nitrate in snow and ice cores”. In: *Journal of Geophysical Research: Atmospheres* 109.D20. DOI: `10.1029/2004JD004991`.

Herron, S. L. and Langway, C. C. (1982). “A comparison of ice fabrics and textures at Camp Century, Greenland and Byrd Station, Antarctica”. In: *Annals of glaciology* 3, pp. 118–124. DOI: `10.3189/S0260305500002639`.

Hindmarsh, R. (2004). “A numerical comparison of approximations to the Stokes equations used in ice sheet and glacier modeling”. In: *Journal of Geophysical Research: Earth Surface* 109.F1. DOI: `10.1029/2003JF000065`.

Hubbard, B. and Glasser, N. F. (2005). *Field techniques in glaciology and glacial geomorphology*. John Wiley & Sons.

Hvidberg, C. S., Grinsted, A., Dahl-Jensen, D., Khan, S. A., Kusk, A., Andersen, J. K., Neckel, N., Solgaard, A., Karlsson, N. B., Kjær, H. A., and Vallelonga, P. (2020). “Surface velocity of the Northeast Greenland Ice Stream (NEGIS): assessment of interior velocities derived from satellite data by GPS”. In: *The Cryosphere* 14.10, pp. 3487–3502. DOI: `10.5194/tc-14-3487-2020`.

Jacobel, R. W. and Hodge, S. M. (1995). “Radar internal layers from the Greenland summit”. In: *Geophysical Research Letters* 22.5, pp. 587–590. DOI: `10.1029/95GL00110`.

Jansen, D., Llorens, M.-G., Westhoff, J., Steinbach, F., Kipfstuhl, S., Bons, P. D., Griera, A., and Weikusat, I. (2016). “Small-scale disturbances in the stratigraphy of the NEEM ice core: observations and numerical model simulations”. In: *The Cryosphere* 10.1, pp. 359–370. DOI: `10.5194/tc-10-359-2016`.

Joughin, I., Fahnestock, M., MacAyeal, D., Bamber, J. L., and Gogineni, P. (2001). "Observation and analysis of ice flow in the largest Greenland ice stream". In: *Journal of Geophysical Research: Atmospheres* 106.D24, pp. 34021–34034. DOI: `10.1029/2001JD900087`.

Joughin, I., Smith, B. E., and Howat, I. M. (2018). "A complete map of Greenland ice velocity derived from satellite data collected over 20 years". In: *Journal of Glaciology* 64.243, pp. 1–11. DOI: `10.1017/jog.2017.73`.

Jouzel, J., Masson-Delmotte, V., Cattani, O., Dreyfus, G., Falourd, S., Hoffmann, G., Minster, B., Nouet, J., Barnola, J. M., Chappellaz, J., Fischer, H., Gallet, J. C., Johnsen, S., Leuenberger, M., Loulergue, L., Luethi, D., Oerter, H., Parrenin, F., Raisbeck, G., Raynaud, D., Schilt, A., Schwander, J., Selmo, E., Souchez, R., Spahni, R., Stauffer, B., Steffensen, J. P., Stenni, B., Stocker, T. F., Tison, J. L., Werner, M., and Wolff, E. W. (2007). "Orbital and Millennial Antarctic Climate Variability over the Past 800,000 Years". In: *Science* 317.5839, pp. 793–796. DOI: `10.1126/science.1141038`.

Kellerhals, T., Brütsch, S., Sigl, M., Knüsel, S., Gäggeler, H. W., and Schwikowski, M. (2010). "Ammonium concentration in ice cores: A new proxy for regional temperature reconstruction?" In: *Journal of Geophysical Research: Atmospheres* 115.D16. DOI: `10.1029/2009JD012603`.

Kindler, P., Guillevic, M., Baumgartner, M., Schwander, J., Landais, A., and Leuenberger, M. (2014). "Temperature reconstruction from 10 to 120 kyr b2k from the NGRIP ice core". In: *Climate of the Past* 10.2, pp. 887–902. DOI: `10.5194/cp-10-887-2014`.

Legrand, M. and Mayewski, P. (1997). "Glaciochemistry of polar ice cores: A review". In: *Reviews of Geophysics* 35.3, pp. 219–243. DOI: `10.1029/96RG03527`.

Li, C. and Born, A. (2019). "Coupled atmosphere-ice-ocean dynamics in Dansgaard-Oeschger events". In: *Quaternary Science Reviews* 203, pp. 1–20. DOI: `10.1016/j.quascirev.2018.10.031`.

Lilien, D. A., Rathmann, N. M., Hvidberg, C. S., and Dahl-Jensen, D. (2021). "Modeling Ice-Crystal Fabric as a Proxy for Ice-Stream Stability". In: *Journal of Geophysical Research: Earth Surface* 126.9, e2021JF006306. DOI: `10.1029/2021JF006306`.

Lorius, C., Jouzel, J., Ritz, C., Merlivat, L., Barkov, N. I., Korotkevich, Y. S., and Kotlyakov, V. M. (1985). "A 150,000-year climatic record from Antarctic ice". In: *Nature* 316.6029, pp. 591–596. DOI: `10.1038/316591a0`.

Lowe, J. J., Ramsey, C. B., Housley, R. A., Lane, C. S., and Tomlinson, E. L. (2015). "The RESET project: constructing a European tephra lattice for refined synchronisation of environmental and archaeological events during the last c. 100 ka". In: *Quaternary Science Reviews* 118. Synchronising Environmental and Archaeological Records using Volcanic Ash Isochrons, pp. 1–17. DOI: `10.1016/j.quascirev.2015.04.006`.

MacAyeal, D. R. (1989). "Large-scale ice flow over a viscous basal sediment: Theory and application to ice stream B, Antarctica". In: *Journal of Geophysical Research: Solid Earth* 94.B4, pp. 4071–4087. DOI: `10.1029/JB094iB04p04071`.

MacAyeal, D. R. (1993). "A tutorial on the use of control methods in ice-sheet modeling". In: *Journal of Glaciology* 39.131, pp. 91–98. DOI: `10.3189/S0022143000015744`.

Maccagnan, M., Barnola, J., Delmas, R., and Duval, P. (1981). "Static electrical conductivity as an indicator of the sulfate content of polar ice cores". In: *Geophysical Research Letters* 8.9, pp. 970–972.

MacGregor, J. A., Fahnestock, M. A., Catania, G. A., Paden, J. D., Gogineni, S. P., Young, S. K., Rybarski, S. C., Mabrey, A. N., Wagman, B. M., and Morlighem, M. (2015). "Radiostratigraphy and age structure of the Greenland Ice Sheet". In: *Journal of Geophysical Research: Earth Surface* 120.2, pp. 212–241. DOI: `10.1002/2014JF003215`.

MacGregor, J. A., Fahnestock, M. A., Catania, G. A., Aschwanden, A., Clow, G. D., Colgan, W. T., Gogineni, S. P., Morlighem, M., Nowicki, S. M. J., Paden, J. D., Price, S. F., and Seroussi, H. (2016). "A synthesis of the basal thermal state of the Greenland Ice Sheet". In: *Journal of Geophysical Research: Earth Surface* 121.7, pp. 1328–1350. DOI: `10.1002/2015JF003803`.

Marcott, S. A., Bauska, T. K., Buizert, C., Steig, E. J., Rosen, J. L., Cuffey, K. M., Fudge, T. J., Severinghaus, J. P., Ahn, J., Kalk, M. L., McConnell, J. R., Sowers, T., Taylor, K. C., White, J. W., and Brook, E. J. (2014). "Centennial-scale changes in the global carbon cycle during the last deglaciation". In: *Nature* 514.7524, pp. 616–619. DOI: `10.1038/nature13799`.

Mojtabavi, S., Wilhelms, F., Cook, E., Davies, S., Sinnl, G., Skov Jensen, M., Dahl-Jensen, D., Svensson, A., Vinther, B., Kipfstuhl, S., Jones, G., Karlsson, N., Faria, S. H., Gkinis, V., Kjær, H., Erhardt, T., Berben, S., Nisancioglu, K., Koldtoft, I., and Rasmussen, S. O. (2020b). "A first chronology for the East GReenland Ice-core Project (EGRIP) over the Holocene and last glacial termination". In: *Climate of the Past* 16.6, pp. 2359–2380. DOI: `10.5194/cp-2019-143`.

Mojtabavi, S., Wilhelms, F., Cook, E., Davies, S. M., Sinnl, G., Skov Jensen, M., Dahl-Jensen, D., Svensson, A. M., Vinther, B. M., Kipfstuhl, S., Karlsson, N. B., Faria, S. H., Gkinis, V., Kjær, H. A., Erhardt, T., Berben, S. M. P., Nisancioglu, K. H., Koldtoft, I., and Rasmussen, S. O. (2020c). "Acidity measured with the Electrical Conductivity Method (ECM) on the EGRIP ice core (down to 1383.84 m depth), converted to hydrogen ion concentration". In: PANGAEA. DOI: `10.1594/PANGAEA.922199`.

Mojtabavi, S., Wilhelms, F., Cook, E., Davies, S. M., Sinnl, G., Skov Jensen, M., Dahl-Jensen, D., Svensson, A. M., Vinther, B. M., Kipfstuhl, S., Karlsson, N. B., Faria, S. H., Gkinis, V., Kjær, H. A., Erhardt, T., Berben, S. M. P., Nisancioglu, K. H., Koldtoft, I., and Rasmussen, S. O. (2020e). "Specific conductivity measured with the dielectric profiling (DEP) technique on the EGRIP ice core, 13.77-1383.84 m depth". In: PANGAEA. DOI: `10.1594/PANGAEA.919313`.

Montagnat, M., Azuma, N., Dahl-Jensen, D., Eichler, J., Fujita, S., Gillet-Chaulet, F., Kipfstuhl, S., Samyn, D., Svensson, A., and Weikusat, I. (2014). "Fabric along the NEEM ice core, Greenland, and its comparison with GRIP and NGRIP ice cores". In: *The Cryosphere* 8.4, pp. 1129–1138. DOI: `10.5194/tc-8-1129-2014`.

Montagnat, M., Buiron, D., Arnaud, L., Broquet, A., Schlitz, P., Jacob, R., and Kipfstuhl, S. (2012). "Measurements and numerical simulation of fabric evolution along the Talos Dome ice core, Antarctica". In: *Earth and Planetary Science Letters* 357, pp. 168–178. DOI: `10.1016/j.epsl.2012.09.025`.

Montagnat, M. and Duval, P. (2000). "Rate controlling processes in the creep of polar ice, influence of grain boundary migration associated with recrystallization". In: *Earth and Planetary Science Letters* 183.1-2, pp. 179–186. DOI: `10.1016/S0012-821X(00)00262-4`.

Monz, M. E., Hudleston, P. J., Prior, D. J., Michels, Z., Fan, S., Negrini, M., Langhorne, P. J., and Qi, C. (2021). "Full crystallographic orientation (*c* and *a* axes) of warm, coarse-grained ice in a shear-dominated setting: a case study, Storglaciären, Sweden". In: *The Cryosphere* 15.1, pp. 303–324. DOI: `10.5194/tc-15-303-2021`.

Moore, J. (1993). "High-resolution dielectric profiling of ice cores". In: *Journal of Glaciology* 39.132, pp. 245–248. DOI: `10.3189/S0022143000015902`.

Moore, J., Mulvaney, R., and Paren, J. (1989). "Dielectric stratigraphy of ice: A new technique for determining total ionic concentrations in polar ice cores". In: *Geophysical Research Letters* 16.10, pp. 1177–1180. DOI: `10.1029/GL016i010p01177`.

Moore, J. and Paren, J. (1987). "A new technique for dielectric logging of Antarctic ice cores". In: *Le Journal de Physique Colloques* 48.C1, pp. C1–155. DOI: `10.1051/jphyscol:1987123`.

Moore, J. C., Wolff, E. W., Clausen, H. B., and Hammer, C. U. (1992). "The chemical basis for the electrical stratigraphy of ice". In: *Journal of Geophysical Research: Solid Earth* 97.B2, pp. 1887–1896. DOI: `10.1029/91JB02750`.

Moore, J. C., Wolff, E. W., Clausen, H. B., Hammer, C. U., Legrand, M. R., and Fuhrer, K. (1994). "Electrical response of the Summit-Greenland ice core to ammonium, sulphuric acid, and hydrochloric acid". In: *Geophysical Research Letters* 21.7, pp. 565–568. DOI: `10.1029/94GL00542`.

Morlighem, M., Rignot, E., Seroussi, H., Larour, E., Ben Dhia, H., and Aubry, D. (2010). "Spatial patterns of basal drag inferred using control methods from a full-Stokes and simpler models for Pine Island Glacier, West Antarctica". In: *Geophysical Research Letters* 37.14. DOI: `10.1029/2010GL043853`.

Musil, G. J. and Doake, C. (1987). "Imaging subglacial topography by a synthetic aperture radar technique". In: *Annals of Glaciology* 9, pp. 170–175. DOI: `10.3189/S0260305500000562`.

NEEM Community members et al. (2013). "Eemian interglacial reconstructed from a Greenland folded ice core". In: *Nature* 493.7433, pp. 489–494. DOI: `10.1038/nature11789`.

Neftel, A., Beer, J., Oeschger, H., Zürcher, F., and Finkel, R. (1985). "Sulphate and nitrate concentrations in snow from South Greenland 1895–1978". In: *Nature* 314.6012, pp. 611–613.

Nye, J. F. (1963). "Correction factor for accumulation measured by the thickness of the annual layers in an ice sheet". In: *Journal of Glaciology* 4.36, pp. 785–788. DOI: `10.3189/S0022143000028367`.

Oswald, G. K. and Gogineni, S. (2011). "Mapping basal melt under the northern Greenland Ice Sheet". In: *IEEE Transactions on Geoscience and Remote Sensing* 50.2, pp. 585–592. DOI: `10.1029/2019JF005241`.

Paden, J., Akins, T., Dunson, D., Allen, C., and Gogineni, P. (2010). "Ice-sheet bed 3-D tomography". In: *Journal of Glaciology* 56.195, pp. 3–11. DOI: `10.3189/002214310791190811`.

Parrenin, F., Barnola, J. M., Beer, J., Blunier, T., Castellano, E., Chappellaz, J., Dreyfus, G., Fischer, H., Fujita, S., Jouzel, J., Kawamura, K., Lemieux-Dudon, B., Loulergue, L., Masson-Delmotte, V., Narcisi, B., Petit, J. R., Raisbeck, G., Raynaud, D., Ruth, U., Schwander, J., Severi, M., Spahni, R., Steffensen, J. P., Svensson, A., Udisti, R., Waelbroeck, C., and Wolff, E. (2007). "The EDC3 chronology for the EPICA Dome C ice core". In: *Climate of the Past* 3.3, pp. 485–497. DOI: `10.5194/cp-3-485-2007`.

Parrenin, F., Petit, J.-R., Masson-Delmotte, V., Wolff, E., Basile-Doelsch, I., Jouzel, J., Lipenkov, V., Rasmussen, S. O., Schwander, J., Severi, M., Udisti, R., Veres, D., and Vinther, B. M. (2012). "Volcanic synchronisation between the EPICA Dome C and Vostok ice cores (Antarctica) 0-145 kyr BP". In: *Climate of the Past* 8.3, pp. 1031–1045. DOI: `10.5194/cp-8-1031-2012`.

Peltier, W. R. and Vettoretti, G. (2014). "Dansgaard-Oeschger oscillations predicted in a comprehensive model of glacial climate: A "kicked" salt oscillator in the Atlantic". In: *Geophysical Research Letters* 41.20, pp. 7306–7313. DOI: `10.1002/2014GL061413`.

Petit, J. R., Raynaud, D., Basile, I., Chappellaz, J., Davisk, M., Ritz, C., Delmotte, M., Legrand, M., Lorius, C., Pe, L., and Saltzmank, E. (1999). "Climate and atmospheric history of the past 420,000 years from the Vostok ice core , Antarctica". In: *Nature* 399, pp. 429–436. DOI: `10.1038/20859`.

Pimienta, P., Duval, P., and Lipenkov, V. Y. (1987). "Mechanical behaviour of anisotropic polar ice". In: *The Physical Basis of Ice Sheet Modelling*. IAHS Publication No. 170. Wallingford, UK: IAHS Press, pp. 57–66.

Raisbeck, G., Yiou, F., Jouzel, J., and Stocker, T. (2007). "Direct north-south synchronization of abrupt climate change record in ice cores using Beryllium 10". In: *Climate of the Past* 3.3, pp. 541–547. DOI: `10.5194/cp-3-541-2007`.

Rasmussen, S. O., Abbott, P. M., Blunier, T., Bourne, A. J., Brook, E., Buchardt, S. L., Buizert, C., Chappellaz, J., Clausen, H. B., Cook, E., Dahl-Jensen, D., Davies, S. M., Guillevic, M., Kipfstuhl, S., Laepple, T., Seierstad, I. K., Severinghaus, J. P., Steffensen, J. P., Stowasser, C., Svensson, A., Vallelonga, P., Vinther, B. M., Wilhelms, F., and Winstrup, M. (2013). "A first chronology for the North Greenland Eemian Ice Drilling (NEEM) ice core". In: *Climate of the Past* 9.6, pp. 2713–2730. DOI: `10.5194/cp-9-2713-2013`.

Rasmussen, S. O., Bigler, M., Blockley, S. P., Blunier, T., Buchardt, S. L., Clausen, H. B., Cvijanovic, I., Dahl-Jensen, D., Johnsen, S. J., Fischer, H., Gkinis, V., Guillevic, M., Hoek, W. Z., Lowe, J. J., Pedro, J. B., Popp, T., Seierstad, I. K., Steffensen, J. P., Svensson, A. M., Vallelonga, P., Vinther, B. M., Walker, M. J., Wheatley, J. J., and Winstrup, M. (2014). "A stratigraphic framework for abrupt climatic changes during the Last Glacial period based on three synchronized Greenland ice-core records: refining and extending the INTIMATE event stratigraphy". In: *Quaternary Science Reviews* 106. Dating, Synthesis, and Interpretation of Palaeoclimatic Records and Model-data Integration: Advances of the INTIMATE project (INTegration of Ice core, Marine and TErrestrial records, COST Action ES0907), pp. 14–28. DOI: `10.1016/j.quascirev.2014.09.007`.

Rhodes, R. H., Fain, X., Stowasser, C., Blunier, T., Chappellaz, J., McConnell, J. R., Romanini, D., Mitchell, L. E., and Brook, E. J. (2013). "Continuous methane measurements from a late Holocene Greenland ice core: Atmospheric and in-situ signals". In: *Earth and Planetary Science Letters* 368, pp. 9–19. DOI: `10.1016/j.epsl.2013.02.034`.

Rignot, E., Xu, Y., Menemenlis, D., Mouginot, J., Scheuchl, B., Li, X., Morlighem, M., Seroussi, H., Broeke, M. v. den, Fenty, I., Cai, C., An, L., and Fleurian, B. d. (2016). "Modeling of ocean-induced ice melt rates of five west Greenland glaciers over the past two decades". In: *Geophysical Research Letters* 43.12, pp. 6374–6382. DOI: `10.1002/2016GL068784`.

Rignot, E. and Kanagaratnam, P. (2006). "Changes in the velocity structure of the Greenland Ice Sheet". In: *Science* 311.5763, pp. 986–990. DOI: `10.1126/science.1121381`.

Robin, G. d. Q., Evans, S., and Bailey, J. T. (1969). "Interpretation of radio echo sounding in polar ice sheets". In: *Philosophical Transactions of the Royal Society of London. Series A, Mathematical and Physical Sciences* 265.1166, pp. 437–505. DOI: `10.1098/rsta.1969.0063`.

Rückamp, M., Kleiner, T., and Humbert, A. (2022). "Comparison of ice dynamics using full-Stokes and Blatter–Pattyn approximation: application to the Northeast Greenland Ice Stream". In: *The Cryosphere* 16.5, pp. 1675–1696. DOI: `10.5194/tc-16-1675-2022`. URL: `https://tc.copernicus.org/articles/16/1675/2022/`.

Ruth, U., Barnola, J.-M., Beer, J., Bigler, M., Blunier, T., Castellano, E., Fischer, H., Fundel, F., Huybrechts, P., Kaufmann, P., Kipfstuhl, S., Lambrecht, A., Morganti, A., Oerter, H., Parrenin, F., Rybak, O., Severi, M., Udisti, R., Wilhelms, F., and Wolff, E. (2007). “" EDML1": a chronology for the EPICA deep ice core from Dronning Maud Land, Antarctica, over the last 150 000 years". In: *Climate of the Past* 3.3, pp. 475–484. DOI: `10.5194/cp-3-475-2007`.

Saito, F., Abe-Ouchi, A., Takahashi, K., and Blatter, H. (2016). "SeaRISE experiments revisited: potential sources of spread in multi-model projections of the Greenland ice sheet". In: *The Cryosphere* 10.1, pp. 43–63. DOI: `10.5194/tc-10-43-2016`.

Schaefer, J. M., Finkel, R. C., Balco, G., Alley, R. B., Caffee, M. W., Briner, J. P., Young, N. E., Gow, A. J., and Schwartz, R. (2016). "Greenland was nearly ice-free for extended periods during the Pleistocene". In: *Nature* 540.7632, pp. 252–255. DOI: `10.1038/nature20146`.

Schlegel, N.-J., Larour, E., Seroussi, H., Morlighem, M., and Box, J. (2015). "Ice discharge uncertainties in Northeast Greenland from boundary conditions and climate forcing of an ice flow model". In: *Journal of Geophysical Research: Earth Surface* 120.1, pp. 29–54. DOI: `10.1002/2014JF003359`.

Schlegel, N.-J., Wiese, D. N., Larour, E. Y., Watkins, M. M., Box, J. E., Fettweis, X., and Van Den Broeke, M. R. (2016). "Application of GRACE to the assessment of model-based estimates of monthly Greenland Ice Sheet mass balance (2003–2012)". In: *The Cryosphere* 10.5, pp. 1965–1989. DOI: `10.5194/tc-10-1965-2016`.

Schoof, C. and Hewitt, I. (2013). "Ice-sheet dynamics". In: *Annual Review of Fluid Mechanics* 45, pp. 217–239. DOI: `10.1146/annurev-fluid-011212-140632`.

Schoof, C. and Hindmarsh, R. C. (2010). "Thin-film flows with wall slip: an asymptotic analysis of higher order glacier flow models". In: *Quarterly journal of mechanics and applied mathematics* 63.1, pp. 73–114. DOI: `10.1093/qjmam/hbp025`.

Schroeder, D. M., Bingham, R. G., Blankenship, D. D., Christianson, K., Eisen, O., Flowers, G. E., Karlsson, N. B., Koutnik, M. R., Paden, J. D., and Siegert, M. J. (2020). "Five decades of radioglaciology". In: *Annals of Glaciology* 61.81, pp. 1–13. DOI: `10.1017/aog.2020.11`.

Schwander, J., Neftel, A., Oeschger, H., and Stauffer, B. (1983). "Measurement of direct current conductivity on ice samples for climatological applications". In: *The Journal of Physical Chemistry* 87.21, pp. 4157–4160. DOI: 10.1021/j100244a036.

Seroussi, H., Morlighem, M., Rignot, E., Khazendar, A., Larour, E., and Mouginot, J. (2013). "Dependence of century-scale projections of the Greenland ice sheet on its thermal regime". In: *Journal of Glaciology* 59.218, pp. 1024–1034. DOI: 10.3189/2013JoG13J054.

Seroussi, H., Morlighem, M., Rignot, E., Larour, E., Aubry, D., Ben Dhia, H., and Kristensen, S. S. (2011). "Ice flux divergence anomalies on 79north Glacier, Greenland". In: *Geophysical Research Letters* 38.9. DOI: 10.1029/2011GL047338.

Shakun, J. D., Corbett, L. B., Bierman, P. R., Underwood, K., Rizzo, D. M., Zimmerman, S. R., Caffee, M. W., Naish, T., Golledge, N. R., and Hay, C. C. (2018). "Minimal East Antarctic Ice Sheet retreat onto land during the past eight million years". In: *Nature* 558.7709, pp. 284–287. DOI: 10.1038/s41586-018-0155-6.

Sigl, M., Fudge, T. J., Winstrup, M., Cole-Dai, J., Ferris, D., McConnell, J. R., Taylor, K. C., Welten, K. C., Woodruff, T. E., Adolphi, F., Bisiaux, M., Brook, E. J., Buizert, C., Caffee, M. W., Dunbar, N. W., Edwards, R., Geng, L., Iverson, N., Koffman, B., Layman, L., Maselli, O. J., McGwire, K., Muscheler, R., Nishiizumi, K., Pasteris, D. R., Rhodes, R. H., and Sowers, T. A. (2016). "The WAIS Divide deep ice core WD2014 chronology – Part 2: Annual-layer counting (0–31 ka BP)". In: *Climate of the Past* 12.3, pp. 769–786. DOI: 10.5194/cp-12-769-2016.

Steffensen, J. P. (2012). "Willi Dansgaard". In: *Polar Record* 48.2, pp. 206–207. DOI: 10.1017/S0032247411000155.

Steinhilber, F., Abreu, J. A., Beer, J., Brunner, I., Christl, M., Fischer, H., Heikkilä, U., Kubik, P. W., Mann, M., McCracken, K. G., Miller, H., Miyahara, H., Oerter, H., and Wilhelms, F. (2012). "9,400 years of cosmic radiation and solar activity from ice cores and tree rings". In: *Proceedings of the National Academy of Sciences* 109.16, pp. 5967–5971. DOI: 10.1073/pnas.1118965109.

Stoll, N. (2019). *A first glimpse into the EGRIP ice core: An analysis of the influence of deformation and recrystallisation on fabric and microstructures of the Northeast Greenland Ice Stream*. Master thesis, University Bremen FB5.

Svensson, A., Dahl-Jensen, D., Steffensen, J. P., Blunier, T., Rasmussen, S. O., Vinther, B. M., Vallelonga, P., Capron, E., Gkinis, V., Cook, E., Kjær, H. A., Muscheler, R., Kipfstuhl, S., Wilhelms, F., Stocker, T. F., Fischer, H., Adolphi, F., Erhardt, T., Sigl, M., Landais, A., Parrenin, F., Buizert, C., McConnell, J. R., Severi, M., Mulvaney, R., and Bigler, M. (2020). "Bipolar volcanic synchronization of abrupt climate change in Greenland and Antarctic ice cores during the last glacial period". In: *Climate of the Past* 16.4, pp. 1565–1580. DOI: 10.5194/cp-16-1565-2020.

Svensson, A., Nielsen, S. W., Kipfstuhl, S., Johnsen, S. J., Steffensen, J. P., Bigler, M., Ruth, U., and Röthlisberger, R. (2005). "Visual stratigraphy of the North Greenland Ice Core Project (NorthGRIP) ice core during the last glacial period". In: *Journal of Geophysical Research: Atmospheres* 110.D2. DOI: 10.1029/2004JD005134.

Taylor, K., Hammer, C., Alley, R., Clausen, H., Dahl-Jensen, D., Gow, A., Gundestrup, N., Kipfstuh, J., Moore, J., and Waddington, E. (1993). "Electrical conductivity measurements from the GISP2 and GRIP Greenland ice cores". In: *Nature* 366.6455, pp. 549–552. DOI: 10.1038/366549a0.

Taylor, K. C., Alley, R. B., Lamorey, G. W., and Mayewski, P. (1997). "Electrical measurements on the Greenland Ice Sheet Project 2 core". In: *Journal of Geophysical Research: Oceans* 102.C12, pp. 26511–26517. DOI: 10.1029/96JC02500.

Taylor, K., Alley, R., Fiacco, J., Grootes, P., Lamorey, G., Mayewski, P., and Spencer, M. J. (1992). "Ice-core dating and chemistry by direct-current electrical conductivity". In: *Journal of Glaciology* 38.130, pp. 325–332. DOI: 10.3189/S0022143000002215.

Thomas, E. R., Wolff, E. W., Mulvaney, R., Steffensen, J. P., Johnsen, S. J., Arrowsmith, C., White, J. W., Vaughn, B., and Popp, T. (2007). “The 8.2 ka event from Greenland ice cores”. In: *Quaternary Science Reviews* 26.1-2, pp. 70–81. DOI: `10.1016/j.quascirev.2006.07.017`.

Thomas, R. E., Negrini, M., Prior, D. J., Mulvaney, R., Still, H., Bowman, M. H., Craw, L., Fan, S., Hubbard, B., Hulbe, C., Kim, D., and Lutz, F. (2021). “Microstructure and crystallographic preferred orientations of an azimuthally oriented ice core from a lateral shear margin: Priestley Glacier, Antarctica”. In: *Frontiers in Earth Science* 9. DOI: `10.3389/feart.2021.702213`.

Thorsteinsson, T. (1996). “Textures and fabrics in the GRIP ice core, in relation to climate history and ice deformation”. In: *Berichte zur Polarforschung (Reports on Polar Research)* 205.

Thorsteinsson, T., Kipfstuhl, J., and Miller, H. (1997). “Textures and fabrics in the GRIP ice core”. In: *Journal of Geophysical Research: Oceans* 102.C12, pp. 26583–26599. DOI: `10.1029/97JC00161`.

Turchetti, S., Dean, K., Naylor, S., and Siegert, M. (2008). “Accidents and opportunities: a history of the radio echo-sounding of Antarctica, 1958–79”. In: *The British Journal for the History of Science* 41.3, pp. 417–444. DOI: `10.1017/S0007087408000903`.

Vettoretti, G., Ditlevsen, P., Jochum, M., and Rasmussen, S. O. (2022). “Atmospheric CO2 control of spontaneous millennial-scale ice age climate oscillations”. In: *Nature Geoscience*, pp. 1–7. DOI: `10.1038/s41561-022-00920-7`.

Vinther, B. M., Clausen, H. B., Johnsen, S. J., Rasmussen, S. O., Andersen, K. K., Buchardt, S. L., Dahl-Jensen, D., Seierstad, I. K., Siggaard-Andersen, M.-L., Steffensen, J. P., Svensson, A., Olsen, J., and Heinemeier, J. (2006). “A synchronized dating of three Greenland ice cores throughout the Holocene”. In: *Journal of Geophysical Research: Atmospheres* 111.D13. DOI: `10.1029/2005JD006921`.

Waddington, E. D., Bolzan, J. F., and Alley, R. B. (2001). “Potential for stratigraphie folding near ice-sheet centers”. In: *Journal of Glaciology* 47.159, pp. 639–648. DOI: `10/cvh5pq`.

Waite, A. H. and Schmidt, S. J. (1962). “Gross Errors in Height Indication from Pulsed Radar Altimeters Operating over Thick Ice or Snow”. In: *Proceedings of the IRE* 50.6, pp. 1515–1520. DOI: `10.1109/JRPROC.1962.288195`.

Walford, M., Holdorf, P., and Oakberg, R. (1977). “Phase-sensitive radio-echo sounding at the Devon Island ice cap, Canada”. In: *Journal of Glaciology* 18.79, pp. 217–229. DOI: `10.3189/S0022143000021316`.

Westhoff, J., Sinnl, G., Svensson, A., Freitag, J., Kjær, H. A., Vallelonga, P., Vinther, B., Kipfstuhl, S., Dahl-Jensen, D., and Weikusat, I. (2022). “Melt in the Greenland EastGRIP ice core reveals Holocene warm events”. In: *Climate of the Past* 18.5, pp. 1011–1034. DOI: `10.5194/cp-18-1011-2022`.

Westhoff, J., Stoll, N., Franke, S., Weikusat, I., Bons, P., Kerch, J., Jansen, D., Kipfstuhl, S., and Dahl-Jensen, D. (2021). “A stratigraphy-based method for reconstructing ice core orientation”. In: *Annals of Glaciology* 62.85-86, pp. 191–202. DOI: `10.1017/aog.2020.76`.

White, J. W. and Steig, E. J. (1998). “Timing is everything in a game of two hemispheres”. In: *Nature* 394.6695, pp. 717–718. DOI: `10.1038/29386`.

Whitlow, S., Mayewski, P., and Dibb, J. (1992). “A comparison of major chemical species seasonal concentration and accumulation at the South Pole and summit, Greenland”. In: *Atmospheric Environment. Part A. General Topics* 26.11, pp. 2045–2054. DOI: `10.1016/0960-1686(92)90089-4`.

Wilhelms, F., Kipfstuhl, J., Miller, H., Heinloth, K., and Firestone, J. (1998). “Precise dielectric profiling of ice cores: a new device with improved guarding and its theory”. In: *Journal of Glaciology* 44.146, pp. 171–174. DOI: `10.3189/S002214300000246X`.

Wilson, C. J., Russell-Head, D. S., and Sim, H. M. (2003). “The application of an automated fabric analyzer system to the textural evolution of folded ice layers in shear zones”. In: *Annals of Glaciology* 37, pp. 7–17. DOI: `10.3189/172756403781815401`.

Winstrup, M., Svensson, A. M., Rasmussen, S. O., Winther, O., Steig, E. J., and Axelrod, A. E. (2012). "An automated approach for annual layer counting in ice cores". In: *Climate of the Past* 8.6, pp. 1881–1895. DOI: `10.5194/cp-8-1881-2012`.

Wolff, E. W., Moore, J. C., Clausen, H. B., Hammer, C. U., Kipfstuhl, J., and Fuhrer, K. (1995). "Long-term changes in the acid and salt concentrations of the Greenland Ice Core Project ice core from electrical stratigraphy". In: *Journal of Geophysical Research: Atmospheres* 100.D8, pp. 16249–16263. DOI: `10.1029/95JD01174`.

Yan, J.-B., Li, L., Nunn, J. A., Dahl-Jensen, D., O'Neill, C., Taylor, R. A., Simpson, C. D., Wattal, S., Steinhage, D., Gogineni, P., Miller, H., and Eisen, O. (2020). "Multiangle, Frequency, and Polarization Radar Measurement of Ice Sheets". In: *IEEE Journal of Selected Topics in Applied Earth Observations and Remote Sensing* 13, pp. 2070–2080. DOI: `10.1109/JSTARS.2020.2991682`.

Chapter 4

Upstream flow effects revealed in the EastGRIP ice core using Monte Carlo inversion of a two-dimensional ice-flow model

Tamara Annina Gerber[1], Christine Schøtt Hvidberg[1], Sune Olander Rasmussen[1], Steven Franke[2], Giulia Sinnl[1], Aslak Grinsted[1], Daniela Jansen[2], and Dorthe Dahl-Jensen[1,3]

[1]*Section for the Physics of Ice, Climate and Earth, Niels Bohr Institute, University of Copenhagen, Copenhagen, Denmark*
[2]*Alfred Wegener Institute, Helmholtz Centre for Polar and Marine Research, Bremerhaven, Germany*
[3]*Centre for Earth Observation Science, University of Manitoba, Winnipeg, Canada*

The Northeast Greenland Ice Stream (NEGIS) is the largest active ice stream on the Greenland Ice Sheet (GrIS) and a crucial contributor to the ice-sheet mass balance. To investigate the ice-stream dynamics and to gain information about the past climate, a deep ice core is drilled in the upstream part of the NEGIS, termed the East Greenland Ice-core Project (EastGRIP). Upstream flow can introduce climatic bias into ice cores through the advection of ice deposited under different conditions further upstream. This is particularly true for EastGRIP due to its location inside an ice stream on the eastern flank of the GrIS. Understanding and ultimately correcting for such effects requires information on the atmospheric conditions at the time and location of snow deposition. We use a two-dimensional Dansgaard–Johnsen model to simulate ice flow along three approximated flow lines between the summit of the ice sheet (GRIP) and EastGRIP. Isochrones are traced in radio-echo-sounding images along these flow lines and dated with the GRIP and EastGRIP ice-core chronologies. The observed depth–age relationship constrains the Monte Carlo method which is used to determine unknown model parameters. We calculate backward-in-time particle trajectories to determine the source location of ice found in the EastGRIP ice core and present estimates of surface elevation and past accumulation rates at the deposition site. Our results indicate that increased snow accumulation with increasing upstream distance is predominantly responsible for the constant annual layer thicknesses observed in the upper part of the ice column at EastGRIP, and the inverted model parameters suggest that basal melting and sliding are important factors determining ice flow in the NEGIS. The results of this study form a basis for applying upstream corrections to a variety of ice-core measurements, and the inverted model parameters are useful constraints for more sophisticated modeling approaches in the future.

4.1 Introduction

The East Greenland Ice-Core Project (EastGRIP) is the first attempt to retrieve a deep ice core inside an active ice stream. The drill site is located in the upstream part of the Northeast Greenland Ice Stream (NEGIS, Fahnestock et al., 1993), which is a substantial contributor to the Greenland Ice Sheet (GrIS) mass balance (Khan et al., 2014) and accounts for around 12 % of its total ice discharge (Rignot and Mouginot, 2012). Large-scale ice-sheet models are essential tools to anticipate the future development of the NEGIS and its potential impact on the stability of the GrIS (Joughin et al., 2001; Khan et al., 2014; Vallelonga et al., 2014). However, results obtained from such models often show a significant deviation from observed surface velocities in the NEGIS and its catchment area (Aschwanden et al., 2016; Mottram et al., 2019). In particular, the high ice-flow velocities in the upstream area of the NEGIS and the clearly defined shear margins are difficult to reproduce with ice-flow models (Beyer et al., 2018). A recent study by Smith-Johnsen et al. (2020b) showed, that the high surface velocities in the onset region of the ice stream could be reproduced with their model, using an exceptionally high and geologically unfeasible geothermal heat flux (Bons et al., 2021). This indicates that additional, yet unknown processes must facilitate ice flow in the NEGIS and that the driving mechanisms governing ice flow are still not understood well enough. The EastGRIP ice core sheds some light on the key processes by revealing unique information about ice dynamics, stress regimes, temperatures and basal properties, all of which are crucial components in ice-flow models.

Chemical and physical properties measured in ice cores reflect the atmospheric conditions at the time and location of snow deposition (e.g. Alley et al., 1993; Petit et al., 1999; Andersen et al., 2004; Marcott et al., 2014). Most of the deep drilling projects in Greenland and Antarctica are located in slow-moving areas at ice domes or near ice divides (e.g. GRIP (Dansgaard et al., 1982), Dome Fuji (Ageta et al., 1998), Dome C (Parrenin et al., 2007)), so the ice core can be expected to represent climate records from this fixed location. For ice cores drilled on the flank of an ice sheet (e.g. GISP2 (Meese et al., 1997), Vostok (Lorius et al., 1985; Petit et al., 1999)) or in areas with higher flow velocities (e.g. Camp Century (Dansgaard et al., 1969), Byrd (Gow et al., 1968), NorthGRIP (Andersen et al., 2004), EDML (Barbante et al., 2006), WAIS Divide (Fudge et al., 2013), NEEM (NEEM Community members et al., 2013)), the ice found at depth was originally deposited further upstream and advected with the horizontal flow.

The spatial variation in accumulation rate, surface temperature and atmospheric pressure can introduce climatic imprints in the ice-core record which stem from the advection of ice deposited under different conditions further upstream. The ice core signal is thus a combination of temporal and spatial variations in climatic components (Fudge et al., 2020). The magnitude of these so-called upstream effects depends on the ice-flow velocity, spatial variability of the precipitation and the sensitivity to atmospheric variations of the quantity under consideration. While well-mixed atmospheric gases, such as carbon dioxide or methane, and dry-deposited impurities are barely affected (Fudge et al., 2020), properties extracted from the ice phase can show significant bias.

Affected measurements include aerosols and cosmogenic isotopes, such as ^{10}Be (Yiou et al., 1997; Finkel and Nishiizumi, 1997; Raisbeck et al., 2007; Delaygue and Bard, 2011), the isotopic composition of water (Dansgaard, 1964; Jouzel et al., 1997; Aizen et al., 2006), the total air content (Raynaud et al., 1997; Eicher et al., 2016) and ice temperatures (Salamatin et al., 1998). Processes such as vertical thinning of the ice column and firn densification are also influenced by upstream effects and have consequences on the annual layer thicknesses (Dahl-Jensen et al., 1993; Rasmussen et al., 2006; Svensson et al., 2008) and the age difference between ice and the enclosed air (Herron and Langway, 1980; Alley et al., 1982). Upstream effects in the EastGRIP ice core are expected to be particularly strong due to the fast ice flow in the upstream area (55 ma^{-1} at EastGRIP, Hvidberg et al., 2020), the strong gradient in the accumulation rate across

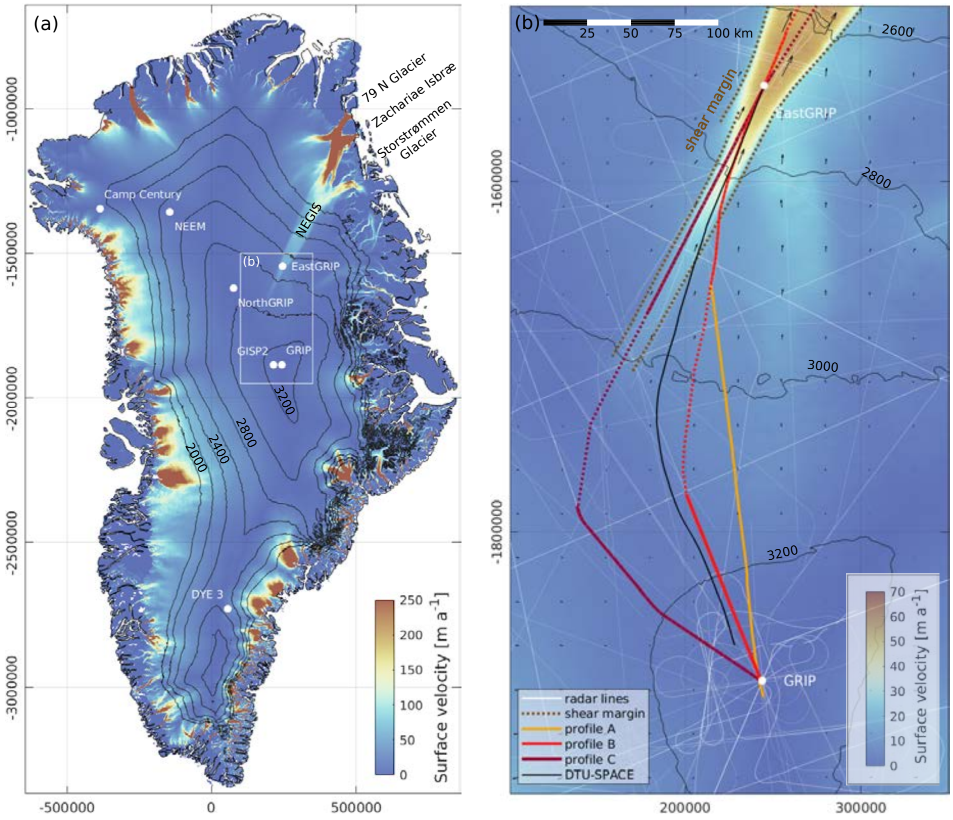

FIGURE 4.1: **a)** Overview of past and ongoing deep ice-core drilling projects on the GrIS (surface elevation and Greenland contour lines by Simonsen and Sørensen, 2017; Greene et al., 2017) and the outline of the study area. The NEGIS appears as a distinct feature in the surface velocities (Joughin et al., 2018). It extends from the central ice divide to the northeastern coast, where it splits up into the three marine-terminating glaciers 79N Glacier, Zachariae Isbræ and Storstrømmen Glacier. **b)** The present-day EastGRIP flow line is derived from the DTU_SPACE surface velocity product (Andersen et al., 2020). Due to the limited availability of radar data along the flow line, we construct three approximate flow lines through a combination of various radar products (profile A–C) between GRIP and EastGRIP. Flow line B and C lack data in the center of the profiles, marked as a dashed line. The downstream parts of line A and B comprise the same radar profile, which crosses the southern shear margin around 82 km upstream of EastGRIP.

Greenland's main ice ridge (Burgess et al., 2010), and the increasing elevation towards the central ice divide (Simonsen and Sørensen, 2017). The correction of these effects in the EastGRIP ice core is necessary to interpret the ice-core measurements within the climatic context and requires information on the conditions at the time and location of snow deposition.

Post-depositional deformation of isochrones observed in radio-echo-sounding (RES) images along flow lines provides information on ice-flow dynamics and can be used to reconstruct past and present flow characteristics. In this study, we use a vertically two-dimensional Dansgaard–Johnsen model to simulate the propagation and deformation of isochrones along three approximated flow lines between the ice-sheet summit (GRIP) and EastGRIP. A Monte-Carlo method is used to determine the unknown model parameters by minimizing the misfit between modeled and observed data. The latter includes the depth of isochrones observed in RES images along the flow lines and a parameter α_{sur} representing the sum of the horizontal strain rates deduced from satellite based surface velocities. From the modeled velocity field, we calculate particle trajectories backwards in time to infer the source location of ice found in the EastGRIP ice core and estimate the accumulation rate at the time of snow deposition. The source characteristics presented here form a basis to correct for upstream effects in various chemical and physical quantities of the EastGRIP ice core. These corrections are important to remove any climatic bias in ice-core measurements which are currently analyzed and will become available in the future. The inverted model parameters give insight into basal properties and ice-flow dynamics along the flow lines and can be used to constrain more sophisticated numerical models of the NEGIS.

4.2 Data and methods

Snow layers deposited at the surface of ice sheets are buried with time and are deformed as a consequence of ice flow. While these isochrones can be observed in RES images today, the ice-flow characteristics which shaped them are generally unknown. This is a typical geophysical inverse problem and can be formulated as $\mathbf{d} = g(\mathbf{m})$, where the function $g(\mathbf{m})$ represents the ice-flow model linking the model parameters ($\mathbf{m}$) with the observed data ($\mathbf{d}$). A variety of inverse methods exist to find the model parameters which reproduce the observed data within their uncertainties. Here, we use a Markov Chain Monte-Carlo method to determine the unknown parameters of a two-dimensional ice-flow model by minimizing the misfit between modeled and observed isochrones and strain rates. This allows us to reconstruct the ice-flow characteristics in the past and to determine the flow trajectories of the EastGRIP ice.

In the coming sections we describe the data and methods underlying our results according to the work flow illustrated in Fig. 4.2. In Sect. 4.2.1 to 4.2.4 we explain how the isochrone depth-age relationship constraining the Monte-Carlo method was obtained. This involves the selection of RES images approximating the EastGRIP flow line (Sect. 4.2.1), extending the existing chronology of the EastGRIP ice core to the current drill depth (Sect. 4.2.2), and the tracing and dating of isochrones in the RES data (Sect. 4.2.3). In Sect. 4.2.4 the ice-flow model is described in detail and in Sect. 4.2.5 we elaborate on the Monte-Carlo method used for parameter sampling. The section numbers are displayed in the corresponding steps in Fig. 4.2.

4.2.1 EastGRIP flow lines

Determining the exact flow line through the EastGRIP ice-core site is important to understand the flow history of the survey area and enables us to reconstruct the location where the ice from the ice core was deposited at the ice-sheet surface. For this, we use high-resolution satellite-based surface velocity products (e.g. Joughin et al., 2018; Gardner et al., 2020; Andersen et al., 2020, see supplementary material Fig. S4.1) to calculate the upstream flow path. Minor uncertainties and bias in these data products affect along-flow tracing and lead to deviations between flow lines derived from different velocity maps. These deviations become more pronounced with increasing distance from the starting point, as the uncertainties propagate along the line and in general become larger in slow-moving areas of the ice sheet (Hvidberg et al., 2020). Due to the small bias, we consider the DTU_SPACE (Andersen et al., 2020) line the most likely current flow line (Fig. 4.1b). Yet, there is no evidence that the present-day velocity field was the same in the past. A slight shift in the NEGIS shear margins or the central ice divide, for instance, would have a large effect on the velocity field and, hence, the determination of the flow line of the EastGRIP ice remains ambiguous.

RES data reveal the internal structure of glaciers and ice sheets and provide valuable information on the ice-flow characteristics, particularly when recorded parallel to the ice flow. The electromagnetic waves used in RES are sensitive to contrasts in dielectric properties of the medium they propagate. In ice sheets, these contrasts arise through density variations in the uppermost part of the ice column (Robin et al., 1969), changes in the crystal orientation fabric (Harrison, 1973), and impurity layers such as volcanic deposits (Paren and Robin, 1975). The latter is the most common reflector type below the firn (Millar, 1982; Eisen et al., 2006), and

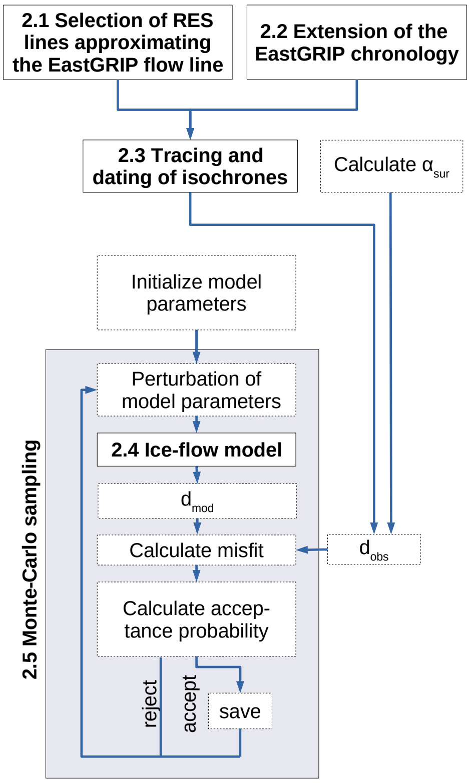

Figure 4.2: Workflow of the applied steps leading to the results described in Sect. 4.3. The main steps are described in Sect. 4.2.1 to 4.2.5 (labeled as 2.1 to 2.5 in Figure) and marked with the corresponding numbers in the figure: The observed data ($\mathbf{d}_{obs}$) constraining the Monte-Carlo method consists of the α_{sur} calculated from the ice surface velocities and the isochrone depths along the flow lines. The latter is obtained by approximating the EastGRIP flow line with selected RES images (Sect. 4.2.1), extending the EastGRIP chronology to the current drill depth (Sect. 4.2.2) and subsequent tracing and dating of isochrones (Sect. 4.2.3). The iterative Monte-Carlo sampling process is illustrated in the gray box (Sect. 4.2.5) and includes data simulation by a Dansgaard–Johnsen ice-flow model described in Sect. 4.2.4.

because it is related to layers deposited over a relatively short period of time, most internal reflection horizons (IRHs) detected by RES can be considered isochrones.

The availability of RES data in the study area is limited, and unfortunately, the flight lines generally do not follow the surface velocity field. We have thus composed three approximated flow lines connecting the EastGRIP (75.63° N, 35.99° W, 2720 m) and the GRIP (72.58° N, 37.63° W, 3230 m) drill sites from the available RES data sets (Fig. 4.1b). The radar data used in this study (Table 4.1) were measured by the Alfred Wegener Institute, Helmholtz Center for Polar and Marine Research (AWI, Franke et al., 2022a) and the Center for Remote Sensing of Ice Sheets (CReSIS, 2020b). The AWI data were recorded by an 8-antenna-element ultra-wideband radar system (MCoRDS5) mounted on the Polar 6 Basler BT-67 aircraft, operating at a frequency range of 180–210 MHz (Franke et al., 2020; Franke et al., 2022a). The CReSIS radar data were measured by a ICORDS 2 (1999) and a MCoRDS 2 (2012) radar system, mounted on a P3 aircraft, at a frequency range of 141.5–158.5 MHz and 180–210 MHz, respectively. Details of the three radar systems are provided in Table 4.2.

The downstream parts of profile A and B consist of the same flight line, which passes through the EastGRIP drill site and intersects the southern shear margin around 82 km upstream of EastGRIP. Outside the NEGIS, the two lines split up and connect to two different RES profiles. Line B remains relatively close to the flow direction of the DTU_SPACE line but has a wide data gap in the center of the profile. In line A, this problem is circumvented by using a radar profile connecting directly to GRIP, which deviates from the observed surface flow field by more than 15 degrees at some locations. Profile C follows the NEGIS trunk all the way to the central ice divide and connects to GRIP over the ice ridge without crossing the shear margin. Similar to flow line B, flow line C contains a substantial data gap between the onset region of the NEGIS and the central ice divide.

To avoid uncertainties related to the proximity of the model boundaries, the flow lines were extended more than 50 km beyond EastGRIP and have a total length of 422 (line A), 421 (line B) and 480 km (line C). To account for any differences in surface elevation or topography between RES data from different years, the ice surface reflections of the radar profiles were aligned to the surface elevation from the Arctic DEM (digital elevation model, Porter et al., 2018). The bed topography in the data gaps of the profiles was derived from the BedMachine v3 data set (Morlighem et al., 2017).

TABLE 4.1: RES profiles used to approximate the EastGRIP flow lines A–C. The data sets were measured between 1999 and 2018 by CReSIS (CReSIS, 2020b) and AWI (Franke et al., 2022a).

Flow line	**Data files**	**Institution**	**Year**	**Radar system**
A	Data_20180512_01_001 – 004	AWI	2018	MCoRDS 5
A	Data_19990512_01_009 – 010	CReSIS	1999	ICoRDS 2
B	Data_20180512_01_001 – 004	AWI	2018	MCoRDS 5
B	Data_19990523_01_016 – 017	CReSIS	1999	ICoRDS 2
C	Data_20180517_01_002 – 004	AWI	2018	MCoRDS 5
C	Data_20120330_03_008 – 011	CReSIS	2012	MCoRDS 2

TABLE 4.2: Operating parameters of the radar systems used for data acquisition. Further details can be found in Gogineni et al. (2001), Byers et al. (2012) and Franke et al. (2022a).

Parameter	**ICORDS 2**	**MCoRDS 2**	**MCoRDS 5**
Bandwidth	141.5–158.5 MHz	180–210 MHz	180–210 MHz
Tx power	200 W	1050 W	6000 W
Waveform	Analogue chirp (SAW)	8 channel chirp (2–3 waveforms)	8 channel chirp (3 waveforms)
Sampling frequency	18.75 MHz	111 MHz	1600 MHz
Transmit channels	1	8	8
Receiving channels	1	15	8
Range resolution	7.6 m	4.3 m	4.3 m

4.2.2 Extending the chronology of EastGRIP from GS-2 to GI-14

The validation of our modeling results and the correct dating of isochrones requires a reliable depth-age scale. The Greenland Ice Core Chronology 2005 (GICC05, Vinther et al., 2006; Rasmussen et al., 2006; Andersen et al., 2006; Svensson et al., 2006) is based on annual layer counting in various Greenland ice cores. It has been transferred to GRIP and other deep drilling sites in Greenland by synchronizing the ice cores with each other using horizons of e.g. volcanic origin (Rasmussen et al., 2008; Seierstad et al., 2014). The upper 1,383.84 m of the EastGRIP ice core were drilled between 2015 and 2018, and synchronized with the NorthGRIP ice core in previous work (Mojtabavi et al., 2020b).

By 2019, the ice-core drilling progressed down to 2,122.45 m, allowing us to extend the existing time scale from 15 ka to 49.9 ka b2k (thousands of years before 2000 CE). As part of the present study, we identified common isochrones between EastGRIP, NorthGRIP and NEEM to transfer the GICC05 chronology to the part of the EastGRIP record which is not yet synchronized. This involved the same methods applied to NEEM by Rasmussen et al. (2013) and to the upper 1,383.84 m of EastGRIP by Mojtabavi et al. (2020b). The isochrones chosen for synchronization purposes are mainly volcanic eruptions, which are registered as brief spikes in the electrical conductivity measurements (ECM, Hammer, 1980). The search of common ECM spikes was performed manually with a strong focus on finding patterns of similarly spaced eruptions rather than single and isolated events. The Matlab program 'Matchmaker' was used to visualize long data stretches and to evaluate the quality of the match (Rasmussen et al., 2008). An iterative multi-observer protocol was applied to reduce problems with confirmation bias and to ensure the reproducibility of the match.

A total of 138 match points were identified between 1,383.84 m and 2,117.77 m, adding to the previously known 381 match points. The match points between EastGRIP and the other two cores are shown in Fig. 4.3, representing all the volcanic tie points. The GICC05 chronology was transferred to EastGRIP by linear interpolation of depths between the match points. The age of the 1,383.84 m match point was already established to be 14,966 years b2k, which is near the termination of Greenland Stadial 2 (GS-2), with a reported maximum counting error (MCE) of 196 years (Mojtabavi et al., 2020b). The age of the deepest match point was established to be 49,909 years b2k, just at the end of Greenland Interstadial 14 (GI-14), with an MCE of 2,066 years.

As in earlier similar work (e.g Rasmussen et al., 2013; Seierstad et al., 2014), very few match points were observed in the stadials, most clearly seen in Fig. 4.3 in the long stadial stages of GS-2 and GS-3. The sparse volcanic signals within stadial periods should not be attributed to a diminished global volcanic activity but rather to increased deposition of alkaline dust that neutralizes volcanic acid, caused by the prevailing colder and drier climatic conditions (Rasmussen et al., 2013). The largest distance between match points was observed across GS-2 and GS-3 and spans about 162 m of EastGRIP ice.

4.2.3 Tracing and dating of isochrones

The depth-age relationship from ice-core chronologies can be extended in the lateral plane by tracing and dating of isochrones in RES images. The depth of these isochrones along the EastGRIP flow lines is part of the observed data used to tune the ice-flow model parameters in the Monte-Carlo inversion. We traced 15 continuous IRHs and one non-continuous reflector along each of the three approximated flow lines with a semi-automatic Matlab program called ′′picking tool′. The algorithm is based on calculating the local slope in each pixel of the RES image, and layers are traced automatically between two user-defined points. Starting from each of these points the algorithm walks along the steepest slope towards the other point. Subsequently, the two lines are weighted by distance to their starting point and combined to one layer. The number of picks required for thorough tracing depends on the data quality and reflector strength.

The total depth uncertainty ($\tilde{z}_t$) was calculated as

$$\tilde{z}_t = \sqrt{\tilde{z}_p^2 + \tilde{z}_{rr}^2}, \tag{4.1}$$

where the depth uncertainty introduced during the picking process ($\tilde{z}_p$) is estimated to be 10 m. The uncertainty related to the radar range resolution ($\tilde{z}_{rr}$) of the corresponding RES image is defined as

$$\tilde{z}_{rr} = \frac{kc}{2B\sqrt{3.15}}, \tag{4.2}$$

where k is the window widening factor of 1.53, c is the speed of light, B is the radar bandwidth and 3.15 is the dielectric permittivity of ice.

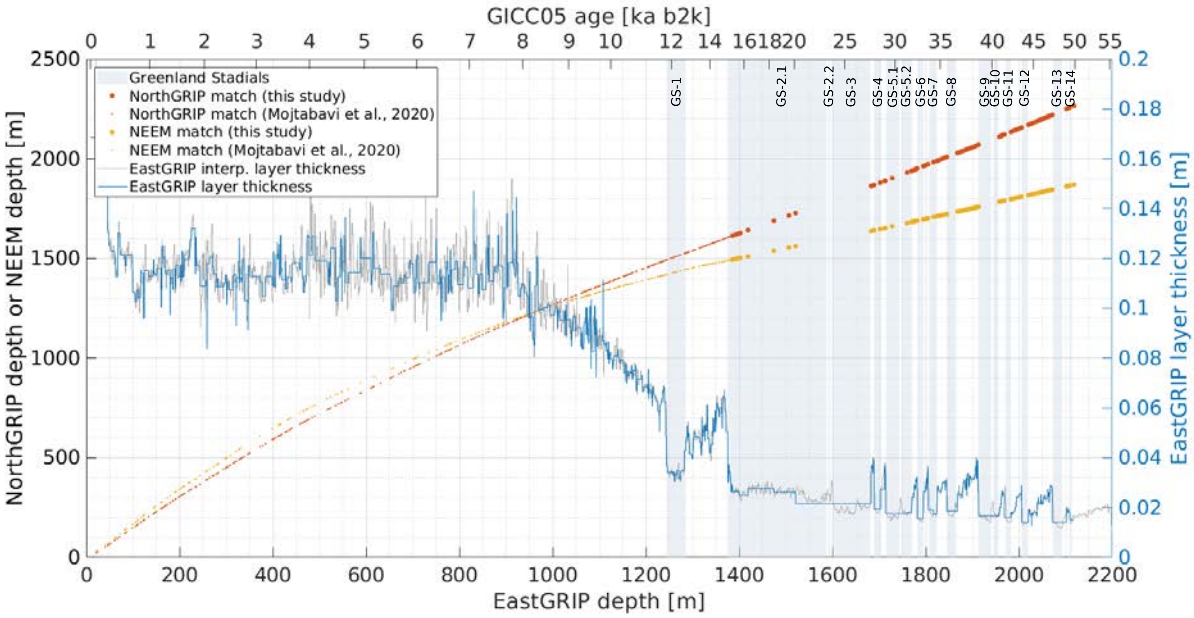

FIGURE 4.3: Synchronization between the EastGRIP, NorthGRIP and NEEM ice cores and comparison of match points obtained in this study with earlier results from Mojtabavi et al. (2020b). The annual layer thickness of EastGRIP was computed after transferring GICC05 ages by linear interpolation to the EastGRIP ice core. The blue curve shows the annual layer thickness obtained by the match points only. The gray line indicates a high-resolution estimate of annual layer thicknesses at EastGRIP, obtained from the linear interpolation between the EastGRIP–NorthGRIP match points and assigning the interpolated EastGRIP depths to the NorthGRIP ages.

The traced IRHs were dated at both drill sites by assigning the reflector depth at GRIP and EastGRIP to the corresponding time scale. In doing so, local irregularities were smoothed out by averaging the depth over ± 250 m around the trace closest to the ice-core location. Because the EastGRIP ice core has not reached the bed yet, we extrapolated the time scale at EastGRIP with two IRHs observed below the current borehole depth to obtain a tentative depth–age relationship between 2,117.77 m and the expected bed depth of 2,668 m.

The total age uncertainty ($\tilde{a}_t$) was estimated by following the approach described in MacGregor et al. (2015), where

$$\tilde{a}_t = \sqrt{\tilde{a}_c^2 + \tilde{a}_{rr}^2 + \tilde{a}_p^2} \tag{4.3}$$

takes into account the age uncertainties associated with the time scale ($\tilde{a}_c$, equivalent to 0.5 MCE), the radar range resolution ($\tilde{a}_{rr}$), and the layer picking process ($\tilde{a}_p$). The uncertainties related to the range resolution are estimated with

$$\tilde{a}_{rr} = \frac{1}{2} \sum \left| a_c \left(z \pm \tilde{z}_{rr} \right) - a_c(z) \right| , \tag{4.4}$$

where a_c is the ice-core age from the GICC05 time scale. Similar to Eq. (4.4), $\tilde{a}_p$ is estimated with

$$\tilde{a}_p = \frac{1}{2} \sum |a_c(z \pm \tilde{z}_p) - a_c(z)|. \tag{4.5}$$

The chosen isochrones show distinct patterns which could be identified in all RES images and allowed us to trace isochrones across disruptions and data gaps. Comparison of the isochrone depths at the ice-core locations obtained from different RES images permits assessment of the quality of the tracing procedure. The high resolution of the radar images recorded in 2018 facilitates isochrone tracing, and the EastGRIP depths obtained from the two different

AWI radar profiles agree to within 1.5 m. At GRIP, the discrepancy between isochrone depths obtained from three different radar profiles can be up to 30 m, which is slightly above the combined depth uncertainty related to the picking process and the resolution of the RES images. Lower range resolution and signal-to-noise ratio in older RES data introduce bias in isochrone identification, and although distinct isochrones were chosen, a miscorrelation between IRHs recorded by different radar systems can not be entirely excluded. Moreover, the CReSIS profiles do not precisely intersect at GRIP and deviate from each other. The radar traces closest to GRIP are thus found at slightly different locations for the three RES images, which explains the higher discrepancy of radar layer depths.

The isochrone dating was conducted for each profile individually, and the obtained depths, ages and uncertainties were averaged over the three lines (Table 4.3). The deepest non-continuous layer which could be identified at EastGRIP is found at a depth of 2,360 ± 11 m and is estimated to be 72,400 ± 1,306 years old. The layer depths of the continuously traced IRHs range from 421 ± 11 m to 2,152 ± 11 m at the EastGRIP location, corresponding to ages of 3,498 ± 94 to 51,920 ± 1,240 years b2k. Reflectors 1–9 were deposited during the Holocene. The remaining reflectors are found in ice from the Last Glacial Period from which reflector 10 and 11 can be attributed to the onset of the Younger Dryas and the Bølling–Allerød. The relation between the GRIP and EastGRIP depths of the traced IRHs fits well with the GICC05 time scale (Mojtabavi et al., 2020b; Rasmussen et al., 2014), and the ages obtained from the two drill sites agree within the uncertainties. We note that the layer dating at EastGRIP consistently leads to younger ages than the dating at GRIP, which is a likely consequence of inaccuracies related to the transformation between ice-core and radar depths.

Due to computational reasons, we did not use all 16 layers for the Monte-Carlo inversion but picked ten isochrones with approximately equal vertical spacing, and used the EastGRIP ages for our simulation of layer propagation. The layers used for the Monte-Carlo simulation are indicated in bold in Table 4.3 and plotted with a consistent color-code in Fig. 4.4, Fig. 4.5 and Fig. 4.7, representing the corresponding ages.

4.2.4 Ice-flow model

A full simulation of ice flow in the catchment area of the NEGIS is a highly under-determined problem (Keisling et al., 2014), lacking geophysical, climatic and ice-core data, some of which will become available in the future. Simpler models do not solve the problem in detail and are thus computationally much cheaper. Hence, limited but still useful information can be obtained from a simplified treatment of ice flow (e.g. Dansgaard et al., 1969; Dahl-Jensen et al., 2003; Waddington et al., 2007; Christianson et al., 2013; Keisling et al., 2014).

Here, we use a two-dimensional Dansgaard–Johnsen model (Dansgaard et al., 1969) to simulate the propagation and deformation of internal layers along approximated flow lines between the ice-sheet summit (GRIP) and EastGRIP. The simplicity of the model makes it well suited for the Monte-Carlo method due to its few model parameters, the allowance for large time steps, and because it has an analytical solution (Grinsted and Dahl-Jensen, 2002). The model assumes ice incompressibility and a constant vertical strain rate down to the so-called kink height (h) below which the strain rate decreases linearly. Basal sliding and melting are included in the model, and the ice-sheet thickness (H) is assumed to be constant in time.

We consider a coordinate system where the x-axis points along the approximated flow line, the y-axis is horizontal and perpendicular to the flow line, and the z-axis indicates the height above the bed. The horizontal velocities parallel ($u_{\|}$) and perpendicular ($u_{\perp}$) to the profiles are described by Grinsted and Dahl-Jensen (2002) as:

$$u_{\|}(z) = \begin{cases} u_{\|,sur}(x,y)\left[(1-f_{bed})\frac{z}{h}+f_{bed}\right], & z \in [0,h] \\ u_{\|,sur}(x,y), & z \in [h,H], \end{cases} \tag{4.6}$$

TABLE 4.3: Characteristics of the traced isochrones connecting the GRIP and EastGRIP ice-core sites. Displayed depths and ages are the average over the three flow lines. Depth uncertainties include the uncertainty related to the picking process and to the radar range resolution. Age uncertainties are related to the GICC05 time-scale uncertainties and isochrone depths. Figure 4.7d illustrates the depth and climatic context of these layers in the EastGRIP ice core, identified with the corresponding layer numbers. The bold layers and the EastGRIP ages were used for the Monte-Carlo inversion and are illustrated with a consistent color-code in Fig. 4.4, Fig. 4.5 and Fig. 4.7.

Layer	GRIP depth [m]	EastGRIP depth [m]	GRIP age [yrs b2k]	EastGRIP age [yrs b2k]
1	733 ± 13	421 ± 11	3,618 ± 73	3,498 ± 94
2	**795 ± 13**	**471 ± 11**	**4,004 ± 74**	**3,945 ± 95**
3	925 ± 13	573 ± 11	4,885 ± 85	4,805 ± 93
4	**1,217 ± 13**	**838 ± 11**	**7,178 ± 106**	**7,139 ± 95**
5	1,262 ± 13	882 ± **11**	7,575 ± 107	7,531 ± 95
6	**1,347 ± 13**	**968 ± 11**	**8,364 ± 122**	**8,321 ± 110**
7	1,374 ± 13	996 ± 11	8,637 ± 124	8,600 ± 113
8	1,533 ± 13	1,153 ± **11**	10,407 ± 162	10,365 ± 149
9	**1,592 ± 13**	**1,208 ± 11**	**11,209 ± 181**	**11,140 ± 168**
10	1,663 ± 13	1,282 ± 11	12,891 ± 327	12,822 ± 290
11	**1,749 ± 13**	**1,355 ± 11**	**14,612 ± 281**	**14,350 ± 206**
12	**2,039 ± 13**	**1,704 ± 11**	**28,633 ± 840**	**28,522 ± 647**
13	**2,193 ± 13**	**1,903 ± 11**	**38,015 ± 994**	**37,914 ± 793**
14	**2,298 ± 13**	**2,035 ± 11**	**45,463 ± 1,189**	**45,174 ± 1,086**
15	**2,395 ± 13**	**2,152 ± 11**	**52,602 ± 1,360**	**51,920 ± 1,240**
16	-	**2,360 ± 11**	-	**72,400 ± 1,306**

$$u_\perp(z) = \begin{cases} u_{\perp,sur}(x,y)\left[(1-f_{bed})\frac{z}{h} + f_{bed}\right], & z \in [0,h] \\ u_{\perp,sur}(x,y), & z \in [h,H] \end{cases} \tag{4.7}$$

where $u_{\parallel,sur}$ and $u_{\perp,sur}$ are the surface velocities parallel and perpendicular to the profile, and the basal sliding factor f_{bed}, is the ratio between the ice velocity at the bed and at the surface.

Ice flow in the vicinity of an ice stream is affected by lateral compression and longitudinal extension, in particular across the shear margins of the NEGIS. We thus introduce $\alpha = \frac{\partial u_\parallel}{\partial x} + \frac{\partial u_\perp}{\partial y}$ as the sum of the horizontal strain rates. Due to ice incompressibility we can write $\alpha + \frac{\partial \omega}{\partial z} = 0$, where ω symbolizes the vertical velocity. The x and y dependency in Eq. (4.6–4.7) only relates to the surface velocity, such that α_{sur} represents the horizontal dependency in the equations and can be calculated from the ice surface velocities.

The vertical velocities (ω) are obtained through integration of the incompressibility relation $\omega(z) = -\int \alpha dz$ (Dansgaard et al., 1969):

$$\omega(z) = \begin{cases} \omega_{bed} - \alpha_{sur}(f_{bed}z + \frac{z^2}{2h}(1-f_{bed})) & z \in [0,h] \\ \omega_{sur} + \alpha_{sur}(H-z) & z \in [h,H]. \end{cases} \tag{4.8}$$

The boundary conditions for the vertical velocity at the bed (ω_{bed}) and surface (ω_{sur}) are

$$\omega_{bed} = -\dot{b} + f_{bed}u_{sur}\frac{\partial E_{bed}}{\partial x} \tag{4.9}$$

$$\omega_{sur} = -\dot{a} + u_{sur}\frac{\partial E_{sur}}{\partial x}, \tag{4.10}$$

where $\dot{b}$ is the positive basal melt rate, $\dot{a}$ is the positive accumulation rate, and E_{bed} and E_{sur} are the bed and surface elevations respectively. From Eq. (4.8) we derive the following expression for the modeled α_{sur}:

$$\alpha_{sur} = \frac{\omega_{bed} - \omega_{sur}}{H - \frac{h}{2}(1 - f_{bed})}. \tag{4.11}$$

Following Grinsted and Dahl-Jensen (2002) and Buchardt and Dahl-Jensen (2007), we adjust the accumulation rates and surface velocities to the climate conditions of the corresponding time with a scaling factor $\xi(t)$:

$$\xi(t) = e^{\kappa_2(\delta^{18}O - \delta^{18}O_w) - \frac{1}{2}\kappa_1(\delta^{18}O^2 - \delta^{18}O_w^2)}, \tag{4.12}$$

$$\text{with} \quad \kappa_1 = \frac{c_w - c_c}{\delta^{18}O_w - \delta^{18}O_c}, \quad \text{and} \quad \kappa_2 = c_w - \delta^{18}O_w \kappa_1.$$

We use the oxygen isotope $\delta^{18}O$ record from NorthGRIP (Andersen et al., 2004) due to its high temporal resolution, and $\delta^{18}O_w = -35.2$ ‰ and $\delta^{18}O_c = -42$ ‰ are typical isotope values for warm interstadial and cold stadial periods, respectively. The parameters c_w and c_c determine the sensitivity of the accumulation rate with varying $\delta^{18}O$ in warm (c_w) and cold (c_c) periods and are defined as (Grinsted and Dahl-Jensen, 2002; Buchardt and Dahl-Jensen, 2007):

$$c_w = \frac{1}{\dot{a}} \frac{\partial \dot{a}}{\partial \delta^{18}O}\bigg|\delta^{18}O = \delta^{18}O_w, \quad c_c = \frac{1}{\dot{a}} \frac{\partial \dot{a}}{\partial \delta^{18}O}\bigg|\delta^{18}O = \delta^{18}O_c. \tag{4.13}$$

To simulate the propagation of ice particles deposited at the surface of the GrIS, Eq. (4.6) and Eq. (4.8) are solved at a time interval of 10 years.

4.2.5 Monte-Carlo sampling

The ice-flow parameters $\dot{a}$, h, f_{bed}, and $\dot{b}$ are defined for intervals of ∼10 km along the flow lines, and form together with the two climate scaling factors, c_c and c_w, the model vector $\mathbf{m}$. This results in a total of 170 (flow line A and B) and 194 (flow line C) model parameters. Each combination of them represents a possible solution to the inverse problem $\mathbf{d} = g(\mathbf{m})$, where $g(\mathbf{m})$ represents the ice-flow model described in the previous section. The data vector $\mathbf{d}$ contains the isochrone depths and α_{sur} determined from the MEaSUREs Multi-year v1 surface velocities (Joughin et al., 2018) at a resolution of one kilometer.

Like in most geophysical inverse problems, many different combinations of model parameters can explain the observed data equally well within the range of their uncertainties and therefore, a non-unique solution does not exist. Probabilistic inverse methods consider many different models and describe them in terms of their plausibility, rather than finding one possible solution. This makes these methods particularly well suited for nonlinear problems, where the probability density in the model space typically shows multiple maxima (Mosegaard and Tarantola, 1995).

Monte-Carlo methods are based on a random number generator which allows the sampling according to the target probability distribution in an efficient way. The gray box in Fig. 4.2 illustrates the iterative sampling process of the Metropolis algorithm (Metropolis et al., 1953) used here: Starting from an initial model ($\mathbf{m}_0$), a random walker explores the model space and proposes new models ($\mathbf{m}_{new}$) which are accepted with a certain probability (P_{accept}). This way of importance sampling avoids unnecessary evaluation of model parameters in low-probability areas (Mosegaard, 1998).

To estimate the initial accumulation rate $\dot{a}_0$, we integrate Eq. (4.8) (see Appendix 4.5) and obtain the following depth–age relationship

$$(H - z) = \frac{\dot{a}}{\alpha_{sur}}(1 - e^{-\mathbf{ff}_{sur}t}), \tag{4.14}$$

where t and z represent the isochrone age and height above the bed, respectively. The accumulation rate $\dot{a}$ is determined with a curve-fitting function, using at least 5 isochrones younger than 10 ka at each point along the flow line. The initial kink height (h_0), basal sliding ($f_{bed,0}$) and basal melt rate ($\dot{b}_0$) are scaled with the normalized surface velocity ($\hat{\mathbf{u}}_{sur}$) as follows:

$$h_0 = H\left(\frac{1}{2} - e_1\hat{\mathbf{u}}_{sur}\right) \tag{4.15}$$

$$f_{bed,0} = e_2\hat{\mathbf{u}}_{sur} \tag{4.16}$$

$$\dot{b}_0 = e_3\hat{\mathbf{u}}_{sur}, \tag{4.17}$$

where $e_1 = 0.4$, $e_2 = 0.8$ and $e_3 = 0.03$, and the initial value for c_w and c_c is assumed to be 0.15 and 0.10 respectively.

In each iteration a new model $\mathbf{m}_{new}$ is proposed as

$$\mathbf{m}_{new} = \mathbf{m}_0 + \mathbf{qA}, \tag{4.18}$$

where $\mathbf{m}_0$ is the initial model and $\mathbf{A}$ contains the perturbation amplitude of the corresponding model parameter. The vector $\mathbf{q}$ defines the random walk in the multidimensional model space and solely depends on the preceding step. In each iteration, i, one model parameter, j, is randomly selected and perturbed as

$$\mathbf{q}_{i+1}(j) = \mathbf{q}_i(j) + \left(r - \frac{1}{2}\right)\mathbf{p}(j), \tag{4.19}$$

where r indicates a random number between 0 and 1, and $\mathbf{p}$ regulates the maximum step length per iteration of the selected parameter type. To achieve a good performance of the Monte-Carlo algorithm, the values of $\mathbf{A}$ and $\mathbf{p}$ (shown in Table 4.4) are chosen such that the acceptance ratio for the individual model parameters lies between 25 % and 75 %.

The quality of the proposed model is evaluated by the function $S(\mathbf{m})$ which describes the misfit between the modeled and observed data (see Appendix 4.5). The new model ($\mathbf{m}_{new}$) is accepted with the acceptance probability (Metropolis et al., 1953)

$$P_{accept} = \min\left(\frac{L(\mathbf{m}_{new})}{L(\mathbf{m}_{old})}, 1\right), \tag{4.20}$$

where $\mathbf{m}_{old}$ is the last accepted model and the likelihood function is defined as $L(\mathbf{m}) = e^{-S(\mathbf{m})}$.

To ensure that parameter sampling is occurring in a physically reasonable range, the a priori probability distribution is assumed to be uniform within the following intervals:

$$\dot{a} \in \left[\dot{a}_0 - 0.02ma^{-1}, \dot{a}_0 + 0.02ma^{-1}\right] \tag{4.21}$$

$$h \in [0, H] \tag{4.22}$$

$$f_{bed} \in [\max(0, f_{bed,0} - 0.3), \min(1, f_{bed,0} + 0.3)] \tag{4.23}$$

$$\dot{b} \in \left[0ma^{-1}, 0.2ma^{-1}\right]. \tag{4.24}$$

The sampling intervals are based on expected values of the corresponding parameter: The initial accumulation rate obtained from the radar stratigraphy is considered to be quite trustworthy but because the local layer approximation is not justified in the survey area (Waddington et al., 2007) we allow the accumulation rate to deviate by 0.02 ma^{-1}. The kink height is limited to the ice-sheet thickness, the basal sliding fraction is allowed to deviate by 30 % from the initial model, and the upper limit of the basal melt rate is based on values suggested at EastGRIP by a recent study (Zeising and Humbert, 2021).

In their initial phase, Markov Chain Monte-Carlo methods move from the starting model towards a high-probability area where the target distribution is sampled. To avoid sampling during this so-called burn-in phase, the first 1×10^6 accepted models are discarded. Since only one parameter is perturbed at a time, successive models are highly correlated. To obtain a distribution of independent models, only every 1000th accepted model is saved. The sampling is continued for 6×10^6 iterations in total.

TABLE 4.4: Perturbation amplitude (**A**) and step length (**p**) of the individual model parameters used for the Monte-Carlo sampling. The sampling parameters were chosen such that the acceptance ratio of the individual model parameters lies between 25 % and 75 %.

Model parameter	**Amplitude (A)**	**Step length (p)**
$\dot{a}$	0.01 ma^{-1}	0.5
$\dot{b}$	0.01 ma^{-1}	1
h	100 m	3
f_{bed}	0.05	2
c_c	0.05	0.5
c_w	0.05	0.5

4.3 Results

4.3.1 Model parameters

Due to the mixed-determined nature of the inverse problem addressed in this study, a unique solution of model parameters does not exist. The Monte-Carlo sampling results in a number of possible models distributed according to the posterior probability. Here, we present the mean model parameters with the standard deviations of the posterior probability distribution and emphasize that the corresponding histograms (Fig. 4.6) are essential to understand the uncertainties of the parameter considered.

The flow-line characteristics and model parameters for each flow line are summarized in Fig. 4.4. The radar profiles with the observed and modeled isochrones are displayed as a function of the distance from the EastGRIP ice-core location. Particle trajectories were calculated from the simulated velocity field with the mean model parameters and indicate the source location of ice found at the modeled isochrone depth in the EastGRIP ice core. The isochrones and particle trajectories are illustrated with the same color-code as in Fig. 4.5 and Fig. 4.7f, indicating the corresponding age. The horizontal strain rates ($\dot{\varepsilon}_{xx}$, $\dot{\varepsilon}_{yy}$ and $\dot{\varepsilon}_{xy}$) were obtained from the MEaSUREs Multi-year v1 surface velocity components (Joughin et al., 2018) parallel ($u_{\parallel}$) and perpendicular ($u_{\perp}$) to the approximated flow line. The strain rates show mostly low, positive values along the flow lines with the exception of the shear-margin crossing in profile A and B, which is characterized by longitudinal extension and lateral compression.

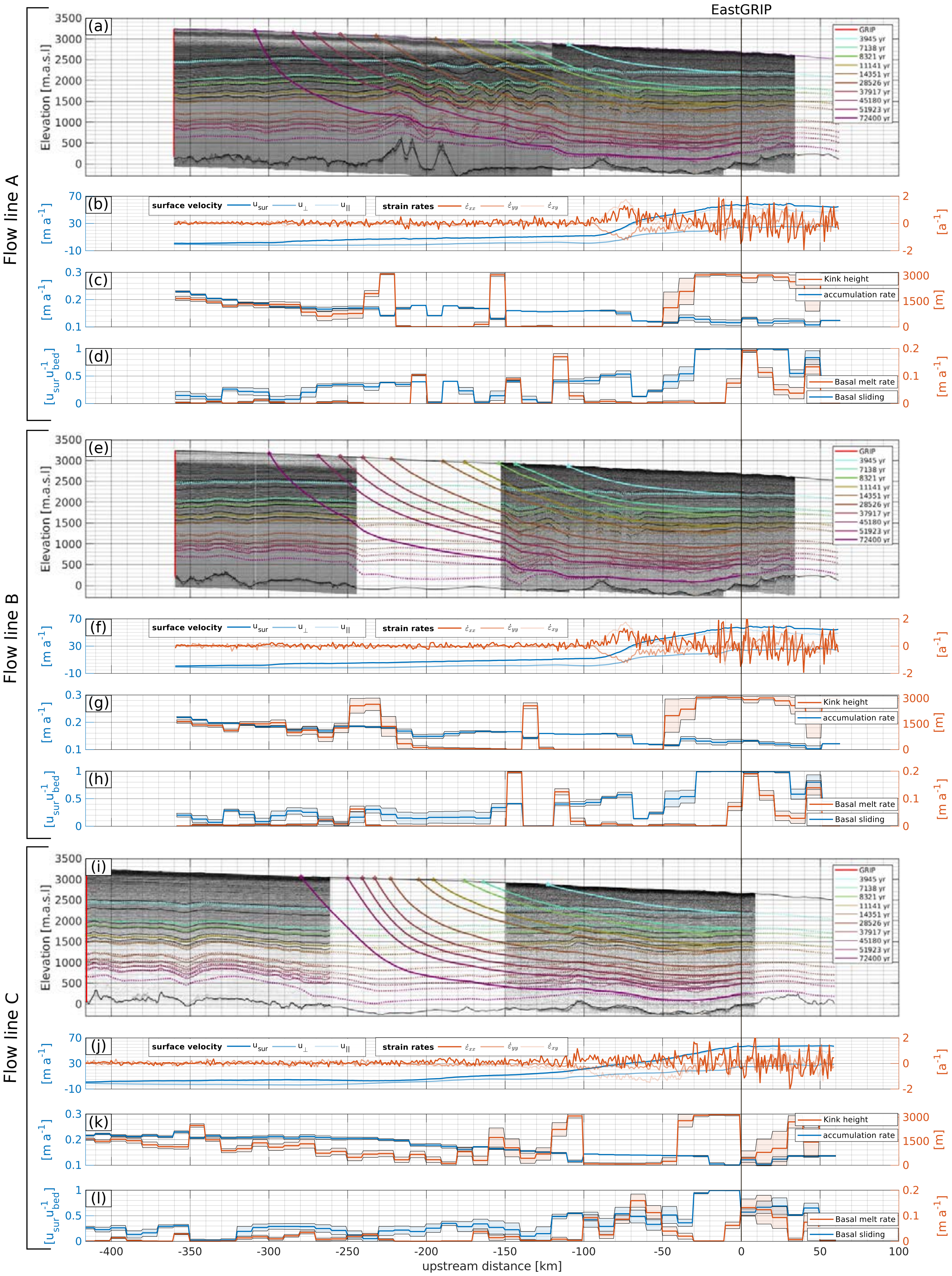
EastGRIP
Flow line A
Flow line B
Flow line C
(a)
(b)
(c)
(d)
(e)
(f)
(g)
(h)
(i)
(j)
(k)
(l)
Elevation [m.a.s.l]
3500
3000
2500
2000
1500
1000
500
0
GRIP
3945 yr
7138 yr
8321 yr
11141 yr
14351 yr
28526 yr
37917 yr
45180 yr
51923 yr
72400 yr
surface velocity
u_{sur}
$u_{\perp}$
$u_{||}$
strain rates
$\dot{\epsilon}_{xx}$
$\dot{\epsilon}_{yy}$
$\dot{\epsilon}_{xy}$
[m a^{-1}]
70
30
-10
[a^{-1}]
2
0
-2
0.3
0.2
0.1
Kink height
accumulation rate
3000
1500
0
[m]
[$u_{sur} u_{bed}^{-1}$]
1
0.5
0
0.2
0.1
Basal melt rate
Basal sliding
-400
-350
-300
-250
-200
-150
-100
-50
0
50
100
upstream distance [km]

FIGURE 4.4: **(Previous page)** Flow-line characteristics and model parameters for the approximated flow lines A **(a–d)**, B **(e–h)**, and C **(i–l)**. IRHs were traced (thin solid lines) in RES images and simulated (dashed lines) with a two-dimensional Dansgaard–Johnsen model **(a, e, i)**. From the modeled velocity field, we calculated particle trajectories (thick solid lines) backwards in time to obtain estimates of the source location for specific depths in the EastGRIP ice core. The colors of the lines indicate the age of the isochrones and the respective time of snow deposition and are identical to the color code in Fig. 4.5 and Fig. 4.7. The horizontal strain rates at the surface were calculated from the MEaSUREs Multi-year v1 (Joughin et al., 2018) surface velocities **(b, f, j)**. The mean and standard deviations of the sampled model parameters accumulation rate, kink height, basal melt rate and basal sliding **(c, d, g, h, k, l)** were obtained from a Monte-Carlo inversion by reducing the misfit between observed and simulated data. All panels are aligned at EastGRIP and the x-axis indicates the distance from the borehole location.

The central observed features are the following:

1. The accumulation rate decreases with increasing distance from the central ice divide. In flow line A and B, it remains almost constant between -220 and -80 km, followed by a drop of about 20 % across the shear margins. In the first ~150 km of flow line C, which corresponds to the ice divide, the accumulation rate remains nearly constant, followed by a gradual decrease with increasing distance along the profile.
2. The kink height fluctuates around the middle of the ice column in the vicinity of the ice ridge and is drawn closer to the bed in the center of the profiles. Locally very high kink heights are observed in flow line A around -230 km and -150 km, in flow line B at -240 km and -140 km, and at -100 km in flow line C. In all profiles, h increases substantially at about -60 km.
3. The basal velocity ranges between 0 and 50 % of the surface velocity outside the NEGIS and increases to 60–100 % in the vicinity of EastGRIP.
4. The basal melt rate in the beginning of the profiles varies between 0 and 0.03 ma^{-1}. As for the kink height, flow line A shows strong melt rate fluctuations in the center of the profile, some of which are also observed in flow line B. At EastGRIP, basal melt rates between 0.05 and 0.1 ma^{-1} are obtained but higher values of up to 0.2 ma^{-1} are reached further downstream.

4.3.2 Monte-Carlo performance

The comparison of modeled and observed isochrones (Fig. 4.5a,c,e) and α_{sur} (supplementary material, Fig. S4.2) shows a good fit in most parts of the flow lines. However, our model is not able to accurately reproduce strong internal layer undulations which are not related to the bed topography or the surface conditions, resulting in a larger misfit where such undulations are present (Fig. 4.5b,d,f). In general, the isochrone misfit tends to be larger for deeper layers. Particularly distinct is the positive misfit at EastGRIP for the deepest layer in all profiles, indicating that the depths of old layers are overestimated. The average isochrone misfit for flow line A, B and C is 2.94 %, 2.34 % and 1.49 % of the respective layer depth.

Histograms in Fig. 4.6 show the sampled probability distribution of model parameters at GRIP and EastGRIP with the corresponding mean and standard deviation displayed on top. Distributions with distinctive single peaks and low standard deviation point towards a good parameter resolution, while multiple maxima or large standard deviations indicate that several models are found to be equally likely. The parameter resolution is in general better in the beginning of the profiles, most clearly represented by the narrow distributions in the accumulation rate, basal melt rate and kink height at GRIP. Exponential distributions imply that a parameter reaches regularization boundaries. This is the case for the basal melt rates at GRIP, the kink

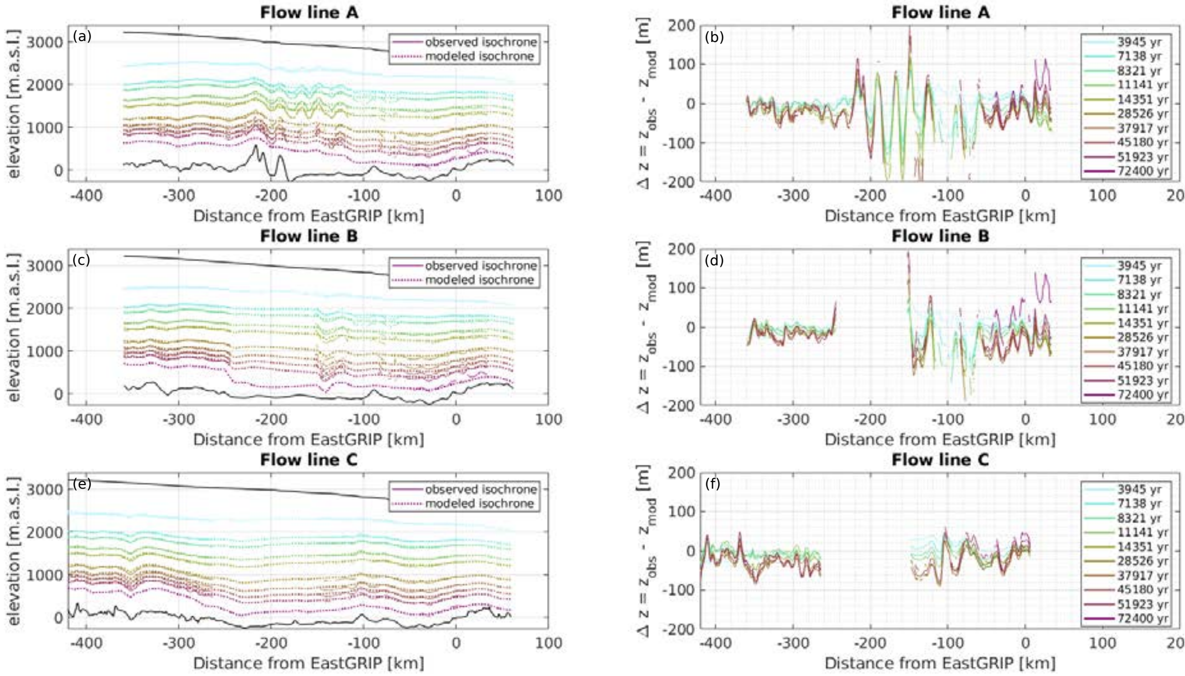

FIGURE 4.5: **(a, c, e)** Modeled and observed isochrones for profile A–C. The model fits the isochrones well in general but fails to reproduce strong layer undulations over short distances, leading to a larger misfit (panel **b, d, f)** where such undulations are present. A positive misfit indicates that the modeled isochrone depth is overestimated which happens in particular for the deepest isochrone towards the end of flow line A and B. As in Fig. 4.4 and Fig. 4.7, the color code represents the age of the corresponding isochrone.

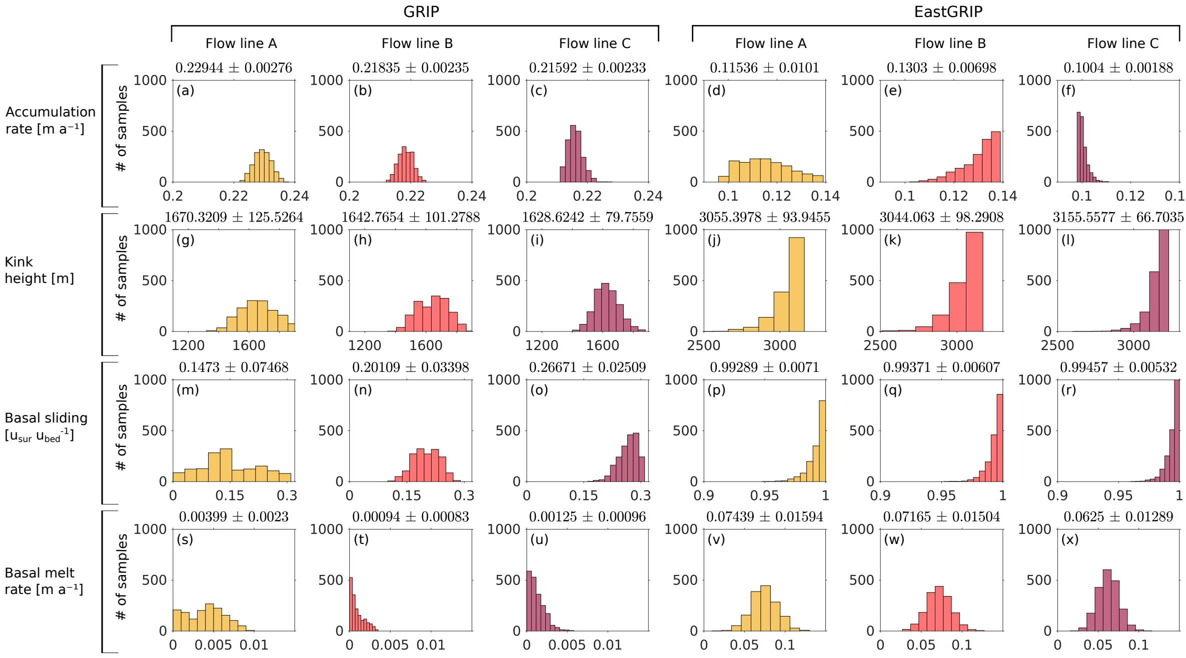

FIGURE 4.6: Histograms of the model parameters accumulation rate, basal melt rate, kink height and basal sliding at GRIP and EastGRIP for each flow line. The corresponding means and standard deviations are displayed on top of the histograms.

height and basal sliding factor at EastGRIP, and the accumulation rate in flow lines B and C at EastGRIP. The climate parameter c_w is found to be 0.10 ± 0.005 for all flow lines. The obtained value for parameter c_c is 0.14 ± 0.003 for flow line A and B, and 0.16 ± 0.004 for flow line C respectively. The histograms of c_w and c_c can be found in the supplementary material, Fig. S4.3.

4.3.3 Ice origin and ice-flow history

TABLE 4.5: Essential quantities for upstream corrections for selected depths of the EastGRIP ice core. The upstream distance, elevation and past accumulation rates, $\dot{a}_{past}$, describe the characteristics of the source location and the conditions during ice deposition. $\dot{a}_{present}$ represents the corresponding present-day accumulation rates at the source location. All quantities are averages over the three flow lines and the uncertainties represent the maximum deviation from the mean.

Depth [m]	**Age** [yr b2k]	**Upstream distance** [km]	**Elevation** [m.a.s.l.]	**Thinning function**	$\dot{\mathbf{a}}_{\mathbf{past}}$ [ma^{-1}]	$\dot{\mathbf{a}}_{\mathbf{present}}$ [ma^{-1}]
100	665	47 ± 3	2,752 ± 10	0.10 ± 0.03	0.12 ± 0.004	0.12 ± 0.015
200	1,553	74 ± 2	2,788 ± 11	0.19 ± 0.08	0.14 ± 0.006	0.14 ± 0.005
300	2,418	92 ± 1	2,837 ± 14	0.16 ± 0.05	0.13 ± 0.005	0.15 ± 0.010
400	3,322	105 ± 7	2,854 ± 6	0.21 ± 0.02	0.14 ± 0.002	0.14 ± 0.031
600	5,037	126 ± 12	2,892 ± 14	0.28 ± 0.00	0.16 ± 0.001	0.16 ± 0.005
800	6,805	146 ± 14	2,920 ± 9	0.35 ± 0.03	0.15 ± 0.005	0.16 ± 0.003
1,000	8,640	165 ± 13	2,944 ± 15	0.42 ± 0.03	0.16 ± 0.004	0.17 ± 0.002
1,200	11,015	183 ± 12	2,965 ± 19	0.41 ± 0.06	0.12 ± 0.010	0.17 ± 0.005
1,400	15,571	200 ± 7	2,993 ± 7	0.46 ± 0.01	0.05 ± 0.001	0.17 ± 0.015
1,600	23,382	217 ± 3	3,027 ± 26	0.52 ± 0.08	0.05 ± 0.007	0.18 ± 0.023
1,800	33,524	234 ± 8	3,054 ± 40	0.72 ± 0.06	0.11 ± 0.028	0.19 ± 0.021
2,000	43,107	252 ± 14	3,079 ± 54	0.73 ± 0.07	0.10 ± 0.019	0.19 ± 0.022
2,200	54,864	271 ± 19	3,108 ± 73	0.83 ± 0.02	0.07 ± 0.006	0.19 ± 0.030
2,400	75,980	293 ± 18	3,136 ± 80	0.83 ± 0.11	0.08 ± 0.034	0.19 ± 0.023
2,600	94,696	322 ± 12	3,171 ± 67	0.94 ± 0.03	0.18 ± 0.044	0.20 ± 0.005

From the modeled velocity field, we calculate particle trajectories backwards in time (Fig. 4.4) which give insight into the source location and flow history of ice found at a certain depth in the EastGRIP ice core, and allow us to determine the accumulation rate during its deposition (Fig. 4.7e). Due to the higher velocities in the ice stream, the ice source location in the upper 1,600 m of the ice core lies further upstream for flow line C compared to flow line A and B. For deeper ice, this trend is reversed, as the velocity along flow line C drops below the velocity of line A and B (Fig. 4.7a). A similar effect manifests itself in the upstream elevation, where higher velocities along flow line C result in higher elevations in the upper part of the ice column, which is compensated by a flatter topographic profile for ice deeper than 1,400 m (Fig. 4.7b).

From the model-inferred in situ accumulation rates, $\dot{a}_m$, and annual layer thicknesses, λ_m, we calculate the ice-core thinning function γ:

$$\gamma = \frac{\dot{a}_m - \lambda_m}{\dot{a}_m}. \tag{4.25}$$

The thinning function increases nearly linearly with depth in the Holocene and shows a considerable decrease in the Younger Dryas and enhanced thinning in the Bølling–Allerød. In the glacial part of the ice core, the thinning function fluctuates between interstadials and stadials. The shift between the three lines results from the slightly different depth–age relationship and

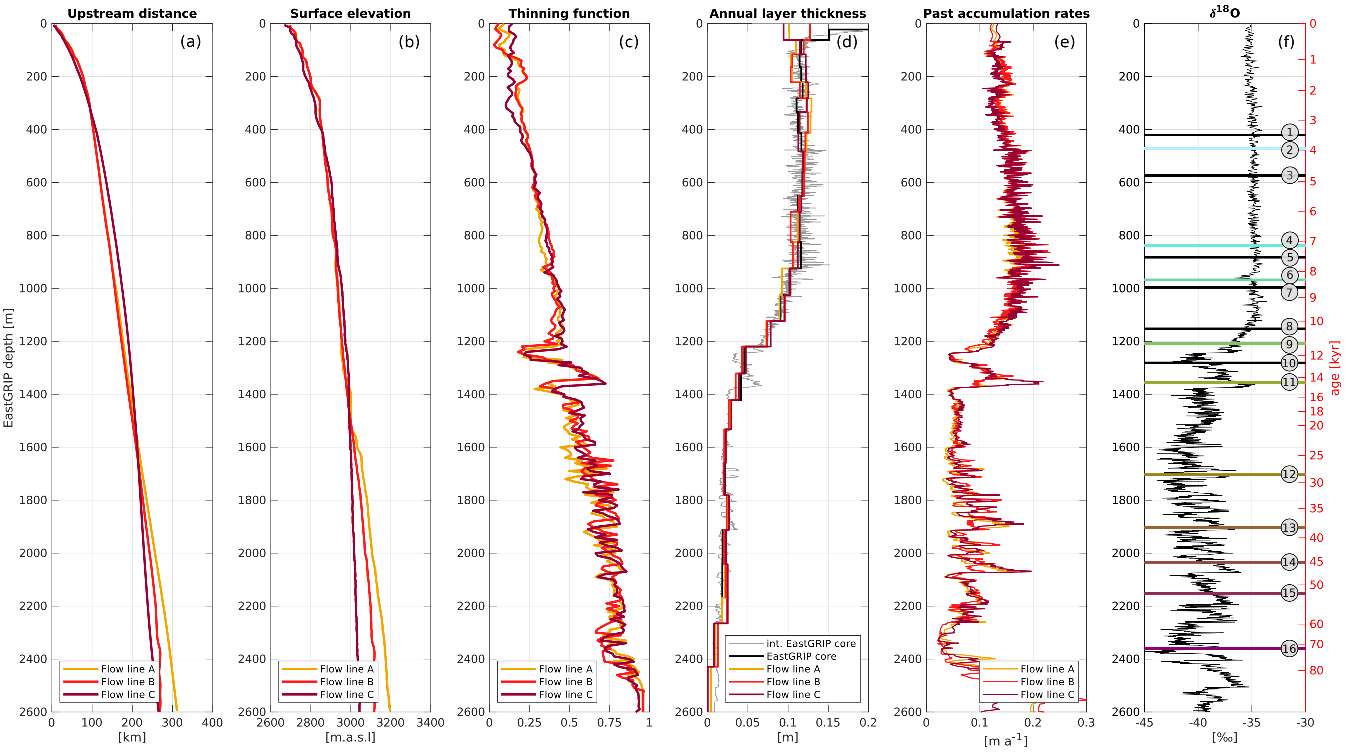

FIGURE 4.7: Modeled upstream distance **a)** and surface elevation **b)** of the source location for ice in the EastGRIP ice core. The thinning function **c)** was calculated from the modeled accumulation rates and annual layer thicknesses **d)** and was combined with the interpolated annual layer thicknesses observed in the ice core **d)** to calculate past accumulation rates in high resolution **e)**. The $\delta^{18}O$ curve from NorthGRIP **f)** was scaled to the EastGRIP depths to put the results into a climatic context and the depths of the traced isochrones from Table 4.3 are displayed with the same color index as in Fig. 4.4 and Fig. 4.5 and labeled with the corresponding layer number.

isochrone misfit obtained from the three profiles. We combine the thinning function with the annual layer thicknesses observed in the EastGRIP ice core, λ_{obs}, to estimate past accumulation rates $\dot{a}_{past}$:

$$\dot{a}_{past} = \frac{\lambda_{obs}}{1-\gamma}. \tag{4.26}$$

We find that the accumulation rate at the deposition site increases from ∼0.12 ma^{-1} to a maximum of 0.249 ma^{-1} for ice at a depth of 912 m, which was deposited approximately 7,800 years b2k. We note that the constant annual layer thicknesses observed in the upper 900 m of the EastGRIP ice core (Mojtabavi et al., 2020b) coincides with the spatial pattern of increasing accumulation along the flow line with increasing upstream distance (Fig. 4.4c,g,k and Fig. 4.7d,e). Ice between 900 m and 1,400 m is characterized by the transition from the Holocene into the Last Glacial Period with decreased accumulation rates in the Younger Dryas and a peak during the Bølling–Allerød (Fig. 4.7e). The accumulation rate at the deposition site for older ice varies between 0.02 ma^{-1} during stadials and 0.196 ma^{-1} during interstadials. The atmosphere in the glacial period was in general colder and dryer, and hence, accumulation rates were typically lower than today (Cuffey and Clow, 1997). However, due to the upstream flow effects, the ice from the interstadials could have been deposited under higher accumulation rates than are observed at the EastGRIP site today.

The variations in the past accumulation-rate between the three flow lines result from both, the varying along-flow accumulation pattern and different upstream distance of the source location. The spread between the three models provides important uncertainty estimates. The average deviation from the mean accumulation rates is 3.9 % in the Holocene and 20 % in the Last Glacial Period. The largest spread between the three flow lines is 68 % observed at a depth of 2,411 m. We remark that, due to missing direct information on the annual layer thicknesses, accumulation rates below the current borehole depth of 2,122.45 m are based on tentative estimates and must be treated accordingly.

4.4 Discussion

4.4.1 Isochrone deformation and ice-flow parameters

Deformation of IRHs occurs as a consequence of bed topography (Robin and Millar, 1982; Jacobel et al., 1993), spatial variations in basal conditions (Weertman, 1976; Whillans, 1976; Whillans and Johnsen, 1983; Catania et al., 2010; Christianson et al., 2013; Leysinger Vieli et al., 2018; Wolovick et al., 2014), spatially varying accumulation rates and corresponding changes in ice-flow geometry (Dansgaard et al., 1969; Weertman, 1976; Whillans, 1976; Whillans and Johnsen, 1983), and as a consequence of convergent ice flow and ice-stream activity (Bons et al., 2016). Areas of enhanced basal melt rates similarly drag down all the layers above, while variations in accumulation rate, kink height and basal sliding lead to depth-dependent deformation of the isochrones (Keisling et al., 2014).

The accumulation rates of $\sim$0.21–0.23 ma^{-1} at GRIP and $\sim$0.1–0.13 ma^{-1} at EastGRIP obtained in this study agree with field observations (Dahl-Jensen et al., 1993; Vallelonga et al., 2014), and the low standard deviations point towards a robust solution. In profiles A and B we observe $\sim$20 % lower accumulation rates inside the ice stream than outside. This agrees to some extent with Riverman et al. (2019), who found 20 % higher accumulation rates in the shear margins compared to the surrounding, although our observations are not confined to the shear margins only. Regularization on the accumulation rate was necessary in our model to avoid unrealistic strong fluctuations along the flow lines.

The bed topography and bed lubrication have a considerable effect on ice-flow parameters. Flow over bed undulations affect the elevation of internal layers due to variations in the longitudinal stresses within the ice (Hvidberg et al., 1997) and is often reflected in the surface topography (Cuffey and Paterson, 2010). If the bed is 'sticky', i.e. the basal sliding is small, the ice is compressed along the flow direction while vertically extended (Weertman, 1976), and IRHs are pushed upwards. At a slippery bed, the opposite is the case, resulting in along-flow extension of IRHs which leads to thinning and thus decreasing distance between the IRHs. Keisling et al. (2014) argued that major fold trains existing independently of bed undulations can be explained by variations in the basal sliding conditions. This is, for instance, observed across shear margins, where local, steady state folds are formed as a response to the basal conditions (Keisling et al., 2014; Holschuh et al., 2014). In flow line A, we observe similar 'fold-trains' on a larger scale downstream of a substantial bed undulation (100–200 km upstream of EastGRIP) and the resulting high basal melt rates and sliding fraction and the low kink heights drag the layers down in the attempt of matching the observed synclines. These strongly deformed isochrones predominantly appear in parts of the flow lines which deviate from the observed surface velocity direction by more than 15 degrees. We thus argue that they are out-of-the-plane effects and that the isochrones along the ice-flow direction are less strongly deformed. Accordingly, it is questionable that the ice in the EastGRIP ice core has experienced such deformation and that the high local basal melt rates are trustworthy. The fact that these folds are not reproduced very well by the model does therefore not put any constraints on the usefulness of our results for upstream corrections.

The NEGIS differs from other ice streams in Greenland and Antarctica through the lack of clear lateral topographic constraints and high ice-flow velocities reaching exceptionally far inland. The positioning of the shear margins of the NEGIS are most likely strongly interconnected to the subglacial water system and the substrate and morphology of the bed (Christianson et al., 2014; Franke et al., 2022a). The vast amount of ice mass is added to the NEGIS by entering the ice stream through the shear margins (Franke et al., 2022a), resulting in a compressional stress regime perpendicular to the ice stream. The sudden increase in the kink height at around 60 km upstream of EastGRIP pushes the isochrones upwards, similar to the effect of lateral compression. The distribution of available melt water and a soft, deformable bed facilitate sliding and thus, ice-flow acceleration at the NEGIS onset (Christianson et al., 2014). Evidence of a locally enhanced geothermal heat flux and basal ice at the melting point has been presented by e.g. Fahnestock et al. (2001b) and MacGregor et al. (2016), and bed lubrication through meltwater production seems to be one of the driving mechanisms for rapid ice flow in the onset region of the NEGIS (Smith-Johnsen et al., 2020a). Our results support these previous findings in the following way: (1) Kink heights close to the bed in large segments along the flow profiles imply that most shear deformation is happening in the lower part of the ice column or at the ice–bed interface. The increased kink height towards the ends of the profiles can be attributed to the compressional stress regime associated with the addition of ice through the shear margins. (2) Basal melt rates of 0.01 ma^{-1} or higher inside the NEGIS suggest that the basal ice temperatures along the flow lines are at the pressure melting point and enough energy is available to produce melt water leading to substantial bed lubrication. (3) Basal sliding is present in most segments of the flow lines, suggesting the presence of melt water or deformation of a soft bed. It increases considerably along the flow lines and significantly contributes to the surface velocity at EastGRIP.

While it is commonly accepted that the NEGIS is initiated by a locally enhanced geothermal heat flux (e.g. Fahnestock et al., 2001b; Alley et al., 2019), the magnitude thereof and the resulting hydrological conditions of the bed are still highly debated. Previous studies using simple strain-rate models in combination with Holocene radar stratigraphy indicate basal melt rates of 0.1 ma^{-1} or higher in the vicinity of EastGRIP (Fahnestock et al., 2001b; Keisling et al., 2014; MacGregor et al., 2016). However, the accuracy of these findings is limited since the local layer approximation (Waddington et al., 2007) is not valid in the surrounding of the NEGIS (Keisling et al., 2014; MacGregor et al., 2016). Remarkably high basal melt rates of 0.16–0.22 ma^{-1} are also suggested by a recent study (Zeising and Humbert, 2021) using an autonomous phase-sensitive radio-echo sounder (ApRES) at EastGRIP. Melt rates in these order of magnitudes would either require an unusual high geothermal heat flux exceeding the continental background (Fahnestock et al., 2001b; Bons et al., 2021) or an additional heat source (Zeising and Humbert, 2021). Alley et al. (2019) discussed the interactions between the GrIS and the geothermal anomaly, presumably caused by the passage of Greenland over the Iceland hot spot (Lawver and Müller, 1994), and hypothesized that an exceptionally unsteady and inhomogeneous geothermal heat flux underneath northeast Greenland could arise through perturbations of the mantle stress regime caused by ice-sheet fluctuations.

Our results indicate basal melt rates at EastGRIP between 0.05 and 0.1 ma^{-1} but higher values of up to 0.2 ma^{-1} are obtained further downstream. However, the depth of the oldest modeled isochrone tends to be overestimated in this part of the flow lines (Fig. 4.5), indicating that the basal melt rate is overestimated. Ice-flow parameters at a certain location affect the isochrones directly above and further downstream and since EastGRIP is near the end of the radar lines, the information constraining the isochrone depths is limited, leading to overall lower parameter resolution than further upstream.

4.4.2 EastGRIP source location and upstream effects

The source region of ice in the EastGRIP ice core extends over more than 300 km upstream. Holocene ice characterizes the upper 1,244 m of the ice core and has been advected up to 197 km. The climatic conditions during the last 8 kyr remained nearly constant with similar accumulation rates as today. However, due to increasing precipitation towards the central ice divide, ice from the past 8 kyr was deposited under increasingly higher accumulation rates with increasing age (Table 4.5). Our results indicate that this upstream effect happens to compensate for the vertical layer thinning and results in the constant annual layer thicknesses observed in the upper 900 m of the EastGRIP ice core (Mojtabavi et al., 2020b). One possible conclusion of this peculiar observation is that snow depositions must have been advected from far enough upstream to allow the compensation of vertical thinning by increased accumulation rates in the source location. This gives reason to the hypothesis that ice-flow velocities in the past 8 kyr must have been similarly fast as today, and that, therefore, the NEGIS has likely been active during this time. However, we believe that RES images and estimates of present-day accumulation rates along the EastGRIP flow line are necessary to evaluate this hypothesis further.

Between 8 ka b2k and the beginning of the Holocene, accumulation rates decreased at the deposition site due to progressively colder and dryer climatic conditions (Cuffey and Clow, 1997) as we go further back in time and transition into the GS-1. The most recent Glacial Period extends from 119,140 to 11,703 years b2k (Walker et al., 2009) and is characterized by Dansgaard–Oeschger events, abrupt transitions between cold stadial and relatively mild interstadial periods (Dansgaard et al., 1982; Johnsen et al., 1992) causing the oscillations in the accumulation rates. Ice from the Last Glacial Period was deposited between 197 and 332 km upstream from EastGRIP. The basal ice at EastGRIP could be more than 100 ka old which, according to our models, has been deposited within about 50 km from the ice divide under conditions similar to those at NorthGRIP and GRIP.

Ice that is entering the NEGIS must somehow penetrate the shear margin, which is an important characteristic of ice flow in ice streams and might have left an imprint on the crystal fabric and texture of ice extracted at EastGRIP. Our modeling results along flow line A and B indicate that ice below 239 m in the EastGRIP ice core has passed the shear margin 82 km from EastGRIP around 1.8 ka b2k. Slightly enhanced annual layer thicknesses observed in the ice core at a depth of 230 m (Fig. 4.3) seem unrelated to short-term warmer and wetter climate and might thus be an effect of enhanced accumulation across the shear margin, supporting our results.

Our results show surface elevations at the deposition site which are up to 500 m higher than EastGRIP at the corresponding time. Assuming a normal thermal and pressure gradient, this implies that ice was deposited under up to $\sim 3.25°C$ colder temperatures and up to 45 hPa lower pressure than conditions found at the borehole location at the time of deposition.

4.4.3 Limitations

The most relevant limitation of this study arises from lacking radar data parallel to the flow field in the upstream area of EastGRIP. The approximated flow lines deviate from the present-day surface flow field in some parts by more than 15 degrees, which presumably introduces out-of-the-plane effects. Data gaps encumbered isochrone tracing and restricted the Monte-Carlo method due to missing information in those areas. The correlated parameters in the Dansgaard–Johnsen model lead to a vast amount of possible solutions, and the fact that the observed data can be reproduced by our model does not prove the validity of the assumed parameters and the physical interpretation thereof. This becomes for instance evident at the GRIP ice-core site, where our results indicate basal sliding of up to 30 %, while the drilling project showed that the bed is frozen at the ice-sheet summit (Dahl-Jensen et al., 1998). The apparent basal sliding might thus represent deformation within a soft bed material rather than actual sliding of the ice over the bed. The spatial and formal resolution of the obtained model parameters is limited, in particular towards the end of the profiles due to limited constraining information further downstream.

By introducing the parameter α, our model accounts for lateral compression and extension on a first degree order, but does not capture the full complexity of the flow field across the shear margins. While these play an essential role in the ice-flow dynamics of the NEGIS (Holschuh et al., 2019b) and are likely to have left an imprint on the ice found in the EastGRIP ice core, the full simulation of the flow field is not attempted for the purpose of upstream corrections. This would require more complex, 3D numerical ice-flow models which are computationally more expensive and thus not suitable for the Monte-Carlo method applied here. Moreover, due to the lack of constraining radar data the information gain in terms of the source characteristics and upstream effects of such a 3D model would be modest.

The elevation of the source location was determined solely from the present-day ice-sheet surface elevation and did not take into account past fluctuations in the ice-sheet thickness. In general, surface elevation changes are relatively minor in the interior areas of central Greenland (Marshall and Cuffey, 2000; Letréguilly et al., 1991). Yet, Vinther et al. (2009) found that the GRIP elevation might have been up to 200 m higher during the early Holocene than today. We did not take into account changes in the ice thickness due to the large uncertainties which would be introduced, particularly in the Last Glacial Period. Our estimates on the surface elevation of the source location must thus not be interpreted as absolute values but rather as relative changes with respect to the surface elevation of the EastGRIP site at the corresponding time.

Lacking data and a general understanding of ice-sheet flow far back in time put up additional constraints, and due to the relatively recent discovery of the NEGIS (Fahnestock et al., 1993), little is known about its evolution in the past. Observations of surface elevation and ice-flow velocities imply that the downstream end of the NEGIS has entered a state of dynamic thinning after at least 25 years of stability (Khan et al., 2014). However, it is not clear for how long the NEGIS has been active and how its catchment geometry changed over time. The assumption of a constant flow field throughout the past 100 kyr is thus the best currently available, but potentially inaccurate, estimate of the past flow regime.

Our results do not give clear evidence on which of the flow lines gives the best results for upstream corrections. Since the present-day EastGRIP flow line is likely located somewhere between flow line A and C, our results can be interpreted as the outer boundaries and we consider the average over the three flow lines the best estimate for the upstream flow characteristics with the corresponding model spread as uncertainties.

4.5 Conclusions

We traced isochrones in RES images along three approximated EastGRIP flow lines connecting the EastGRIP and GRIP drill sites. A two-dimensional Dansgaard–Johnsen model was used to simulate the propagation of isochrones along these flow lines. The simplicity of the model allowed us to invert for the ice-flow parameters accumulation rate, basal melt rate, kink height and basal sliding fraction, which give limited but helpful insight into basal properties and ice-flow dynamics and can be used to constrain large-scale ice-sheet models.

On the basis of our modeled two-dimensional velocity field, we calculated particle trajectories backwards in time to determine the deposition site of ice found in the EastGRIP ice core. We present estimates of the upstream distance, surface elevation and accumulation rate at the time and location of ice deposition. This is valuable and necessary information for interpreting ice-core measurements, and to separate past climate variability from non-local imprints introduced by upstream effects. Our studies show that spatially increasing accumulation rates with increasing upstream distance along the flow line are mainly responsible for the constant annual layer thicknesses observed for the last 8 kyr in the EastGRIP ice core.

The lack of radar data along the EastGRIP flow line is the biggest limitation of this study.

None of the three simulated flow lines accurately represents the present-day flow field but can be regarded as upper and lower limits framing the upstream effects. The acquisition of further radar data along NEGIS flow lines in the future would thus provide more accurate and valuable insights into the flow history of the EastGRIP ice and the NEGIS.

Appendix A

A.1 Notation

z	height above bed
x, y	direction parallel, perpendicular to the flow profile
$\tilde{z}_t, \tilde{z}_p, \tilde{z}_{rr}$	total, picking related, radar related isochrone depth uncertainty
k	radar window widening factor
c	speed of light
B	radar band width
$\tilde{a}_t, \tilde{a}_p, \tilde{a}_{rr}, \tilde{a}_c$	total, picking related, radar related, ice-core related age uncertainty
a_c	ice-core age
$u_{\|\|}(z), u_{\|\|,sur}$	flow-line-parallel velocity at depth, at the surface
$u_{\perp}(z), u_{\perp,sur}$	flow-line-perpendicular velocity at depth, at the surface
$\hat{\mathbf{u}}_{sur}$	normalized surface velocity along the flow line
$\omega(z), \omega_{sur}, \omega_{bed}$	vertical velocity at depth, at the surface, at the bed
$f_{bed}, f_{bed,0}$	basal sliding fraction, initial basal sliding fraction
h, h_0	kink height, initial kink height
H	ice thickness
α	sum of horizontal strain rates $\dot{\varepsilon}_{xx} + \dot{\varepsilon}_{yy}$
E_{bed}	bed elevation above sea level
E_{sur}	surface elevation above sea level
$\dot{a}, \dot{a}_m, \dot{a}_c, \dot{a}_{past}, \dot{a}_{present}$	positive accumulation rate, Monte-Carlo inferred, ice-core inferred, past, present
$\dot{b}$	positive basal melt rate
$e_{1,2,3}$	scaling factors for initial model parameters
$\xi(t)$	climatic scaling factor
t	time b2k
c_c, c_w	sensitivity of accumulation rates in cold stadial, warm interstadial periods
$\partial^{18}O_c, \partial^{18}O_w$	typical isotope values for cold stadial, warm interstadial periods
$\mathbf{d}, \mathbf{d}_{obs}, \mathbf{d}_{model}$	data space, observed, modeled data
$\mathbf{m}, \mathbf{m}_{old}, \mathbf{m}_{new}$	model space, old, new model
σ_z, σ_α	data uncertainty on isochrone depth, α_{sur}
P_{accept}	acceptance probability
L	likelihood function
S	misfit function
$\lambda, \lambda_m, \lambda_{obs}$	annual layer thickness, modeled, observed
γ	ice-core thinning function
$\dot{\varepsilon}_{xx}, \dot{\varepsilon}_{yy}, \dot{\varepsilon}_{xy}$	horizontal strain rates

A.2 Derivation of Eq. (4.14)

The vertical velocity in the upper part of the ice column is given by

$$w(z) = w_{sur} + \alpha_{sur}(H - z) = \frac{dz}{dt}, \qquad z \in [h, H]. \tag{4.27}$$

Assuming that the surface slope is close to zero, $\frac{\partial E_{sur}}{\partial x} \simeq 0$, integration of Eq. (4.27) with separation of variables results in:

A.3 Definition of the misfit function S(m)

The function $S(\mathbf{m})$ is defined as:

$$S(\mathbf{m}) = \frac{1}{2}\left(\frac{1}{10}\sum_{l=1}^{10}\left(\frac{1}{n_z}\sum_{n=1}^{n_z}\mathbf{M}_z^2\right) + \frac{1}{n_\alpha}\sum_{n=1}^{n_\alpha}\mathbf{M}_\alpha^2\right) * 1000, \tag{4.28}$$

where l runs through the 10 layers, n_z and n_α are the number of observed isochrone depths and α_{sur} along the flow lines, and

$$\mathbf{M}_z = \frac{\mathbf{d}_{mod,z} - \mathbf{d}_{obs,z}}{\sigma_z} \quad \text{and} \quad \mathbf{M}_\alpha = \frac{\mathbf{d}_{mod,\alpha} - \mathbf{d}_{obs,\alpha}}{\sigma_\alpha}. \tag{4.29}$$

The matrix $\mathbf{M}_z$ describes the misfit between modeled ($\mathbf{d}_{mod,z}$) and observed ($\mathbf{d}_{obs,z}$) isochrones, and the vector $\mathbf{M}_\alpha$ is the misfit between modeled ($\mathbf{d}_{mod,\alpha}$) and observed ($\mathbf{d}_{obs,\alpha}$) α_{sur}. The data uncertainty σ_z is the maximum depth uncertainty of 13 m, and the uncertainty on α_{sur} (σ_α) is assumed to be 10 % of the maximum observed α_{sur}. The factor 1000 is a tuning parameter to ensure the acceptance ratio remains between 25 % and 75 %.

Author contributions

DDJ and TAG designed and carried out the study. AG developed the code used for isochrone tracing. AG and CSH derived the EastGRIP flow lines. DJ was co-investigator for the AWI radar survey and acquired the data in the field. SF processed the radar data obtained during the EGRIP-NOR-2018 AWI flight campaign. SOR, GS and TAG synchronized the EastGRIP ice core with NorthGRIP and NEEM and extended the timescale to the current drill depth. TAG prepared the manuscript with contributions from all co-authors.

Supplementary Material

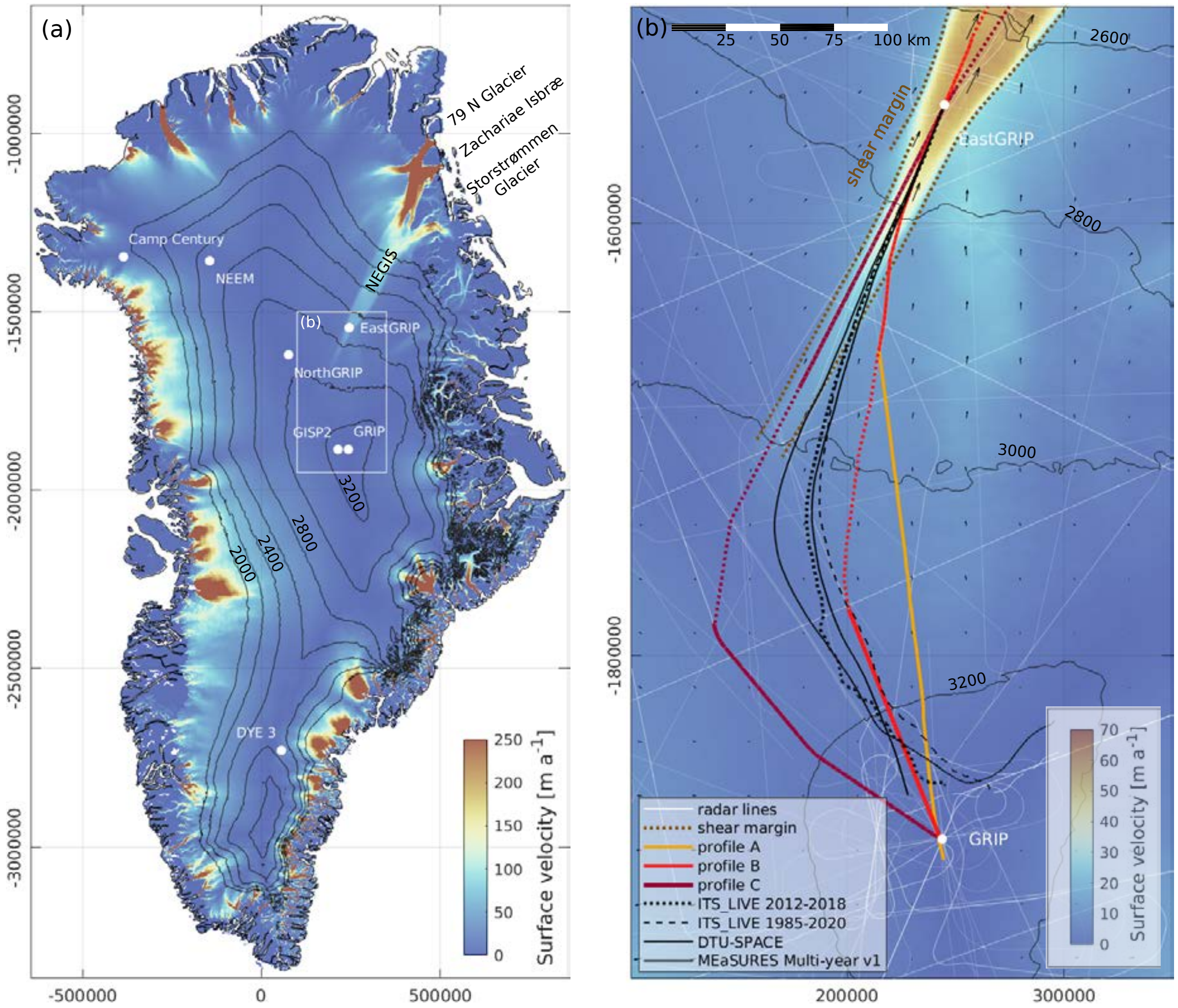

FIGURE S4.1: **a)** Overview of past and ongoing deep ice-core drilling projects on the GrIS (surface elevation and Greenland contour lines by Simonsen and Sørensen, 2017; Greene et al., 2017) and the outline of the study area. **b)** The black lines are flow lines traced from the satellite-based surface velocity products MEaSUREs Multi-year v1 (Joughin et al., 2018), MEaSUREs ITS_LIVE (Gardner et al., 2020) and DTU-SPACE (Andersen et al., 2020). The velocity products are bias-corrected before deriving the flow lines upstream from EastGRIP, and the spread of these flow lines indicates the uncertainty in the upstream flow path (for a complete discussion see Hvidberg et al., 2020). Due to the limited availability of radar data along the flow line, we construct three approximate flow lines through a combination of various radar products (profile A–C) between GRIP and EastGRIP. Flow line B and C lack data in the center of the profiles, marked as a dashed line. The downstream parts of line A and B comprise the same radar profile, which crosses the southern shear margin 82 km upstream of EastGRIP.

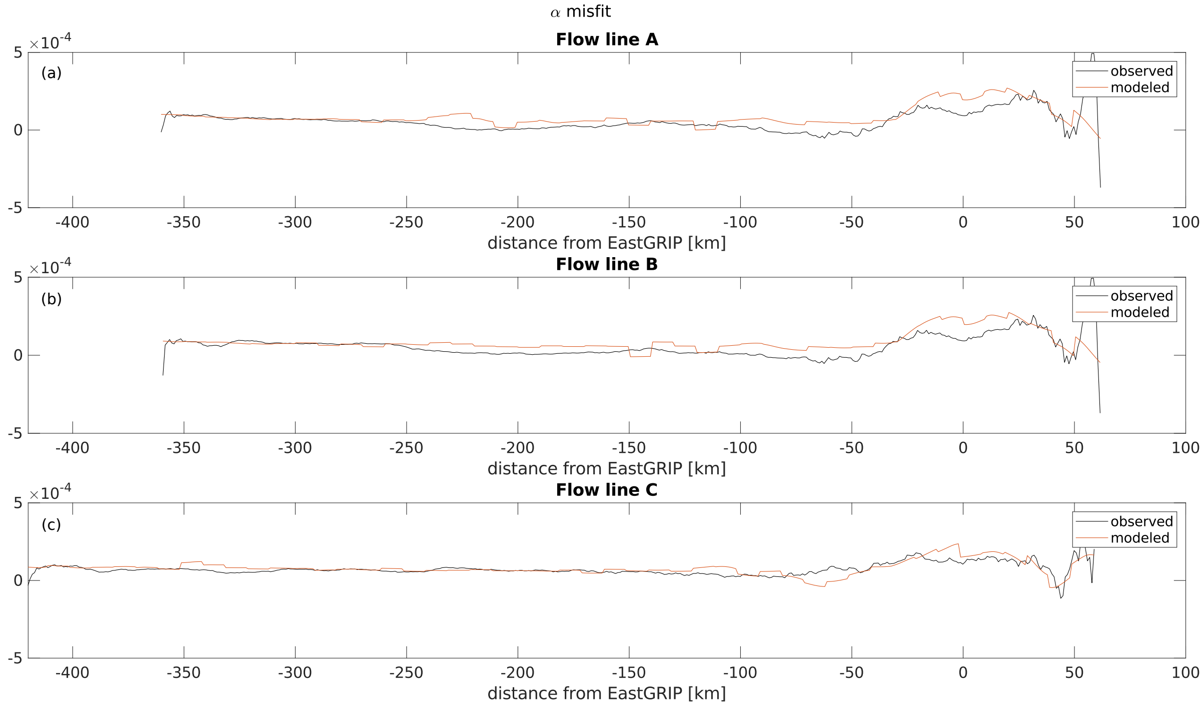

FIGURE S4.2: Observed and modeled α for flow line A–C.

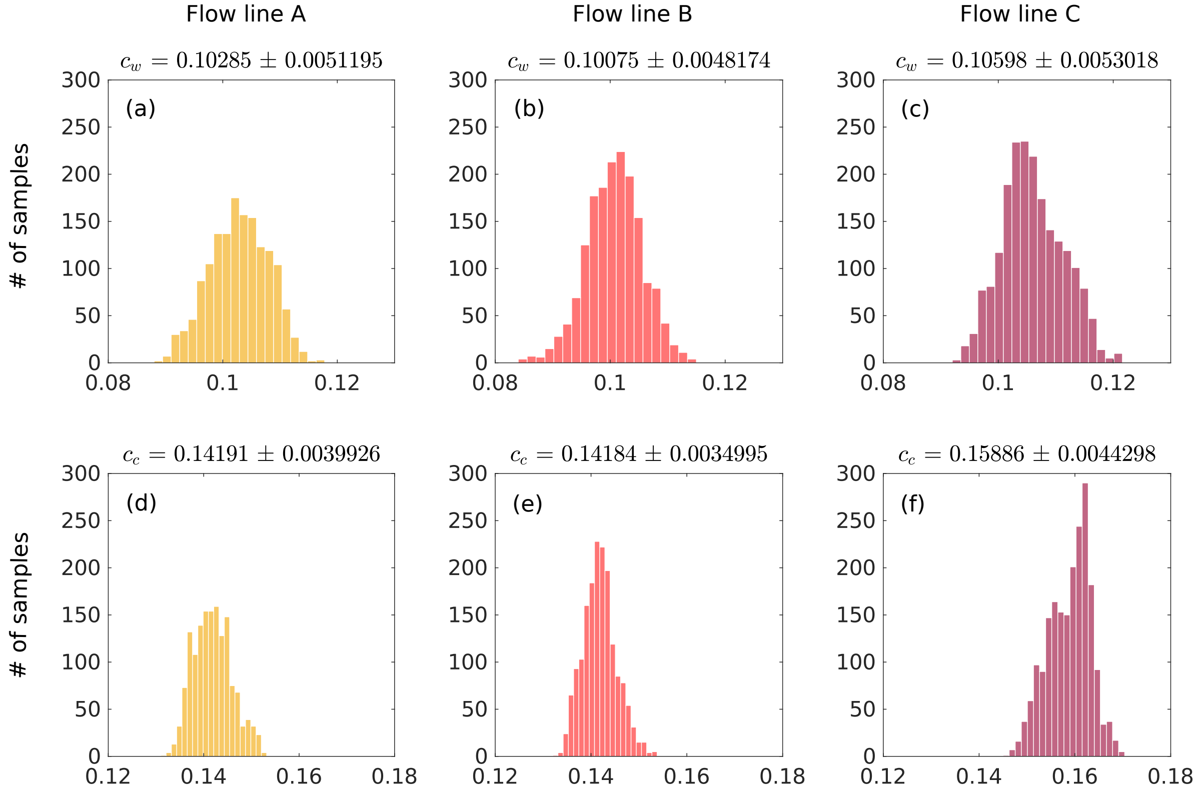

FIGURE S4.3: Histograms of the climate parameters c_w (**a–c**) and c_c (**d–f**) for flow line A–C.

References

Ageta, Y., Azuma, N., Fujii, Y., Fujino, K., Fujita, S., Furukawa, T., Hondoh, T., Kameda, T., Kamiyama, K., Katagiri, K., Kawada, K., Kawamura, T., Kobayashi, S., Mae, S., Maeno, H., Miyahara, T., Motoyama, H., Nakayama, Y., Naruse, R., Nishio, F., Saitoh, K., Saitoh, T., Shimbori, K., Shiraiwa, T., Shoji, H., Takahashi, A., Takahashi, S., Tanaka, Y., Yokoyama, K., and Watanabe, O. (1998). "Deep ice-core drilling at Dome Fuji and glaciological studies in east Dronning Maud Land, Antarctica". In: *Annals of Glaciology* 27, pp. 333–337. DOI: `10.3189/1998aog27-1-333-337`.

Aizen, V. B., Aizen, E. M., Joswiak, D. R., Fujita, K., Takeuchi, N., and Nikitin, S. A. (2006). "Climatic and atmospheric circulation pattern variability from ice-core isotope/geochemistry records (Altai, Tien Shan and Tibet)". In: *Annals of Glaciology* 43, pp. 49–60. DOI: `10.3189/172756406781812078`.

Alley, R. B., Meese, D. A., Shuman, C. A., Gow, A. J., Taylor, K. C., Grootes, P. M., White, J. W., Ram, M., Waddington, E. D., Mayewski, P. A., and Zielinski, G. A. (1993). "Abrupt increase in Greenland snow accumulation at the end of the Younger Dryas event". In: *Nature* 362.6420, pp. 527–529. DOI: `10.1038/362527a0`.

Alley, R. B., Pollard, D., Parizek, B. R., Anandakrishnan, S., Pourpoint, M., Stevens, N. T., MacGregor, J. A., Christianson, K., Muto, A., and Holschuh, N. (2019). "Possible Role for Tectonics in the Evolving Stability of the Greenland Ice Sheet". In: *Journal of Geophysical Research: Earth Surface* 124.1, pp. 97–115. DOI: `10.1029/2018JF004714`.

Alley, R. B., Bolzan, J. F., and Whillans, I. M. (1982). "Polar firn densification and grain growth". In: *Annals of Glaciology* 3, pp. 7–11. DOI: `doi:10.3189/S0260305500002433`.

Andersen, J. K., Kusk, A., Boncori, J. P. M., Hvidberg, C. S., and Grinsted, A. (2020). "Improved ice velocity measurements with Sentinel-1 TOPS interferometry". In: *Remote Sensing* 12.12, pp. 1–22. DOI: `10.3390/rs12122014`.

Andersen, K. K., Azuma, N., Barnola, J. M., Bigler, M., Biscaye, P., Caillon, N., Chappellaz, J., Clausen, H. B., Dahl-Jensen, D., Fischer, H., Flückiger, J., Fritzsche, D., Fujii, Y., Goto-Azuma, K., Grønvold, K., Gundestrup, N. S., Hansson, M., Huber, C., Hvidberg, C. S., Johnsen, S. J., Jonsell, U., Jouzel, J., Kipfstuhl, S., Landais, A., Leuenberger, M., Lorrain, R., Masson-Delmotte, V., Miller, H., Motoyama, H., Narita, H., Popp, T., Rasmussen, S. O., Raynaud, D., Rothlisberger, R., Ruth, U., Samyn, D., Schwander, J., Shoji, H., Siggard-Andersen, M. L., Steffensen, J. P., Stocker, T., Sveinbjörnsdóttir, A. E., Svensson, A., Takata, M., Tison, J. L., Thorsteinsson, T., Watanabe, O., Wilhelms, F., and White, J. W. (2004). "High-resolution record of Northern Hemisphere climate extending into the last interglacial period". In: *Nature* 431.7005, pp. 147–151. DOI: `10.1038/nature02805`.

Andersen, K. K., Svensson, A., Johnsen, S. J., Rasmussen, S. O., Bigler, M., Röthlisberger, R., Ruth, U., Siggaard-Andersen, M. L., Peder Steffensen, J., Dahl-Jensen, D., Vinther, B. M., and Clausen, H. B. (2006). "The Greenland Ice Core Chronology 2005, 15-42 ka. Part 1: constructing the time scale". In: *Quaternary Science Reviews* 25.23-24, pp. 3246–3257. DOI: `10.1016/j.quascirev.2006.08.002`.

Aschwanden, A., Fahnestock, M. A., and Truffer, M. (2016). "Complex Greenland outlet glacier flow captured". In: *Nature communications* 7.1, pp. 1–8. DOI: `10.1038/ncomms10524`.

Barbante, C. et al. (2006). "One-to-one coupling of glacial climate variability in Greenland and Antarctica". In: *Nature* 444.7116, pp. 195–198. DOI: `10.1038/nature05301`.

Beyer, S., Kleiner, T., Aizinger, V., Rückamp, M., and Humbert, A. (2018). "A confined–unconfined aquifer model for subglacial hydrology and its application to the Northeast Greenland Ice Stream". In: *The Cryosphere* 12.12, pp. 3931–3947. DOI: `10.5194/tc-12-3931-2018`.

Bons, P. D., Riese, T. de, Franke, S., Llorens, M.-G., Sachau, T., Stoll, N., Weikusat, I., Westhoff, J., and Zhang, Y. (2021). "Comment on "Exceptionally high heat flux needed to sustain the

Northeast Greenland Ice Stream" by Smith-Johnsen et al.(2020)". In: *The Cryosphere* 15.5, pp. 2251–2254. DOI: `10.5194/tc-15-2251-2021`.

Bons, P. D., Jansen, D., Mundel, F., Bauer, C. C., Binder, T., Eisen, O., Jessell, M. W., Llorens, M.-G., Steinbach, F., Steinhage, D., and Weikusat, I. (2016). "Converging flow and anisotropy cause large-scale folding in Greenland's ice sheet". In: *Nature communications* 7.1, pp. 1–6. DOI: `10.1038/ncomms11427`.

Buchardt, S. L. and Dahl-Jensen, D. (2007). "Estimating the basal melt rate at NorthGRIP using a Monte Carlo technique". In: *Annals of Glaciology* 45, pp. 137–142. DOI: `10.3189/172756407782282435`.

Burgess, E. W., Forster, R. R., Box, J. E., Mosley-Thompson, E., Bromwich, D. H., Bales, R. C., and Smith, L. C. (2010). "A spatially calibrated model of annual accumulation rate on the Greenland Ice Sheet (1958-2007)". In: *Journal of Geophysical Research: Earth Surface* 115.2, pp. 1–14. DOI: `10.1029/2009JF001293`.

Byers, K. J., Harish, A. R., Seguin, S. A., Leuschen, C. J., Rodriguez-Morales, F., Paden, J., Arnold, E. J., and Hale, R. D. (2012). "A modified wideband dipole antenna for an airborne VHF ice-penetrating radar". In: *IEEE Transactions on Instrumentation and Measurement* 61.5, pp. 1435–1444. DOI: `10.1109/TIM.2011.2181780`.

Catania, G., Hulbe, C., and Conway, H. (2010). "Grounding-line basal melt rates determined using radar-derived internal stratigraphy". In: *Journal of Glaciology* 56.197, pp. 545–554. DOI: `10.3189/002214310792447842`.

Christianson, K., Parizek, B. R., Alley, R. B., Horgan, H. J., Jacobel, R. W., Anandakrishnan, S., Keisling, B. A., Craig, B. D., and Muto, A. (2013). "Ice sheet grounding zone stabilization due to till compaction". In: *Geophysical Research Letters* 40.20, pp. 5406–5411. DOI: `10.1002/2013GL057447`.

Christianson, K., Peters, L. E., Alley, R. B., Anandakrishnan, S., Jacobel, R. W., Riverman, K. L., Muto, A., and Keisling, B. A. (2014). "Dilatant till facilitates ice-stream flow in northeast Greenland". In: *Earth and Planetary Science Letters* 401, pp. 57–69. DOI: `10.1016/j.epsl.2014.05.060`.

CReSIS (2020b). *Radar Depth Sounder Data Products, Lawrence, Kansas, USA*. URL: `http://data.cresis.ku.edu/`.

Cuffey, K. M. and Clow, G. D. (1997). "Temperature, accumulation, and ice sheet elevation in central Greenland through the last deglacial transition". In: *Journal of Geophysical Research: Oceans* 102.C12, pp. 26383–26396. DOI: `10.1029/96JC03981`.

Cuffey, K. M. and Paterson, W. S. B. (2010). *The physics of glaciers*. eng. 4. ed. Amsterdam: Butterworth-Heinemann/Elsevier.

Dahl-Jensen, D., Johnsen, S. J., Hammer, C. U., Clausen, H. B., and Jouzel, J. (1993). "Past Accumulation rates derived from observed annual layers in the GRIP ice core from Summit, Central Greenland". In: *Ice in the Climate System* 112.Ice in the Climate System, pp. 517–532. DOI: `10.1007/978-3-642-85016-5_29`.

Dahl-Jensen, D., Mosegaard, K., Gundestrup, N., Clow, G. D., Johnsen, S. J., Hansen, A. W., and Balling, N. (1998). "Past temperatures directly from the Greenland ice sheet". In: *Science* 282.5387, pp. 268–271. DOI: `10.1126/science.282.5387.268`.

Dahl-Jensen, D., Gundestrup, N., Gogineni, S. P., and Miller, H. (2003). "Basal melt at NorthGRIP modeled from borehole, ice-core and radio-echo sounder observations". In: *Annals of Glaciology* 37, pp. 207–212. DOI: `10.3189/172756403781815492`.

Dansgaard, W., Clausen, H. B., Gundestrup, N., Hammer, C. U., Johnsen, S. F., Kristinsdottir, P. M., and Reeh, N. (1982). "A new Greenland deep ice core". In: *Science* 218.4579, pp. 1273–1277. DOI: `10.1126/science.218.4579.1273`.

Dansgaard, W., Johnsen, S. J., Møller, J., and Langway Jr, C. C. (1969). "One thousand centuries of climatic record from Camp Century on the Greenland ice sheet". In: *Science* 166.3903, pp. 377–381. DOI: `10.1126/science.166.3903.377`.

Dansgaard, W. (1964). “Stable isotopes in precipitation”. In: *tellus* 16.4, pp. 436–468. DOI: 10.3402/tellusa.v16i4.8993.

Delaygue, G. and Bard, E. (2011). “An Antarctic view of Beryllium-10 and solar activity for the past millennium”. In: *Climate Dynamics* 36.11-12, pp. 2201–2218. DOI: 10.1007/s00382-010-0795-1.

Eicher, O., Baumgartner, M., Schilt, A., Schmitt, J., Schwander, J., Stocker, T. F., and Fischer, H. (2016). “Climatic and insolation control on the high-resolution total air content in the NGRIP ice core”. In: *Climate of the Past* 12.10, pp. 1979–1993. DOI: 10.5194/cp-12-1979-2016.

Eisen, O., Wilhelms, F., Steinhage, D., and Schwander, J. (2006). “Improved method to determine radio-echo sounding reflector depths from ice-core profiles of permittivity and conductivity”. In: *Journal of Glaciology* 52.177, pp. 299–310. DOI: 10.3189/172756506781828674.

Fahnestock, M., Abdalati, W., Joughin, I., Brozena, J., and Gogineni, P. (2001b). “High geothermal heat flow, basal melt, and the origin of rapid ice flow in central Greenland”. In: *Science* 294.5550, pp. 2338–2342. DOI: 10.1126/science.1065370.

Fahnestock, M., Bindschadler, R., Kwok, R., and Jezek, K. (1993). “Greenland Ice Sheet Surface Properties and Ice Dynamics from ERS-1 SAR Imagery”. In: *Science* 262.5139, pp. 1530–1534. DOI: 10.1126/science.262.5139.1530.

Finkel, R. C. and Nishiizumi, K. (1997). “Beryllium 10 concentrations in the Greenland Ice Sheet Project 2 ice core from 3-40 ka”. In: *Journal of Geophysical Research: Oceans* 102.C12, pp. 26699–26706. DOI: 10.1029/97JC01282.

Franke, S., Jansen, D., Binder, T., Paden, J. D., Dörr, N., Gerber, T. A., Miller, H., Dahl-Jensen, D., Helm, V., Steinhage, D., Weikusat, I., Wilhelms, F., and Eisen, O. (2022a). “Airborne ultra-wideband radar sounding over the shear margins and along flow lines at the onset region of the Northeast Greenland Ice Stream”. In: *Earth System Science Data* 14.2, pp. 763–779. DOI: 10.5194/essd-14-763-2022.

Franke, S., Jansen, D., Binder, T., Dörr, N., Helm, V., Paden, J., Steinhage, D., and Eisen, O. (2020). “Bed topography and subglacial landforms in the onset region of the Northeast Greenland Ice Stream”. In: *Annals of Glaciology* 61.81, pp. 143–153. DOI: 10.1017/aog.2020.12.

Fudge, T. J., Lilien, D. A., Koutnik, M., Conway, H., Stevens, C. M., Waddington, E. D., Steig, E. J., Schauer, A. J., and Holschuh, N. (2020). “Advection and non-climate impacts on the South Pole Ice Core”. In: *Climate of the Past* 16.3, pp. 819–832. DOI: 10.5194/cp-16-819-2020.

Fudge, T. J., Steig, E. J., Markle, B. R., Schoenemann, S. W., Ding, Q., Taylor, K. C., McConnell, J. R., Brook, E. J., Sowers, T., White, J. W., Alley, R. B., Cheng, H., Clow, G. D., Cole-Dai, J., Conway, H., Cuffey, K. M., Edwards, J. S., Lawrence Edwards, R., Edwards, R., Fegyveresi, J. M., Ferris, D., Fitzpatrick, J. J., Johnson, J., Hargreaves, G., Lee, J. E., Maselli, O. J., Mason, W., McGwire, K. C., Mitchell, L. E., Mortensen, N., Neff, P., Orsi, A. J., Popp, T. J., Schauer, A. J., Severinghaus, J. P., Sigl, M., Spencer, M. K., Vaughn, B. H., Voigt, D. E., Waddington, E. D., Wang, X., and Wong, G. J. (2013). “Onset of deglacial warming in West Antarctica driven by local orbital forcing”. In: *Nature* 500.7463, pp. 440–444. DOI: 10.1038/nature12376.

Gardner, A. S., Fahnestock, M. A., and Scambos, T. A. (2020). *ITS_LIVE Regional Glacier and Ice Sheet Surface Velocities*. DOI: 10.5067/6II6VW8LLWJ7.

Gogineni, S., Tammana, D., Braaten, D., Leuschen, C., Akins, T., Legarsky, J., Kanagaratnam, P., Stiles, J., Allen, C., and Jezek, K. (2001). “Coherent radar ice thickness measurements over the Greenland ice sheet”. In: *Journal of Geophysical Research: Atmospheres* 106.D24, pp. 33761–33772. DOI: 10.1029/2001JD900183.

Gow, A. J., Ueda, H. T., and Garfield, D. E. (1968). “Antarctic ice sheet: Preliminary results of first core hole to bedrock”. In: *Science* 161.3845, pp. 1011–1013. DOI: 10.1126/science.161.3845.1011.

Greene, C. A., Gwyther, D. E., and Blankenship, D. D. (2017). “Antarctic Mapping Tools for Matlab”. In: *Computers & Geosciences* 104, pp. 151–157. DOI: 10.1016/j.cageo.2016.08.003.

Grinsted, A. and Dahl-Jensen, D. (2002). “A Monte Carlo-tuned model of the flow in the North-GRIP area”. In: *Annals of Glaciology* 35, pp. 527–530. DOI: 10.3189/172756402781817130.

Hammer, C. U. (1980). “Acidity of polar ice cores in relation to absolute dating, past volcanism, and radio–echoes”. In: *Journal of Glaciology* 25.93, pp. 359–372. DOI: 10/hwsm.

Harrison, C. H. (1973). “Radio Echo Sounding of Horizontal Layers in Ice”. In: *Journal of Glaciology* 12.66, pp. 383–397. DOI: 10.3189/s0022143000031804.

Herron, M. M. and Langway, C. C. (1980). “Firn densification: an empirical model.” In: *Journal of Glaciology* 25.93, pp. 373–385. DOI: 10.1017/S0022143000015239.

Holschuh, N., Christianson, K., and Anandakrishnan, S. (2014). “Power loss in dipping internal reflectors, imaged using ice-penetrating radar”. In: *Annals of Glaciology* 55.67, pp. 49–56. DOI: 10.3189/2014AoG67A005.

Holschuh, N., Lilien, D., and Christianson, K. (2019b). “Thermal weakening, convergent flow, and vertical heat transport in the Northeast Greenland Ice Stream shear margins”. In: *Geophysical Research Letters* 46.14, pp. 8184–8193. DOI: 10.1029/2019GL083436.

Hvidberg, C. S., Grinsted, A., Dahl-Jensen, D., Khan, S. A., Kusk, A., Andersen, J. K., Neckel, N., Solgaard, A., Karlsson, N. B., Kjær, H. A., and Vallelonga, P. (2020). “Surface velocity of the Northeast Greenland Ice Stream (NEGIS): assessment of interior velocities derived from satellite data by GPS”. In: *The Cryosphere* 14.10, pp. 3487–3502. DOI: 10.5194/tc-14-3487-2020.

Hvidberg, C. S., Keller, K., Gundestrup, N. S., Tscherning, C. C., and Forsberg, R. (1997). “Mass balance and surface movement of the Greenland ice sheet at summit, Central Greenland”. In: *Geophysical Research Letters* 24.18, pp. 2307–2310. DOI: 10.1029/97GL02280.

Jacobel, R. W., Gades, A. M., Gottschling, D. L., Hodge, S. M., and Wright, D. L. (1993). “Interpretation of radar-detected internal layer folding in West Antarctic ice streams”. In: *Journal of Glaciology* 39.133, pp. 528–537. DOI: 10.3189/S0022143000016427.

Johnsen, S. J., Clausen, H. B., Dansgaard, W., Fuhrer, K., Gundestrup, N., Hammer, C. U., Iversen, P., Jouzel, J., Stauffer, B., and Steffensen, J. P. (1992). “Irregular glacial interstadials recorded in a new Greenland ice core”. In: *Nature* 359.6393, pp. 311–313. DOI: 10.1038/359311a0.

Joughin, I., Fahnestock, M., MacAyeal, D., Bamber, J. L., and Gogineni, P. (2001). “Observation and analysis of ice flow in the largest Greenland ice stream”. In: *Journal of Geophysical Research: Atmospheres* 106.D24, pp. 34021–34034. DOI: 10.1029/2001JD900087.

Joughin, I., Smith, B. E., and Howat, I. M. (2018). “A complete map of Greenland ice velocity derived from satellite data collected over 20 years”. In: *Journal of Glaciology* 64.243, pp. 1–11. DOI: 10.1017/jog.2017.73.

Jouzel, J., Alley, R. B., Cuffey, K. M., Dansgaard, W., Grootes, P., Hoffmann, G., Johnsen, S. J., Koster, R. D., Peel, D., Shuman, C. A., Stievenard, M., Stuiver, M., and White, J. (1997). “Validity of the temperature reconstruction from water isotopes in ice cores”. In: *Journal of Geophysical Research: Oceans* 102.C12, pp. 26471–26487. DOI: 10.1029/97JC01283.

Keisling, B. A., Christianson, K., Alley, R. B., Peters, L. E., Christian, J. E., Anandakrishnan, S., Riverman, K. L., Muto, A., and Jacobel, R. W. (2014). “Basal conditions and ice dynamics inferred from radar-derived internal stratigraphy of the northeast Greenland ice stream”. In: *Annals of Glaciology* 55.67, pp. 127–137. DOI: 10.3189/2014AoG67A090.

Khan, S. A., Kjær, K. H., Bevis, M., Bamber, J. L., Wahr, J., Kjeldsen, K. K., Bjørk, A. A., Korsgaard, N. J., Stearns, L. A., Van Den Broeke, M. R., Liu, L., Larsen, N. K., and Muresan,

I. S. (2014). “Sustained mass loss of the northeast Greenland ice sheet triggered by regional warming”. In: *Nature Climate Change* 4.4, pp. 292–299. DOI: `10.1038/nclimate2161`.

Lawver, L. A. and Müller, R. D. (1994). “Iceland hotspot track”. In: *Geology* 22.4, pp. 311–314. DOI: `10.1130/0091-7613(1994)022<0311:IHT>2.3.CO;2`.

Letréguilly, A., Reeh, N., and Huybrechts, P. (1991). “The Greenland ice sheet through the last glacial-interglacial cycle”. In: *Palaeogeography, Palaeoclimatology, Palaeoecology* 90.4, pp. 385–394. DOI: `10.1016/S0031-0182(12)80037-X`.

Leysinger Vieli, G. J., Martín, C., Hindmarsh, R. C., and Lüthi, M. P. (2018). “Basal freeze-on generates complex ice-sheet stratigraphy”. In: *Nature Communications* 9.1, pp. 1–13. DOI: `10.1038/s41467-018-07083-3`.

Lorius, C., Jouzel, J., Ritz, C., Merlivat, L., Barkov, N. I., Korotkevich, Y. S., and Kotlyakov, V. M. (1985). “A 150,000-year climatic record from Antarctic ice”. In: *Nature* 316.6029, pp. 591–596. DOI: `10.1038/316591a0`.

MacGregor, J. A., Fahnestock, M. A., Catania, G. A., Paden, J. D., Gogineni, S. P., Young, S. K., Rybarski, S. C., Mabrey, A. N., Wagman, B. M., and Morlighem, M. (2015). “Radiostratigraphy and age structure of the Greenland Ice Sheet”. In: *Journal of Geophysical Research: Earth Surface* 120.2, pp. 212–241. DOI: `10.1002/2014JF003215`.

MacGregor, J. A., Fahnestock, M. A., Catania, G. A., Aschwanden, A., Clow, G. D., Colgan, W. T., Gogineni, S. P., Morlighem, M., Nowicki, S. M. J., Paden, J. D., Price, S. F., and Seroussi, H. (2016). “A synthesis of the basal thermal state of the Greenland Ice Sheet”. In: *Journal of Geophysical Research: Earth Surface* 121.7, pp. 1328–1350. DOI: `10.1002/2015JF003803`.

Marcott, S. A., Bauska, T. K., Buizert, C., Steig, E. J., Rosen, J. L., Cuffey, K. M., Fudge, T. J., Severinghaus, J. P., Ahn, J., Kalk, M. L., McConnell, J. R., Sowers, T., Taylor, K. C., White, J. W., and Brook, E. J. (2014). “Centennial-scale changes in the global carbon cycle during the last deglaciation”. In: *Nature* 514.7524, pp. 616–619. DOI: `10.1038/nature13799`.

Marshall, S. J. and Cuffey, K. M. (2000). “Peregrinations of the Greenland Ice Sheet divide in the last glacial cycle: Implications for central Greenland ice cores”. In: *Earth and Planetary Science Letters* 179.1, pp. 73–90. DOI: `10.1016/S0012-821X(00)00108-4`.

Meese, D. A., Gow, A. J., Alley, R. B., Zielinski, G. A., Grootes, P. M., Ram, M., Taylor, K. C., Mayewski, P. A., and Bolzan, J. F. (1997). “The Greenland Ice Sheet Project 2 depth-age scale: Methods and results”. In: *Journal of Geophysical Research: Oceans* 102.C12, pp. 26411–26423. DOI: `10.1029/97JC00269`.

Metropolis, N., Rosenbluth, A. W., Rosenbluth, M. N., Teller, A. H., and Teller, E. (1953). “Equation of state calculations by fast computing machines”. In: *The Journal of Chemical Physics* 21.6, pp. 1087–1092. DOI: `10.1063/1.1699114`.

Millar, D. (1982). “Acidity levels in ice sheets from radio echo-sounding”. In: *Annals of Glaciology* 3, pp. 199–203. DOI: `10.3189/S0260305500002779`.

Mojtabavi, S., Wilhelms, F., Cook, E., Davies, S., Sinnl, G., Skov Jensen, M., Dahl-Jensen, D., Svensson, A., Vinther, B., Kipfstuhl, S., Jones, G., Karlsson, N., Faria, S. H., Gkinis, V., Kjær, H., Erhardt, T., Berben, S., Nisancioglu, K., Koldtoft, I., and Rasmussen, S. O. (2020b). “A first chronology for the East GReenland Ice-core Project (EGRIP) over the Holocene and last glacial termination”. In: *Climate of the Past* 16.6, pp. 2359–2380. DOI: `10.5194/cp-2019-143`.

Morlighem, M., Williams, C. N., Rignot, E., An, L., Arndt, J. E., Bamber, J. L., Catania, G., Chauché, N., Dowdeswell, J. A., Dorschel, B., Fenty, I., Hogan, K., Howat, I., Hubbard, A., Jakobsson, M., Jordan, T. M., Kjeldsen, K. K., Millan, R., Mayer, L., Mouginot, J., Noël, B. P. Y., O'Cofaigh, C., Palmer, S., Rysgaard, S., Seroussi, H., Siegert, M. J., Slabon, P., Straneo, F., Broeke, M. R. van den, Weinrebe, W., Wood, M., and Zinglersen, K. B. (2017). “BedMachine v3: Complete Bed Topography and Ocean Bathymetry Mapping of Greenland From Multibeam Echo Sounding Combined With Mass Conservation”. In: *Geophysical Research Letters* 44.21, pp. 11, 051–11, 061. DOI: `10.1002/2017GL074954`.

Mosegaard, K. and Tarantola, A. (1995). “Monte Carlo sampling of solutions to inverse problems”. In: *Journal of Geophysical Research* 100.B7, pp. 12431–12447. DOI: 10.1029/94jb03097.

Mosegaard, K. (1998). “Resolution analysis of general inverse problems through inverse Monte Carlo sampling”. In: *Inverse problems* 14.3, p. 405. DOI: 10.1088/0266-5611/14/3/004.

Mottram, R., B. Simonsen, S., Høyer Svendsen, S., Barletta, V. R., Sandberg Sørensen, L., Nagler, T., Wuite, J., Groh, A., Horwath, M., Rosier, J., Solgaard, A., Hvidberg, C. S., and Forsberg, R. (2019). “An Integrated View of Greenland Ice Sheet Mass Changes Based on Models and Satellite Observations”. In: *Remote Sensing* 11.12. DOI: 10.3390/rs11121407.

NEEM Community members et al. (2013). “Eemian interglacial reconstructed from a Greenland folded ice core”. In: *Nature* 493.7433, pp. 489–494. DOI: 10.1038/nature11789.

Paren, J. and Robin, G. d. Q. (1975). “Internal reflections in polar ice sheets”. In: *Journal of Glaciology* 14.71, pp. 251–259. DOI: 10.3189/S0022143000021730.

Parrenin, F., Barnola, J. M., Beer, J., Blunier, T., Castellano, E., Chappellaz, J., Dreyfus, G., Fischer, H., Fujita, S., Jouzel, J., Kawamura, K., Lemieux-Dudon, B., Loulergue, L., Masson-Delmotte, V., Narcisi, B., Petit, J. R., Raisbeck, G., Raynaud, D., Ruth, U., Schwander, J., Severi, M., Spahni, R., Steffensen, J. P., Svensson, A., Udisti, R., Waelbroeck, C., and Wolff, E. (2007). “The EDC3 chronology for the EPICA Dome C ice core”. In: *Climate of the Past* 3.3, pp. 485–497. DOI: 10.5194/cp-3-485-2007.

Petit, J. R., Raynaud, D., Basile, I., Chappellaz, J., Davisk, M., Ritz, C., Delmotte, M., Legrand, M., Lorius, C., Pe, L., and Saltzmank, E. (1999). “Climate and atmospheric history of the past 420,000 years from the Vostok ice core , Antarctica”. In: *Nature* 399, pp. 429–436. DOI: 10.1038/20859.

Porter, C., Morin, P., Howat, I., Noh, M. J., Bates, B., Peterman, K., Keesey, S., Schlenk, M., Gardiner, J., and Tomko, K. (2018). “ArcticDEM”. In: *Harvard Dataverse* 1.

Raisbeck, G., Yiou, F., Jouzel, J., and Stocker, T. (2007). “Direct north-south synchronization of abrupt climate change record in ice cores using Beryllium 10”. In: *Climate of the Past* 3.3, pp. 541–547. DOI: 10.5194/cp-3-541-2007.

Rasmussen, S. O., Abbott, P. M., Blunier, T., Bourne, A. J., Brook, E., Buchardt, S. L., Buizert, C., Chappellaz, J., Clausen, H. B., Cook, E., Dahl-Jensen, D., Davies, S. M., Guillevic, M., Kipfstuhl, S., Laepple, T., Seierstad, I. K., Severinghaus, J. P., Steffensen, J. P., Stowasser, C., Svensson, A., Vallelonga, P., Vinther, B. M., Wilhelms, F., and Winstrup, M. (2013). “A first chronology for the North Greenland Eemian Ice Drilling (NEEM) ice core”. In: *Climate of the Past* 9.6, pp. 2713–2730. DOI: 10.5194/cp-9-2713-2013.

Rasmussen, S. O., Andersen, K. K., Svensson, A. M., Steffensen, J. P., Vinther, B. M., Clausen, H. B., Siggaard-Andersen, M. L., Johnsen, S. J., Larsen, L. B., Dahl-Jensen, D., Bigler, M., Röthlisberger, R., Fischer, H., Goto-Azuma, K., Hansson, M. E., and Ruth, U. (2006). “A new Greenland ice core chronology for the last glacial termination”. In: *Journal of Geophysical Research: Atmospheres* 111.6, pp. 1–16. DOI: 10.1029/2005JD006079.

Rasmussen, S., Seierstad, I., Andersen, K. K., Bigler, M., Dahl-Jensen, D., and Johnsen, S. (2008). “Synchronization of the NGRIP, GRIP, and GISP2 ice cores across MIS 2 and palaeoclimatic implications”. In: *Quaternary Science Reviews* 27.1-2, pp. 18–28. DOI: 10.1016/j.quascirev.2007.01.016.

Rasmussen, S. O., Bigler, M., Blockley, S. P., Blunier, T., Buchardt, S. L., Clausen, H. B., Cvijanovic, I., Dahl-Jensen, D., Johnsen, S. J., Fischer, H., Gkinis, V., Guillevic, M., Hoek, W. Z., Lowe, J. J., Pedro, J. B., Popp, T., Seierstad, I. K., Steffensen, J. P., Svensson, A. M., Vallelonga, P., Vinther, B. M., Walker, M. J., Wheatley, J. J., and Winstrup, M. (2014). “A stratigraphic framework for abrupt climatic changes during the Last Glacial period based on three synchronized Greenland ice-core records: refining and extending the INTIMATE event stratigraphy". In: *Quaternary Science Reviews* 106. Dating, Synthesis, and Interpretation of Palaeoclimatic Records and Model-data Integration: Advances of the INTIMATE project (INTegration of Ice core, Marine and TErrestrial records, COST Action ES0907), pp. 14–28. DOI: 10.1016/j.quascirev.2014.09.007.

Raynaud, D., Chappellaz, J., Ritz, C., and Martinerie, P. (1997). "Air content along the Greenland Ice Core Project core: A record of surface climatic parameters and elevation in central Greenland". In: *Journal of Geophysical Research: Oceans* 102.C12, pp. 26607–26613. DOI: 10.1029/97JC01908.

Rignot, E. and Mouginot, J. (2012). "Ice flow in Greenland for the international polar year 2008–2009". In: *Geophysical Research Letters* 39.11, pp. 1–7. DOI: 10.1029/2012GL051634.

Riverman, K. L., Alley, R. B., Anandakrishnan, S., Christianson, K., Holschuh, N. D., Medley, B., Muto, A., and Peters, L. E. (2019). "Enhanced Firn Densification in High-Accumulation Shear Margins of the NE Greenland Ice Stream". In: *Journal of Geophysical Research: Earth Surface* 124.2, pp. 365–382. DOI: 10.1029/2017JF004604.

Robin, G. d. Q., Evans, S., and Bailey, J. T. (1969). "Interpretation of radio echo sounding in polar ice sheets". In: *Philosophical Transactions of the Royal Society of London. Series A, Mathematical and Physical Sciences* 265.1166, pp. 437–505. DOI: 10.1098/rsta.1969.0063.

Robin, G. d. Q. and Millar, D. H. M. (1982). "Flow Of Ice Sheets In The Vicinity Of Subglacial Peaks". In: *Annals of Glaciology* 3, pp. 290–294. DOI: 10.3189/s0260305500002949.

Salamatin, A. N., Lipenkov, V. Y., Barkov, N. I., Jouzel, J., Petit, J. R., and Raynaud, D. (1998). "Ice core age dating and paleothermometer calibration based on isotope and temperature profiles from deep boreholes at Vostok Station (East Antarctica)". In: *Journal of Geophysical Research: Atmospheres* 103.D8, pp. 8963–8977. DOI: 10.1029/97JD02253.

Seierstad, I. K., Abbott, P. M., Bigler, M., Blunier, T., Bourne, A. J., Brook, E., Buchardt, S. L., Buizert, C., Clausen, H. B., Cook, E., Dahl-Jensen, D., Davies, S. M., Guillevic, M., Johnsen, S. J., Pedersen, D. S., Popp, T. J., Rasmussen, S. O., Severinghaus, J. P., Svensson, A., and Vinther, B. M. (2014). "Consistently dated records from the Greenland GRIP, GISP2 and NGRIP ice cores for the past 104ka reveal regional millennial-scale δ18O gradients with possible Heinrich event imprint". In: *Quaternary Science Reviews* 106, pp. 29–46. DOI: 10.1016/j.quascirev.2014.10.032.

Simonsen, S. B. and Sørensen, L. S. (2017). "Implications of changing scattering properties on Greenland ice sheet volume change from Cryosat-2 altimetry". In: *Remote Sensing of Environment* 190, pp. 207–216. DOI: 10.1016/j.rse.2016.12.012.

Smith-Johnsen, S., Schlegel, N. J., Fleurian, B. de, and Nisancioglu, K. H. (2020a). "Sensitivity of the Northeast Greenland Ice Stream to Geothermal Heat". In: *Journal of Geophysical Research: Earth Surface* 125.1, pp. 1–14. DOI: 10.1029/2019JF005252.

Smith-Johnsen, S., De Fleurian, B., Schlegel, N., Seroussi, H., and Nisancioglu, K. (2020b). "Exceptionally high heat flux needed to sustain the Northeast Greenland Ice Stream". In: *The Cryosphere* 14.3, pp. 841–854. DOI: 10.5194/tc-14-841-2020.

Svensson, A., Andersen, K. K., Bigler, M., Clausen, H. B., Dahl-Jensen, D., Davies, S. M., Johnsen, S. J., Muscheler, R., Parrenin, F., Rasmussen, S. O., Röthlisberger, R., Seierstad, I., Steffensen, J. P., and Vinther, B. M. (2008). "A 60 000 year Greenland stratigraphic ice core chronology". In: *Climate of the Past* 4.1, pp. 47–57. DOI: 10.5194/cp-4-47-2008.

Svensson, A., Andersen, K. K., Bigler, M., Clausen, H. B., Dahl-Jensen, D., Davies, S. M., Johnsen, S. J., Muscheler, R., Rasmussen, S. O., Röthlisberger, R., Peder Steffensen, J., and Vinther, B. (2006). "The Greenland ice core chronology 2005, 15–42 ka. Part 2: comparison to other records". In: *Quaternary Science Reviews* 25.23-24, pp. 3258–3267. DOI: 10.1029/2005JD006079.

Vallelonga, P., Christianson, K., Alley, R. B., Anandakrishnan, S., Christian, J. E. M., Dahl-Jensen, D., Gkinis, V., Holme, C., Jacobel, R. W., Karlsson, N. B., Keisling, B. A., Kipfstuhl, S., Kjær, H. A., Kristensen, M. E. L., Muto, A., Peters, L. E., Popp, T., Riverman, K. L., Svensson, A. M., Tibuleac, C., Vinther, B. M., Weng, Y., and Winstrup, M. (2014). "Initial results from geophysical surveys and shallow coring of the Northeast Greenland Ice Stream (NEGIS)". In: *The Cryosphere* 8.4, pp. 1275–1287. DOI: `10.5194/tc-8-1275-2014`.

Vinther, B. M., Clausen, H. B., Johnsen, S. J., Rasmussen, S. O., Andersen, K. K., Buchardt, S. L., Dahl-Jensen, D., Seierstad, I. K., Siggaard-Andersen, M.-L., Steffensen, J. P., Svensson, A., Olsen, J., and Heinemeier, J. (2006). "A synchronized dating of three Greenland ice cores throughout the Holocene". In: *Journal of Geophysical Research: Atmospheres* 111.D13. DOI: `10.1029/2005JD006921`.

Vinther, B., Buchardt, S., Clausen, H., Dahl-Jensen, D., Johnsen, S., Fisher, D., Koerner, R., Raynaud, D., Lipenkov, V., Andersen, K. K., Blunier, T., Rasmussen, S. O., Steffensen, J. P., and Svensson, A. M. (2009). "Holocene thinning of the Greenland ice sheet". In: *Nature* 461.7262, pp. 385–388. DOI: `10.1038/nature08355`.

Waddington, E. D., Neumann, T. A., Koutnik, M. R., Marshall, H. P., and Morse, D. L. (2007). "Inference of accumulation-rate patterns from deep layers in glaciers and ice sheets". In: *Journal of Glaciology* 53.183, pp. 694–712. DOI: `10.3189/002214307784409351`.

Walker, M., Johnes, S., Rasmussen, S. O., Popp, T., Steffensen, J.-P., Gibbard, P., Hoek, W., Lowe, J., Andrews, J., Björck, S., Cwynar, L. C., Hughen, K., Kershaw, P., Kromer, B., Litt, T., Lowe, D. J., Nakagawa, T., Newnham, R., and Schwander, J. (2009). "Formal definition and dating of the GSSP (Global Stratotype Section and Point) for the base of the Holocene using the Greenland NGRIP ice core, and selected auxiliary records". In: *Journal of Quaternary Science* 24.1, pp. 3–17. DOI: `10.1002/jqs`.

Weertman, J. (1976). "Sliding–no sliding zone effect and age determination of ice cores". In: *Quaternary Research* 6.2, pp. 203–207. DOI: `10.1016/0033-5894(76)90050-8`.

Whillans, I. M. (1976). "Radio-echo layers and the recent stability of the West Antarctic ice sheet". In: *Nature* 264.5582, pp. 152–155. DOI: `10.1038/264152a0`.

Whillans, I. M. and Johnsen, S. J. (1983). "Longitudinal variations in glacial flow: theory and test using data from the Byrd Station strain network, Antarctica." In: *Journal of Glaciology* 29.101, pp. 78–97. DOI: `10.1017/S0022143000005165`.

Wolovick, M. J., Creyts, T. T., Buck, W. R., and Bell, R. E. (2014). "Traveling slippery patches produce thickness-scale folds in ice sheets". In: *Geophysical Research Letters* 41.24, pp. 8895–8901. DOI: `10.1002/2014GL062248`.

Yiou, F., Raisbeck, G. M., Baumgartner, S., Beer, J., Hammer, C., Johnsen, S., Jouzel, J., Kubik, P. W., Lestringuez, J., Stiévenard, M., Suter, M., and Yiou, P. (1997). "Beryllium 10 in the Greenland Ice Core Project ice core at Summit, Greenland". In: *Journal of Geophysical Research: Oceans* 102.C12, pp. 26783–26794. DOI: `10.1029/97JC01265`.

Zeising, O. and Humbert, A. (2021). "Indication of high basal melting at the EastGRIP drill site on the Northeast Greenland Ice Stream". In: *The Cryosphere* 15.7, pp. 3119–3128. DOI: `10.5194/tc-15-3119-2021`.

Chapter 5

Ice crystal fabric causes directional hardening of the Northeast Greenland Ice Stream

Tamara Annina Gerber[1], David Lilien[2], Nicholas Rathmann[1], Steven Franke[3], Tun Jan Young[4], Fernando Valero-Delgado[3], Reza Ershadi[5], Reinhard Drews[5], Ole Zeising[3], Angelika Humbert[3,6], Nicolas Stoll[3], Aslak Grinsted[1], Christine Hvidberg[1], Daniela Jansen[3], Heinrich Miller[3], Veit Helm[3], Daniel Steinhage[3], Charles O'Neill[7], John Paden[8], Prasad Gogineni[7], Dorthe Dahl-Jensen[1,2], and Olaf Eisen[3,6]

[1] *Section for the Physics of Ice, Climate and Earth, Niels Bohr Institute, University of Copenhagen, Copenhagen, Denmark*
[2] *Center for Earth Observation Science, University of Manitoba, Winnipeg, Canada*
[3] *Alfred Wegener Institute, Helmholtz Center for Polar and Marine Research, Bremerhaven, Germany*
[4] *Scott Polar Research Institute, University of Cambridge, Cambridge, United Kingdom*
[5] *Department of Geosciences, Tübingen University, Tübingen, Germany*
[6] *Department of Geosciences, University of Bremen, Bremen, Germany*
[7] *Remote Sensing Center, University of Alabama, Tuscaloosa, USA*
[8] *Center for Remote Sensing of Ice Sheets (CReSIS), University of Kansas, Lawrence, USA*

Ice streams are prominent dynamic features in ice sheets that transport large amounts of ice from the interior to the ocean. Their future behavior constitutes one of the biggest uncertainties in projections of sea-level rise. One central understudied property regarding ice flow is the anisotropy of the ice fabric, i.e. the bulk orientation of ice crystals' lattice. Strong fabric anisotropy is known to affect the effective viscosity of ice, but has not yet been quantified over large areas in key regions of ice sheets, such as ice streams. Here, we present a comprehensive analysis of the depth-averaged distribution of ice fabric in the upstream part of the North-East Greenland Ice Stream (NEGIS). Our results are based on a combination of methods applied to extensive airborne and ground-based radar surveys, ice- and firn-core observations, and numerical ice-flow modeling. They show a strong spatial variability of the horizontal fabric anisotropy and a rapid crystal reorganization related to the ice-stream geometry. Our findings indicate that the fabric anisotropy causes the ice inside the ice stream to be harder for pure shear in along-flow direction by approximately one order of magnitude compared to isotropic ice.

5.1 Introduction

The molecular orientation of the crystals that comprise glacier ice exerts an important physical control over its bulk mechanical properties and the enhancement of ice flow (Duval et al., 1983; Budd and Jacka, 1989). In the absence of strain, the crystal orientation fabric (COF), or simply *fabric*, of snow and ice tends to be close to isotropic, so the c-axes point in random directions. In many places of ice sheets, however, deformation causes an apparent rotation of c-axes towards the direction of dominant compression (Gow and Williamson, 1976; Faria et al., 2014). In other words, anisotropic crystal fabrics reflect past ice deformation while simultaneously affecting the present-day mechanical properties.

Most state-of-the-art large-scale ice-flow models either ignore the mechanical anisotropy of ice entirely (e.g. Winkelmann et al., 2011), or infer an isotropic enhancement factor that subsumes some effect of anisotropy (Rathmann and Lilien, 2021; Ranganathan et al., 2021). Such enhancement factors are often tuned as model parameters or based on experimental values. In both cases, a thorough understanding of the spatial and temporal variation of the fabric anisotropy is missing (e.g. Graham et al., 2018). While this might be of minor relevance in slow-moving parts of ice sheets, major discrepancies between modeled and observed surface velocities exist in highly dynamic areas such as ice streams (e.g. Aschwanden et al., 2016; Albrecht et al., 2020). Anisotropy could be one of the reasons for these discrepancies, as it affects the ice viscosity and potentially also basal sliding obtained by inversion methods (Rückamp et al., 2022).

Ice streams are the primary source of dynamic ice mass loss and are hence of great importance in the dynamics and stability of ice sheets (e.g. Bennett, 2003; Mouginot et al., 2019). Accordingly, it is crucial to accurately reproduce ice streams in prognostic ice-sheet models to reduce uncertainties in estimates of future ice-sheet evolution and sea-level rise. In regions of fast flow with lateral compression and extension through flow acceleration, the development of strong, spatially variable fabrics is expected and might facilitate streaming ice (Lilien et al., 2021). A number of models capable of simulating fabric evolution or its effects on ice flow (e.g. Thorsteinsson, 2002; Gillet-Chaulet et al., 2006), as well as combining these two mechanisms (Martín et al., 2009), were developed decades ago. However, both the application of these models to ice streams, as well as in-situ observations of the COF, are still rare.

Direct observations of COFs in ice cores are limited by being point measurements and by the uncertain orientation of the core. Furthermore, most deep ice cores are drilled at ice domes or at ice divides, where the ice tends to flow slowly, and fabrics are primarily a result of uniaxial or confined compression (Alley, 1988). These sites are unlikely to represent the fabric in more dynamic areas, such as ice streams and their immediate surrounding where the strain history is more complex.

Radio-Echo-Sounding (RES) surveys are widely used in glaciology for mapping of ice thicknesses, basal properties and internal stratigraphy (e.g. Gogineni et al., 2001; MacGregor et al., 2015; Christianson et al., 2016; Jordan et al., 2018; Schroeder et al., 2020; Franke et al., 2020; Franke et al., 2022a; Bodart et al., 2021). Horizontal anisotropy influences RES signals (e.g. Fujita et al., 2006; Eisen et al., 2007) and techniques have recently been developed to derive information on the horizontal component of the ice-crystal fabric from RES (e.g. Young et al., 2021; Mojtabavi et al., 2022; Ershadi et al., 2022). The uniaxial birefringent property of ice crystals leads to slightly different velocities of radar waves depending on the wave polarization relative to the preferred orientation of the c-axes. In areas where a horizontally anisotropic COF prevails, two different effects are observed in radargrams that can be related to the strength of anisotropy: 1) Interference of wave components traveling at different speeds leads to nodes of increased/decreased radar return power (e.g. Fujita et al., 2006), and 2) travel-time anomalies for waves reflected of the internal layers as the transmitting antenna polarization is changed (Mojtabavi et al., 2022).

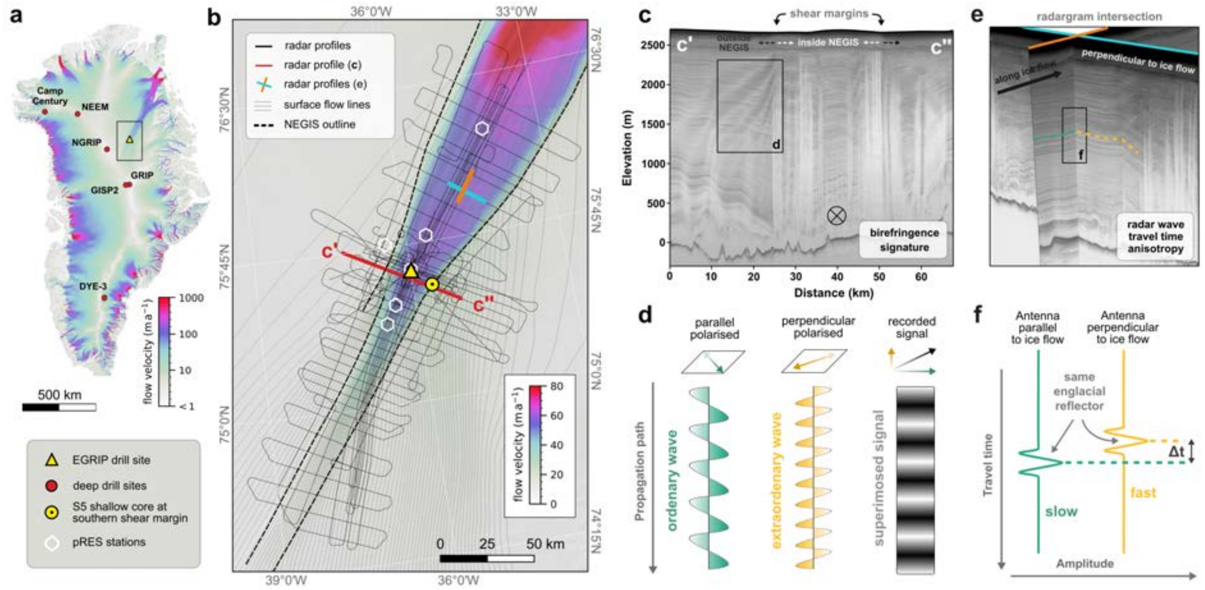

FIGURE 5.1: **a**) Surface ice-flow velocities of the Greenland ice sheet (Joughin et al., 2018) with the locations of deep ice-core drill sites and the outline of the study area. **b**) NEGIS onset region and collected observations. **c**) Example of an airborne radargram crossing the ice stream near the EastGRIP ice coring site, showing internal birefringence-induced extinction node lines particularly pronounced near the shear margins. As illustrated in panel **d**), the birefringence power extinction nodes arise in horizontally anisotropic ice through interference of two orthogonal radar wave components traveling at slightly different wave speeds (See SI for details). **e**) Two intersecting radar profiles, and **f**) schematic example of travel-time differences of internal reflections.

In this study, we use the characteristic radar signals generated by the orientation of the crystal axes in the ice to characterize the distribution of anisotropy at the onset of the largest ice stream in Greenland, the Northeast Greenland Ice Stream (NEGIS). Using an extensive dataset of different radar measurements and a combination of different methods, we can determine for the first time the distribution of anisotropy on the horizontal plane over a large area. Together with ice-flow modeling and comparison with ice-core observations, we can constrain the mechanical anisotropy and enhancement factors for different deformation types and directions. Our results show a spatially variable fabric anisotropy which considerably affects the ice stiffness in dependence on the deformation mechanism and direction. Our results on the distribution of the mechanical effects of anisotropy on ice flow have not been previously considered in this form in ice flow models and thus represent an important contribution towards improving our understanding and predictions of ice flow on the overall behavior of ice sheets.

5.2 Fabric distribution of the NEGIS onset region

We analyzed the ice crystal fabric related birefringence effects and travel-time anisotropy of radar waves using a composite of different radio-glaciological data sets (Supplementary Information (SI), Section S5.2). Our survey region covers an area of ∼24,000 km^2 and encompasses the fast flowing central part as well as the shear margins of the NEGIS onset region (Fig. 5.1a). The data comprises an extensive airborne ultra-wideband radar survey (Franke et al., 2022b), a ground-based radar profile across the northwestern shear margin near the East GReenland Ice-core Project (EastGRIP) deep ice-core site, as well as phase-sensitive Radio-Echo-Sounding (pRES) measurements at six distinct locations (Fig. 5.1b). By combining these radar data sets we obtain a spatially extensive, high-resolution and robust understanding of the distribution of the depth-averaged anisotropy in the horizontal plane in an active ice stream. For an extended understanding and validation of our methods, we compare these analytical results from radar observations with those obtained from two different fabric-evolution models (Elmer/Ice; see Lilien et al. 2021 and Specfab; see Rathmann et al. 2021). Moreover, we make use of in-situ observations from the EastGRIP ice core at the ice-stream center (Westhoff et al., 2021) as well as from a shallow ice core (S5) retrieved at the southeastern shear margin.

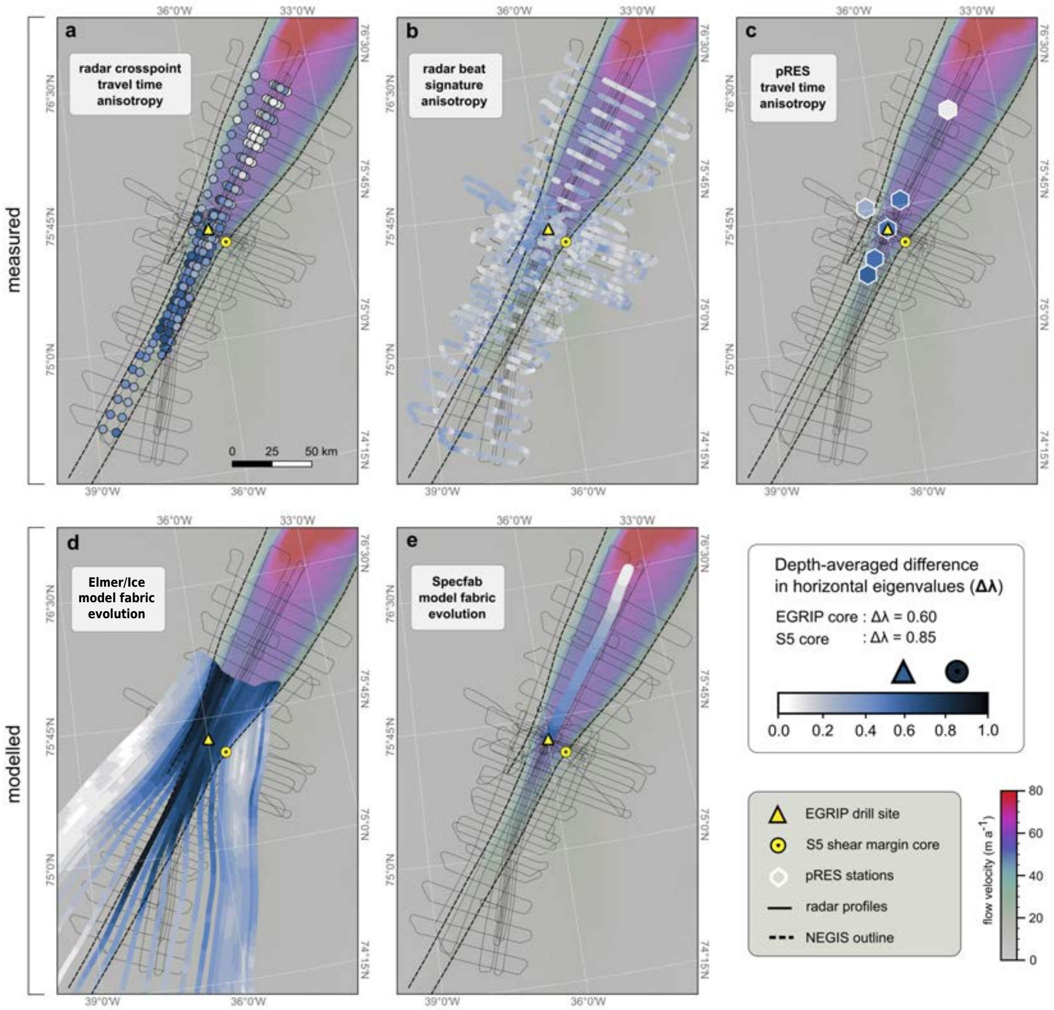

FIGURE 5.2: Depth-averaged difference in horizontal eigenvalues ($\Delta\lambda$) inferred by **a)** radar crosspoint travel-time anisotropy, **b)** radar beat-signature analysis, **c)** pRES travel-time anisotropy, and modeled by a **d)** fabric evolution model implemented in Elmer/Ice, and **e)** specfab fabric evolution model along a flow line initiated at EastGRIP. Both, the travel-time anisotropy as well as beat-signature approach are sensitive to the fabric orientation relative to the antenna orientation and should thus be regarded as lower limits, while the results obtained from pRES and fabric evolution models can be regarded as absolute values.

Our analysis of the radar crosspoint travel times, radar beat signature and pRES travel times (Figs. 5.2a–c) consistently show that the depth-averaged difference of eigenvalues in the horizontal plane ($\Delta\lambda$; from now on referred to as horizontal anisotropy) is generally high in the ice-stream center in the upstream part of the NEGIS, suggesting the development of a fabric with a pronounced horizontal anisotropy. Downstream of EastGRIP where the ice stream widens, the horizontal anisotropy gradually disappears within a distance of ~50 km, indicating a transition into a vertically symmetric fabric configuration. The beat-signature analyses show some weaker results, which are potentially related to the averaging nature of the approach as well as the usage of multispectral radar signals subject to slightly dispersive attenuation. The data gap in the vicinity of the shear zones is a consequence of the strongly folded internal stratigraphy at the shear margins over a width of 5–10 km (Fig. 5.1c). The resulting loss of radar return-power related to steeply inclined layers (Holschuh et al., 2014) prevents us from obtaining robust results in that region. Outside the ice stream, the strongest anisotropic effects are observed near the shear margins, which gradually decrease over distances of less than five ice thicknesses.

The modeling results from Elmer/Ice show the development of vertical girdle ($\Delta\lambda = 0.5–0.7$) in the ice-stream interior (Fig. 5.2d). The strongest modeled horizontal anisotropy is obtained in the northwestern shear margin by a horizontal single maximum with a horizontal anisotropy of $\sim$0.9. The model also suggests an abrupt fabric evolution across the southern shear margin, although the anisotropy there is slightly less pronounced. Because of stability constraints related to high ice flow velocities at the model boundaries, the model domain of Elmer/Ice does not extend farther downstream and does therefore not capture our observations of decreasing horizontal anisotropy downstream. We instead use the Specfab fabric evolution model (Rathmann et al., 2021) to simulate the fabric development for an ice parcel with an EastGRIP-type girdle experiencing the deformation along a downstream flow line. The modeled fabric evolution of this simple experiment shows a gradual decrease of the horizontal anisotropy, as the fabric transitions from a girdle to isotropy (Fig. 5.2e). We notice here, however, that vertical shear is ignored in this simulation, as it cannot be inferred from the surface velocities directly, and that other vertically symmetric fabrics, e.g., single maximum, could develop if this component is non-negligible.

Our modeled (Elmer/Ice) and measured (radar-derived) horizontal anisotropy agrees with the vertical girdle ($\Delta\lambda = 0.6$) observed over large depths in the EastGRIP ice core (Westhoff et al., 2021). Moreover, the results of our radar-based analyses and the Specfab fabric evolution modeling consistently indicate a decreasing horizontal anisotropy in the downstream part of the NEGIS. However, we cannot make a definitive conclusion about the downstream fabric type, since we cannot distinguish between the vertically symmetric variants (i.e. isotropy vs. vertical single maximum). With respect to the shear margins, the Elmer/Ice modeled horizontal anisotropy ($\Delta\lambda = 0.48$) is slightly smaller than observed at the southeastern shear margin in the S5 shallow core ($\Delta\lambda = 0.85$). However, the simulations indicate the development of a horizontal single maximum comparable to the observations in the S5 core in the northwestern shear margin. Due to the limited signal return-power, the fabric distribution within the shear margins cannot be confirmed independently by radar-based analyses. Outside the NEGIS, the pRES measurement indicates a decreasing anisotropy, which agrees with the results from the beat-signature analyses and Elmer/Ice.

Based on the measured and modeled spatial distribution of horizontal anisotropy in the NEGIS onset, we observe that the fabric rapidly adjusts to changing strain-rate regimes, confirming results obtained from fabric-evolution modeling studies (e.g. Lilien et al., 2021; Llorens et al., 2022). A vertical girdle develops inside the NEGIS in the upstream and central part of our survey area, where the ice experiences lateral compression, vertical thinning and along-flow extension. Downstream of EastGRIP, where the ice stream widens, the applied stress relaxes due to a decrease in flow acceleration and compression perpendicular to ice flow. As a consequence the fabric strength diminishes and the c-axes rotate back into vertical symmetry. The exact fabric type remains ambiguous due to the limitations of our methods. Hence, the decrease in horizontal anisotropy can be explained by various vertically symmetric fabrics. The transition time for this change (considering the present-day ice-dynamic configuration) is approximately 800 years. Due to flow acceleration, convergence and horizontal simple shear in the shear margin, the fabric changes from a vertical to a strong horizontal single maximum, as indicated by Elmer/Ice and the S5 core, but not independently confirmed by radar-based observations. While the fabric strength and type can be inferred by a variety of methods applied here, its orientation can only be determined by Elmer/Ice (SI Section S5.3.1). In general, the smallest modeled fabric eigenvector points in the direction of lowest stress, which in most cases is close to the direction of flow. However, horizontal shear causes the rotation of eigenvectors away from the flow lines, which leads to a notable transition of eigenvector orientation in the vicinity of the shear margins.

5.3 Soft ice and hard ice – a question of fabric and strain orientation

The local deformation rate of glacier ice depends on its viscosity structure which is predominantly controlled by temperature and the crystal fabric, although other factors such as grain size distribution, impurities, and water content play a notable but minor role (Kuiper et al., 2020b,a; Fan et al., 2020; Fan et al., 2021). Strong crystal fabrics have long been known to change the directional viscosity of ice by several orders of magnitude compared to isotropic ice (e.g. Shoji and Langway, 1985; Pimienta et al., 1987). However, the influence of COF on the flow behavior on large scales has not yet been investigated on the basis of observations. We therefore evaluate the effect of the fabric-induced directional viscosities over NEGIS by calculating bulk directional enhancement factors (following Rathmann et al. 2021 and Rathmann and Lilien 2021) based on our modeling results and radar observations of fabric anisotropy. The enhancement factors are defined as the longitudinal and shear strain rates with respect to the principal fabric directions, divided by the expected strain-rate magnitude assuming isotropic ice. In this context, an enhancement factor of 1 is, by definition, identical to the viscosity of isotropic ice under otherwise identical conditions (e.g. temperature and impurity content). Enhancement factors below or above 1 imply a decrease or increase in susceptibility towards the corresponding deformation and strain orientation.

The in-situ strain-rate enhancements depend on the alignment between the principal strain direction and fabric orientation (Shoji and Langway, 1985). While the former can partially be estimated from surface velocities, the latter is, however, not possible to infer from direct radar-based observations on large spatial scales. The enhancement factors presented here are therefore calculated assuming the stress tensor is coaxial with the fabric principal frame. In this sense, our method estimates the *eigenenhancements*, understood as the maximal effect that fabric anisotropy can have on flow under favorable conditions where the stress tensor is aligned with fabric (i.e. an upper-bound estimate). While this is likely true for both the ice-stream interior and outside, considerable stress–fabric misalignment is expected and modeled in the shear margins (SI Fig. S5.11). Notice that the term 'along-flow' thus represents the direction of the smallest horizontal eigenvalue, which in most places is close to the true flow direction with exception of the shear margins and their vicinity.

Our calculations on flow enhancement can only reproduce COF induced hardening or softening of the material, but not account for other factors influencing the viscosity, such as the pile up of dislocations (Eshelby et al., 1951). Our measurements only provide information about the horizontal anisotropy, however we require a full fabric description of the second and fourth or structure tensors for the calculation of the enhancement factors (Rathmann et al., 2021). Therefore, we use assumptions for the missing anisotropy components that are based on the Elmer/Ice modeling results and on the information from the EastGRIP and S5 ice cores (SI Section S5.4).

We propose that, with respect to pure shear along-flow deformation, the ice inside NEGIS is one order of magnitude harder as compared to isotropic ice and around three times harder as the ice outside the ice stream. We base this claim on the fact that inside of the ice stream, the enhancement factors for along-flow compression/extension (pure shear) are generally small (0.1–0.2), both in the calculation based on radar measurements (cross-point and beat frequency) and for the modeling with Elmer/Ice (Fig. 5.3a–c). The values for the flow enhancement based on the radar data are slightly lower in the upstream part as compared to the downstream part. Moreover, the enhancement derived from the beat frequency analysis shows much lower values inside the ice stream (0.1–0.2) as outside (~ 0.5), which lies in good agreement with the Elmer/Ice modeling (Figure 5.3b,c). Our observations are in line with Llorens et al. (2016), who show in their simulations that differential stress grows during pure shear deformation of ice, leading to ice stiffening.

The horizontal anisotropy makes the ice slightly harder for horizontal shear along flow outside the ice stream, but significantly softer inside the ice stream. This effect is found to be stronger in the modeled results compared to the radar observations (Fig. 5.3d–f). In addition both radar measurement-based flow enhancement suggests that the ice upstream of EastGRIP is easier to shear horizontally as downstream of EastGRIP (Fig. 5.3d,e). The strongest evolution from low to high enhancement factors are obtained in the shear margins by Elmer/Ice, confirming the assumption that the shear margins of NEGIS are soft when subject to horizontal shear deformation. The modeled fabric orientation near the shear margins does not align with the ice-flow direction, so the horizontal shear enhancement along the flow-direction (flowframe) and in the direction of the fabric axes (eigenframe) is considerably different (SI Section S5.4). Due to missing direct observations of the c-axis orientation in the shear margins it remains unclear what role the fabric in the shear margins plays in terms of constraining the ice stream and/or facilitating rapid ice flow. We also emphasize that in the downstream part of the survey area, our results are biased by the ambiguities related to vertical fabric symmetry. The enhancements shown in Fig. 5.3 are based on assumptions that result in a vertical single maximum at the downstream end, but that they would look differently in case of isotropy or other vertically symmetric fabrics, which can, however, not be determined without further investigations.

To illustrate the significance and magnitude of the flow enhancement on deformation, we compare it to the influence that temperature would have on viscosity, by calculating temperature-dependent enhancements for isotropic ice (SI Section S5.4.3). We find that a similar along-flow stiffness for pure shear (E_{xx}) cannot realistically be achieved through temperature anomalies, as it would require the ice stream being approximately 30°C colder than the surrounding ice. The along-flow stiffness also prevails outside the shear margins, albeit less pronounced. Assuming that the surrounding ice has an average temperature of –20°C, a shear enhancement factor of two could be obtained by a temperature anomaly of 6.6°C across the shear margins. This estimate is in line with the results of Holschuh et al. (2019a), who used a 3D-thermomechanical model and showed that temperature anomalies of up to 6°C are plausible in the NEGIS shear margins. This suggest that fabric anisotropy and temperature might be equally important for shear margin softening.

5.4 Anisotropy matters – implications for ice-stream sensitivity

Our results suggest that the adjustment of ice crystal axes in response to ice flow is probably the only ice-dynamic process that can evolve to mechanically soften or harden ice. The evolution of the fabric type, flow enhancement, and thus, the effect on the viscosity depends on the deformation type and direction (Fig. 5.4). While ice tends to be harder to deform along ice flow in terms of pure shear, it becomes softer for horizontal simple shear inside NEGIS as well as in the shear margins. We show that the effect of anisotropy on the mechanical processes in the ice plays a comparably important role as ice temperature. This highlights the so far mostly neglected but fundamental importance of considering COF anisotropy for ice-flow modeling towards a more realistic prediction of ice discharge from ice streams and thus, an improved prediction of future sea-level rise.

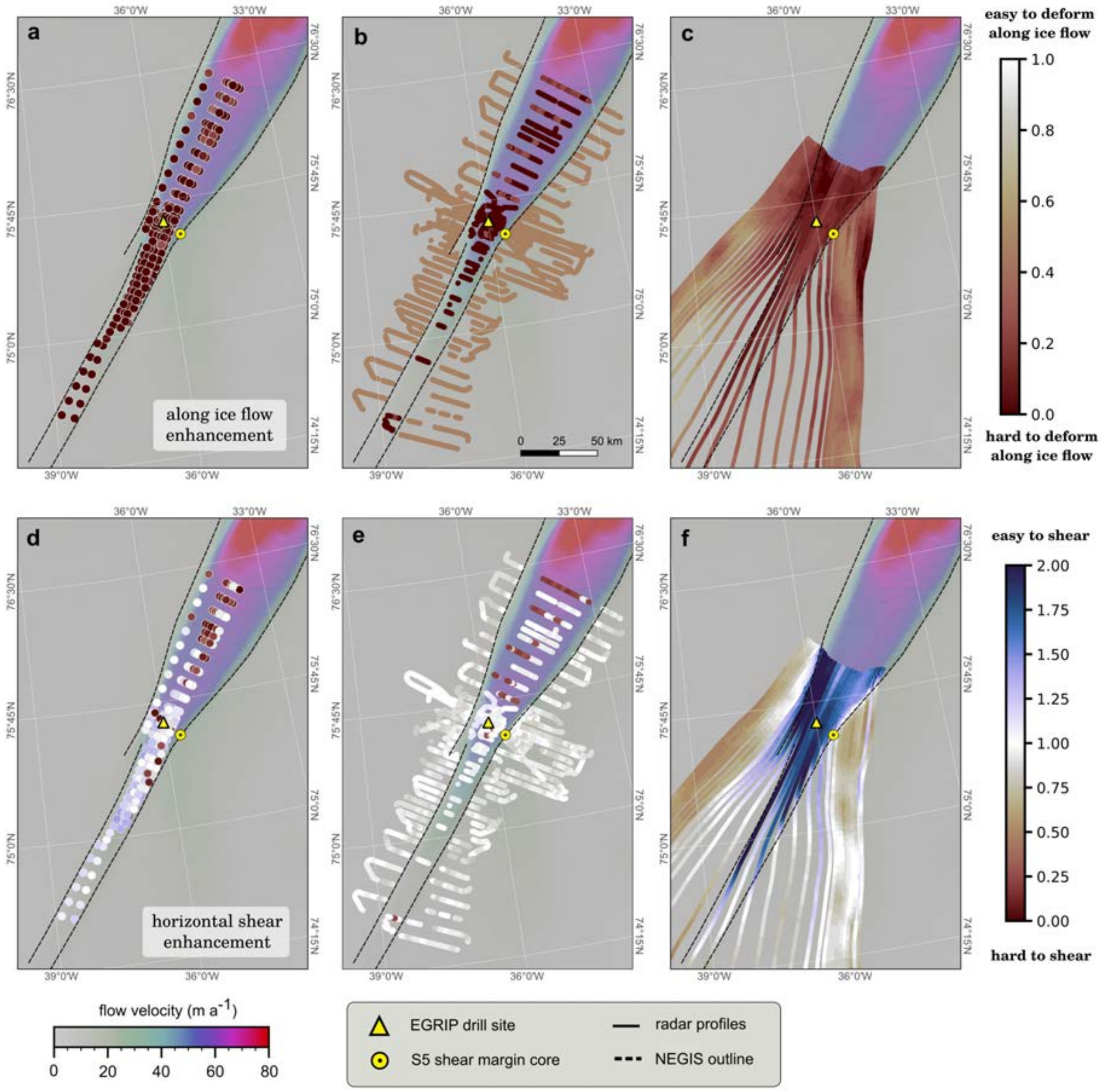

FIGURE 5.3: Flow enhancement factors for along-flow pure-shear compression/extension (E_{xx}, **a–c**) and horizontal shear deformation (E_{xy}, **d–f**). Both, compressional/extensional and shear enhancement factors are calculated from the fabric results obtained from travel-time anisotropy (**a, d**), beat-signature analysis (**b, e**), and Elmer/Ice flow modeling (**c, f**). Note that the enhancement factors displayed in this figure are calculated in the eigenframe (fabric coordinate system), since the true orientation relative to the flow direction is only known from the fabric-evolution model. The term 'along-flow' thus represents the direction of the smallest horizontal eigenvalue, which in most places is close to the true flow direction with exception of the shear margins and their vicinity (see SI for further details).

Numerous observations prove that calving events can rapidly increase ice-flow velocities far inland (e.g. Nettles et al., 2008; Rignot et al., 2004), and in particular in ice streams with low basal friction (e.g. Thomas, 2004). Such and similar perturbations at the glacier front or at the bed, propagate upstream through geometrical changes in the flow field or through direct transmission of membrane stresses (i.e. longitudinal stresses). Williams et al. (2012) found that disturbances on decadal or subdecadal forcing periods propagate upstream through processes dominated by pure shear and that the decay length of the perturbations is longer for ice of higher viscosity. A simple calculation of the characteristic time for viscous response (SI,

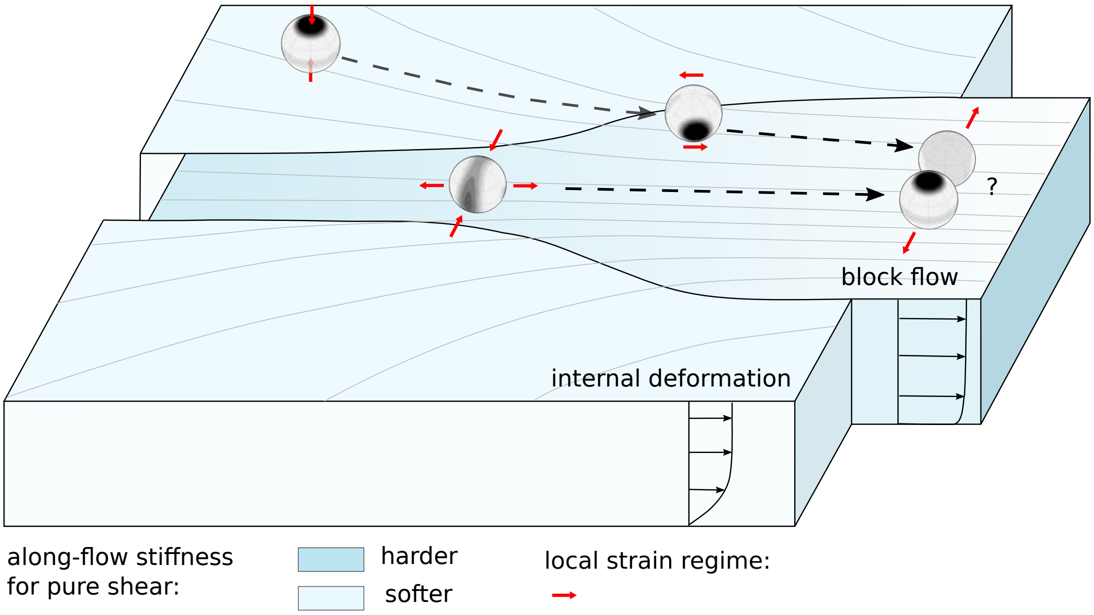

FIGURE 5.4: Illustration of fabric evolution in the NEGIS: The fabric-evolution model in Elmer/Ice suggests that outside the ice stream the fabric is dominated by vertical compression, resulting in a vertical single maximum of increasing strength with depth. Towards the shear margins, the fabric rotates into a horizontal single maximum dominated by horizontal shear and observed in ice cores and our modeling results. In the upstream part of the NEGIS, the flow acceleration and lateral compression due to flow channeling results in a vertical girdle which diffuses further downstream to a vertically symmetric fabric configuration. The fabric in the upper part of the NEGIS leads to considerable stiffening of ice for pure-shear deformation in flow direction. Our methods do not allow us to determine the fabric type and its effect on the viscosity downstream due to ambiguities related to vertical symmetry.

Section S5.5) suggests that the reaction time for pure shear is approximately ten times shorter for ice with $E_{xx} = 0.1$ in comparison to isotropy. Our findings are therefore relevant, as they imply that surge events or changes in basal water pressure, for instance, could propagate farther upstream and result in a faster response in ice streams with fabric anisotropy that causes along-flow stiffening. Ice streams could therefore potentially be more sensitive towards external disturbances than commonly assumed.

Recent findings by Rückamp et al. (2022) indicate further implications of our results, as they showed that the differences in simulated surface velocities between full-stokes models and higher-order models using e.g. the Blatter–Pattyn approximation are much larger for ice with higher viscosity in comparison to isotropic or softer ice. In that sense, our findings advocate the necessity of using full-Stokes models in highly dynamic areas such as ice streams.

Although our results suggest that the ice-stream margins are soft for horizontal shear, the role they play in maintaining the ice stream remains unclear. The horizontal single maximum observed in the S5 core and simulated by Elmer/Ice can facilitate horizontal shear by a factor of two. A similar enhancement could, however, be obtained from strong shear heating, as well as by the presence of temperate ice or water in the shear margins (e.g. Hunter et al., 2021). Both temperature and the fabric likely play a role in the shear-margin viscosity, however, we can not state whether the fabric is oriented in a preferable way to facilitate shear deformation.

Our results of strongly anisotropic fabric detectable by radar remote sensing methods also open a new avenue for improving our characterization of water (H_2O) ice and other extraterrestrial ice bodies. Together with our observed time scale of fabric evolution on the order of hundreds of years under terrestrial conditions, the mapping of ice fabric on other planetary bodies with polarized orbiting radar satellites would improve our understanding of their bulk physical properties. This would eventually contribute to inferring the dynamic evolution of both, regional ice masses as on Mars or Pluto, as well as planetary bodies as a whole, e.g., in the case of completely ice-covered moons like Europa.

5.5 Online Methods

We derived the horizontal fabric anisotropy from ground-based and airborne radar profiles, as well as from pRES measurements at distinct locations. In addition, these results are complemented and validated by fabric evolution models, as well as in-situ observations in the EastGRIP and S5 deep and shallow ice cores respectively. All approaches yield consistent results with respect to the spatial distribution of the horizontal fabric difference across and along the ice stream. Details on each method, validation and uncertainties are presented and discussed in the SI.

5.5.1 Data

We are using an extensive set of airborne radar sounding data (EastGRIP-NOR-2018 survey) which was recorded in 2018 over the onset region of NEGIS and its shear margins (Franke et al., 2022b). The survey was conducted with a Multichannel Coherent Radar Depth Sounder (MCoRDS 5) mounted on the Polar 6 BT-67 airplane. The radar system consists of eight antenna elements functioning as both, transmitter and receiver using a transmit–receive switch. The antennas were oriented such that the E-field polarization is parallel to the flight direction (HH polarization), and the transmitting wave beam was pointed towards nadir. The profiles were recorded using linear frequency-modulated chirps in the frequency band of 180–210 MHz at a pulse repetition frequency of 10 kHz, and the received signal was sampled at a frequency of 1.6 GHz. The airplane was flying at an approximate altitude of 360 m and a velocity of 260 km/h. Processing was performed with the post-processing CReSIS Toolbox (CReSIS, 2020a) and includes pulse compression using a Tukey time–domain weighting and filtering with a Hanning window. We refer to Franke et al. (2022b) for further details.

The airborne survey was complemented with a dedicated ground-based UHF radar profile (see Fig. S5.5 in SI), recorded with an 8-element transmit and receive system in T-configuration and a mean frequency of 750 MHz with a bandwidth of 300 MHz. This system provides a higher horizontal and vertical resolution than the airborne data, but covers less distance. Further system details and the data processing are described in Yan et al. (2020).

In addition, we are using polarimetric measurements with a ground-based phase-sensitive Radio-Echo Sounder (pRES; Brennan et al., 2014; Nicholls et al., 2015), which allows to determine vertical displacements of repeated measurements with an accuracy in millimeters. Between 2017 and 2019, we performed six polarimetric pRES measurements inside and outside the ice stream within 85 km around EastGRIP. At each site, besides the HH-polarized measurement, a measurement with VV-polarization was carried out by rotating the transmitting and the receiving antenna in horizontal direction by 90°. During each measurement, the pRES transmitted 100 chirps ranging from 200 to 400 MHz over a period of 1 s. The received signal was sampled at 40 kHz. For data processing, we followed Brennan et al. (2014) and Stewart (2018) in order to get amplitude and phase profiles as a function of two-way travel time.

5.5.2 Travel-time anisotropy and beat-signature analyses

Radar waves are decomposed in ordinary and extraordinary rays when traveling through polycrystalline ice with bulk anisotropic dielectric properties. The differences in wave speed result in a two-way travel–time difference Δt when reflected at the same reflector at depth and received at the surface. The value of the Δt depends directly on the strength of the horizontal anisotropy. Fujita et al. (2006) developed a matrix-based model that is able to calculate the expression of bulk anisotropy in radar data for a vertically propagating wave in a medium with one principle axis of the fabric also oriented vertically. They showed with synthetic results as well as observational data that distinct nodes and extinction features in the return power are generated for birefringent ice and anisotropic scattering as a function of depth. Of particular interest for our application is the appearance of the so-called co-polarization node. In the case of purely birefringent ice without anisotropic scattering, this node is strongest (i.e. has the least backscatter power) for a co-polarized antenna orientation of $\pi/4$ or $3\pi/4$ with respect to the main principle component of the bulk fabric and indicates a $\pi/2$ periodicity with depth (Fujita et al., 2006).

Both, the travel-time anisotropy and the appearance of co-polarization nodes can be exploited to derive the horizontal anisotropy of the fabric at a location. We applied these two approaches to airborne and ground-based radar profiles, as well as to pRES measurements at distinct locations. The individual methods are described in detail in the SI Section S5.2.

5.5.3 Modeling of fabric evolution

We used the ice-flow model Elmer/Ice (Zwinger et al., 2007; Gagliardini et al., 2013) to simulate the fabric evolution in the catchment area of NEGIS, assuming that the fabric evolves solely by lattice rotation. The model couples the processes of fabric evolution, ice flow and heat flow (Lilien et al., 2021), and was solved along 31 flow tubes. Each model domain is 2.5D following a flow line while simultaneously accounting for convergent/divergent transverse flow. The model was run for each flow tube for 5 kyr, after which the results are insensitive to initial conditions, and fabric changes can be assumed negligible. For further details of the model and our application in NEGIS, the reader is referred to Lilien et al. (2021) and Section S5.3.1 in the SI.

To extend the modeled data beyond the domain of Elmer/Ice, which, due to loss of numerical stability associated with high ice-flow velocities, only extends 40 km downstream of EastGRIP, we use the spectral fabric model for polycrystalline materials by Rathmann et al. (2021) to explore the fabric evolution in the downstream part of NEGIS. We thereby consider an ice parcel seeded at EastGRIP with an initial fabric similar to the average girdle-type measured in the ice core (Westhoff et al., 2021) and let it travel downstream along a flow line obtained from the surface velocities by Joughin et al. (2018). The Lagrangian fabric update of the parcel for incremental steps of one year is given by strain-rate tensors derived from the surface velocities in the corresponding flow line segment. The end of the simulation corresponds to a distance of approximately 120 km from EastGRIP and an advection time of 2,000 years. Further details of the model and our application can be found in Section S5.3.2 of the SI and in Rathmann et al. (2021).

5.5.4 Flow enhancement tensor

To estimate the effect of fabrics on directional ice viscosities, we calculated the directional enhancement factors following the approach by Rathmann et al. (2021) and Rathmann and Lilien (2021). The enhancement factors are defined as the strain-rate ratio between anisotropic and isotropic ice, whereby the anisotropic rheology is estimated by averaging a transversely isotropic monocrystal rheology over all grain orientations in a polycrystal (see Section S5.4 in the SI and Rathmann et al., 2021; Rathmann and Lilien, 2021). While our radar-based fabric analyses only allow inferring the difference in horizontal eigenvalues ($\Delta\lambda$), the required full fabric estimate can be obtained by applying a few assumptions about the expected fabric types inside/outside the ice stream and in the vicinity of the shear margin. These assumptions (detailed in Section S5.4 in the SI) are based on observations in ice cores and results obtained from fabric evolution models.

Besides the COF, temperature is the major factor controlling the ice viscosity. For comparison, we used the calculated enhancement tensors to estimate the temperature difference (ΔT, relative to a reference temperature of –20°C) that would be required to obtain ice softening/hardening equivalent to that suggested by the COF. Thereby, ΔT is obtained from the temperature-dependent enhancement factors assuming isotropic ice. For further details, see Section S5.4.3 in the SI.

Supplementary Information

S5.1 Background

When water freezes under conditions prevailing on Earth's surface, H_2O molecules are arranged in layers of hexagonal rings. The plane of these rings is called the *basal plane* and the perpendicular direction is termed the *c-axis*. A consequence of the hexagonal crystal structure is that shearing along the basal plane occurs much easier than the deformation in any other direction (Duval et al., 1983), causing mechanical anisotropy.

Glacier ice consists of billions of individual crystals, and their orientation strongly affects the bulk mechanical ice properties. After the initial deposition of snow and its transformation into ice, the c-axes generally point in random directions, so the bulk property of ice is isotropic. With time and as a consequence of ice deformation through uniaxial vertical compression and ice flow, the size, shape and orientation of crystals is altered as atoms escape from one crystal lattice to another by mechanisms generally summarized as recrystallization processes (e.g. Kamb, 1959; Kamb, 1972; Azuma and Higashi, 1985; Alley, 1988): Driven by differences in the free energy between adjacent crystal lattices, larger crystals grow at the cost of smaller ones (normal grain growth), reducing the free energy of the system. Similarly, the free energy is reduced by transferring molecules from deformed high-energy grains to low-energy grains. This so-called migration recrystallization leads to the growth of grains with a preferred orientation at the cost of others. Rotation recrystallization describes the formation of new grain boundaries caused by the alignment of dislocations through bending stresses. Lastly, new grains can nucleate in areas where the crystal lattice is highly distorted and grow by consuming their neighbors. Unlike normal grain growth and rotation recrystallization, the processes of migration recrystallization and grain nucleation alter the fabric considerably and lead to bulk anisotropy of ice, with c-axes generally pointing in the direction of predominant compression (Gow and Williamson, 1976; Azuma and Higashi, 1985).

The orientation of ice crystals is directly measured in ice-core thin sections with fabric analyzers (e.g. Wilen et al., 2003; Wilson et al., 2003) and is commonly represented as a second-order orientation tensor, $\mathbf{a}^{(2)}$, describing the density distribution of c-axes orientations: its eigenvectors, $\mathbf{a}_i$, and the corresponding eigenvalues, λ_i, describe the orientation and length of the three main axes (e.g. Durand et al., 2006; Thorsteinsson et al., 1997; Woodcock, 1977). By convention, the three eigenvalues are defined as $\lambda_1 \leq \lambda_2 \leq \lambda_3$ and $\lambda_1 + \lambda_2 + \lambda_3 = 1$.

The crystal orientation fabric (COF) is a product of the accumulated strain, so different deformation regimes in ice sheets cause characteristic fabrics. At ice domes, the predominant strain comprises vertical compression, which increases with depth. As a result, typical fabric profiles obtained from ice cores drilled near topographic domes show a transition from roughly isotropic ice ($\lambda_1 \approx \lambda_2 \approx \lambda_3$) in the top regions of the ice sheet to a vertical single maximum of increasing strength with depth ($\lambda_3 \gg \lambda_1 \approx \lambda_2$) (e.g. Thorsteinsson et al., 1997; Azuma et al., 1999; Durand et al., 2009; Montagnat et al., 2012; Diprinzio et al., 2005). At ice divides, horizontal extension exists in addition to the vertical compression, which typically results in a girdle fabric, where $\lambda_1 \ll \lambda_2 \approx \lambda_3$ (e.g. Wang et al., 2002a; Lipenkov et al., 1989; Faria et al., 2014; Fitzpatrick et al., 2014; Montagnat et al., 2014). Close to the bed, the deformation regime is dominated by simple shear, where a single maximum fabric oriented perpendicular to the shear plane tends to develop (e.g. Cuffey et al., 2000; Herron and Langway, 1982; Gow et al., 1997; Thorsteinsson et al., 1997). This can also be observed by ice deformation experiments (Bouchez and Duval, 1982; Journaux et al., 2019) and in a few ice cores retrieved in shear margins (Thomas et al., 2021; Samyn et al., 2008; Gerbi et al., 2021; Monz et al., 2021), where simple shear also prevails.

Ice cores provide direct and detailed information on the COF, but the logistical cost, technical challenges, particularly in fast-flowing ice and shear margins, difficulty in reconstructing the absolute orientation of the core and their limitation of being a point measurement make ice cores impractical for a spatially extensive evaluation of the fabric type. Indirect geophysical methods applied from or above the ice surface create the link between the small scale of laboratory experiments and ice–core observations to the large-scale coverage required for ice-flow models and the complete understanding of ice-stream dynamics.

We combine different approaches to map the horizontal fabric anisotropy: (i) travel-time difference of radar reflections from different polarizations applied on airborne RES and ground-based pRES data (see Section S5.2.1 and Section S5.2.3), (ii) beat-signature analysis of fabric-induced modulation of the backscattered radar power in airborne and ground-based RES profiles (Section S5.2.2), and (iii) modeling of fabric evolution (Section S5.3). All applied methods yield consistent results with respect to the spatial distribution of the horizontal fabric difference across and along the ice stream and are consistent with direct observations in ice cores at the ice-stream center (EastGRIP core) and the southeastern shear margin (S5 shallow core) (Section S5.2.4).

S5.2 Analytical methods

The propagation of radar waves is determined by the complex relative dielectric constant

$$\varepsilon^* = \varepsilon' - i\frac{\gamma}{\omega\varepsilon_0}, \tag{5.1}$$

where the real part, ε', is the relative dielectric permittivity, and the imaginary part corresponds to the dielectric loss factor depending on the electrical conductivity, γ, the angular frequency, ω, and the dielectric permittivity of free space, ε_0. For simplicity, primes are omitted henceforth, and all ε symbols refer to the relative dielectric permittivity, unless stated otherwise. Most englacial reflections are caused by density contrasts in the uppermost part of the ice column (Robin et al., 1969) and impurity layers (Paren and Robin, 1975), although reflections can also occur from abrupt changes in the COF (Eisen et al., 2007; Matsuoka et al., 2012). The conductivity of ice mainly depends on its impurity content and temperatures, so the imaginary part of the permittivity constant can be assumed to be isotropic for near–vertical incidence. In contrast, the bulk permittivity shows directional dependence related to the COF.

Ice crystals show uniaxial birefringence, so the real part of the dielectric permittivity tensor of a monocrystal can be written as

$$\boldsymbol{\varepsilon}^m = \begin{pmatrix} \varepsilon_\perp^m & 0 & 0 \\ 0 & \varepsilon_\perp^m & 0 \\ 0 & 0 & \varepsilon_\parallel^m \end{pmatrix}, \tag{5.2}$$

where $\varepsilon_\perp^m$ and $\varepsilon_\parallel^m$ are the relative dielectric permittivities perpendicular and parallel to the crystal c-axis. At radar frequencies, the dielectric anisotropy of a monocrystal, $\Delta\varepsilon^m = \varepsilon_\parallel^m - \varepsilon_\perp^m$, is approximately $\Delta\varepsilon^m \simeq 0.034 - 0.035$ (Matsuoka et al., 1997).

In polycrystalline ice, the permittivity of the bulk tensor relates to the single ice crystal as follows (e.g. Fujita et al., 2006):

$$\boldsymbol{\varepsilon} = \begin{pmatrix} \varepsilon_x & 0 & 0 \\ 0 & \varepsilon_y & 0 \\ 0 & 0 & \varepsilon_z \end{pmatrix} = \begin{pmatrix} \varepsilon_\perp^m + \Delta\varepsilon^m\lambda_x & 0 & 0 \\ 0 & \varepsilon_\perp^m + \Delta\varepsilon^m\lambda_y & 0 \\ 0 & 0 & \varepsilon_\perp^m + \Delta\varepsilon^m\lambda_z \end{pmatrix}, \tag{5.3}$$

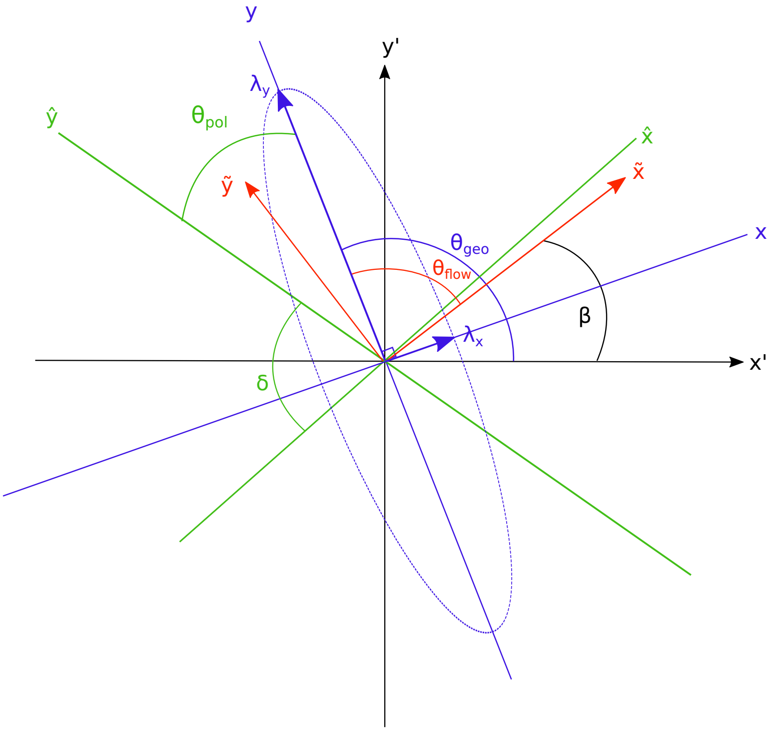

FIGURE S5.1: Coordinate systems used in this study: geographical coordinates in polar stereographic projection are denoted as x' and y'. Ice flows in $\tilde{x}$–direction, defined from geographic east counterclockwise by angle β. θ_{flow} is the angle between the flow direction and the eigenvector corresponding to the larger horizontal fabric eigenvalue. The eigenframe is denoted by x and y, whereby x points in the direction of the smaller horizontal eigenvalue (in most cases close to ice-flow direction). Radar waves at crosspoins are polarized in $\hat{x}$ and $\hat{y}$ respectively, and related to the eigenframe by angle θ_{pol}. δ is the smaller angle between the polarization directions. θ_{geo} is the angle between geographic East and the larger horizontal eigenvalue.

where ε_x, ε_y and ε_z correspond to the directional permittivities. Here, the coordinate system represents the principal fabric axes, whose lengths are determined by the COF eigenvalues λ_x, λ_y and λ_z. The orientation of the COF in ice sheets is related to deformation through ice flow, but the ability to determine its strength and type strongly depends on its orientation relative to the radar wave polarization. To describe these relations, we introduce four coordinate systems (Fig. S5.1) where x' and y' are the geographic coordinates, $\tilde{x}$ and $\tilde{y}$ point parallel and perpendicular to the ice-flow direction, $\hat{x}$ and $\hat{y}$ describe the polarization directions of two orthogonal radar waves, and x and y denote the fabric eigenframe, as mentioned above. For nadir surveys, the radar waves transmitted at the surface of ice sheets travel vertically through the ice column and are polarized perpendicular to the direction of propagation. The radar wave speed is essentially determined by the bulk dielectric permittivity in the polarization direction, hence, RES is only sensitive toward horizontal variations of the dielectric permittivity:

$$\Delta\varepsilon = \varepsilon_y - \varepsilon_x = \Delta\varepsilon^m(\lambda_y - \lambda_x) = \Delta\varepsilon^m\Delta\lambda. \tag{5.4}$$

We therefore assume the vertical direction, z, is consistent for all coordinate systems and define it as depth below the ice-sheet surface.

The electromagnetic wave speed, c, is determined by the complex dielectric constant as follows:

$$c = \frac{c_0}{\sqrt{\varepsilon*}} \approx \frac{c_0}{\sqrt{\varepsilon}}, \tag{5.5}$$

where c_0 is the speed of light in free space. Since the real part of the relative dielectric constant of ice is several orders of magnitude larger than the dielectric loss factor, the latter has a diminishing effect, so the wave speed primarily depends on ε. If the dielectric permittivities vary in two polarization directions, i.e. $\varepsilon_{\hat{x}} \neq \varepsilon_{\hat{y}}$, the wave speeds and wavelengths of two radar waves polarized in $\hat{x}$ and $\hat{y}$ differ slightly. Consequently, the travel-time difference, Δt, between the reflected signal of radar waves with different antenna polarizations is related to the horizontal anisotropy of the ice.

As introduced in the online methods, radar waves are decomposed in ordinary and extraordinary rays when traveling through polycrystalline ice with bulk anisotropic dielectric properties. In the following sections, the methods to derive the horizontal anisotropy from observable effects of radar wave decomposition are described in detail.

S5.2.1 Travel-time analysis of radar crosspoints

The EastGRIP-NOR-2018 radar dataset was recorded as a dense grid across the ice stream with antennas polarized parallel to the flight direction (HH), so at each radar line crosspoint (CP), two radar traces with different antenna polarizations lie close to each other. The travel-time difference, Δt, between two orthogonally polarized waves is related to the horizontal fabric anisotropy through:

$$\Delta t = t_{\hat{y}} - t_{\hat{x}} = \frac{2(\sqrt{\varepsilon_{\hat{y}}} - \sqrt{\varepsilon_{\hat{x}}})}{c_0} z, \tag{5.6}$$

where $t_{\hat{x}}$ and $t_{\hat{y}}$ are the recorded two-way travel times in the corresponding polarization directions $\hat{x}$ and $\hat{y}$. c_0 is the speed of light and $\varepsilon_{\hat{x}}$ and $\varepsilon_{\hat{y}}$ are the directional dielectric permittivities in the directions of radar polarization.

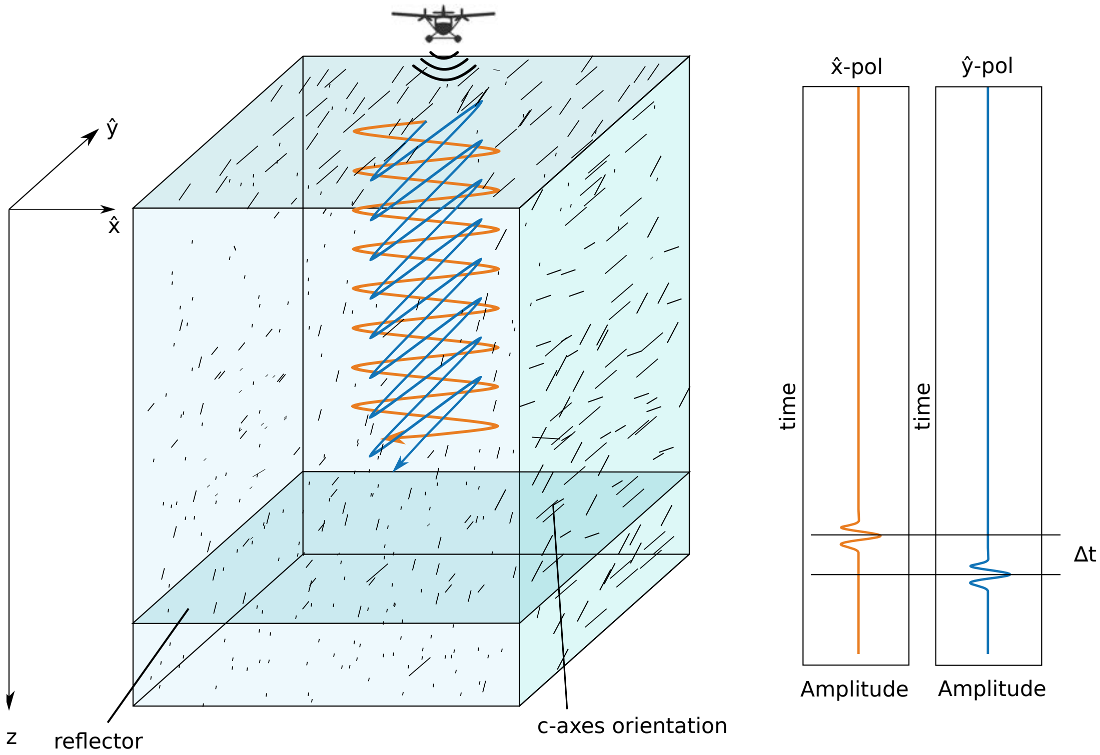

FIGURE S5.2: A reflecting interface at depth z and a horizontally anisotropic fabric leads to a travel-time difference (Δt) of the reflected signal. In this example, the c-axes are predominantly oriented in $\hat{y}$-direction, so the $\hat{y}$-polarized wave travels at a slightly slower wave speed and the reflection signal is delayed in comparison to the $\hat{x}$-polarized signal.

Travel–time picking and time-depth conversion

We manually pick $t_{\hat{x}}$ and $t_{\hat{y}}$ of prominent reflections observed in the closest traces of crossing radar profiles with intersection angles of approximately 90°. To account for eventual differences in the flight height of the aircraft, we shift time zero to the first break of the air–ice interface. We moreover use a spline interpolation to increase the temporal resolution from 0.033 μs to 0.001 μs.

In the EastGRIP ice core, the dielectric permittivity was inferred from Dielectric Profiling (DEP) by Mojtabavi et al. (2020a) and is used here to estimate the electromagnetic wave speed profile through the ice column. In the firn layers, the dielectric permittivity is controlled by the density and increases with depth. Below the transition into pure ice, changes in the permittivity, and thus also in the electromagnetic wave speed, occur mainly due to the COF. However, the instrument sensitivity of the DEP device is not high enough to measure these effects (Wilhelms et al., 1998). To estimate the radar wave speeds while eliminating instrument noise, we assume a firn permittivity of 1.55 (Mojtabavi et al., 2022) at the ice-sheet surface and extrapolate the smoothed DEP profile (moving average with 5 m window length) from the core onset (13 m depth) to the surface. Below the transition into pure ice at ∼200 m we assume a constant permittivity of 3.15.

While the DEP-inferred wave-speed profile is a reasonable representation at EastGRIP, we recognize that variations and inhomogeneities in firn densification can lead to spatially varying wave speed profiles. While temperature and accumulation rate only vary mildly over distances relevant in this study, increased deformation accelerates densification in the shear margins (e.g. Riverman et al., 2019; Vallelonga et al., 2014; Christianson et al., 2014; Oraschewski and Grinsted, 2021). Consequently, the vertical density and electromagnetic wave speed gradients can be expected to be stronger in the vicinity of the shear margins. Assuming a spatially constant wave speed profile could therefore affect the analysis of the CPs in the immediate vicinity of the shear margins. Most of the CPs analyzed here are more than 2 km away from the shear zone, though, so the wave speed assumption is arguably justified in most cases.

The depth of the picked reflections is estimated by converting the average travel times $\bar{t} = \frac{1}{2}(t_{\hat{x}} + t_{\hat{y}})$ to depth, using the DEP-based wave-speed profile. From Eq. (5.6) we define a maximum threshold for the depth-dependent travel-time anisotropy resulting from a horizontal single maximum fabric, assuming that $\varepsilon_{\parallel}^{m} = 3.167$ and $\varepsilon_{\perp}^{m} = 3.133$, i.e. $\Delta\varepsilon^{m} = 0.034$ (Matsuoka et al., 1997). Picked reflections where Δt exceeds the corresponding threshold are considered outliers and discarded. We further remove picked reflections that deviate by more than two standard-deviations from the trend of the time–depth profile. Crosspoints, where less than five reflections could be clearly identified, are excluded from further analyses.

Deriving the apparent horizontal fabric anisotropy

The picked two-way travel times $(t_{\hat{x}}, t_{\hat{y}})$ of two waves reflected at the same depth, z, but polarized in $\hat{x}$ and $\hat{y}$ directions respectively, are given by:

$$t_{\hat{x}} = \frac{2\sqrt{\varepsilon_{\hat{x}}(z)}}{c_0} z \quad \text{and} \quad t_{\hat{y}} = \frac{2\sqrt{\varepsilon_{\hat{y}}(z)}}{c_0} z. \tag{5.7}$$

While inferring the depth-varying permittivities from Eq. (5.7) is possible in theory, it is unfeasible here due to the relatively large uncertainties on $t_{\hat{x}}$ and $t_{\hat{y}}$ (elaborated on below). By replacing $\varepsilon_{\hat{x}}$ and $\varepsilon_{\hat{y}}$ with the depth-averaged permittivities $\overline{\varepsilon_{\hat{x}}}$ and $\overline{\varepsilon_{\hat{y}}}$, Eq. (5.7) can be linearized so

$$t_{\hat{x}} = \frac{2\sqrt{\overline{\varepsilon_{\hat{x}}}}}{c_0} z = m_{\hat{x}} z \quad \text{and} \quad t_{\hat{y}} = \frac{2\sqrt{\overline{\varepsilon_{\hat{y}}}}}{c_0} z = m_{\hat{y}} z. \tag{5.8}$$

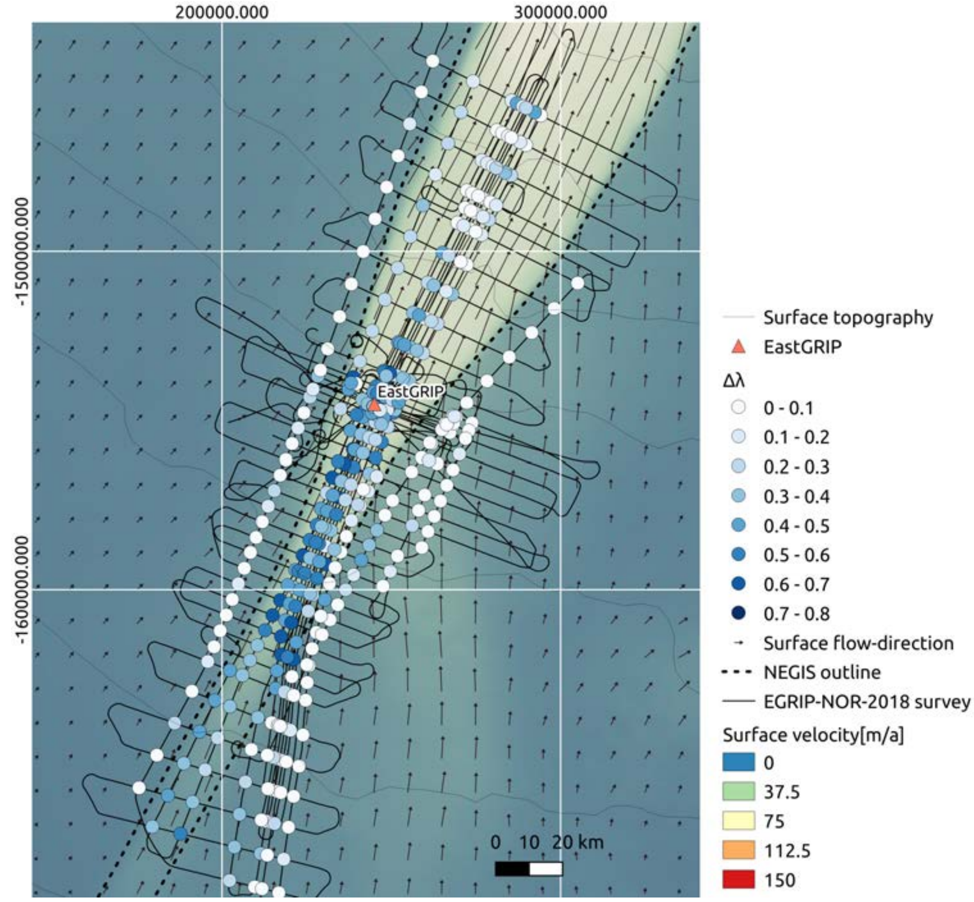

FIGURE S5.3: Horizontal fabric anisotropy ($\Delta\lambda$) from the travel-time analysis at radar crosspoints.

By determining the slopes $m_{\hat{x}}$ and $m_{\hat{y}}$ from a linear regression through the picked travel times, the depth-averaged apparent horizontal dielectric anisotropy ($\Delta\varepsilon_a$) can be derived from

$$\Delta\varepsilon_a = \overline{\varepsilon_{\hat{x}}} - \overline{\varepsilon_{\hat{y}}} = \frac{c_0^2}{4}(m_{\hat{x}}^2 - m_{\hat{y}}^2), \tag{5.9}$$

which relates to the apparent difference in the horizontal eigenvalues as follows:

$$\Delta\lambda_a = \lambda_{\hat{x}} - \lambda_{\hat{y}} = \frac{\Delta\varepsilon_a}{\Delta\varepsilon^m}. \tag{5.10}$$

We emphasize that the apparent horizontal anisotropy ($\Delta\lambda_a$) inferred by this method is not equivalent to the absolute horizontal fabric anisotropy ($\Delta\lambda$) if the polarization of the two radar traces does not align with the two horizontal eigenvectors. $\Delta\lambda_a$ can thus be regarded as a lower-bound estimate of the horizontal anisotropy. Figure S5.3 shows the horizontal anisotropy for all analyzed crosspoints. The map of horizontal anisotropy of all analyzed crosspoints (Fig. S5.3) shows that almost no evidence of anisotropy is obtained for CPs outside of the shear margins. This disagrees with the results obtained from other methods (i.e. beat-signature analysis and Elmer/Ice fabric evolution model) and is likely a consequence of the method sensitivity towards the alignment between radar polarization and fabric orientation. In comparison to the other methods used in this study, the crosspoint analysis of travel-time anisotropy is regarded to be less reliable outside the ice stream.

To evaluate the robustness of our method, we compare six CPs close to the EastGRIP drill site that are separated by less than 50 m from each other. Within this distance, fabric variations can be assumed to be negligible. We investigate the sensitivity to varying depths by employing three linear regressions through different depth points at 0 m, 200 m and 500 m. The corresponding travel times at 200 m and 500 m are calculated from the $\overline{\varepsilon_{\hat{x}}}$ and $\overline{\varepsilon_{\hat{y}}}$ inferred from the regression through the origin. The regressions running through 200 m and 500 m result in higher horizontal anisotropy values due to the higher relative weight of greater depths, where the fabric is likely to be more pronounced (Table S5.2). Table S5.1 shows an example of the analysis for CP3.

TABLE S5.1: Example of travel-time anisotropy analysis for CP 3: $t_{\hat{x}}$ and $t_{\hat{y}}$ are the travel times picked from reflections at depth z from $\hat{x}$- and $\hat{y}$-polarized radar traces, respectively. Δt is the travel-time anisotropy ($t_{\hat{y}} - t_{\hat{x}}$). Superscript 0 indicates travel times and travel-time anisotropy from a linear regression through the origin, superscript 200 and 500 denote the corresponding values for linear regression through 200 m and 500 m point respectively. $\overline{\varepsilon_{\hat{x}}}$, $\overline{\varepsilon_{\hat{y}}}$ and $\Delta\varepsilon_a$ at the bottom of the table are the directional dielectric permittivities and apparent horizontal permittivity anisotropy derived from the corresponding linear regression.

z	$t_{\hat{x}}$	$t_{\hat{y}}$	Δt	$t^0_{\hat{x}}$	$t^0_{\hat{y}}$	Δt^0	$t^{200}_{\hat{x}}$	$t^{200}_{\hat{y}}$	Δt^{200}	$t^{500}_{\hat{x}}$	$t^{500}_{\hat{y}}$	Δt^{500}
0	-	-	-	*0*	*0*	*0*	-	-	-	-	-	-
200	-	-	-	-	-	-	*2.347*	*2.353*	*0.0063*	-	-	-
459.8	5.313	5.319	0.005	5.395	5.409	0.015	5.397	5.412	0.015	-	-	-
484.6	5.604	5.614	0.009	5.686	5.701	0.015	5.688	5.704	0.016	-	-	-
500	-	-	-	-	-	-	-	-	-	*5.866*	*5.882*	*0.016*
540.9	6.269	6.283	0.013	6.346	6.363	0.017	6.349	6.367	0.018	6.357	6.376	0.019
560	6.504	6.500	-0.004	6.570	6.588	0.018	6.573	6.591	0.018	6.582	6.602	0.020
709.3	8.272	8.267	-0.005	8.322	8.344	0.022	8.326	8.349	0.023	8.336	8.362	0.025
735.7	8.580	8.586	0.006	8.632	8.655	0.023	8.635	8.659	0.024	8.646	8.673	0.026
755.8	8.813	8.828	0.016	8.868	8.891	0.024	8.871	8.896	0.025	8.883	8.910	0.027
772.6	9.014	9.025	0.011	9.065	9.089	0.024	9.068	9.094	0.025	9.080	9.108	0.028
782.1	9.133	9.132	-0.001	9.176	9.201	0.025	9.180	9.206	0.026	9.192	9.220	0.028
807.5	9.425	9.441	0.016	9.474	9.500	0.026	9.478	9.505	0.026	9.490	9.519	0.029
828.3	9.674	9.683	0.009	9.718	9.744	0.026	9.722	9.749	0.027	9.735	9.764	0.030
851.9	9.949	9.968	0.019	9.995	10.022	0.027	9.999	10.027	0.028	10.012	10.043	0.030
931.7	10.889	10.917	0.028	10.931	10.961	0.030	10.936	10.966	0.030	10.950	10.983	0.033
981.8	11.481	11.511	0.030	11.519	11.550	0.031	11.524	11.556	0.032	11.539	11.574	0.035
1030.4	12.064	12.080	0.016	12.089	12.122	0.033	12.094	12.128	0.034	12.110	12.147	0.037
1165.2	13.648	13.688	0.039	13.671	13.708	0.037	13.677	13.715	0.038	13.694	13.736	0.042
1222.5	14.324	14.369	0.045	14.343	14.382	0.039	14.349	14.389	0.040	14.368	14.411	0.044
1916.8	22.525	22.608	0.082	22.489	22.550	0.061	22.499	22.561	0.063	22.528	22.596	0.069
2048.5	24.085	24.167	0.082	24.034	24.099	0.065	24.045	24.111	0.067	24.075	24.149	0.073
2166.1	25.475	25.562	0.087	25.414	25.483	0.069	25.425	25.496	0.071	25.458	25.535	0.077
2674.3	31.491	31.580	0.089	31.377	31.461	0.085	31.390	31.477	0.087	31.430	31.526	0.096
				$\overline{\varepsilon_{\hat{x}}}$	$\overline{\varepsilon_{\hat{y}}}$	$\Delta\varepsilon_a$	$\overline{\varepsilon_{\hat{x}}}$	$\overline{\varepsilon_{\hat{y}}}$	$\Delta\varepsilon_a$	$\overline{\varepsilon_{\hat{x}}}$	$\overline{\varepsilon_{\hat{y}}}$	$\Delta\varepsilon_a$
				3.093	3.110	0.017	3.096	3.113	0.017	3.104	3.122	0.019

Uncertainties in travel-time anisotropy

Most uncertainties in this method arise from determining the travel times $t_{\hat{x}}$ and $t_{\hat{y}}$. The range resolution of the recorded signal corresponds to a temporal resolution of 0.033 μs, but by interpolating the waveform within the sampling interval, we reduce the picking uncertainty to

TABLE S5.2: Comparison of travel-time analysis at six crosspoins near EastGRIP (Fig. S5.4). The table shows the apparent horizontal anisotropy $\Delta\lambda_a$ inferred from a regression through the origin, $\Delta\lambda_a^0$, 200 m, $\Delta\lambda_a^{200}$, and 500 m, $\Delta\lambda_a^{500}$. δ is the angle between the two crossing flight lines and $\tilde{a}(\Delta\lambda_a)$ and $\tilde{s}(\Delta\lambda_a)$ are the mean and standard deviations of $\Delta\lambda$ inferred from the three different regression lines.

CP	$\Delta\lambda_a^0$	$\Delta\lambda_a^{200}$	$\Delta\lambda_a^{500}$	δ
1	0.435	0.448	0.488	89.9
2	0.389	0.403	0.443	78.0
3	0.492	0.508	0.556	86.1
4	0.400	0.405	0.433	86.6
5	0.505	0.515	0.546	89.7
6	0.381	0.400	0.456	89.2
$\tilde{a}(\Delta\lambda)$	0.434	0.447	0.487	
$\tilde{s}(\Delta\lambda)$	0.054	0.053	0.053	

roughly ± 0.01 μs. The compared radar traces were not recorded concurrently in space and time, so differences in background noise can arise from variations in weather conditions, flight height or surface structures and might lead to signal alteration. The distance between the parallel-flow and the across-flow radar traces is 11.7 m at maximum, so geometrical effects are assumed to be small but cannot be excluded entirely. Further uncertainties could be introduced from the time–to–depth conversion and the assumption of a spatially constant electromagnetic wave speed profile.

S5.2.2 Beat-signature analysis

For a transmitted wave whose polarization plane is not aligned with one of the horizontal anisotropy axes, the electric field can be regarded as the superposition of two components, E_x and E_y. The difference in the wave speed leads to a phase shift and hence a polarization rotation, causing extinction nodes in radar return power (Matsuoka et al., 2012; Fujita et al., 2006). In the absence of anisotropic scattering, these nodes are most pronounced when the transmitted wave is polarized at an angle of 45° from the horizontal eigenvector $\mathbf{a}_x$, and the phase differences are proportional to the radar wave frequency and the degree of horizontal anisotropy (Fujita et al., 2006). As explained above, the difference in the horizontal components of the bulk dielectric permittivities $\Delta\varepsilon$ defined in Eq. (5.4) causes a continuous difference in two-way travel time, $\Delta t(z)$, of the two principle waves, which can also be expressed as a phase difference $\phi(z) = 2\omega\Delta t(z)$, where the factor 2 arises from the consideration of two-way traveling and $\omega = 2\pi f$ is the angular frequency of the radar wave with center frequency f. The change of ϕ with depth gives rise to a continuous modulation of the backscattered power. In analogy to signal mixing, this can also be considered as a beat or modulation frequency f_{mod} from two superimposed waves at slightly different frequencies or wavelengths, in our cases originating from the wave speed differences, as expressed in (5.6). The beat-signature results in destructive interference, a so-called co-polarization extinction node, when the phase difference ϕ between the ordinary and extraordinary wave is an odd multiple of π (Fujita et al., 2006). Neglecting anisotropic backscatter and approximating Eq. (13) in Fujita et al. (2006) with a Taylor expansion (Jordan et al., 2019) results in

$$\phi(z) = \frac{4\pi f}{c_0} \int_z^0 \frac{\Delta\varepsilon(z)}{2\sqrt{\varepsilon_{xy}}} dz = \frac{2\pi f}{c_0} \Delta\varepsilon^m \int_z^0 \frac{\Delta\lambda(z)}{\sqrt{\varepsilon_{xy}}} dz \tag{5.11}$$

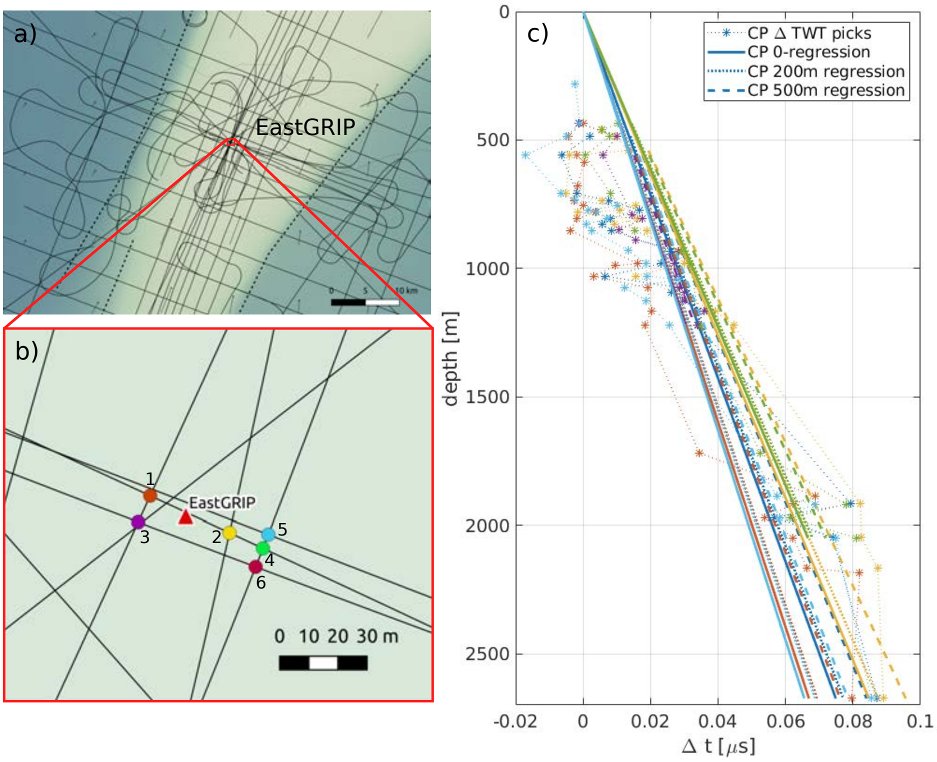

FIGURE S5.4: **a–b**) Location and **c)** travel-time difference of six crosspoints in the vicinity of EastGRIP. The right panel shows difference in the picked travel times with depth (dashed lines) and the fit of a first-degree polynomial (solid line) from which the apparent horizontal anisotropy $\Delta\lambda_a$ was derived.

where ε_{xy} is the mean of the horizontal relative permittivities. Assuming a vertically constant fabric with a constant difference $\Delta\lambda$ and thus permittivities, equation (5.11) simplifies to

$$\phi(z) = \frac{2\pi f \Delta\varepsilon^m}{c_0\sqrt{\varepsilon_{xy}}}\Delta\lambda z. \tag{5.12}$$

Using the wave number k_{mod} of the beat signature to relate the phase difference ϕ to propagated depth z allows us to write

$$\phi(z) = 2k_{mod}z = \frac{4\pi\sqrt{\varepsilon_{xy}}f_{mod}}{c_0}z. \tag{5.13}$$

Here, again, the first factor of 2 arises from the consideration of two-way propagation.

Setting equation (5.13) equal to (5.12) finally yields

$$\Delta\lambda = \frac{2\varepsilon_{xy}}{\Delta\varepsilon^m}\frac{f_{mod}}{f}, \tag{5.14}$$

thus linearly connecting the horizontal anisotropy to the beat frequency f_{mod} and the center frequency f of the radar system.

In Eq. (5.14), we can also use the period $T_{mod} = f_{mod}^{-1}$ of the beat signal, e.g. directly from a radargram in the time domain and pick the time difference between neighboring minima/nodes, to obtain

$$\Delta\lambda = \frac{2\varepsilon_{xy}}{f\Delta\varepsilon^m}\frac{1}{T_{mod}}. \tag{5.15}$$

Minima in the beat signal are caused if the two waves are out of phase, i.e. if they have a phase difference $\Delta\phi = (2n+1)\pi$, i.e. uneven multiples of π. Considering the beat signal as the image of a wave in the two-way travel-time domain (as we can see it in the radargram) with phase θ_{mod} we can write

$$\theta_{mod} = k_{mod} s = k_{mod} \frac{c_0 t}{\sqrt{\varepsilon}}, \tag{5.16}$$

with $k_{mod} = \frac{2\pi}{l_{mod}}$ being the wave number and l_{mod} the wavelength of the beat (or modulation) signal. The second factor s is the propagated path, which can be calculated from the two-way travel time t. The travelpath s is twice the actual depth as plotted in a radargram, $s = 2z$, and therefore

$$\theta_{mod} = 2k_{mod} z. \tag{5.17}$$

In the simplest case of two neighboring minima, separated by depth Δz, the phases θ_{mod} at these two minima are 2π apart, i.e. $\Delta\theta_{mod} = 2\pi$. Thus we can write

$$\Delta\theta_{mod} = 2\pi = 2k_{mod}\Delta z = 2\frac{2\pi}{l_{mod}}\Delta z \tag{5.18}$$

which is yields

$$l_{mod} = 2\Delta z. \tag{5.19}$$

i.e. the wavelength l_{mod} of the beat signal is twice the distance between two minima.

Young et al. (2021) exploited this effect along shallow airborne radar profiles over the eastern shear margin of Thwaites Glacier to deduce the bulk anisotropy in the upper part of the ice sheet. We apply the same approach here to derive the vertical fabric variations, as described in the following subsections.

Manual determination of horizontal anisotropy from birefringence-induced power loss

To investigate the possibility of depth-variable fabric asymmetry (or to evaluate the limitations of the assumption of a depth-constant fabric asymmetry), we employ the semi-manual methods of Young et al. (2021) over a representative subset of radargrams aligning both parallel and perpendicular to the ice-flow direction. For each radargram frame, the birefringent minima are manually traced following a two-dimensional convolution with window dimensions of 138 × 344 m^2 and 87 × 278 m^2 for the UHF 750 MHz and AWI-UWB 195 MHz radargrams, respectively. The resulting traces are then automatically aligned to and smoothed over the 'true' locations of the nearest birefringent minima using a Gaussian-weighted moving average algorithm with a 500 m window. Examples for two profiles perpendicular to ice flow and near the EastGRIP drill site are shown in Fig. S5.5 (UHF system with 750 MHz) and Fig. S5.6 (AWI-UWB system with 195 MHz). The method, in principle, also allows to determine the variation of the fabric with depth, averaging over the vertical distance of two nodelines.

Semi-automatic determination of horizontal anisotropy from beat frequency

Although the manual determination of the fabric resolves vertical variations of the beat frequencies – i.e. the distance between node lines – to derive the variation of the horizontal fabric difference, the applicability to large data sets is limited as it is a very time–consuming process. We therefore developed an automated approach, which extracts the beat frequency f_{mod} from radargrams by spectrogram analysis. The AWI UWB radargrams, which have been processed in the standard processing chain (see Franke et al., 2022b), are further processed by a bandpass filter (100–750 kHz), time cutting the upper section including the multiple, and the lower section including the bed reflection and strong folds, and a second application of the same bandpass filter. The remaining part of the radargram contains backscatter variations mainly caused by internal layers, most of which are of volcanic origin (Mojtabavi et al., 2022) and the beat-frequency modulation of the backscattered power caused by horizontal anisotropy. All

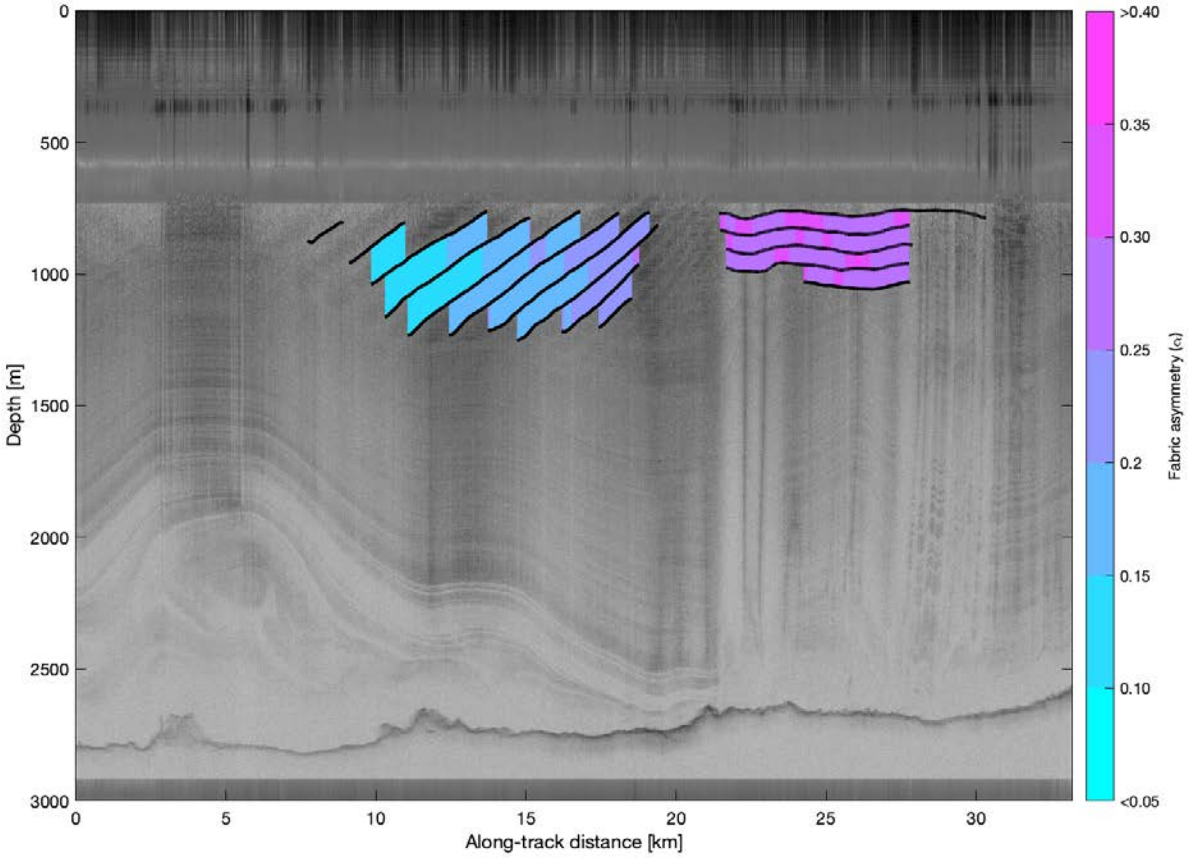

FIGURE S5.5: Radargram recorded with the UHF Mills Cross system (Yan et al., 2020) with a center frequency of 750 MHz. The profile runs from EastGRIP (right) towards the north, perpendicular to ice flow and across the shear margin, with a turn at the end (left). The signature in the upper 700 m shows an artifact from the source chirp, the bed reflection is visible around 2700–2800 m. Between 700 and 1200 m depth, beat signatures are highlighted. The horizontal fabric anisotropy is derived from the distance of neighboring node lines and is indicated by color, using the approach of Young et al. (2021) .

pre-processed traces of a radargram are then concatenated to obtain one long time series. We use the MATLAB^{TM} *spectrum* function to calculate a continuous spectrum of the time series, using frequency limits of 100 to 750 kHz, default segmentation with 50 % overlap of neighboring segments for spectral estimates. This results in a spectrogram of the radar return power in the range of 100–750 kHz along the radar profile. Depending on the location, the spectrograms clearly show modes originating from the beat frequency (Fig. S5.7). In a next step, we automatically extract the frequency of those dominating modes as a function of position, which is then manually checked for consistency and corrected for artifacts. Finally, we obtain a distribution of the dominating beat frequency, which is converted to $\Delta\lambda$ by Eq. (5.14) (see Fig. S5.7 for an example). We estimate the uncertainty in $\Delta\lambda$ to be around 0.05, i.e. 5% of its theoretical maximum. However, the limitations are in parts ambiguities in the spectral analysis, for instance, if internal layers are spaced at an equal vertical distance comparable to the beat signatures. The approach is, therefore, most applicable in regions where the horizontal anisotropy is spatially changing, i.e. along radar profiles perpendicular to the flow field and across the shear margins. The results are best suited for the interpretation of the overall spatial distribution of the anisotropy rather than depicting the fabric at a particular location without taking the spatial distribution into account.

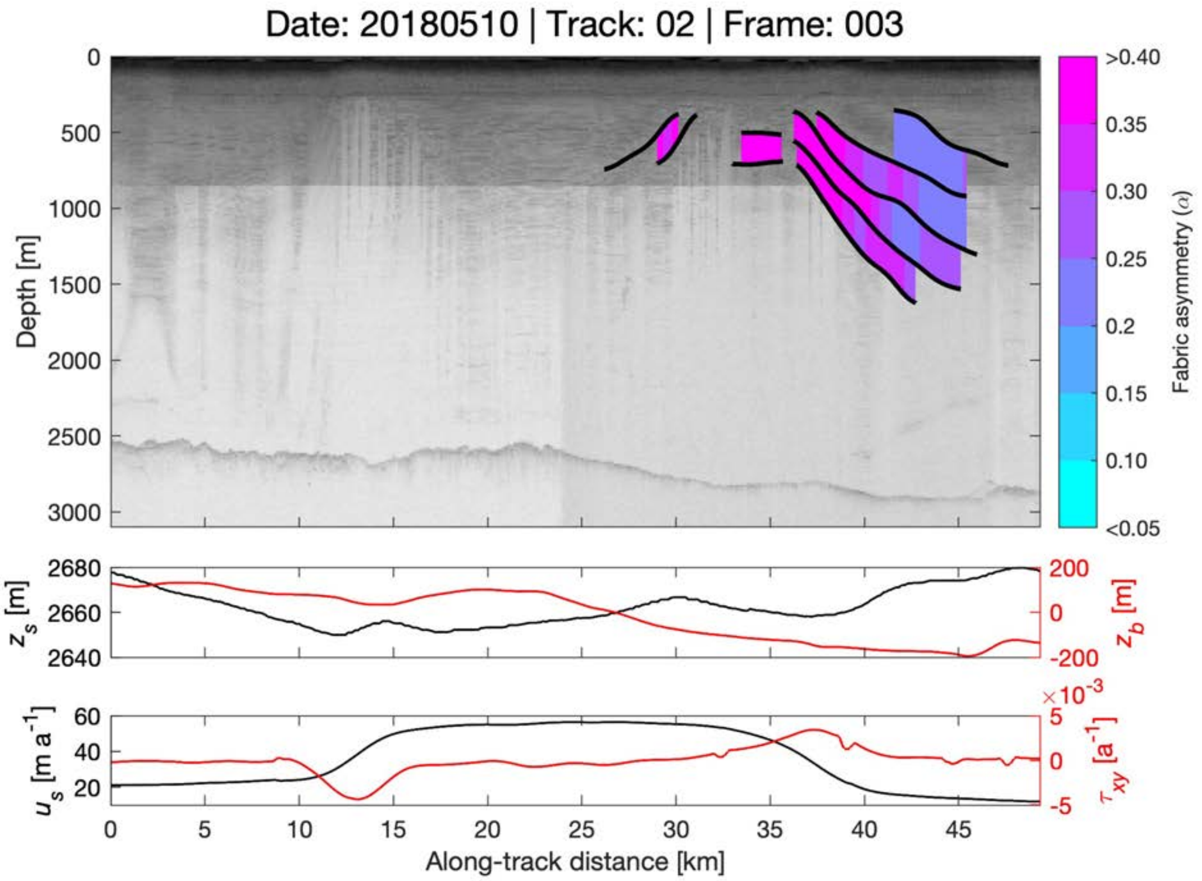

FIGURE S5.6: Radargram recorded with the AWI UWB radar system with a center frequency of 195 MHz. The profile crosses NEGIS, with EastGRIP in the center, from southeast (left) to northwest (right), perpendicular to ice flow and across both shear margins. The part northwest of EastGRIP is close to the ground-based radar profile shown in Figure S5.5. The horizontal fabric anisotropy derived from the distance of neighboring node lines is again indicated by color, using the approach of Young et al. (2021).

Forward modeling of birefrigence induced anisotropy

To demonstrate the effect of modeled polarimetric radio signal propagation through an ice column, we use the Fujita et al. (2006) matrix-based model for a frequency of $f = 195$ MHz. Each model case in Fig. S5.8 shows the effect of a slightly different horizontal anisotropy within the ice column defined by the difference between the two horizontal eigenvalues ($\Delta\lambda$). The other parameters in the models, including the anisotropic scattering (set to zero) and fabric orientation, remain constant. More details about the features in the forward model and the effect of other parameters are explained in Ershadi et al. (2022).

S5.2.3 Travel-time analysis of polarimetric pRES measurements

In general, the analysis of the horizontal fabric anisotropy from the polarimetric pRES measurements follows the method described in section S5.2.1. First, we calculate the vertical travel-time difference between the HH- and the VV-polarized measurements from the cross-correlation of the amplitude- and the phase-profiles. This method is widely used to derive vertical strain from repeated pRES measurements (e.g. Stewart et al., 2019; Vaňková et al., 2020; Zeising and Humbert, 2021) and is described in detail in Stewart (2018). Before calculating the cross-correlation, we apply the time-depth conversion and divide the HH-polarized measurement into segments

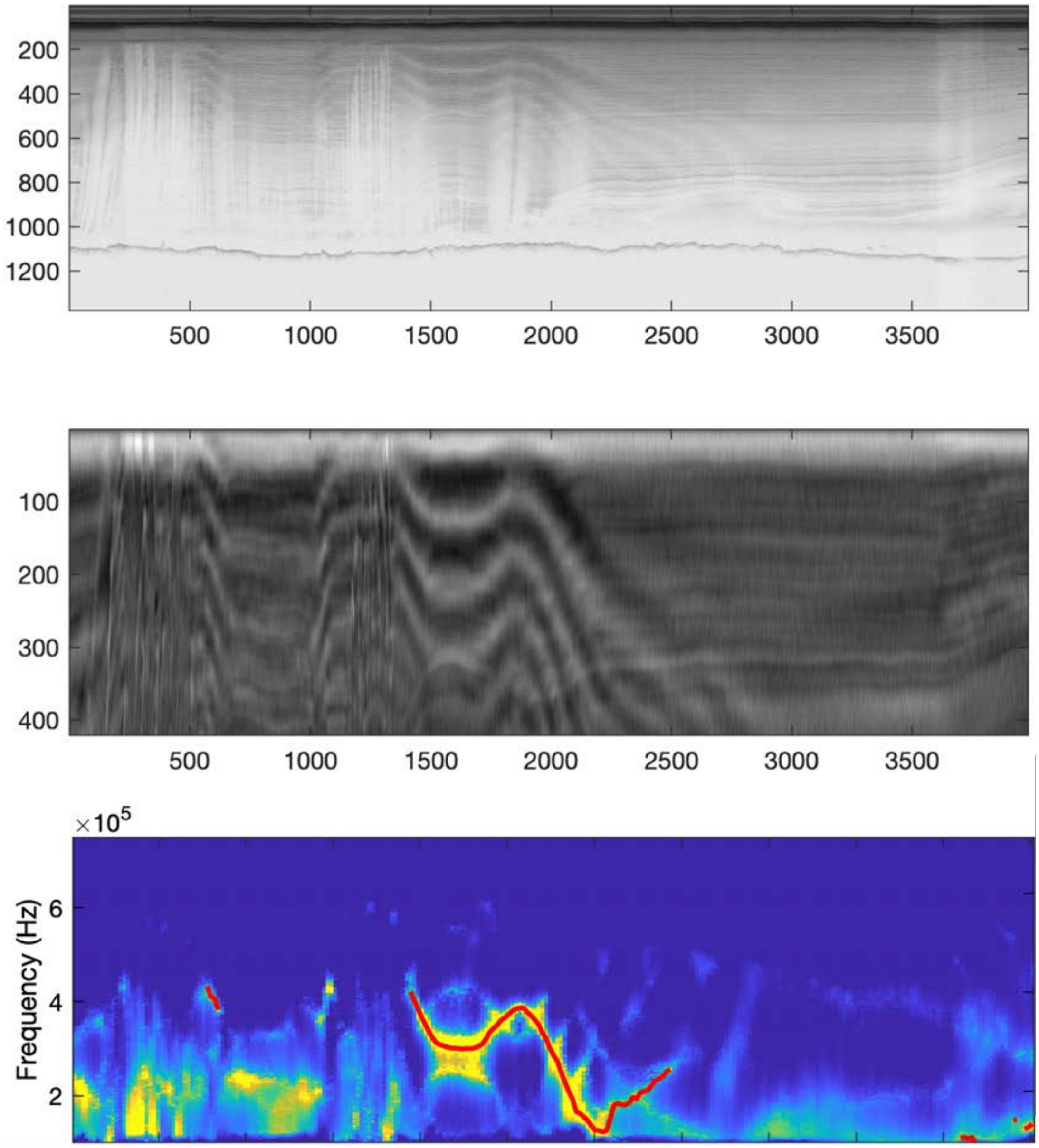

FIGURE S5.7: Example of spectrogram analysis for UWB profile 20180512-02-006 (x-axis: trace no., y-axis: sample no.): in the original radargram (top) filtered and cropped (middle), before applying the spectral analysis. From the spectrogram (bottom, relative power spectral density in color) we obtain a manually checked and corrected distribution of f_{mod} (red line) from which the horizontal anisotropy is calculated using Eq. (5.14).

of 6 m depth with 3 m overlaps, starting at a depth of 20 m. The cross-correlation between the HH- and the VV-polarized measurements are then calculated for each segment. A first coarse range difference with a resolution of $>$ 5 cm is derived from the lag with the largest amplitude-correlation value for segments with a correlation coefficient higher than 0.8. However, a low signal-to-noise level prevents the estimation of the coarse-range difference from a depth of roughly 1500 m and deeper.

In order to derive the fine-range difference with millimeter-resolution, we use the phase shifts from the cross-correlation of the phase profiles. Here, we manually track the vertical distribution of the minimum phase-shift nearby the coarse-range differences. We finally derive the vertical distribution of the range difference (Δz) and the corresponding travel-time anisotropy

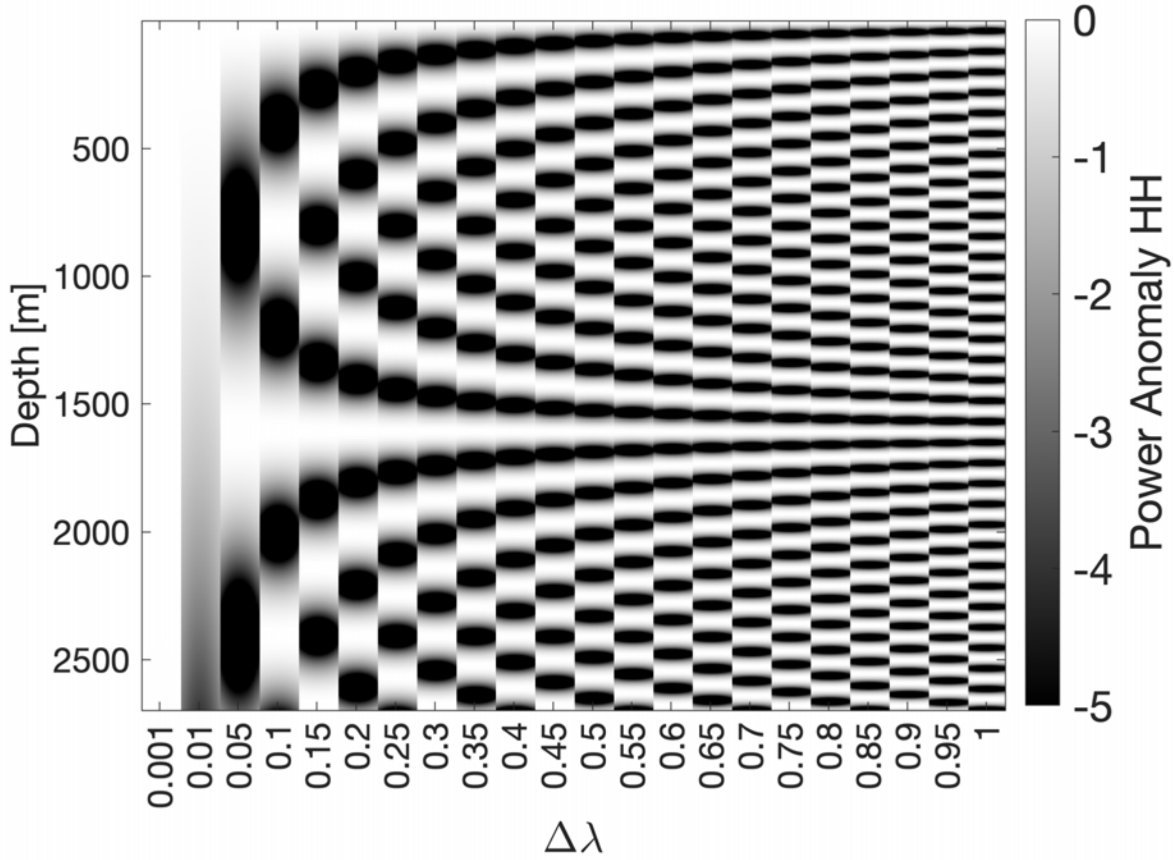

FIGURE S5.8: Synthetic calculation of power anomaly for HH polarization in a horizontally anisotropic medium for $\Delta\lambda$ ranging from 0.001 to 1 (x-axis) for an ice thickness of 2700 m (y-axis). Each of the 22 columns shows the power anomaly for a rotation of the polarization from 81 to 100°. The extinction nodes caused by birefringence corresponds to the black nodes (i.e. lower power). Connecting nodes for a fixed polarization would yield the extinction node lines as see in radargrams (e.g. Figs. S5.7, S5.6 and S5.5). For very low $\Delta\lambda = 0.001$, no node is present. For $\Delta\lambda = 0.01$, the first node extends over the full ice column, for $\Delta\lambda = 0.05$ two nodes appear, etc. The calculations were done with a matrix-based model (Fujita et al., 2006; Jordan et al., 2019), closely following the approach by Ershadi et al. (2022).

(Δt) from the selected lag and phase shift of each segment.

Next, we calculate the horizontal fabric anisotropy from the two-way travel-time difference. In contrast to the crosspoint analysis of the airborne radar survey, the high vertical resolution of Δt obtained from pRES allows the estimation of the depth-varying permittivity. Thus, we determine the slopes $m_{\hat{x}}(z)$ and $m_{\hat{y}}(z)$ (see Eq. (5.8)) as a function of depth by calculating the average slopes of the travel-time difference in a 200 m moving window, after smoothing with a 24 m moving median. Finally, we derive the difference in horizontal dielectric anisotropy and the difference in the horizontal eigenvalues from Eqs. (5.9) and (5.10). An example from the measuring site 31 km upstream of EastGRIP is shown in Fig. S5.9.

S5.2.4 Ice-core analysis

Observational fabric data was retrieved from two ice cores: the deep EastGRIP ice core and a close-by shallow core in the southeastern shear margin of NEGIS called S5. The preparation and measurement of the samples follow the same principles. All analyzed samples are vertical to the ice-core axis and have dimensions of about 90×70×0.3 mm^3. The sample surfaces were carefully polished with a microtome knife in the EastGRIP trench at -18 °C. After one hour of

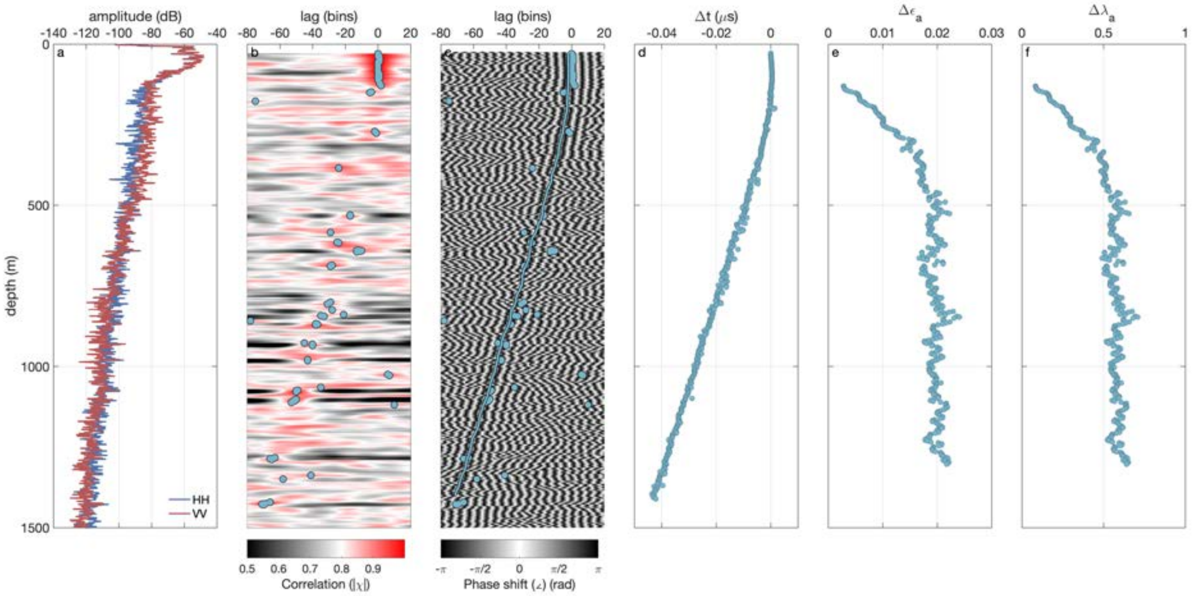

FIGURE S5.9: Analysis of the difference in horizontal eigenvalues from HH- and VV-polarized pRES measurements. The pRES measurements showed here were performed in the ice-stream center, 31 km upstream of EastGRIP. (a) Comparison of amplitude profiles of HH- (blue line) and VV-polarized (red line) measurement as a function of depth. (b) Cross-correlation ($|\chi|$) of both measurements as a function of lag and depth. Blue dots mark the lag of best correlation of the segment for those exceeding the correlation value of 0.8. (c) Phase shift as a function of lag and depth. The blue dots are the same as in (b). The blue line marks the tracked minimum phase shift. (d) Difference in two-way travel time between both measurements at the same depth. (e) Difference in horizontal dielectric anisotropy $\Delta\varepsilon_a$. (f) Difference in horizontal eigenvalues $\Delta\lambda_a$.

controlled sublimation, c-axes were measured with an automated fabric analyzer by Russel-Head Instruments (FA G50). The data was background corrected before processing, and the COF was derived via digital image processing. Here, we use the COF observations to validate our observations and modeling results. The COF information from the EastGRIP ice core stems from depths of 1830 m, 2024 m, and 2087 m, as shown in Westhoff et al. (2021), and shows a vertical girdle with a superimposed horizontal single maximum. Three samples at a depth of 68 m in the S5 shallow core show a strong horizontal single maximum fabric.

S5.3 Fabric evolution models

We use two fabric evolution models (Elmer/Ice and Specfab) to produce a more spatially complete map of fabric that can be compared to the analytical results. The simulations are detailed in the following sections.

S5.3.1 Elmer/Ice

Elmer/Ice is an open source, full-Stokes ice-flow model using the finite element method. It solves the combined problems of ice flow, heat flow and fabric evolution, thus accounting for both the fabric evolution due to temperature and deformation as well as the effect of the fabric on the mechanical properties of ice.

Model equations

Ice flow is described by the incompressible Stokes equations.

$$\nabla \cdot \boldsymbol{u} = 0, \tag{5.20}$$

where $\boldsymbol{u}$ is the velocity, and

$$\nabla \cdot \boldsymbol{\sigma} + \rho_\mathrm{i} \boldsymbol{g} = 0, \tag{5.21}$$

where $\boldsymbol{\sigma}$ is the Cauchy stress tensor, ρ_i the density of ice, and $\boldsymbol{g}$ the force of gravity. These equations are linked using a nonlinear extension to the General Orthotropic Linear Flow Law (Gillet-Chaulet et al., 2005) that, by analogy to Glen's flow law, introduces nonliterary through the second invariant of the deviatoric stress tensor (Ma et al., 2010):

$$\boldsymbol{\tau} = \eta_0 \sum_{r=1}^{3} \eta_r \mathrm{tr}(\boldsymbol{M}_r \cdot \dot{\boldsymbol{\epsilon}}) \mathrm{dev}(\boldsymbol{M}_r) + \eta_{r+3} \mathrm{dev}(\dot{\boldsymbol{\epsilon}} \cdot \boldsymbol{M}_r + \boldsymbol{M}_r \cdot \dot{\boldsymbol{\epsilon}}) \tag{5.22}$$

where $\eta_{1\ldots6}(\boldsymbol{a}^{(2)})$ are six dimensionless viscosities as a function of the fabric, tr denotes trace, dev the deviatoric portion of a tensor, $\boldsymbol{M}_{1\ldots3}$ the structure tensors that are the dyadic products of the fabric's symmetry axes (i.e. of the eigenvectors of $\boldsymbol{a}^{(2)}$), and $\eta_0 = (\tau_e^{1-n})/2A(T)$, with τ_e the second invariant of $\mathrm{dev}(\boldsymbol{\sigma})$. $A(T)$ is the temperature-dependent prefactor from Glen's flow law, and n the flow-law exponent (taken to be 3). The $\eta_{1\ldots6}(\boldsymbol{a}^{(2)})$ are found using a visco-plastic self-consistent model (Castelnau et al., 1998), assuming that ice with a single maximum fabric deforms 10 times more quickly than isotropic ice given equal shear stress while it compresses 2.5 times more slowly along the direction of the fabric maximum.

The model is solved along flowtubes, so Eqs. (5.20) and (5.21) are modified to account for a parameterized, flow-transverse coordinate $\tilde{y}$

$$\frac{\partial \sigma_{\tilde{x}\tilde{x}}}{\partial \tilde{x}} + \frac{\partial \sigma_{\tilde{x}z}}{\partial z} + \frac{\sigma_{\tilde{x}\tilde{x}} - \sigma_{\tilde{y}\tilde{y}}}{W(\tilde{x})} \frac{\partial W(\tilde{x})}{\partial \tilde{x}} = 0 \tag{5.23}$$

and

$$\frac{\partial \sigma_{\tilde{x}z}}{\partial \tilde{x}} + \frac{\partial \sigma_{zz}}{\partial z} + \frac{\sigma_{\tilde{x}z}}{W(\tilde{x})} \frac{\partial W(\tilde{x})}{\partial \tilde{x}} = \rho_\mathrm{i} g \tag{5.24}$$

for a flowband with width $W(\tilde{x})$ (e.g. Hvidberg, 1996).

Fabric evolution is assumed to occur solely by lattice rotation so that

$$\frac{\mathrm{D}\boldsymbol{a}^{(2)}}{\mathrm{D}t} = \boldsymbol{W} \cdot \boldsymbol{a}^{(2)} - \boldsymbol{a}^{(2)} \cdot \boldsymbol{W} - (\boldsymbol{C} \cdot \boldsymbol{a}^{(2)} + \boldsymbol{a}^{(2)} \cdot \boldsymbol{C}) + 2\boldsymbol{a}^{(4)} : \boldsymbol{C} + \boldsymbol{D} \tag{5.25}$$

where $\boldsymbol{W}$ is the spin tensor (anti-symmetric portion of the deformation), : is the double inner product, and

$$\boldsymbol{C} = (1 - \alpha)\dot{\boldsymbol{\epsilon}} + \alpha k_s A \tau_e^{n-1} \boldsymbol{\tau} \tag{5.26}$$

where α is an interaction parameter controlling the relative importance of bulk stress and strain in causing fabric evolution and $\boldsymbol{D}$ is used for regularization. We take $\alpha = 0.06$ (Ma et al., 2010). The term $2\boldsymbol{a}^{(4)} : \boldsymbol{C}$ in (5.25) is approximated using an invariant-based fit to a parameterized ODF to get $\boldsymbol{a}^{(4)}$ as a function of $\boldsymbol{a}^{(2)}$ (Gagliardini and Meyssonnier, 1999; Gillet-Chaulet et al., 2006). We use the regularization

$$\boldsymbol{D}\left(\boldsymbol{a}^{(2)}\right) = \begin{cases} \xi e^{\frac{\ln(10)T}{10}} (1 - 3a_{ij}^{(2)}) ||\boldsymbol{C}||_2 & \text{if } i = j \\ \xi e^{\frac{\ln(10)T}{10}} (-3a_{ij}^{(2)}) ||\boldsymbol{C}||_2 & \text{if } i \neq j \end{cases}, \tag{5.27}$$

with $\xi = 2.0 \times 10^{-3}$.

The temperature is determined using the standard advection-diffusion equation,

$$\rho_{\mathrm{i}} q \left(\frac{\partial T}{\partial t} + \boldsymbol{u} \cdot \nabla T \right) = \nabla \cdot (\kappa \nabla T) + \Psi, \tag{5.28}$$

where q and κ are the heat capacity and conductivity of ice, respectively, and $\Psi = \boldsymbol{\sigma} : \dot{\boldsymbol{\epsilon}}$ is the strain heating.

Horizontal shear is large in much of the NEGIS catchment, and occurs out of the plane of the 2.5-D model used here. $\dot{\epsilon}_{\tilde{x}\tilde{y}}$ is therefore parameterized in the fabric evolution equations. The portion of horizontal shear experienced in the model plane is

$$\dot{\epsilon}_{\tilde{x}\tilde{y}} = \frac{1}{2} \frac{\partial u}{\partial \tilde{y}} - \frac{u}{2r}, \tag{5.29}$$

where r is the radius of curvature of the flow line. We assume that the intensity of shear at depth scales with the along-flow velocity so

$$\frac{\partial u}{\partial \tilde{y}} \approx \frac{\partial u_{\mathrm{s}}}{\partial \tilde{y}} \frac{u(z)}{u_{\mathrm{s}}} \tag{5.30}$$

where u_{s} is the surface velocity. Combining (5.29) and (5.30), the horizontal shear strain rate in model coordinates can be approximated as

$$\dot{\epsilon}_{\tilde{x}\tilde{y}}(z) \simeq \frac{1}{2} \left(\frac{\partial u_{\mathrm{s}}}{\partial \tilde{y}} \frac{u(z)}{u_{\mathrm{s}}} - \frac{u(z)}{r} \right). \tag{5.31}$$

We neglect the contribution of $\dot{\epsilon}_{\tilde{x}z}$ to the fabric evolution, since that term can be shown to be small (Reeh, 1988). In addition, we neglect the effect of the horizontal shear upon the effective viscosity but include it in the temperature evolution. Before each simulation, we calculate r and $\frac{\partial u_s}{\partial \tilde{y}}$ for each model domain from a multi-year InSAR composite (Joughin et al., 2018), smoothed to 2-km resolution, and these remain fixed throughout the model runs.

Simulations

We run the model along a set of 31 flow lines in the upper catchment of NEGIS. At closest approach to the EastGRIP core site, model domains are separated by 2.5 km across flow (leading to a total width of 75 km spanned by the domains). Each model domain is 2.5D, i.e. a flowband, following a flow line while accounting for transverse convergence/divergence. We find W by tracing particle paths upstream in the measured InSAR velocities (Joughin et al., 2018), starting from a flowband half-width of 2.5 times the ice thickness (total flowband width ∼12.5 km) near the EastGRIP core site. Flowbands are wide enough to average out some of the effects of small-scale topography that can detrimentally affect flow-line models (Sergienko, 2012), but overlap with each other at some points (Fig. S5.10). Note that convergence towards the ice stream leads to significant narrowing of the central flowbands, while outer bands experience little effect from the extra half dimension. The ice surface and bed elevations defining the model geometry are determined using the average values in the across-flow directions from ArcticDEM (Porter et al., 2018) and Bedmachine v3 (Morlighem et al., 2017), respectively. In order to perform all calculations in ice-equivalent thickness, surface elevations are modified by subtracting 18 m everywhere to account for the firn-air content as estimated from RACMO 2.3.1 (Ligtenberg et al., 2018). Each model domain uses a triangular mesh with 100-m vertical and 250-m horizontal resolution. For each flowband, we run a 5-kyr transient simulation, after which changes in fabric in the areas of interest are negligible. Initial conditions are reasonable guesses for fabric and

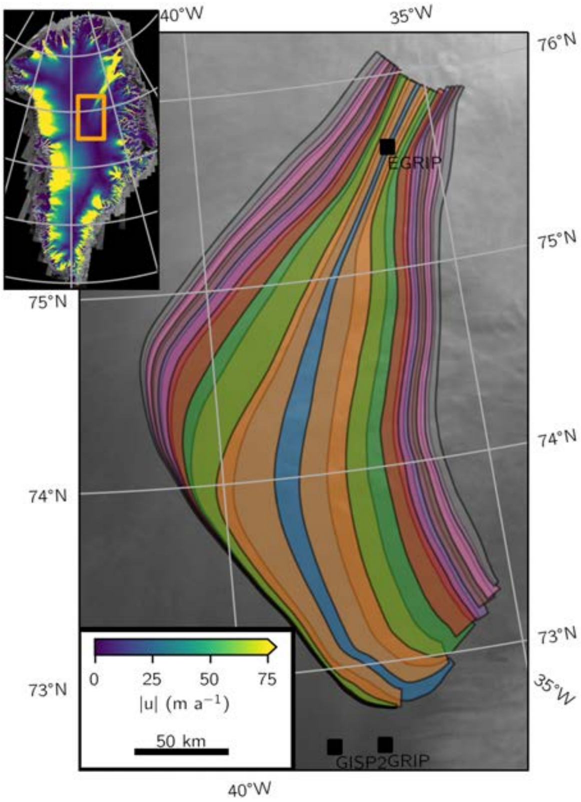

FIGURE S5.10: Model domains of the Elmer/Ice flow model. Every other domain across flow is plotted. Background from RADARSAT (Joughin et al., 2016). Inset shows location in Greenland, plotted atop ice-flow velocities (Joughin et al., 2018).

temperature, but simulations are long enough that there is no sensitivity to the exact choice. Time stepping uses a second-order backwards difference with variable time steps of 0.01–1.0 years.

Boundary Conditions

At the surface, we simply impose zero normal stress. The accumulation rate is taken to match the 1970–2016 mean from RACMO2.3 (Noël et al., 2015). At the basal boundary, we use the pattern of basal melt inferred from radar and 1-D modeling from MacGregor et al. (2016), with freeze-on zeroed out. In addition, we scale the overall pattern of basal mass loss in order to achieve mass balance (requiring a reduction of up to 50% compared to the published values), so that final ice thicknesses remained realistic.

At the downstream end of the domain, within the ice stream, we impose that the horizontal velocity matches the surface velocity at all depths, i.e. we force all motion to take place via sliding. Because we expect significant sensitivity to this assumption within a few ice thicknesses of the boundary, the model domains are designed to extend sufficiently far so as to isolate these effects from the EastGRIP validation point. When motion is purely the result of sliding, Eq. (5.20) implies that vertical strain rate is constant, so the vertical velocity varies linearly with depth. We assume that the downstream boundary is at its steady state thickness, so impose that the vertical velocity varies linearly from the accumulation rate, i.e. $u_3(S) = -a$, at the surface to the melt rate at the bed.

At the inflow boundary, we impose a depth-variable horizontal velocity scaled to match observations at the surface (Joughin et al., 2018). Assuming that ice is isothermal, isotropic, and flows purely by internal deformation, the velocity can be shown to follow (Raymond, 1983):

$$u_{\mathrm{in}}(z) = u_{\mathrm{s,in}} \left[1 - \left(\frac{H_{\mathrm{in}} - z}{H_{\mathrm{in}}} \right)^{n+1} \right], \tag{5.32}$$

where H_{in} is the ice thickness at inflow, and we take $n = 4$ as an ad-hoc fit to the weakening from fabric and temperature found at depth within the model domain at $n = 3$.

To reasonably match observed surface velocities, the model requires a variable basal velocity. We impose a spatially variable basal drag using the results of inverse modeling using a 3-dimensional model of the upper catchment of NEGIS, determined in the same manner as Holschuh et al. (2019a) but updated to suit the region of interest here. We use a linear Weertman sliding law, i.e. $\tau_b = Bu^m$, where $m = 1$ and B is determined from the inverse results. In the final 2 km of the domain, the inversion-determined B is linearly tapered to zero to ensure a smooth transition to the plug-flow boundary condition we use there.

We assume that the surface ice is isotropic, while at the upstream end we impose the profile from the NorthGRIP ice core (Wang et al., 2002b), though the results are insensitive to this choice since memory of this condition is erased before reaching the downstream end of the model domain. For temperature boundary conditions, the surface is held at the 1970–2013 2-m temperature from RACMO 2.3 (Noël et al., 2015) and the geothermal heat flux at the base is taken from a global gridded product (Davies, 2013).

Results

Before analyzing results, we define the coordinate system to have flow at angle β counter clockwise from North Polar Stereographic east, and the largest fabric eigenvalue at θ^{geo} (Fig. S5.1). Note that for the fabric, angles are equivalent mod(180°), since *c*-axes do not have a direction, but we choose to define them to be in the range $0^\circ \leq \theta^{\mathrm{geo}} \leq 180^\circ$. The depth-averaged horizontal eigenvalue differences are shown in Fig. S5.11. The range of $\Delta\lambda$ is 0–0.9, with 95% of values in the range 0–0.67. The very high values ($\Delta\lambda > 0.6$) imply a horizontal single maximum, intermediate values ($\Delta\lambda \sim$0.3-0.6) generally indicate a vertical girdle, and low values provide little information (vertical single maxima, weak vertical girdles, and isotropy all have weak horizontal anisotropy). At every point in map view, the depth-averaged $\Delta\lambda$ hides vertical structure; fabrics are universally isotropic in the surface, and are generally vertical single maxima near the bed, though in some regions the basal fabric is partway between a vertical girdle and vertical single maximum.

Horizontal shear causes rotation of the horizontal eigenvectors away from the model's $\tilde{x}$ and $\tilde{y}$ vectors (Fig. S5.11c), and generally leads to a horizontal single maximum near the ice-stream shear margins. The single maximum is stronger in the northwestern margin than the southeastern one, despite the northwestern margin being more diffuse. However, since the fabric results from the integrated strain history, this difference is unsurprising; due to residence times in the margin, the total horizontal shear experienced by a flow line is larger in the northwest margin. In geographic coordinates, the direction of the largest eigenvector is highly variable, as it is influenced both by shear and the flow direction, but it retains a notable transition at the shear margins (Fig. S5.11b).

Limitations

Though this is arguably the most advanced coupled model of fabric and flow, it still has a number of shortcomings, particularly for dynamic areas. First, the fabric evolution considers only lattice rotation; a number of studies suggest that dynamic recrystallization plays a role in the fabric evolution in warm ice, and even in colder conditions when stress is high (see Faria et

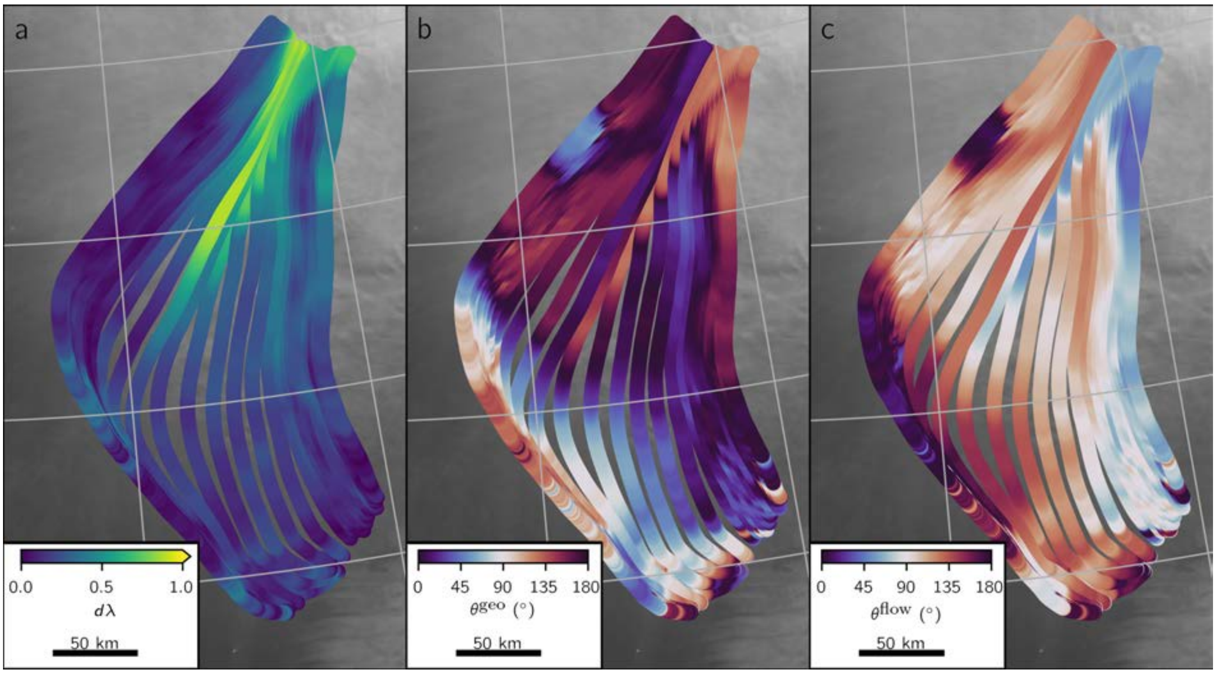

FIGURE S5.11: Results from anisotropic flow modeling. **a)** The horizontal eigenvalue difference, $\Delta\lambda$. **b)** The rotation of the largest horizontal eigenvector from Polar Stereographic x'. **c)** The rotation of the largest horizontal eigenvector from model x.

al., 2014, and references therein). While the full stress state is included the parameterized half dimension, the model is not fully three dimensional. As a result, the across-flow resolution is very coarse (effectively 2.5 km), and the horizontal shear stresses must be imposed. Imposing the horizontal stress requires smoothing of remotely sensed velocity products to obtain reasonable strain rates, which may degrade sharp gradients in the fabric. While the model assumes isotropic ice at the surface, ice cores often show anisotropic fabrics near the surface (Stoll et al., 2021; Westhoff et al., 2021). Despite these limitations, the model matches the pattern of fabric inferred from radar and measured by ice cores well enough to provide a reasonable estimate of the fabric between data points.

S5.3.2 Downstream fabric evolution modeling with 'Specfab'

Radar-inferred horizontal anisotropies over NEGIS decrease downstream of EastGRIP. The model domain of our Elmer/Ice flow model simulations extends, however, only approximately 40 km downstream of EastGRIP due to loss of numerical stability associated with higher downstream ice-flow velocities. Hence, the fabric evolution downstream can not be validated with the ice-flow model. Instead, we use the spectral fabric model for polycrystalline materials by Rathmann et al. (2021) to simulate the fabric evolution of an ice parcel along the flow line passing through EastGRIP. The model is a kinematic model in the sense that c-axes rotate in response the velocity gradient field (apparent strain-induced rotation of c-axes), and not stress or temperature.

Specifically, we consider an ice parcel seeded at EastGRIP with a girdle-type fabric that matches the average fabric measured in the ice core (Westhoff et al., 2021)

$$\boldsymbol{a}^{(2)} = \begin{pmatrix} 0 & 0 & 0 \\ 0 & 0.6 & 0 \\ 0 & 0 & 0.4 \end{pmatrix}, \tag{5.33}$$

and let it travel downstream along a flow line derived by the MeASUREs multi-year surface velocity field (Joughin et al., 2018). The flow line is divided into segments of distance traveled in one year. For each segment, the strain-rate tensor, $\dot{\boldsymbol{\epsilon}}$, is derived from surface velocities in a curvelinear coordinate system following the flow line under an assumption of negligible vertical shear and incompressibility:

$$\dot{\epsilon}_{\tilde{x}\tilde{x}} = \frac{\partial u}{\partial \tilde{x}}, \quad \dot{\epsilon}_{\tilde{y}\tilde{y}} = \frac{\partial v}{\partial \tilde{y}}, \quad \dot{\epsilon}_{\tilde{z}\tilde{z}} = -\dot{\epsilon}_{\tilde{x}\tilde{x}} - \dot{\epsilon}_{\tilde{y}\tilde{y}}, \tag{5.34}$$

$$\dot{\epsilon}_{\tilde{x}\tilde{y}} = \frac{1}{2}\left(\frac{\partial u}{\partial \tilde{y}} + \frac{\partial v}{\partial \tilde{x}}\right) \quad \dot{\epsilon}_{\tilde{x}z} = \dot{\epsilon}_{\tilde{y}z} = 0. \tag{5.35}$$

In addition, the spin is assumed to vanish, as the flow line is relatively straight:

$$\frac{1}{2}\left(\tilde{\nabla}\mathbf{u} - (\tilde{\nabla}\mathbf{u})^{\mathrm{T}}\right) = \mathbf{0}. \tag{5.36}$$

For each one-year time-step, the Lagrangian update to the parcel's fabric is given by the strain-rate and spin tensors over the traversed flow-line segment. The end of the flow-line corresponds to 2000 years downstream of EastGRIP. Figure S5.12 shows snapshots of the corresponding normalized c-axes distribution (orientation distribution function) at intervals of 1000 years. The initial girdle is found to slowly evolve into near-isotropic ice at the downstream end of the flow line. We emphasize, however, that the fabric evolution model is a linear partial differential equation. As such, any unaccounted, superimposed mode of deformation would lead to a corresponding superimposed imprint on the modeled c-axis distributions. For example, if vertical simple shear is present (not modeled here), a superimposed vertical single-maximum is to be expected that has little-to-no horizontal anisotropy. Such contributions to the total fabric pattern are, however, not detectable by our radar methodology which requires horizontal anisotropy to be present.

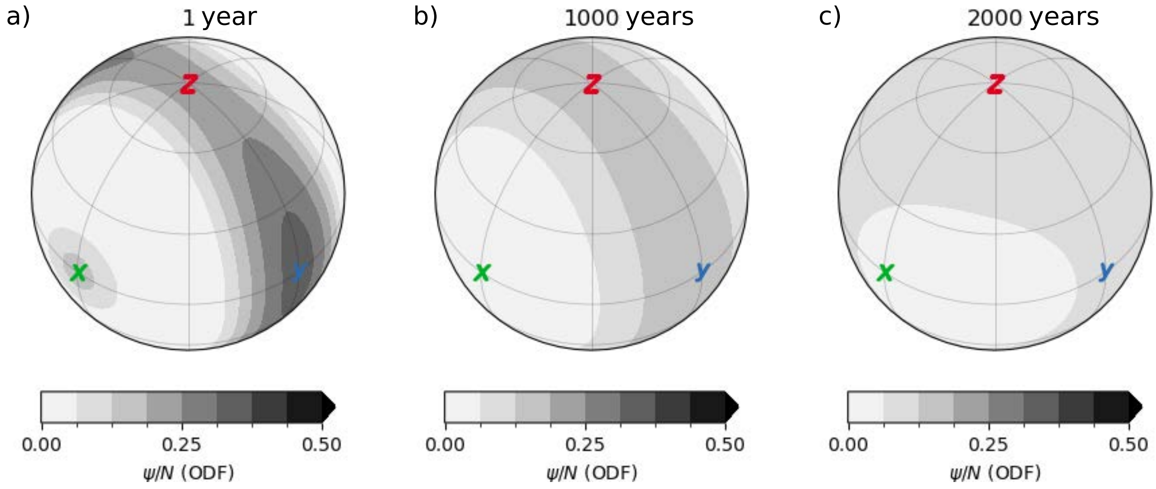

FIGURE S5.12: Fabric evolution along a downstream flow line starting at EastGRIP. The EastGRIP-type girdle in **a)** transforms rapidly into a weaker girdle shown in **b)** before it dissolves almost entirely into near-isotropic ice in **c)**. The fabric was calculated using the 'Specfab' model developed by Rathmann et al. (2021), with strain-rate tensors derived from the surface velocities (Joughin et al., 2018).

S5.4 Flow enhancement factors

To evaluate the effect that the inferred crystal fabric has upon ice flow, we calculate the bulk directional enhancement factors following Rathmann et al. (2021) and Rathmann and Lilien (2021), defined as the anisotropic-to-isotropic strain-rate ratio (Thorsteinsson, 2001)

$$E_{vw} = \frac{\dot{\epsilon}_{vw}}{\dot{\epsilon}_{vw}^{\mathrm{iso}}}, \tag{5.37}$$

where vw indicates the component (direction) of interest, and $\dot{\epsilon}_{vw}$ is the corresponding component of the bulk strain-rate tensor. While the denominator in Eq. (5.37) can be replaced by Glen's isotropic flow law, the numerator requires an anisotropic rheology that depends on the fabric state. The latter can be estimated by averaging a transversely isotropic monocrystal rheology over all grain orientations, with monocrystal rheological parameters chosen such that observed, bulk directional enhancements are reproduced (Rathmann et al., 2021; Rathmann and Lilien, 2021). For this purpose, a linear-viscous monocrystal rheology has previously been suggested to suffice upon carefully selecting a polycrystal stress–strain-rate homogenization scheme (Rathmann and Lilien, 2021). We refer the reader to Rathmann and Lilien (2021) for details, but find it instructive to write out the bulk strain rate resulting from assuming a pure stress homogenization:

$$\begin{aligned}\dot{\boldsymbol{\epsilon}} = \langle \dot{\boldsymbol{\epsilon}}'(\boldsymbol{\tau}) \rangle = A' \Bigg[\boldsymbol{\tau} - \frac{E'_{cc} - 1}{2} (\boldsymbol{\tau} \cdot\cdot \langle \boldsymbol{c}^2 \rangle) \boldsymbol{I} + \frac{3(E'_{cc} - 1) - 4(E'_{ca} - 1)}{2} \boldsymbol{\tau} \cdot\cdot \langle \boldsymbol{c}^4 \rangle \\ + (E'_{ca} - 1)(\boldsymbol{\tau} \cdot \langle \boldsymbol{c}^2 \rangle + \langle \boldsymbol{c}^2 \rangle \cdot \boldsymbol{\tau}) \Bigg],\end{aligned} \tag{5.38}$$

where $\boldsymbol{\tau}$ is the bulk deviatoric stress tensor, E'_{cc} and E'_{ca} are the monocrystal strain-rate enhancements for compression and extension along the c-axis and shearing along the basal plane, respectively, $\boldsymbol{I}$ is the identity, and A' is an isotropic rate factor. From this simple model (5.38), it is clear that the bulk enhancements effectively depend on the second and fourth-order structure tensors, $\langle \boldsymbol{c}^2 \rangle$ and $\langle \boldsymbol{c}^4 \rangle$, defined as the average over the second and fourth outer product of the individual crystal orientations ($\boldsymbol{c}_i$):

$$\boldsymbol{a}^{(2)} = \langle \boldsymbol{c}^2 \rangle = \frac{1}{N} \sum_i^N \boldsymbol{c}_i \otimes \boldsymbol{c}_i, \tag{5.39}$$

and

$$\boldsymbol{a}^{(4)} = \langle \boldsymbol{c}^4 \rangle = \frac{1}{N} \sum_i^N \boldsymbol{c}_i \otimes \boldsymbol{c}_i \otimes \boldsymbol{c}_i \otimes \boldsymbol{c}_i. \tag{5.40}$$

Indeed, in the more complicated mixed stress–strain-rate homogenization scheme used here, the resulting enhancements also depend on the fabric as quantified by $\boldsymbol{a}^{(2)}$ and $\boldsymbol{a}^{(4)}$ (not shown).

Notice that due to division in Eq. (5.37), the enhancement factors are independent of A' and the magnitude of the stress tensor. The same applies, in principle, to other isotropic contributions to the viscosity, such as temperature and impurities, insofar so they can be captured by modifying A'.

Finally, we note that in the case of a single-maximum or girdle fabric, the principal fabric directions can be taken without ambiguity to be the eigenvectors of $\boldsymbol{a}^{(2)}$. If one eigenvector is aligned with the vertical z-direction, $\boldsymbol{a}^{(2)}$ can be written in its eigenbasis as

$$\boldsymbol{a}^{(2)} = \begin{pmatrix} \lambda_x & 0 & 0 \\ 0 & \lambda_y & 0 \\ 0 & 0 & \lambda_z \end{pmatrix}. \tag{5.41}$$

S5.4.1 Estimating the second-order structure tensor from horizontal anisotropy

Our observational methodologies allow for inferring the difference in horizontal eigenvalues only, $\Delta\lambda = \lambda_y - \lambda_x$. However, by applying a few assumptions about the fabric type to be expected over the different regions of NEGIS, guided by ice-core fabric observations from EastGRIP and its shear margin, as well as modeling results, $\boldsymbol{a}^{(2)}$ can be reconstructed from $\Delta\lambda$:

1. **Inside the ice stream**: both the fabric evolution model and the EastGRIP ice core indicate the presence of a girdle in the ice-stream center, so that $\lambda_x \approx 0$. If combined with the definitions $\lambda_x + \lambda_y + \lambda_z = 1$ and $\Delta\lambda = \lambda_y - \lambda_x$, it follows that:

$$\begin{aligned} \lambda_x &= 0, \\ \lambda_y &= \Delta\lambda, \\ \lambda_z &= 1 - \Delta\lambda, \end{aligned} \tag{5.42}$$

   or equivalently

$$\mathbf{a}^{(2)} = \begin{pmatrix} 0 & 0 & 0 \\ 0 & \Delta\lambda & 0 \\ 0 & 0 & 1 - \Delta\lambda \end{pmatrix}. \tag{5.43}$$

2. **In the vicinity of the shear margins:** Ice cores and our fabric evolution modeling indicate the formation of strong horizontal single-maximum fabrics in the shear margin and its vicinity, with the largest-eigenvalue eigenvector pointing approximately perpendicular to the shear margin. We thus propose that $\lambda_x \approx \lambda_z$, from which it follows that

$$\begin{aligned} \lambda_x \approx \lambda_z &\approx \tfrac{1-\Delta\lambda}{3}, \\ \lambda_y &\approx \tfrac{1+2\Delta\lambda}{3}, \end{aligned} \tag{5.44}$$

   and therefore

$$\mathbf{a}^{(2)} = \begin{pmatrix} \frac{1-\Delta\lambda}{3} & 0 & 0 \\ 0 & \frac{1+2\Delta\lambda}{3} & 0 \\ 0 & 0 & \frac{1-\Delta\lambda}{3} \end{pmatrix}. \tag{5.45}$$

3. **Outside the shear margins:** In this regime, we lack direct observations from ice cores. Modeling results suggest that λ_x is small, but not zero. We therefore assume the more relaxed condition $\lambda_x \approx 0.1$, from which it follows that

$$\begin{aligned} \lambda_x &= 0.1, \\ \lambda_y &= 0.1 + \Delta\lambda, \\ \lambda_z &= 0.8 - \Delta\lambda, \end{aligned} \tag{5.46}$$

and therefore

$$\mathbf{a}^{(2)} = \begin{pmatrix} 0.1 & 0 & 0 \\ 0 & 0.1 + \Delta\lambda & 0 \\ 0 & 0 & 0.8 - \Delta\lambda \end{pmatrix}. \tag{5.47}$$

S5.4.2 Estimating the fourth-order structure tensor from the second-order tensor

In order to estimate the directional enhancement factors, both $\boldsymbol{a}^{(2)}$ and $\boldsymbol{a}^{(4)}$ must be known. Although our methodology is restricted in providing only $\boldsymbol{a}^{(2)}$ from radar observations, $\boldsymbol{a}^{(4)}$ can be calculated from correlations with $\boldsymbol{a}^{(2)}$, derived from ice-core fabrics and fabric modeling, as elaborated on in the following.

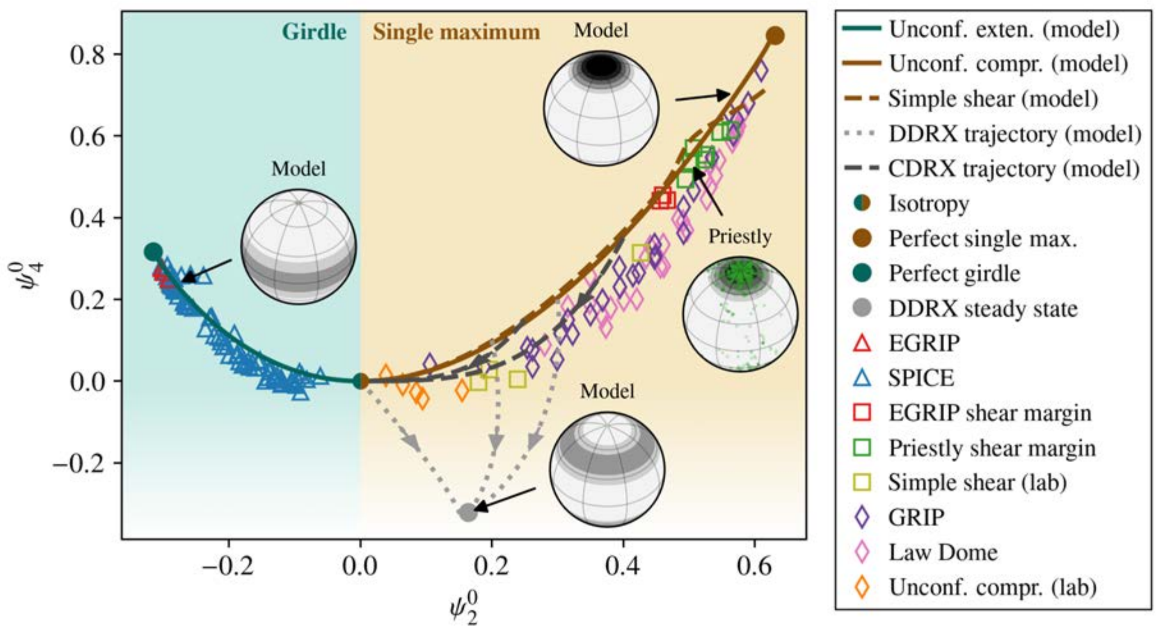

FIGURE S5.13: Correlation between the forth-order spectral coefficient, ψ_4^0, and the second-order coefficient, ψ_2^0, for girdle and single maximum fabrics. Ice-core data from EastGRIP (Westhoff et al., 2021) and SPICE (Voigt et al., 2017) follow the model-predicted correlation (full line) for unconfined extension. For single maximum fabrics, ice-core data (Thomas et al., 2021; Thorsteinsson et al., 1997; Treverrow et al., 2016) and deformation tests (Fan et al., 2020) tend to fall slightly below the modeled correlation line predicted for unconfined vertical compression and simple shear, possibly due to the influence of dynamic recrystallization (see main text). Both cores taken in our survey area (red markers), however, agree well with the modeled correlation.

The structure tensors, Eqs. (5.39) and (5.40), can be calculated from the second- ($l = 2$) and fourth-order ($l = 4$) complex expansion coefficients of the orientation distribution function (ODF) (Rathmann et al., 2021)

$$\mathrm{ODF}(\vartheta, \varphi) = \frac{1}{N} \sum_{l=0}^{\infty} \sum_{m=-l}^{l} \psi_l^m Y_l^m(\vartheta, \varphi), \tag{5.48}$$

where Y_l^m are the spherical harmonic expansion functions, depending on the co-latitude ϑ and longitude φ, and ψ_l^m are the complex expansion coefficients. In the case of a perfect single-maximum or girdle fabric (as considered here), the independent expansion coefficient reduce to just two real numbers. This follows immediately from the fact that if the fabric is rotated into a frame where it is horizontally symmetric, only ψ_2^0 and ψ_4^0 can be nonzero (only the modes Y_l^0 are rotationally symmetric around the z axis). As a consequence, if a correlation can be constructed between ψ_2^0 and ψ_4^0, then $\boldsymbol{a}^{(4)}$ can be constructed from $\boldsymbol{a}^{(2)}$ for single maximum and girdle fabrics since $\boldsymbol{a}^{(2)}$ depends exclusively on ψ_2^m (Rathmann et al., 2021).

Figure S5.13 shows a scatter plot of measured correlations (markers) between ψ_2^0 and ψ_4^0, calculated from published c-axis data from ice cores drilled at domes and extensional/flank flows sites (references provided in the figure text). Note that all c-axes distributions have been rotated into a frame where they are approximately rotationally symmetric around the z-axis for this method to work; of course, once the correlation has been applied to determine ψ_4^0, the resulting ODF can be rotated back into its original orientation.

The full lines in Fig. S5.13 show the corresponding modeled effect of lattice rotation (strain-induced rotation of c-axes) using the model by Rathmann et al. (2021), shown here for unconfined extension, leading to a perfect girdle, and for unconfined compression, leading to a perfect single maximum. Although the observed correlation for single-maximum fabrics falls slightly below the model line, fabric samples from the EastGRIP ice core (red squares) agree well with the modeled correlation, as does the NEGIS shear margin ice core (red triangles). In this work, we therefore assume that the correlation between ψ_2^0 and ψ_4^0 is given exactly by the modeled correlation (full line). We find, however, that the effect of discontinuous migration recrystallization (DDRX; dotted light gray line) and continuous recrystallization (CDRX; dashed dark gray line) might explain the discrepancy between observed and modeled correlations elsewhere.

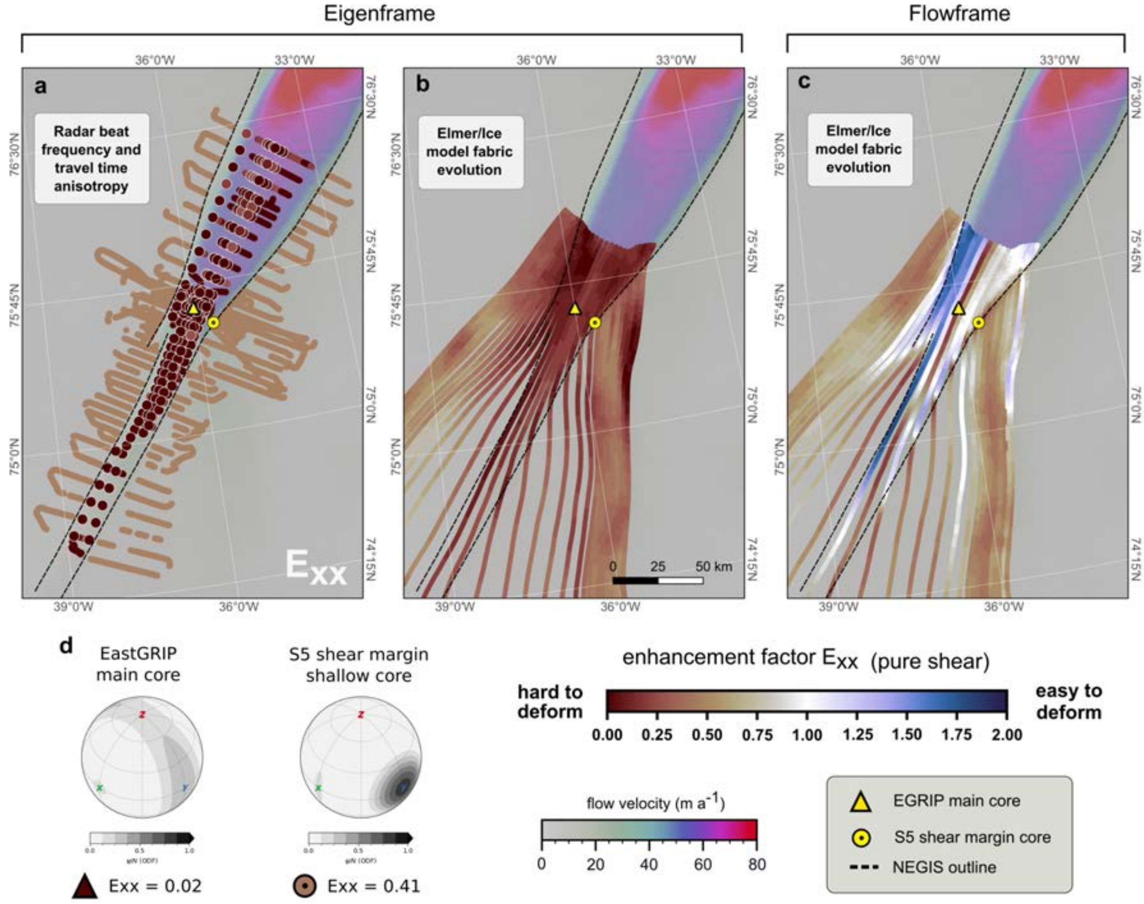

FIGURE S5.14: Enhancement factor E_{xx} (pure shear along ice flow). Panel (a) shows the enhancement factors derived from the radar measurements (both from the crosspoint analysis and beat frequency anisotropy analysis). Panel (b) and (c) show the enhancement factors derived from the Elmer/Ice fabric modeling. Note that Panels (a) and (b) represent the enhancement factors with respect to the *eigenframe* and panel (c) with respect to the *flowframe*. The respective stereographic projections of the c-axes and enhancement factors derived from the two ice-core locations (EastGRIP main core and S5 shear margin core) are shown in (d).

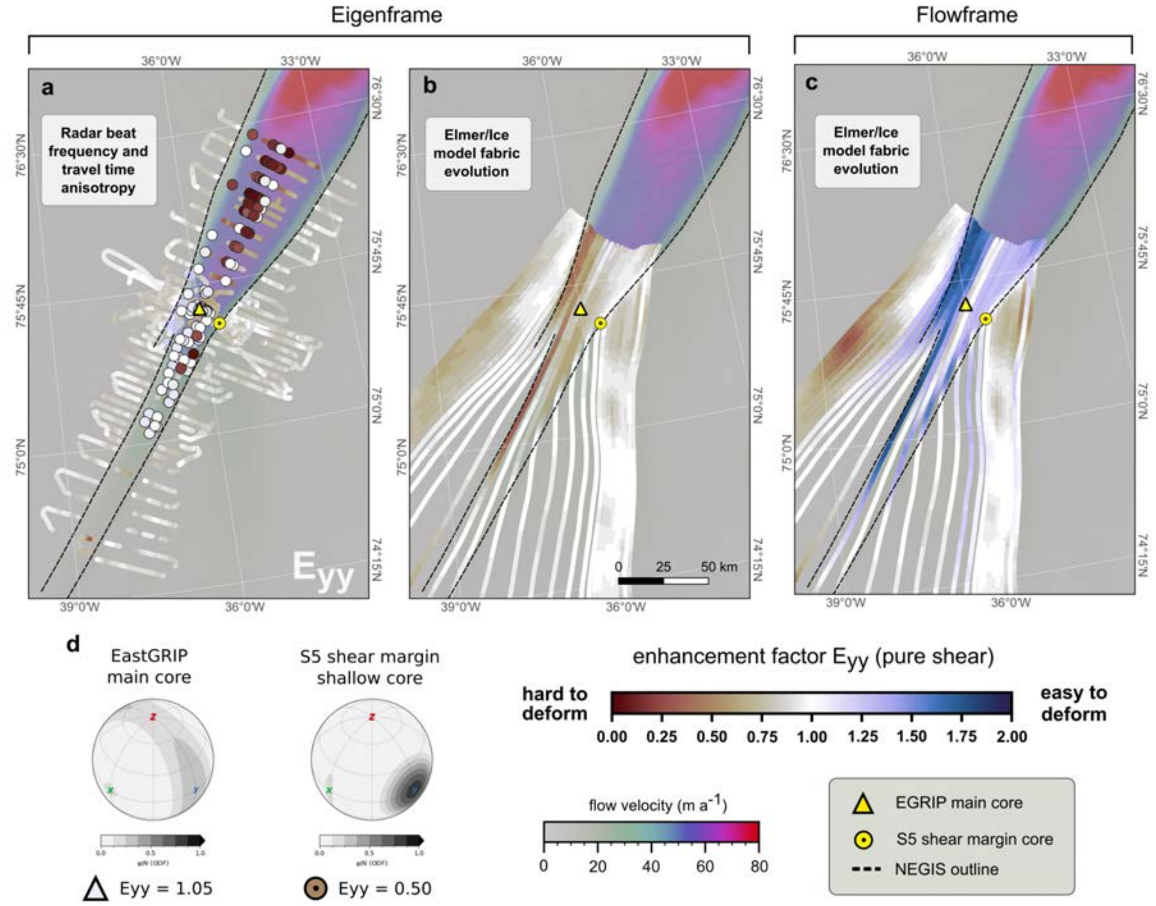

FIGURE S5.15: Enhancement factor E_{yy} (pure shear perpendicular to ice flow). Panel (a) shows the enhancement factors derived from the radar measurements (both from the crosspoint analysis and beat frequency anisotropy analysis). Panel (b) and (c) show the enhancement factors derived from the Elmer/Ice fabric modeling. Note that Panels (a) and (b) represent the enhancement factors with respect to the *eigenframe* and panel (c) with respect to the *flowframe*. The respective stereographic projections of the c-axes and enhancement factors derived from the two ice-core locations (EastGRIP main core and S5 shear margin core) are shown in (d).

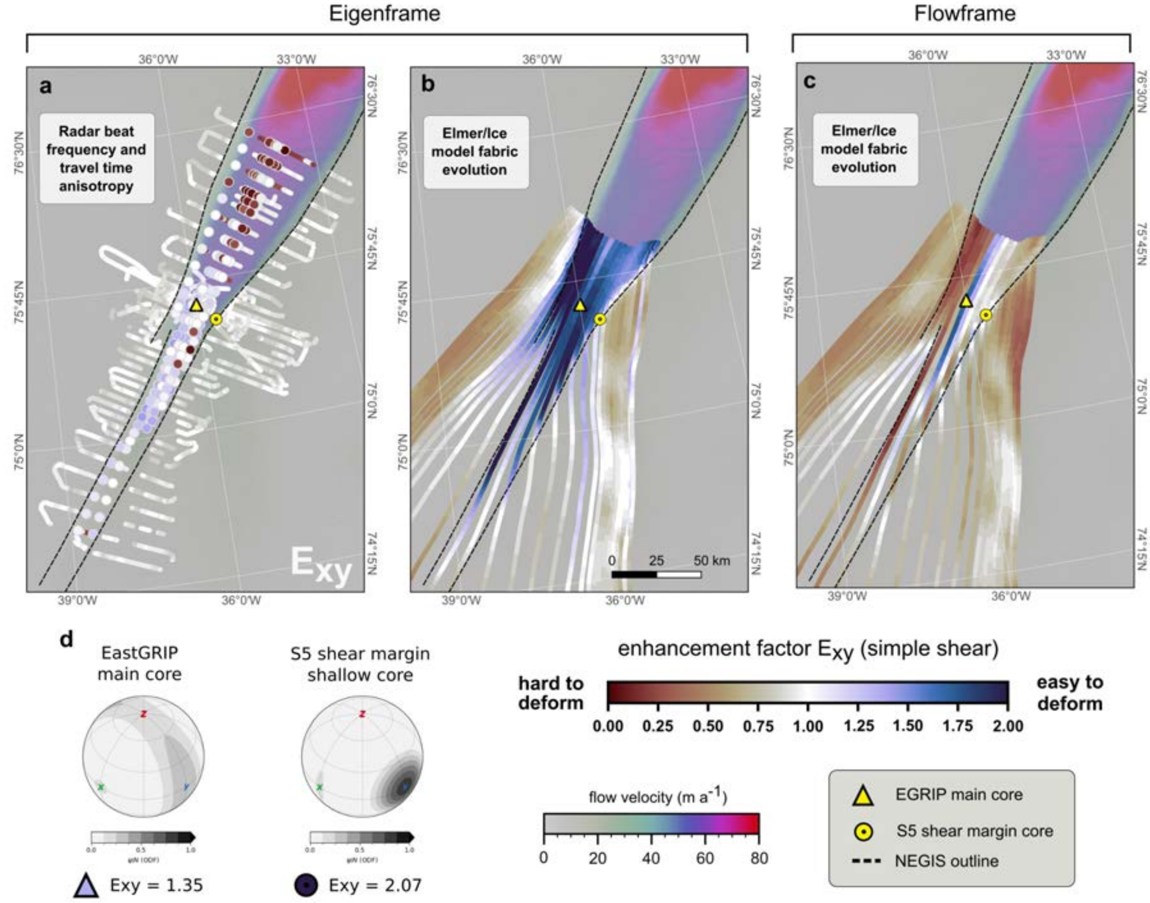

FIGURE S5.16: Enhancement factor E_{xy} (simple shear along to ice flow). Panel (a) shows the enhancement factors derived from the radar measurements (both from the crosspoint analysis and beat frequency anisotropy analysis). Panel (b) and (c) show the enhancement factors derived from the Elmer/Ice fabric modeling. Note that Panels (a) and (b) represent the enhancement factors with respect to the *eigenframe* and panel (c) with respect to the *flowframe*. The respective stereographic projections of the c-axes and enhancement factors derived from the two ice-core locations (EastGRIP main core and S5 shear margin core) are shown in (d).

S5.4.3 Equivalent enhancement due to temperature

Temperature is, besides the fabric effects, the most important factor controlling the ice viscosity. To evaluate the potential significance of either effect, we estimate the equivalent temperature difference required to obtain a similar enhancement in the corresponding direction from the enhancement factors provided above. Modified to the effect of temperature, Eq. (5.37) becomes:

$$E = \frac{\dot{\boldsymbol{\epsilon}}(\boldsymbol{\tau}, T_2)}{\dot{\boldsymbol{\epsilon}}(\boldsymbol{\tau}, T_1)} = \frac{A(T_2)\boldsymbol{\tau}^n}{A(T_1)\boldsymbol{\tau}^n}. \tag{5.49}$$

At temperatures below –10°C, the temperature dependence of the creep parameter A can be described by a simple Arrhenius relationship

$$E = \frac{A_0 \exp(-\frac{Q}{RT_2})\boldsymbol{\tau}^n}{A_0 \exp(-\frac{Q}{RT_1})\boldsymbol{\tau}^n} = \exp\left(\frac{Q}{R}\left(\frac{1}{T_1} - \frac{1}{T_2}\right)\right), \tag{5.50}$$

whereby the prefactor A_0 and the stress tensor $\boldsymbol{\tau}^n$ cancels out and R is the universal gas constant. Field measurements and laboratory measurements show that the activation energy Q is approximately 60 kJmol^{-1} for temperatures below –10°C (Weertman, 1983).

The temperatures T_1, T_2 are given in Kelvin, and can be expressed as $\Delta T = T_2 - T_1$. Equation (5.50) can thus be re-written as

$$\Delta T = \frac{{T_1}^2 \frac{R}{Q} \ln(E)}{1 - T_1 \frac{R}{Q} \ln(E)}. \tag{5.51}$$

Here, we assume that the reference temperature T_1 equals –20°C. We find that the resulting temperature anomaly relevant for the obtained enhancements is relatively insensitive toward the choice of T_1, as long as the ice is colder than –10°C (Fig. S5.17). For higher temperatures, however, the assumed value of the activation energy Q no longer holds, implying that similar enhancements could be achieved by smaller temperature anomalies in the presence of temperate ice. While this could possibly be relevant in the shear margins, we believe that temperate ice is unlikely to be found in major parts of the ice column inside and outside the ice stream. Fig. S5.18–S5.20 show the temperature anomalies (ΔT) which would be required to obtain similar viscosities as for the directional enhancements due to fabric (Fig. S5.14–Fig. S5.16).

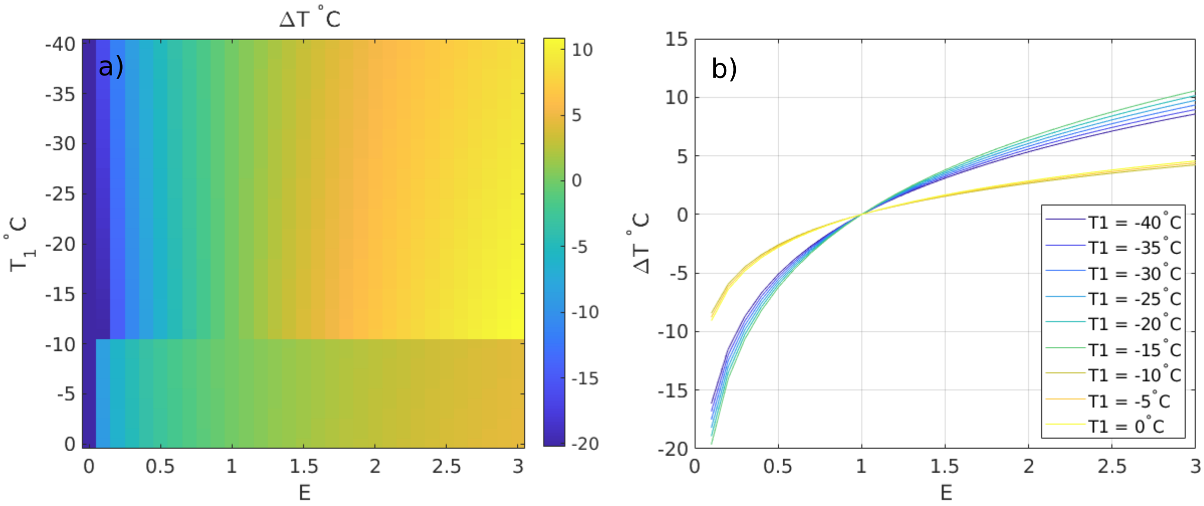

FIGURE S5.17: **a)** Temperature difference ΔT for varying enhancement factors E and a given reference temperature T_1. **b)** Sensitivity of ΔT on the choice of the reference temperature T_1. For temperatures below –20°C the activation energy Q is assumed to be 60 kJmol^{-1} whereas for temperatures above –10°C Q=152 kJmol^{-1} is assumed, leading to a stronger effect on the flow enhancement for smaller temperature variations than for colder ice. Within the two temperature regimes the sensitivity to T_1 is minor.

S5.5 Characteristic time

The characteristic time for a viscous response is defined as

$$\tau_{char} = \frac{(2+2\mu)\eta}{E}, \tag{5.52}$$

where the Poisson ratio μ in ice can be assumed to be 0.325, and the Young's modulus E is approximately 10^9 Pa. An enhancement of 0.1, equivalent to the viscosity η being ten times larger than for isotropic ice, would imply that the characteristic time is ten times smaller. Ergo, a viscous deformation happens ten times faster in ice that is harder for pure-shear deformation along-flow in comparison to isotropy.

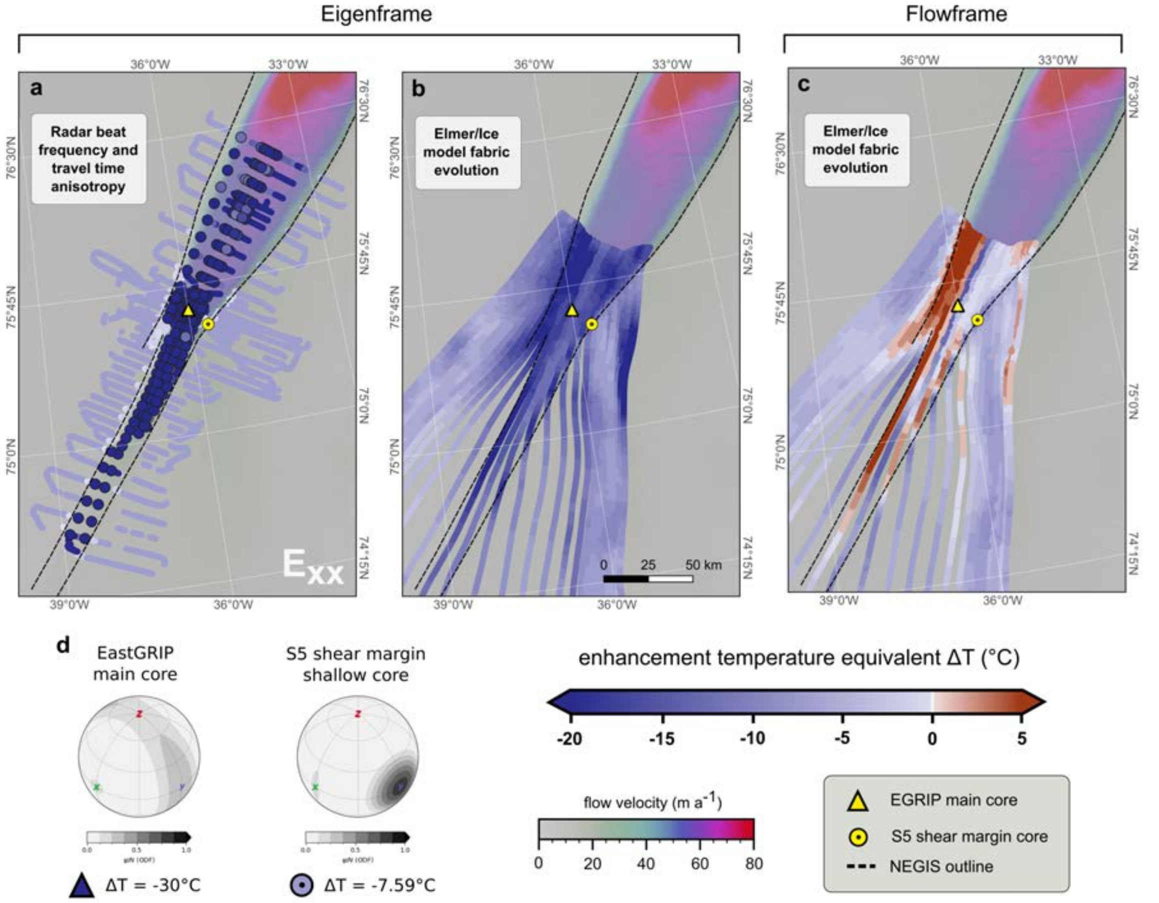

FIGURE S5.18: Temperature anomaly ΔT which would be required to obtain an (isotropic) flow enhancement as suggested by the fabric for pure-shear deformation along flow (E_{xx}). Akin to Fig. S5.14, panel **a)** shows the temperature anomalies equivalent to the enhancements obtained from radar observations, **b)** and **c)** those for the modeling results in eigenframe and flowframe respectively, and **d)** correspond to the observations in the two ice cores. Temperature anomalies are calculated for a reference temperature of –20°C.

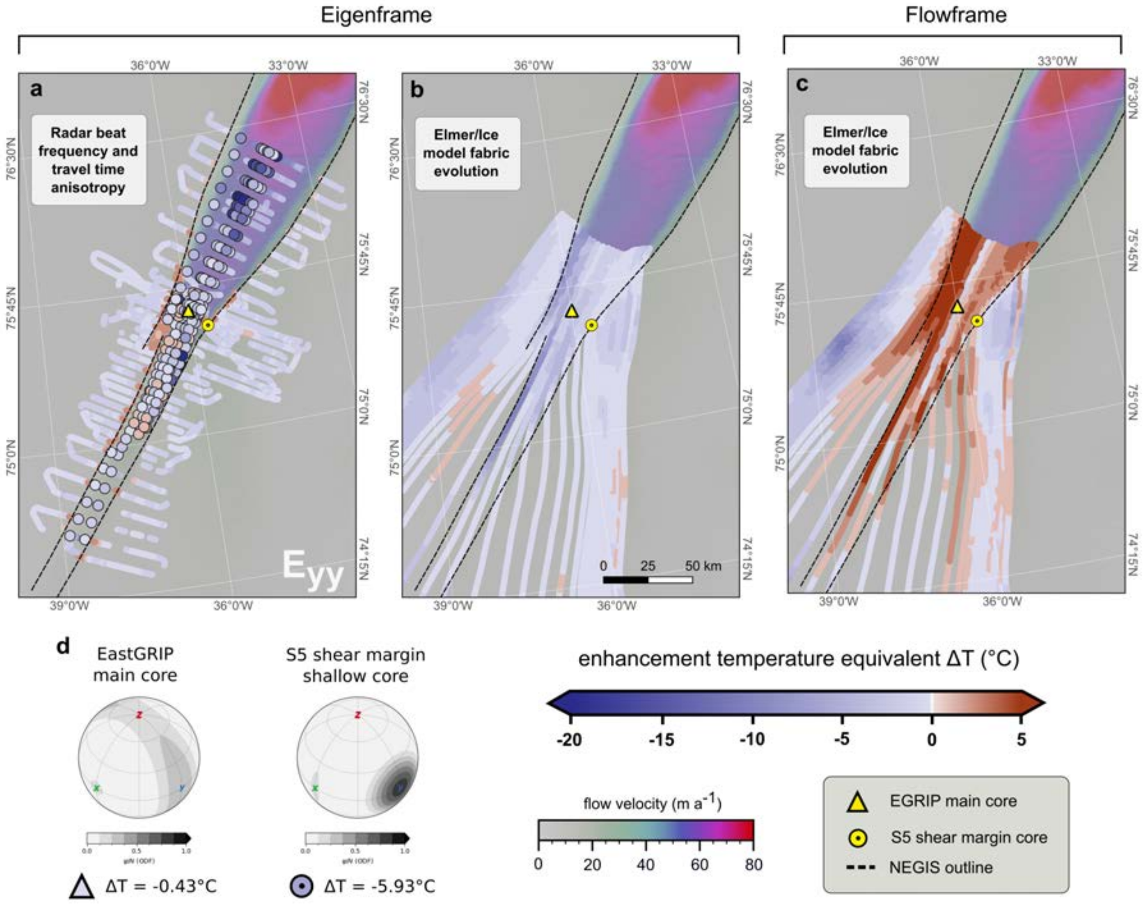

FIGURE S5.19: Temperature anomaly ΔT which would be required to obtain an (isotropic) flow enhancement as suggested by the fabric for pure-shear deformation perpendicular to flow (E_{yy}). Akin to Fig. S5.15, panel **a)** shows the temperature anomalies equivalent to the enhancements obtained from radar observations, **b)** and **c)** those for the modeling results in eigenframe and flowframe respectively, and **d)** correspond to the observations in the two ice cores. Temperature anomalies are calculated for a reference temperature of –20°C.

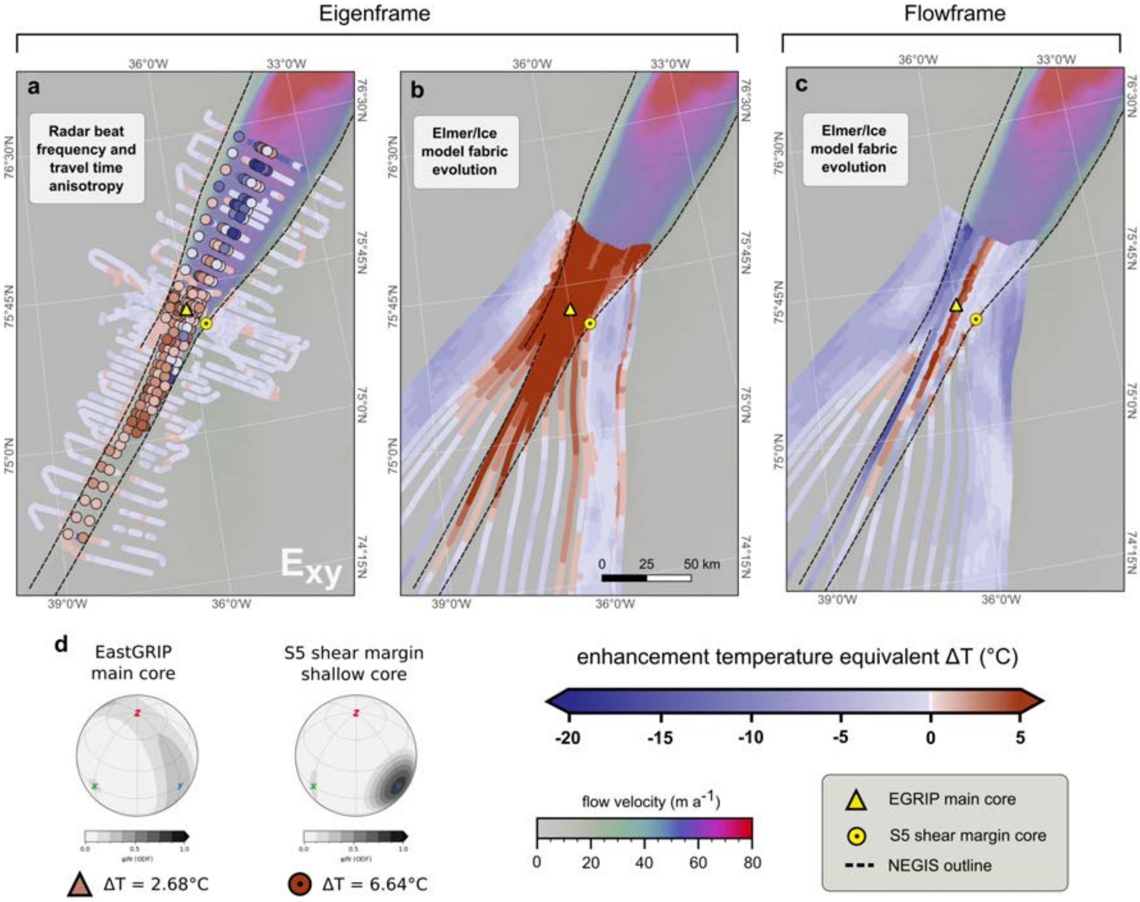

FIGURE S5.20: Temperature anomaly ΔT which would be required to obtain an (isotropic) flow enhancement as suggested by the fabric for horizontal simple-shear deformation (E_{xy}). Akin to Fig. S5.16, panel **a)** shows the temperature anomalies equivalent to the enhancements obtained from radar observations, **b)** and **c)** those for the modeling results in eigenframe and flowframe respectively, and **d)** correspond to the observations in the two ice cores. Temperature anomalies are calculated for a reference temperature of –20°C.

S5.6 Notation (not exhaustive)

x', y'	geographic east, north
$\tilde{x}, \tilde{y}$	direction parallel, transverse to ice flow
$\hat{x}, \hat{y}$	flow-parallel, flow perpendicular radar antenna polarization
x, y	direction of smaller, larger horizontal eigenvalue
z	depth below ice-sheet surface
θ^{flow}	angle between ice-flow direction and largest horizontal fabric eigenvector
θ^{geo}	angle between geographic east and largest horizontal fabric eigenvector
θ^{pol}	angle between radar polarization and horizontal fabric eigenvectors
β	angle between geographic east and ice-flow direction
$\boldsymbol{a}^{(2)}, \boldsymbol{a}^{(4)}$	second, fourth order fabric orientation tensor
$\boldsymbol{a}_{1,2,3}$	fabric eigenvectors
$\lambda_{1,2,3}, \lambda_{x,y,z}$	fabric eigenvalues of increasing size, in x, y, z direction
$\varepsilon*$	complex dielectric constant
$\varepsilon, \varepsilon_0$	relative dielectric permittivity, permittivity of free space
γ	electrical conductivity
κ	thermal conductivity
ω	angular frequency
$\boldsymbol{\varepsilon}^m, \boldsymbol{\varepsilon}$	dielectric permittivity tensor for monocrystal, polycrystal
$\varepsilon^m_{\parallel}, \varepsilon^m_{\perp}$	dielectric permittivity parallel, perpendicular to the c-axis
$\Delta\varepsilon^m, \Delta\varepsilon$	dielectric anisotropy of a monocrystal, polycrystal
ε_{xy}	horizontal mean of relative dielectric permittivity of a polycrystal
$\Delta\varepsilon_a$	apparent horizontal dielectric anisotropy between radar polarization directions $\tilde{x}$ and $\tilde{y}$
$\Delta\lambda_a$	apparent difference in horizontal eigenvalues between radar polarization directions
$\Delta\lambda$	difference in horizontal eigenvalues
c, c_0	electromagnetic wave speed, speed of light
E_x, E_y	electromagnetic wave components in principal fabric directions x and y
$t_{\hat{x}}, t_{\hat{y}}$	two-way travel time for $\hat{x}$, $\hat{y}$ polarized wave reflection
$\bar{t}, \Delta t$	mean, difference of two-way travel time between waves with different antenna polarization
$\overline{\varepsilon_{\hat{x}}}, \overline{\varepsilon_{\hat{y}}}$	depth-averaged directional permittivities
ϕ	phase difference between ordinary and extraordinary wave
f	center frequency of radar system
f_{mod}, T_{mod}	power modulation frequency, period
k	wave number
$\boldsymbol{u}, \boldsymbol{v}, \boldsymbol{w}$	ice-flow velocities flow-parallel, flow-transverse, vertical
$\boldsymbol{\sigma}$	Cauchy stress tensor
ρ_i	density of ice
g	force of gravity
$\boldsymbol{\tau}$	deviatoric stress tensor

$\boldsymbol{M}_{1,2,3}$	structure tensors
n	flow law exponent
A	flow-law prefactor
T	temperature
$W(\tilde{x})$	width of flowband
$\boldsymbol{W}$	spin tensor
$\dot{\boldsymbol{\epsilon}}$	strain rate tensor
Ψ	strain heating
r	flow-line curvature
H	ice thickness
η	ice viscosity
q	heat capacity
E_{vw}	flow enhancement factor in direction vw
E'_{cc}, E'_{ca}	enhancement of a monocrystal along the c-axis, basal plane
$\boldsymbol{c}_i$	c-axis orientation of monocrystal
ψ_l^m	complex spectral expansion coefficient
Y_l^m	spherical harmonics expansion function
R	universal gas constant
Q	activation energy

Author Contributions

OE and TAG designed and coordinated this study. TAG evaluated the airborne radar cross-points and developed the approach used here to derive horizontal anisotropy from travel-time differences. OE developed the spectrogram analysis, TJY developed the node-line analysis, FVD, TJY and OE analyzed the beat signatures. DL performed the fabric evolution simulations with Elmer/Ice. RE simulated the beat frequency modulation under supervision of RD. OZ and AH performed and analyzed the pRES measurements. NS analyzed the fabric of the East-GRIP and S5 cores. NR and TAG designed and performed the calculations of the enhancement factors and equivalent temperatures with help from AG and CH. NR and TAG simulated the downstream fabric evolution with the specfab model. OE and DJ were PI and Co-PI of the airborne radar campaign, SF and DJ processed the data with support from VH and JP. DS, VH, CO, PG, HM, DDJ and OE designed, coordinated resp. collected and processed the ground-based radar survey. SF and TAG made the main figures of the article. TAG, OE, DL, NR, TJY, RE and SF wrote the manuscript and supplement with contributions and comments from all remaining authors.

References

Albrecht, T., Winkelmann, R., and Levermann, A. (2020). “Glacial-cycle simulations of the Antarctic Ice Sheet with the Parallel Ice Sheet Model (PISM)–Part 2: Parameter ensemble analysis”. In: *The Cryosphere* 14.2, pp. 633–656. DOI: 10.5194/tc-14-633-2020.

Alley, R. B. (1988). “Fabrics in polar ice sheets: development and prediction”. In: *Science* 240.4851, pp. 493–495. DOI: 10.1126/science.240.4851.493.

Aschwanden, A., Fahnestock, M. A., and Truffer, M. (2016). “Complex Greenland outlet glacier flow captured”. In: *Nature communications* 7.1, pp. 1–8. DOI: 10.1038/ncomms10524.

Azuma, N. and Higashi, A. (1985). “Formation processes of ice fabric pattern in ice sheets”. In: *Annals of Glaciology* 6, pp. 130–134. DOI: 10.3189/1985AoG6-1-130-134.

Azuma, N., Wang, Y., Mori, K., Narita, H., Hondoh, T., Shoji, H., and Watanabe, O. (1999). “Textures and fabrics in the Dome F (Antarctica) ice core”. In: *Annals of Glaciology* 29, pp. 163–168. DOI: 10.3189/172756499781821148.

Bennett, M. R. (2003). “Ice streams as the arteries of an ice sheet: their mechanics, stability and significance”. In: *Earth-Science Reviews* 61.3-4, pp. 309–339. DOI: 10.1016/S0012-8252(02)00130-7.

Bodart, J. A., Bingham, R. G., Ashmore, D. W., Karlsson, N. B., Hein, A. S., and Vaughan, D. G. (2021). “Age-Depth Stratigraphy of Pine Island Glacier Inferred From Airborne Radar and Ice-Core Chronology”. In: *Journal of Geophysical Research: Earth Surface* 126.4. e2020JF005927 2020JF005927, e2020JF005927. DOI: https://doi.org/10.1029/2020JF005927.

Bouchez, J. and Duval, P. (1982). “The fabric of polycrystalline ice deformed in simple shear: experiments in torsion, natural deformation and geometrical interpretation”. In: *Texture, Stress, and Microstructure* 5.3, pp. 171–190.

Brennan, P. V., Lok, L. B., Nicholls, K., and Corr, H. (2014). “Phase-sensitive FMCW radar system for high-precision Antarctic ice shelf profile monitoring”. In: *IET Radar, Sonar & Navigation* 8.7, pp. 776–786. DOI: 10.1049/iet-rsn.2013.0053.

Budd, W. F. and Jacka, T. (1989). “A review of ice rheology for ice sheet modelling”. In: *Cold Regions Science and Technology* 16.2, pp. 107–144. DOI: 10.1016/0165-232X(89)90014-1.

Castelnau, O., Shoji, H., Mangeney, A., Milsch, H., Duval, P., Miyamoto, A., Kawada, K., and Watanabe, O. (1998). “Anisotropic behavior of GRIP ices and flow in Central Greenland”. In: *Earth and Planetary Science Letters* 154.1-4, pp. 307–322. DOI: 10.1016/S0012-821X(97)00193-3.

Christianson, K., Jacobel, R. W., Horgan, H. J., Alley, R. B., Anandakrishnan, S., Holland, D. M., and DallaSanta, K. J. (2016). “Basal conditions at the grounding zone of Whillans Ice Stream, West Antarctica, from ice-penetrating radar”. In: *Journal of Geophysical Research: Earth Surface* 121.11, pp. 1954–1983. DOI: https://doi.org/10.1002/2015JF003806.

Christianson, K., Peters, L. E., Alley, R. B., Anandakrishnan, S., Jacobel, R. W., Riverman, K. L., Muto, A., and Keisling, B. A. (2014). “Dilatant till facilitates ice-stream flow in northeast Greenland”. In: *Earth and Planetary Science Letters* 401, pp. 57–69. DOI: 10.1016/j.epsl.2014.05.060.

CReSIS (2020a). *cresis-toolbox*. Version 3.0.1. URL: https://doi.org/10.5281/zenodo.5683959.

Cuffey, K., Conway, H., Gades, A. M., Hallet, B., Lorrain, R., Severinghaus, J. P., Steig, E. J., Vaughn, B., and White, J. W. (2000). “Entrainment at cold glacier beds”. In: *Geology* 28.4, pp. 351–354. DOI: 10.1130/0091-7613(2000)28<351:EACGB>2.0.CO;2.

Davies, J. H. (2013). “Global map of solid Earth surface heat flow”. In: *Geochemistry, Geophysics, Geosystems* 14.10, pp. 4608–4622. DOI: 10.1002/ggge.20271.

Diprinzio, C., Wilen, L., Alley, R., Fitzpatrick, J., Spencer, M., and Gow, A. (2005). “Fabric and texture at Siple Dome, Antarctica”. In: *Journal of Glaciology* 51.173, pp. 281–290. DOI: 10.3189/172756505781829359.

Durand, G., Gagliardini, O., Thorsteinsson, T., Svensson, A., Kipfstuhl, S., and Dahl-Jensen, D. (2006). “Ice microstructure and fabric: an up-to-date approach for measuring textures”. In: *Journal of Glaciology* 52.179, pp. 619–630. DOI: `10.3189/172756506781828377`.

Durand, G., Svensson, A., Persson, A., Gagliardini, O., Gillet-Chaulet, F., Sjolte, J., Montagnat, M., and Dahl-Jensen, D. (2009). “Evolution of the texture along the EPICA Dome C ice core”. In: *Low Temperature Science* 68.Supplement, pp. 91–105.

Duval, P., Ashby, M., and Anderman, I. (1983). “Rate-controlling processes in the creep of polycrystalline ice”. In: *The Journal of Physical Chemistry* 87.21, pp. 4066–4074. DOI: `10.1021/j100244a014`.

Eisen, O., Hamann, I., Kipfstuhl, S., Steinhage, D., and Wilhelms, F. (2007). “Direct evidence for continuous radar reflector originating from changes in crystal-orientation fabric”. In: *The Cryosphere* 1.1, pp. 1–10. DOI: `10.5194/tc-1-1-2007`.

Ershadi, M. R., Drews, R., Martín, C., Eisen, O., Ritz, C., Corr, H., Christmann, J., Zeising, O., Humbert, A., and Mulvaney, R. (2022). “Polarimetric radar reveals the spatial distribution of ice fabric at domes and divides in East Antarctica”. In: *The Cryosphere* 16.5, pp. 1719–1739. DOI: `10.5194/tc-16-1719-2022`.

Eshelby, J., Frank, F., and Nabarro, F. (1951). “XLI. The equilibrium of linear arrays of dislocations.” In: *The London, Edinburgh, and Dublin Philosophical Magazine and Journal of Science* 42.327, pp. 351–364. DOI: `10.1080/14786445108561060`.

Fan, S., Hager, T., Prior, D. J., Cross, A. J., Goldsby, D. L., Qi, C., Negrini, M., and Wheeler, J. (2020). “Temperature and strain controls on ice deformation mechanisms: insights from the microstructures of samples deformed to progressively higher strains at -10, -20 and $-30\,°C$”. In: *The Cryosphere Discussions* 2020, pp. 1–43. DOI: `10.5194/tc-2020-2`.

Fan, S., Cross, A. J., Prior, D. J., Goldsby, D. L., Hager, T. F., Negrini, M., and Qi, C. (2021). “Crystallographic Preferred Orientation (CPO) Development Governs Strain Weakening in Ice: Insights From High-Temperature Deformation Experiments”. In: *Journal of Geophysical Research: Solid Earth* 126.12. e2021JB023173 2021JB023173, e2021JB023173. DOI: `10.1029/2021JB023173`.

Faria, S. H., Weikusat, I., and Azuma, N. (2014). “The microstructure of polar ice. Part I: Highlights from ice core research”. In: *Journal of Structural Geology* 61, pp. 2–20. DOI: `10.1016/j.jsg.2013.09.010`.

Fitzpatrick, J. J., Voigt, D. E., Fegyveresi, J. M., Stevens, N. T., Spencer, M. K., Cole-Dai, J., Alley, R. B., Jardine, G. E., Cravens, E. D., Wilen, L. A., Fudge, T., and Mcconnell, J. R. (2014). “Physical properties of the WAIS Divide ice core”. In: *Journal of Glaciology* 60.224, pp. 1181–1198. DOI: `10.3189/2014JoG14J100`.

Franke, S., Jansen, D., Binder, T., Paden, J. D., Dörr, N., Gerber, T. A., Miller, H., Dahl-Jensen, D., Helm, V., Steinhage, D., Weikusat, I., Wilhelms, F., and Eisen, O. (2022a). “Airborne ultra-wideband radar sounding over the shear margins and along flow lines at the onset region of the Northeast Greenland Ice Stream”. In: *Earth System Science Data* 14.2, pp. 763–779. DOI: `10.5194/essd-14-763-2022`.

Franke, S., Jansen, D., Binder, T., Paden, J. D., Dörr, N., Gerber, T. A., Miller, H., Dahl-Jensen, D., Helm, V., Steinhage, D., Weikusat, I., Wilhelms, F., and Eisen, O. (2022b). “Airborne ultra-wideband radar sounding over the shear margins and along flow lines at the onset region of the Northeast Greenland Ice Stream”. In: *Earth System Science Data* 14.2, pp. 763–779. DOI: `10.5194/essd-14-763-2022`.

Franke, S., Jansen, D., Binder, T., Dörr, N., Helm, V., Paden, J., Steinhage, D., and Eisen, O. (2020). “Bed topography and subglacial landforms in the onset region of the Northeast Greenland Ice Stream”. In: *Annals of Glaciology* 61.81, pp. 143–153. DOI: `10.1017/aog.2020.12`.

Fujita, S., Maeno, H., and Matsuoka, K. (2006). “Radio-wave depolarization and scattering within ice sheets: a matrix-based model to link radar and ice-core measurements and its application”. In: *Journal of Glaciology* 52.178, pp. 407–424. DOI: 10.3189/172756506781828548.

Gagliardini, O. and Meyssonnier, J. (1999). “Analytical derivations for the behavior and fabric evolution of a linear orthotropic ice polycrystal”. In: *Journal of Geophysical Research: Solid Earth* 104.B8, pp. 17797–17809. DOI: 10.1029/1999JB900146.

Gagliardini, O., Zwinger, T., Gillet-Chaulet, F., Durand, G., Favier, L., Fleurian, B. de, Greve, R., Malinen, M., Martı́n, C., Råback, P., Ruokolainen, J., Sacchettini, M., Schäfer, M., Seddik, H., and Thies, J. (2013). “Capabilities and performance of Elmer/Ice, a new-generation ice sheet model”. In: *Geoscientific Model Development* 6.4, pp. 1299–1318. DOI: 10.5194/gmd-6-1299-2013. URL: https://gmd.copernicus.org/articles/6/1299/2013/.

Gerbi, C., Mills, S., Clavette, R., Campbell, S., Bernsen, S., Clemens-Sewall, D., Lee, I., Hawley, R., Kreutz, K., Hruby, K., and al., et (2021). “Microstructures in a shear margin: Jarvis Glacier, Alaska”. In: *Journal of Glaciology* 67.266, pp. 1163–1176. DOI: 10.1017/jog.2021.62.

Gillet-Chaulet, F., Gagliardini, O., Meyssonnier, J., Montagnat, M., and Castelnau, O. (2005). “A user-friendly anisotropic flow law for ice-sheet modelling”. In: *Journal of Glaciology* 51.172, pp. 3–14. DOI: 10.3189/172756505781829584.

Gillet-Chaulet, F., Gagliardini, O., Meyssonnier, J., Zwinger, T., and Ruokolainen, J. (2006). “Flow-induced anisotropy in polar ice and related ice-sheet flow modelling”. In: *J. Non-Newtonian Fluid Mech* 134, pp. 33–43. DOI: 10.1016/j.jnnfm.2005.11.005.

Gogineni, S., Tammana, D., Braaten, D., Leuschen, C., Akins, T., Legarsky, J., Kanagaratnam, P., Stiles, J., Allen, C., and Jezek, K. (2001). “Coherent radar ice thickness measurements over the Greenland ice sheet”. In: *Journal of Geophysical Research: Atmospheres* 106.D24, pp. 33761–33772. DOI: 10.1029/2001JD900183.

Gow, A., Meese, D., Alley, R., Fitzpatrick, J., Anandakrishnan, S., Woods, G., and Elder, B. (1997). “Physical and structural properties of the Greenland Ice Sheet Project 2 ice core: A review”. In: *Journal of Geophysical Research: Oceans* 102.C12, pp. 26559–26575. DOI: 10.1029/97JC00165.

Gow, A. J. and Williamson, T. (1976). “Rheological implications of the internal structure and crystal fabrics of the West Antarctic ice sheet as revealed by deep core drilling at Byrd Station”. In: *Geological Society of America Bulletin* 87.12, pp. 1665–1677. DOI: 10.1130/0016-7606(1976)87<1665:RIOTIS>2.0.CO;2.

Graham, F. S., Morlighem, M., Warner, R. C., and Treverrow, A. (2018). “Implementing an empirical scalar constitutive relation for ice with flow-induced polycrystalline anisotropy in large-scale ice sheet models”. In: *The Cryosphere* 12.3, pp. 1047–1067. DOI: 10.5194/tc-12-1047-2018.

Herron, S. L. and Langway, C. C. (1982). “A comparison of ice fabrics and textures at Camp Century, Greenland and Byrd Station, Antarctica”. In: *Annals of glaciology* 3, pp. 118–124. DOI: 10.3189/S0260305500002639.

Holschuh, N., Lilien, D. A., and Christianson, K. (2019a). “Thermal Weakening, Convergent Flow, and Vertical Heat Transport in the Northeast Greenland Ice Stream Shear Margins”. In: *Geophysical Research Letters* 46.14, pp. 8184–8193. DOI: 10.1029/2019GL083436.

Holschuh, N., Christianson, K., and Anandakrishnan, S. (2014). “Power loss in dipping internal reflectors, imaged using ice-penetrating radar”. In: *Annals of Glaciology* 55.67, pp. 49–56. DOI: 10.3189/2014AoG67A005.

Hunter, P., Meyer, C., Minchew, B., Haseloff, M., and Rempel, A. (2021). “Thermal controls on ice stream shear margins”. In: *Journal of Glaciology* 67.263, pp. 435–449. DOI: 10.1017/jog.2020.118.

Hvidberg, C. S. (1996). “Steady-state thermomechanical modelling of ice flow near the centre of large ice sheets with the finite-element technique”. In: *Annals of Glaciology* 23, pp. 116–123. DOI: 10.3189/S026030550001332X.

Jordan, T. M., Williams, C. N., Schroeder, D. M., Martos, Y. M., Cooper, M. A., Siegert, M. J., Paden, J. D., Huybrechts, P., and Bamber, J. L. (2018). “A constraint upon the basal water distribution and thermal state of the Greenland Ice Sheet from radar bed echoes”. In: *The Cryosphere* 12.9, pp. 2831–2854. DOI: 10.5194/tc-12-2831-2018.

Jordan, T. M., Schroeder, D. M., Castelletti, D., Li, J., and Dall, J. (2019). “A polarimetric coherence method to determine ice crystal orientation fabric from radar sounding: application to the NEEM Ice Core Region”. In: *IEEE Transactions on Geoscience and Remote Sensing* 57.11, pp. 8641–8657. DOI: 10.1109/TGRS.2019.2921980.

Joughin, I., Smith, B. E., and Howat, I. M. (2018). “A complete map of Greenland ice velocity derived from satellite data collected over 20 years”. In: *Journal of Glaciology* 64.243, pp. 1–11. DOI: 10.1017/jog.2017.73.

Joughin, I. R., Smith, B. E., Howat, I. M., Moon, T., and Scambos, T. A. (2016). “A SAR record of early 21st century change in Greenland”. In: *Journal of Glaciology* 62.231, pp. 1–10. DOI: 10.1017/jog.2016.10.

Journaux, B., Chauve, T., Montagnat, M., Tommasi, A., Barou, F., Mainprice, D., and Gest, L. (2019). “Recrystallization processes, microstructure and crystallographic preferred orientation evolution in polycrystalline ice during high-temperature simple shear”. In: *The Cryosphere* 13.5, pp. 1495–1511. DOI: 10.5194/tc-13-1495-2019.

Kamb, B. (1972). “Experimental recrystallization of ice under stress”. In: *Washington DC American Geophysical Union Geophysical Monograph Series* 16, pp. 211–241. DOI: 10.1029/GM016p0211.

Kamb, W. B. (1959). “Ice petrofabric observations from Blue Glacier, Washington, in relation to theory and experiment”. In: *Journal of Geophysical Research* 64.11, pp. 1891–1909. DOI: 10.1086/626571.

Kuiper, E.-J. N., De Bresser, J. H., Drury, M. R., Eichler, J., Pennock, G. M., and Weikusat, I. (2020a). “Using a composite flow law to model deformation in the NEEM deep ice core, Greenland–Part 2: The role of grain size and premelting on ice deformation at high homologous temperature”. In: *The Cryosphere* 14.7, pp. 2449–2467. DOI: 10.5194/tc-14-2449-2020.

Kuiper, E.-J. N., Weikusat, I., De Bresser, J. H., Jansen, D., Pennock, G. M., and Drury, M. R. (2020b). “Using a composite flow law to model deformation in the NEEM deep ice core, Greenland–Part 1: The role of grain size and grain size distribution on deformation of the upper 2207 m”. In: *The Cryosphere* 14.7, pp. 2429–2448. DOI: 10.5194/tc-14-2429-2020.

Ligtenberg, S. R. M., Kuipers Munneke, P., Noël, B. P. Y., and Broeke, M. R. van den (2018). “Brief communication: Improved simulation of the present-day Greenland firn layer (1960–2016)”. In: *The Cryosphere* 12.5, pp. 1643–1649. DOI: 10.5194/tc-12-1643-2018.

Lilien, D. A., Rathmann, N. M., Hvidberg, C. S., and Dahl-Jensen, D. (2021). “Modeling Ice-Crystal Fabric as a Proxy for Ice-Stream Stability”. In: *Journal of Geophysical Research: Earth Surface* 126.9, e2021JF006306. DOI: 10.1029/2021JF006306.

Lipenkov, V. Y., Barkov, N., Duval, P., and Pimienta, P. (1989). “Crystalline texture of the 2083 m ice core at Vostok Station, Antarctica”. In: *Journal of Glaciology* 35.121, pp. 392–398. DOI: 10.3189/S0022143000009321.

Llorens, M.-G., Griera, A., Bons, P. D., Weikusat, I., Prior, D. J., Gomez-Rivas, E., Riese, T. de, Jimenez-Munt, I., García-Castellanos, D., and Lebensohn, R. A. (2022). “Can changes in deformation regimes be inferred from crystallographic preferred orientations in polar ice?” In: *The Cryosphere* 16.5, pp. 2009–2024. DOI: 10.5194/tc-16-2009-2022. URL: https://tc.copernicus.org/articles/16/2009/2022/.

Llorens, M.-G., GRIERA, A., BONS, P. D., ROESSIGER, J., LEBENSOHN, R., EVANS, L., and WEIKUSAT, I. (2016). “Dynamic recrystallisation of ice aggregates during co-axial viscoplastic deformation: a numerical approach”. In: *Journal of Glaciology* 62.232, pp. 359–377. DOI: 10.1017/jog.2016.28.

Ma, Y., Gagliardini, O., Ritz, C., Gillet-Chaulet, F., Durand, G., and Montagnat, M. (2010). "Enhancement factors for grounded ice and ice shelves inferred from an anisotropic ice-flow model". In: *Journal of Glaciology* 56.199, pp. 805–812. DOI: `10.3189/002214310794457209`.

MacGregor, J. A., Fahnestock, M. A., Catania, G. A., Paden, J. D., Gogineni, S. P., Young, S. K., Rybarski, S. C., Mabrey, A. N., Wagman, B. M., and Morlighem, M. (2015). "Radiostratigraphy and age structure of the Greenland Ice Sheet". In: *Journal of Geophysical Research: Earth Surface* 120.2, pp. 212–241. DOI: `10.1002/2014JF003215`.

MacGregor, J. A., Fahnestock, M. A., Catania, G. A., Aschwanden, A., Clow, G. D., Colgan, W. T., Gogineni, S. P., Morlighem, M., Nowicki, S. M. J., Paden, J. D., Price, S. F., and Seroussi, H. (2016). "A synthesis of the basal thermal state of the Greenland Ice Sheet". In: *Journal of Geophysical Research: Earth Surface* 121.7, pp. 1328–1350. DOI: `10.1002/2015JF003803`.

Martín, C., Gudmundsson, G. H., Pritchard, H. D., and Gagliardini, O. (2009). "On the effects of anisotropic rheology on ice flow, internal structure, and the age-depth relationship at ice divides". In: *Journal of Geophysical Research: Earth Surface* 114.F4. DOI: `10.1029/2008JF001204`.

Matsuoka, K., Power, D., Fujita, S., and Raymond, C. F. (2012). "Rapid development of anisotropic ice-crystal-alignment fabrics inferred from englacial radar polarimetry, central West Antarctica". In: *Journal of Geophysical Research: Earth Surface* 117.F3. DOI: `10.1029/2012JF002440`.

Matsuoka, T., Fujita, S., Morishima, S., and Mae, S. (1997). "Precise measurement of dielectric anisotropy in ice Ih at 39 GHz". In: *Journal of Applied Physics* 81.5, pp. 2344–2348. DOI: `10.1063/1.364238`.

Mojtabavi, S., Wilhelms, F., Cook, E., Davies, S. M., Sinnl, G., Skov Jensen, M., Dahl-Jensen, D., Svensson, A., Vinther, B. M., Kipfstuhl, S., Jones, G., Karlsson, N. B., Faria, S. H., Gkinis, V., Kjær, H. A., Erhardt, T., Berben, S. M. P., Nisancioglu, K. H., Koldtoft, I., and Rasmussen, S. O. (2020a). "A first chronology for the East Greenland Ice-core Project (EGRIP) over the Holocene and last glacial termination". In: *Climate of the Past* 16.6, pp. 2359–2380. DOI: `10.5194/cp-16-2359-2020`.

Mojtabavi, S., Eisen, O., Franke, S., Jansen, D., Steinhage, D., Paden, J., Dahl-Jensen, D., Weikusat, I., Eichler, J., and Wilhelms, F. (2022). "Origin of englacial stratigraphy at three deep ice core sites of the Greenland Ice Sheet by synthetic radar modelling". In: *Journal of Glaciology*, pp. 1–13. DOI: `10.1017/jog.2021.137`.

Montagnat, M., Azuma, N., Dahl-Jensen, D., Eichler, J., Fujita, S., Gillet-Chaulet, F., Kipfstuhl, S., Samyn, D., Svensson, A., and Weikusat, I. (2014). "Fabric along the NEEM ice core, Greenland, and its comparison with GRIP and NGRIP ice cores". In: *The Cryosphere* 8.4, pp. 1129–1138. DOI: `10.5194/tc-8-1129-2014`.

Montagnat, M., Buiron, D., Arnaud, L., Broquet, A., Schlitz, P., Jacob, R., and Kipfstuhl, S. (2012). "Measurements and numerical simulation of fabric evolution along the Talos Dome ice core, Antarctica". In: *Earth and Planetary Science Letters* 357, pp. 168–178. DOI: `10.1016/j.epsl.2012.09.025`.

Monz, M. E., Hudleston, P. J., Prior, D. J., Michels, Z., Fan, S., Negrini, M., Langhorne, P. J., and Qi, C. (2021). "Full crystallographic orientation (c and a axes) of warm, coarse-grained ice in a shear-dominated setting: a case study, Storglaciären, Sweden". In: *The Cryosphere* 15.1, pp. 303–324. DOI: `10.5194/tc-15-303-2021`.

Morlighem, M., Williams, C. N., Rignot, E., An, L., Arndt, J. E., Bamber, J. L., Catania, G., Chauché, N., Dowdeswell, J. A., Dorschel, B., Fenty, I., Hogan, K., Howat, I., Hubbard, A., Jakobsson, M., Jordan, T. M., Kjeldsen, K. K., Millan, R., Mayer, L., Mouginot, J., Noël, B. P. Y., O'Cofaigh, C., Palmer, S., Rysgaard, S., Seroussi, H., Siegert, M. J., Slabon, P., Straneo, F., Broeke, M. R. van den, Weinrebe, W., Wood, M., and Zinglersen, K. B. (2017). "BedMachine v3: Complete Bed Topography and Ocean Bathymetry Mapping of Greenland From Multibeam Echo Sounding Combined With Mass Conservation". In: *Geophysical Research Letters* 44.21, pp. 11, 051–11, 061. DOI: `10.1002/2017GL074954`.

Mouginot, J., Rignot, E., Bjørk, A. A., Van den Broeke, M., Millan, R., Morlighem, M., Noël, B., Scheuchl, B., and Wood, M. (2019). "Forty-six years of Greenland Ice Sheet mass balance from 1972 to 2018". In: *Proceedings of the national academy of sciences* 116.19, pp. 9239–9244. DOI: 10.1073/pnas.1904242116.

Nettles, M., Larsen, T. B., Elosegui, P., Hamilton, G. S., Stearns, L. A., Ahlstrøm, A. P., Davis, J. L., Andersen, M. L., Juan, J. de, Khan, S. A., Stenseng, L., Ekström, G., and Forsberg, R. (2008). "Step-wise changes in glacier flow speed coincide with calving and glacial earthquakes at Helheim Glacier, Greenland". In: *Geophysical Research Letters* 35.24. DOI: 10.1029/2008GL036127.

Nicholls, K. W., Corr, H. F., Stewart, C. L., Lok, L. B., Brennan, P. V., and Vaughan, D. G. (2015). "A ground-based radar for measuring vertical strain rates and time-varying basal melt rates in ice sheets and shelves". In: *Journal of Glaciology* 61.230, pp. 1079–1087. DOI: 10.3189/2015JoG15J073.

Noël, B., Van De Berg, W. J., Van Meijgaard, E., Kuipers Munneke, P., Van De Wal, R. S. W., and Van Den Broeke, M. R. (2015). "Evaluation of the updated regional climate model RACMO2.3 : Summer snowfall impact on the Greenland Ice Sheet". In: *The Cryosphere* 9.5, pp. 1831–1844. DOI: 10.5194/tc-9-1831-2015.

Oraschewski, F. M. and Grinsted, A. (2021). "Modeling enhanced firn densification due to strain softening". In: *The Cryosphere Discussions*, pp. 1–24.

Paren, J. and Robin, G. d. Q. (1975). "Internal reflections in polar ice sheets". In: *Journal of Glaciology* 14.71, pp. 251–259. DOI: 10.3189/S0022143000021730.

Pimienta, P., Duval, P., and Lipenkov, V. Y. (1987). "Mechanical behaviour of anisotropic polar ice". In: *The Physical Basis of Ice Sheet Modelling*. IAHS Publication No. 170. Wallingford, UK: IAHS Press, pp. 57–66.

Porter, C., Morin, P., Howat, I., Noh, M. J., Bates, B., Peterman, K., Keesey, S., Schlenk, M., Gardiner, J., and Tomko, K. (2018). "ArcticDEM". In: *Harvard Dataverse* 1.

Ranganathan, M., Minchew, B., Meyer, C. R., and Gudmundsson, G. H. (2021). "A new approach to inferring basal drag and ice rheology in ice streams, with applications to West Antarctic ice streams". In: *Journal of Glaciology* 67.262, pp. 229–242. DOI: 10.1017/jog.2020.95.

Rathmann, N. M., Hvidberg, C. S., Grinsted, A., Lilien, D. A., and Dahl-Jensen, D. (2021). "Effect of an orientation-dependent non-linear grain fluidity on bulk directional enhancement factors". In: *Journal of Glaciology* 67.263, pp. 569–575. DOI: 10.1017/jog.2020.117.

Rathmann, N. M. and Lilien, D. A. (2021). "Inferred basal friction and mass flux affected by crystal-orientation fabrics". In: *Journal of Glaciology*, pp. 1–17. DOI: 10.1017/jog.2021.88.

Raymond, C. F. (1983). "Deformation in the Vicinity of Ice Divides". In: *Journal of Glaciology* 29.103, pp. 357–373. DOI: 10.3189/S0022143000030288.

Reeh, N. (1988). "A Flow-line Model for Calculating the Surface Profile and the Velocity, Strainrate, and Stress Fields in an Ice Sheet". In: *Journal of Glaciology* 34.116, pp. 46–55. DOI: 10.3189/S0022143000009059.

Rignot, E., Casassa, G., Gogineni, P., Krabill, W., Rivera, A., and Thomas, R. (2004). "Accelerated ice discharge from the Antarctic Peninsula following the collapse of Larsen B ice shelf". In: *Geophysical research letters* 31.18. DOI: 10.1029/2004GL020697.

Riverman, K. L., Alley, R. B., Anandakrishnan, S., Christianson, K., Holschuh, N. D., Medley, B., Muto, A., and Peters, L. E. (2019). "Enhanced Firn Densification in High-Accumulation Shear Margins of the NE Greenland Ice Stream". In: *Journal of Geophysical Research: Earth Surface* 124.2, pp. 365–382. DOI: 10.1029/2017JF004604.

Robin, G. d. Q., Evans, S., and Bailey, J. T. (1969). "Interpretation of radio echo sounding in polar ice sheets". In: *Philosophical Transactions of the Royal Society of London. Series A, Mathematical and Physical Sciences* 265.1166, pp. 437–505. DOI: 10.1098/rsta.1969.0063.

Rückamp, M., Kleiner, T., and Humbert, A. (2022). "Comparison of ice dynamics using full-Stokes and Blatter–Pattyn approximation: application to the Northeast Greenland Ice Stream". In: *The Cryosphere* 16.5, pp. 1675–1696. DOI: `10.5194/tc-16-1675-2022`. URL: `https://tc.copernicus.org/articles/16/1675/2022/`.

Samyn, D., Svensson, A., and Fitzsimons, S. (2008). "Dynamic implications of discontinuous recrystallization in cold basal ice: Taylor Glacier, Antarctica". In: *Journal of Geophysical Research: Earth Surface* 113.F3. DOI: `10.1029/2006JF000600`.

Schroeder, D. M., Bingham, R. G., Blankenship, D. D., Christianson, K., Eisen, O., Flowers, G. E., Karlsson, N. B., Koutnik, M. R., Paden, J. D., and Siegert, M. J. (2020). "Five decades of radioglaciology". In: *Annals of Glaciology* 61.81, pp. 1–13. DOI: `10.1017/aog.2020.11`.

Sergienko, O. V. (2012). "The effects of transverse bed topography variations in ice-flow models". In: *Journal of Geophysical Research: Earth Surface* 117.F3, n/a–n/a. DOI: `10/gpc3qk`.

Shoji, H. and Langway, C. C. (1985). "Mechanical Properties of Fresh Ice Core from Dye 3, Greenland". In: *Greenland Ice Core: Geophysics, Geochemistry, and the Environment*. American Geophysical Union (AGU), pp. 39–48. DOI: `10.1029/GM033p0039`.

Stewart, C. L., Christoffersen, P., Nicholls, K. W., Williams, M. J., and Dowdeswell, J. A. (2019). "Basal melting of Ross Ice Shelf from solar heat absorption in an ice-front polynya". In: *Nature Geoscience* 12.6, p. 435. DOI: `10.1038/s41561-019-0356-0`.

Stewart, C. L. (2018). "Ice-ocean interactions beneath the north-western Ross Ice Shelf, Antarctica". PhD thesis. University of Cambridge. DOI: `10.17863/CAM.21483`.

Stoll, N., Eichler, J., Hörhold, M., Erhardt, T., Jensen, C., and Weikusat, I. (2021). "Microstructure, micro-inclusions, and mineralogy along the EGRIP ice core–Part 1: Localisation of inclusions and deformation patterns". In: *The Cryosphere* 15.12, pp. 5717–5737. DOI: `10.5194/tc-15-5717-2021`.

Thomas, R. E., Negrini, M., Prior, D. J., Mulvaney, R., Still, H., Bowman, M. H., Craw, L., Fan, S., Hubbard, B., Hulbe, C., Kim, D., and Lutz, F. (2021). "Microstructure and crystallographic preferred orientations of an azimuthally oriented ice core from a lateral shear margin: Priestley Glacier, Antarctica". In: *Frontiers in Earth Science* 9. DOI: `10.3389/feart.2021.702213`.

Thomas, R. H. (2004). "Force-perturbation analysis of recent thinning and acceleration of Jakobshavn Isbræ, Greenland". In: *Journal of Glaciology* 50.168, pp. 57–66. DOI: `10/cvrgdd`.

Thorsteinsson, T., Kipfstuhl, J., and Miller, H. (1997). "Textures and fabrics in the GRIP ice core". In: *Journal of Geophysical Research: Oceans* 102.C12, pp. 26583–26599. DOI: `10.1029/97JC00161`.

Thorsteinsson, T. (2001). "An analytical approach to deformation of anisotropic ice-crystal aggregates". In: *Journal of Glaciology* 47.158, pp. 507–516. DOI: `10.3189/172756501781832124`.

Thorsteinsson, T. (2002). "Fabric development with nearest-neighbor interaction and dynamic recrystallization". In: *Journal of Geophysical Research: Solid Earth* 107.B1, ECV–3. DOI: `10.1029/2001JB000244`.

Treverrow, A., Jun, L., and Jacka, T. H. (2016). "Ice crystal *c*-axis orientation and mean grain size measurements from the Dome Summit South ice core, Law Dome, East Antarctica". In: *Earth System Science Data* 8.1, pp. 253–263. DOI: `10.5194/essd-8-253-2016`.

Vallelonga, P., Christianson, K., Alley, R. B., Anandakrishnan, S., Christian, J. E. M., Dahl-Jensen, D., Gkinis, V., Holme, C., Jacobel, R. W., Karlsson, N. B., Keisling, B. A., Kipfstuhl, S., Kjær, H. A., Kristensen, M. E. L., Muto, A., Peters, L. E., Popp, T., Riverman, K. L., Svensson, A. M., Tibuleac, C., Vinther, B. M., Weng, Y., and Winstrup, M. (2014). "Initial results from geophysical surveys and shallow coring of the Northeast Greenland Ice Stream (NEGIS)". In: *The Cryosphere* 8.4, pp. 1275–1287. DOI: `10.5194/tc-8-1275-2014`.

Vaňková, I., Nicholls, K. W., Corr, H. F., Makinson, K., and Brennan, P. V. (2020). "Observations of tidal melt and vertical strain at the Filchner-Ronne Ice Shelf, Antarctica". In: *Journal of Geophysical Research: Earth Surface* 125.1, e2019JF005280. DOI: `10.1029/2019JF005280`.

Voigt, D. et al. (2017). "c-axis fabric of the South pole ice core". In: *SPC14. US Antarctic Program (USAP) Data Center. Dataset. doi* 10, p. 601057. DOI: 10.15784/601057.

Wang, Y., Thorsteinsson, T., Kipfstuhl, J., Miller, H., Dahl-Jensen, D., and Shoji, H. (2002a). "A vertical girdle fabric in the NorthGRIP deep ice core, North Greenland". In: *Annals of Glaciology* 35, pp. 515–520. DOI: 10.3189/172756402781817301.

Wang, Y., Thorsteinsson, T., Kipfstuhl, J., Miller, H., Dahl-Jensen, D., and Shoji, H. (2002b). "A vertical girdle fabric in the NorthGRIP deep ice core, North Greenland". In: *Annals of Glaciology* 35, pp. 515–520. DOI: 10.3189/172756402781817301.

Weertman, J. (1983). "Creep deformation of ice". In: *Annual Review of Earth and Planetary Sciences* 11.1, pp. 215–240. DOI: 10.1146/annurev.ea.11.050183.001243.

Westhoff, J., Stoll, N., Franke, S., Weikusat, I., Bons, P., Kerch, J., Jansen, D., Kipfstuhl, S., and Dahl-Jensen, D. (2021). "A stratigraphy-based method for reconstructing ice core orientation". In: *Annals of Glaciology* 62.85-86, pp. 191–202. DOI: 10.1017/aog.2020.76.

Wilen, L., Diprinzio, C., Alley, R., and Azuma, N. (2003). "Development, principles, and applications of automated ice fabric analyzers". In: *Microscopy research and technique* 62.1, pp. 2–18. DOI: 10.1002/jemt.10380.

Wilhelms, F., Kipfstuhl, J., Miller, H., Heinloth, K., and Firestone, J. (1998). "Precise dielectric profiling of ice cores: a new device with improved guarding and its theory". In: *Journal of Glaciology* 44.146, pp. 171–174. DOI: 10.3189/S002214300000246X.

Williams, C. R., Hindmarsh, R. C., and Arthern, R. J. (2012). "Frequency response of ice streams". In: *Proceedings of the Royal Society A: Mathematical, Physical and Engineering Sciences* 468.2147, pp. 3285–3310. DOI: 10.1098/rspa.2012.0180.

Wilson, C. J., Russell-Head, D. S., and Sim, H. M. (2003). "The application of an automated fabric analyzer system to the textural evolution of folded ice layers in shear zones". In: *Annals of Glaciology* 37, pp. 7–17. DOI: 10.3189/172756403781815401.

Winkelmann, R., Martin, M. A., Haseloff, M., Albrecht, T., Bueler, E., Khroulev, C., and Levermann, A. (2011). "The Potsdam parallel ice sheet model (PISM-PIK)–Part 1: Model description". In: *The Cryosphere* 5.3, pp. 715–726. DOI: 10.5194/tc-5-715-2011.

Woodcock, N. (1977). "Specification of fabric shapes using an eigenvalue method". In: *Geological Society of America Bulletin* 88.9, pp. 1231–1236. DOI: 10.1130/0016-7606(1977)88<1231:SOFSUA>2.0.CO;2.

Yan, J.-B., Li, L., Nunn, J. A., Dahl-Jensen, D., O'Neill, C., Taylor, R. A., Simpson, C. D., Wattal, S., Steinhage, D., Gogineni, P., Miller, H., and Eisen, O. (2020). "Multiangle, Frequency, and Polarization Radar Measurement of Ice Sheets". In: *IEEE Journal of Selected Topics in Applied Earth Observations and Remote Sensing* 13, pp. 2070–2080. DOI: 10.1109/JSTARS.2020.2991682.

Young, T., Schroeder, D. M., Jordan, T. M., Christoffersen, P., Tulaczyk, S. M., Culberg, R., and Bienert, N. L. (2021). "Inferring ice fabric from birefringence loss in airborne radargrams: Application to the eastern shear margin of Thwaites Glacier, West Antarctica". In: *Journal of Geophysical Research: Earth Surface* 126.5, e2020JF006023. DOI: 10.1029/2020JF006023.

Zeising, O. and Humbert, A. (2021). "Indication of high basal melting at the EastGRIP drill site on the Northeast Greenland Ice Stream". In: *The Cryosphere* 15.7, pp. 3119–3128. DOI: 10.5194/tc-15-3119-2021.

Zwinger, T., Greve, R., Gagliardini, O., Shiraiwa, T., and Lyly, M. (2007). "A full Stokes-flow thermo-mechanical model for firn and ice applied to the Gorshkov crater glacier, Kamchatka". In: *Annals of Glaciology* 45, pp. 29–37. DOI: 10.3189/172756407782282543.

Chapter 6

Simulating radio-echo sounding response from the internal stratigraphy of ice sheets with GprMax

Tamara Annina Gerber[1], Steven Franke[2], and Dorthe Dahl-Jensen[1,3]

[1]*Section for the Physics of Ice, Climate and Earth, Niels Bohr Institute, University of Copenhagen, Copenhagen, Denmark*
[2]*Alfred Wegener Institute, Helmholtz Centre for Polar and Marine Research, Bremerhaven, Germany*
[3]*Centre for Earth Observation Science, University of Manitoba, Winnipeg, Canada*

Abstract

Radio-echo sounding (RES) is the most efficient technique for gaining information about the thickness, internal stratigraphy and basal properties of glaciers and ice sheets on large spatial scales. The knowledge obtained from RES is a crucial input for ice flow models which simulate the future evolution of ice sheets and their contribution to global sea level rise. Radar waves are sensitive to changes in the dielectric properties of ice, which are affected by impurities, temperature, density and the crystal orientation fabric (COF). Distinguishing between different origins of englacial reflections and understanding how geometrical effects influence the propagation and scattering of radar waves is essential for an accurate interpretation of radargrams. Numerical simulations are a helpful tool to investigate the characteristics of radar wave response in a theoretical setting, and one-dimensional models have successfully been used in previous studies to determine the origin of englacial reflections. The open-source software GprMax solves the 3D Maxwell's equations using the finite difference time domain method and allows to investigate geometrical structures and more complex material properties. Here we simulate the radar response of the internal stratigraphy near the East GReenland Ice-core Project (EastGRIP) and explore the anisotropic effects of the crystal orientation fabric and directional layer roughness observed in the EastGRIP ice core. The results obtained in this study are useful for the design and data interpretation of future radar surveys, in particular for multi-polarization systems. We further discuss challenges encountered in using GprMax for glaciological studies and provide suggestions for future applications.

6.1 Introduction

Radio-Echo-Sounding (RES) is a powerful geophysical method based on principles of electromagnetic wave propagation. Dielectric contrasts in the subsurface cause reflection, refraction and scattering of the transmitted wave and affect the signal which is recorded at or above the surface. This concept is used for a wide spectrum of applications, ranging from localizing archaeological, military and geological targets (e.g. Vaughan, 1986; Benson, 1995; Yu et al., 1999; Neal, 2004) over determining the extent of environmental contamination (e.g. Daniels et al., 1995; Knight, 2001) to identifying obstructions, cracks or corrosion in construction and engineering projects (e.g. Solla et al., 2012; Hong et al., 2015; Ludeno et al., 2020). Glacier ice is nearly transparent for electromagnetic waves at radar frequencies (Waite and Schmidt, 1962; Turchetti et al., 2008), so the signal absorption is small. Targets located several kilometers below the surface of an ice body can, therefore, easily be surveyed, whereas the penetration depth in most other geological materials is limited to a few meters or less. The recognition of the great potential of radioglaciology has led to an extensive and systematic surveying of glaciers and ice sheets with ground-based (e.g. Pälli et al., 2002) and airborne (Steinhage et al., 1999; Schroeder et al., 2020) systems. One of the most common goals of these surveys is to determine the ice thickness and basal properties from reflections at the ice-bed interface, which act as important constraints for ice sheet models (e.g. Steinhage et al., 1999; Li et al., 2012; Bamber et al., 2013; Gogineni et al., 2014; Franke et al., 2020). Isochronous englacial reflections moreover permit the analysis of the ice sheet stratigraphy and can provide valuable information on flow structures (Arcone et al., 2005; Campbell et al., 2013; MacGregor et al., 2015; Winter et al., 2015).

The origin of these so-called Internal Reflection Horizons (IRH), is reasonably well understood, but the distinction between the material properties that cause the dielectric contrast in the ice is not always straightforward. Reflections in the upper few hundred meters of ice sheets are primarily caused by density variations (affecting permittivity) (Robin et al., 1969; Millar, 1981; Eisen et al., 2004). Below the transition into dense ice, reflections can arise from abrupt changes in the crystal orientation fabric (COF, affecting permittivity) (Eisen et al., 2007), or by contrasts in the ice conductivity (Paren and Robin, 1975; Fujita et al., 1999; Eisen et al., 2004). The latter is understood to be the most common reflector type and is in most cases attributed to impurity layers from depositional processes of, for example, volcanic origin (Eisen et al., 2003a), or impurity contrasts related to climatic transitions, e.g. Dansgaard-Oeschger events during the Last Glacial Period (Rasmussen et al., 2013). IRHs associated with conductivity contrasts are therefore assumed to be isochrones, and can provide valuable information on ice flow dynamics or basal processes (e.g. Arcone et al., 2005; Campbell et al., 2013; MacGregor et al., 2015; Winter et al., 2015).

Changes in COF are sometimes related to climatic transitions (Durand et al., 2007), but can also be a result of ice deformation (e.g. Gow et al., 1968; Azuma and Higashi, 1985). Reflections associated with COF changes do therefore not necessarily represent horizons of uniform age. So far, only one distinct IRH in Antarctica could be directly linked to an abrupt COF change observed in the nearby EPICA Dronning Maud Land (EDML) ice core (Eisen et al., 2007). COF-induced reflections can be distinguished from those related to conductivity contrasts by using multi-frequency experiments (Fujita et al., 1999) or by analyzing the anisotropic return power (Eisen et al., 2007). Anisotropy can be measured by rotating the radar antennas or with multi-polarization systems which have become more common in recent years (Dall et al., 2010; Yan et al., 2020). However, COF is not the only mechanism that can induce anisotropy in the return signal, as directional layer roughness or elongated structures like air bubbles and crevasses could affect the radar signal in a similar fashion (Drews et al., 2012).

Numerical simulations are a helpful tool to investigate the effects of certain dielectric properties and geometries in the subsurface in a theoretical setting. One-dimensional Finite-Difference Time-Domain (FDTD) models have successfully been used in the past to investigate the nature of internal reflections (e.g. Eisen et al., 2003a,b, 2004; Eisen et al., 2007; Mojtabavi et al., 2022). Effects of birefringence and anisotropic scattering on the radar return power have been studied with matrix-based models (Fujita et al., 2006; Ershadi et al., 2022; Rathmann et al., 2022) which show the relation between horizontal anisotropy and power extinction modulation in dependence of the antenna polarization.

The open-source software GprMax (Warren et al., 2016), solves the Maxwell's equations in 3D to simulate the propagation of radar waves using the FDTD method. The 3D solution allows the representation of more complex geometrical structures, including the simulation of anisotropic materials and rough interfaces. The thorough documentation, availability of user libraries and possibility of scripting input files makes GprMax particularly user-friendly, while parallelization with OpenMP and the implemented GPU-based solver allow efficiency in using high-performance computers. GprMax has been used for a wide range of applications, including a few glaciological studies simulating for instance the RES response from permafrost (Titov and Krylov, 2015; Schennen et al., 2017; Sokolov et al., 2020), basal crevasses in Antarctica (Hillebrand et al., 2021), sea ice thickness (Matsumoto et al., 2018, 2019), englacial drainage systems (Catania et al., 2008), and CO_2 ice on Mars (Xu et al., 2022).

Here, we use GprMax to simulate the electromagnetic response of the internal stratigraphy in the Northeast Greenland Ice Stream (NEGIS), particularly focusing on anisotropic effects from COF and directional layer roughness. We use measurements and observations from the East Greenland Ice-core Project (EastGRIP) which is located in the NEGIS onset region to describe the ice characteristics. The ice-core data includes dielectric properties measured by Di-Electric Profiling (DEP) and Electrical Conductivity Measurement (ECM), COF analyses, and indication of folded layers observed in visual stratigraphy (Westhoff et al., 2021). We perform a set of simulations in order to 1) characterize the origin, depth and age of distinct internal reflections observed in radargrams recorded in the vicinity of the ice-core drill site, 2) investigate the anisotropic effects caused by the COF observed in the ice core, and 3) simulate anisotropic scattering and depolarization effects that potentially result from directional layer roughness.

6.2 Background

6.2.1 Internal reflections

The complex relative dielectric constant determines the propagation of radar waves and is defined as (Davis and Annan, 1989)

$$\varepsilon^* = \varepsilon' - i\varepsilon'', \tag{6.1}$$

where the real part ε' is the dielectric permittivity relative to the permittivity of free space ε_0. The imaginary part ε'' is the relative dielectric loss factor and can also be described as

$$\varepsilon'' = \frac{\sigma}{\omega\varepsilon_0}, \tag{6.2}$$

with σ being the electrical conductivity of the medium and ω is the angular frequency of the electromagnetic wave. Since the permittivity is several orders of magnitude larger than the conductivity, the electromagnetic wavespeed, c, is dominated by ε'

$$c = \frac{c_0}{\sqrt{\varepsilon'}}, \tag{6.3}$$

where c_0 is the speed of light. Contrasts in either the dielectric permittivity or the conductivity can cause radar wave reflections.

In the upper few hundred meters, variations in the ice density is the dominant cause of reflections (Eisen et al., 2004), affecting primarily the ice permittivity which can be measured in ice cores with DEP. In deeper ice, the density remains at a constant level and permittivity variations of roughly 1% are related to changes in the COF (Fujita et al., 2000). The ice conductivity is most affected by chemical impurities which are responsible for the majority of internal reflections below the transition into dense ice (Wolff et al., 1997). Both, the permittivity and conductivity are dependent on temperature, but contrasts are normally not strong enough to cause reflections. While density- and conductivity-induced reflections are isotropic, the return signal of COF-induced reflections is in most cases characterized by some degree of anisotropy.

6.2.2 Mechanisms of anisotropy

Anisotropic return power has been observed in several places in ice sheets (Doake, 1981; Drews et al., 2012) and can be caused by birefringence effects, anisotropic scattering, or a combination of both (Fujita et al., 2006). Ice crystals are uniaxial birefringent, so the dielectric permittivity is slightly larger along the c-axis than in the direction of the basal plane (Matsuoka et al., 1997). The COF, i.e. the orientation of the crystal lattice in the bulk, determines the dielectric anisotropy of polycrystalline ice and, COF's that result in some degree of horizontal anisotropy inevitably lead to birefringence effects in nadir surveys (Drews et al., 2012). In birefringent materials, electromagnetic waves are split into an ordinary and an extraordinary component which travel at slightly different velocities. The constructive/destructive interference between these components gives rise to modulation of the return power whereby the beat frequency (frequency of power extinction nodes with depth) depends on the degree of horizontal anisotropy (Fujita et al., 2006). A few recent studies have focused on determining the COF from birefringence-induced power modulation observed in radargrams (e.g. Brisbourne et al., 2019; Jordan et al., 2020; Ershadi et al., 2022; Young et al., 2021, see also Chapter 5). Because the ordinary and extraordinary wave components can only travel along the principal axes of the dielectric permittivity tensor, these birefringence effects are strongest for waves polarized 45° from the principal COF axes (Fujita et al., 2006), resulting in a 90° periodicity of the return signal with respect to the antenna polarization.

Anisotropic scattering is the result of anisotropic characteristics of the reflection origin and shows a periodicity of 180° (Drews et al., 2012). Reflections caused by abrupt changes in COF are in most cases anisotropic (Fujita et al., 2006), because the relative change in the directional permittivity is likely related to the rotation of fabrics which are not vertically symmetric. One example is the reflection caused by the transition from a vertical girdle to a vertical single maximum observed by Eisen et al. (2007). Other, COF-independent mechanisms of anisotropic scattering like elongated air bubbles or directional interface roughness are known to exist and have been discussed e.g. by Drews et al. (2012). The effect of elongated bubbles observed in ice cores (e.g. Ueltzhöffer et al., 2010) has been investigated by a number of studies. Most of the findings suggest a minor effect on the backscattered power (Robin et al., 1969; Hargreaves, 1978; Fujita et al., 2000), although the anisotropy can be stronger than the one from COF if the bubbles are stratified (Ackley and Keliher, 1979). In any case, effects from air bubbles seem to be more important in shallower depths where the bubble size is larger and radar frequencies tend to be higher (Drews et al., 2012).

Evidence of interface roughness is found in the visual stratigraphy in a number of ice cores (e.g. Thorsteinsson, 1996; Alley et al., 1997; Svensson et al., 2005; Faria et al., 2010; Fitzpatrick et al., 2014; Jansen et al., 2016; Westhoff et al., 2021) which show strongly disturbed and folded layers in certain parts. The folding amplitude varies typically from less than 1 cm to a few decimeters and although indication of the existence of larger-scale folds has been found (e.g. Jansen et al., 2016), the direct observation is limited by the core diameter of ∼10 cm.

The EastGRIP ice core is drilled in the highly dynamic onset region of the NEGIS where surface velocities of 55 ma^{-1} are measured (Hvidberg et al., 2020). Here, the visual stratigraphy shows a strong directionality of the layer roughness which is interpreted as folds with the folding axes oriented parallel to the flow-direction (Westhoff et al., 2021). While the type and size of the folds is comparable to other ice cores, the strong directionality of the roughness seems unique for EastGRIP (Westhoff et al., 2021). The visual stratigraphy observations are limited to the glacial period where the impurity content is high and the stratigraphy becomes visible due to the occurrence of cloudy bands (Svensson et al., 2005). The stratigraphy at EastGRIP is therefore best observed at depths larger than 1375 m (Westhoff et al., 2021), but similar folds could also exist at shallower depths. So far, little is known of whether directional roughness as observed in the EastGRIP core also exists on larger, radar-relevant scales and how that would affect RES data recorded in the field. Since the folded stratigraphy at EastGRIP and in other cores is interpreted to be a consequence of ice deformation rather than remains of surface structures (Svensson et al., 2005; Westhoff et al., 2021), potential effects on RES images could result in a useful method of mapping surface roughness and retrieve information on the ice deformation history.

6.2.3 Ice-core data

The dielectric properties of the EastGRIP ice core were measured in the field until the current borehole depth of 2122.4 m. The ECM was recorded with a method based on Hammer (1980) at a 1 mm resolution (Mojtabavi et al., 2020c). The DEP data was measured at 250 kHz with the instrument based on Moore and Paren (1987) and Moore (1993), and which was later further developed by Wilhelms et al. (1998) at a resolution of 5mm (Mojtabavi et al., 2020e,d). The COF has been analyzed in discrete samples at intervals of approximately 10–15 m (Stoll, 2019) using an automated fabric analyzer (Wilen et al., 2003; Wilson et al., 2003). The fabric is statistically described in terms of eigenvalues (e.g. Thorsteinsson et al., 1997; Durand et al., 2006), which are by convention defined as $\lambda_1 < \lambda_2 < \lambda_3$ and $\lambda_1 + \lambda_2 + \lambda_3 = 1$. The EastGRIP COF shows a transition from a single maximum in the top 100 m ($\lambda_3 \gg \lambda_1 \approx \lambda_2$) towards a vertical girdle ($\lambda_1 \ll \lambda_2 \approx \lambda_3$), with λ_1 pointing in the direction of flow (Stoll, 2019). The COF data from the EastGRIP ice core is available to this study but the full dataset has not been published yet. Therefore we are restricted in showing the fabric here and refer to Stoll (2019), where part of the data is shown and discussed.

6.3 GprMax Simulations

GprMax solves the Maxwells equations with the FDTD grid based on Yee cells (Yee, 1966). In 3D models, the Maxwell's equations are solved for transverse electromagnetic mode (TEM). For 2D models, the transverse magnetic mode (TM) is used by defining a single cell slice of the domain so the electric and magnetic field components in the invariant direction are set to zero. The 3D Maxwell's equations thus reduce to a corresponding 2D form. Numerically induced dispersion (Kunz and Luebbers, 1993; Giannopoulos, 1998) is kept as low as possible by ensuring that the spatial discretization (Δx, Δy, Δz) is at least ten times smaller than the smallest wavelength of the propagating electromagnetic fields. To ensure numerical stability, the time step (Δt) is calculated based on the spatial discretization using the CFL condition (De Moura and Kubrusly, 2013):

$$\Delta t = \frac{1}{c_0\sqrt{\frac{1}{(\Delta x)^2} + \frac{1}{(\Delta y)^2} + \frac{1}{(\Delta z)^2}}}. \tag{6.4}$$

Absorbing boundary conditions are implemented by using Perfectly Matched Layers (PML) (for details see Giannakis et al., 2012), and all simulations presented here are run with double precision.

We first simulate the RES response from the internal stratigraphy using dielectric measurements and fabric observations from the EastGRIP ice core (Section 6.3.1). Then we use a simplified model with only one or two reflectors to study the effects on layer roughness in general (2D simulations) and directional roughness (3D simulations) similar to the folded layers observed in the EastGRIP ice core (Section 6.3.2)

6.3.1 Internal stratigraphy

We simulate the radar response from the electrical stratigraphy measured in the EastGRIP ice core, while also accounting for effects related to the COF. We perform four simulations in total: First we use the conductivity inferred from DEP measurements and assume a permittivity profile derived from the DEP record, but using a constant value below the transition into pure ice (henceforth called *isotropic permittivity profile*). Second, we use the ECM-inferred conductivity instead while keeping the remaining model identical. Lastly we investigate the effect of the COF by correcting the isotropic permittivity profile with the horizontal fabric eigenvalues parallel and perpendicular to the ice flow direction.

Both, the DEP- and ECM-inferred conductivity profiles (Fig. 6.1a,b) are downsampled to a resolution of 0.02m, and the ECM conductivity is scaled so that its mean value is identical with the mean of the DEP conductivity. Both profiles are extrapolated from the drill trench at 13.75 m depth to a surface value of 4.05×10^{-5} Sm^{-1} (Winter et al., 2017). The isotropic permittivity (Fig. 6.1c,d) is set to a constant value of 3.15 below the transition into pure ice (~170m depth), following Mojtabavi et al. (2022). In the shallower part we smooth the DEP-inferred permittivity profile with a moving-average filter of 5m length to avoid simulated reflections caused by instrument noise and interpolate the signal to a surface permittivity of 1.55 (Mojtabavi et al., 2022).

The directional permittivities (Fig. 6.1d) for waves polarized in the principle horizontal fabric directions can be estimated by correcting the mean (isotropic) permittivity profile with the corresponding eigenvalues λ_x and λ_y:

$$\varepsilon'_i = \varepsilon'_{iso} + \Delta\varepsilon(\lambda_i - \frac{1}{3}), \tag{6.5}$$

where ε'_i is the relative dielectric permittivity in the ith direction, ε' is the average (isotropic) dielectric permittivity, and λ_i is the directional eigenvalue.

The model size is kept identical for all sets of simulations and has a width of 2.4 m, a depth of 2124.5 m, and a spatial resolution of 0.02 m. A hertzian dipole is used to represent the source positioned at the ice sheet surface which is separated from the upper model boundary by a 2 m thick layer of free space. The antenna polarization for two-dimensional models used here necessarily is in the invariant direction (y), imitating a line source. We use a ricker wavelet with 195 MHz center frequency to mimic similar wavelengths as the EGRIP-NOR-2018 radar data recorded in the NEGIS onset, which uses a linear chirp in the frequency band 180–210 MHz (Franke et al., 2022b). The receiver is located at the same position as the source and records the signal for a period of 30 ns. To ensure that no reflections are coming from the model boundaries we use a layer of 30 PML cells on all sides. In all models the relative permeability is set to one and the magnetic loss is assumed to be zero Ωm^{-1}. The simulations were run on the HPC facilities of Compute Canada (https://www.computecanada.ca/home/) with six CPU threads using ~2.82GB RAM and a solving time of ~10 hours.

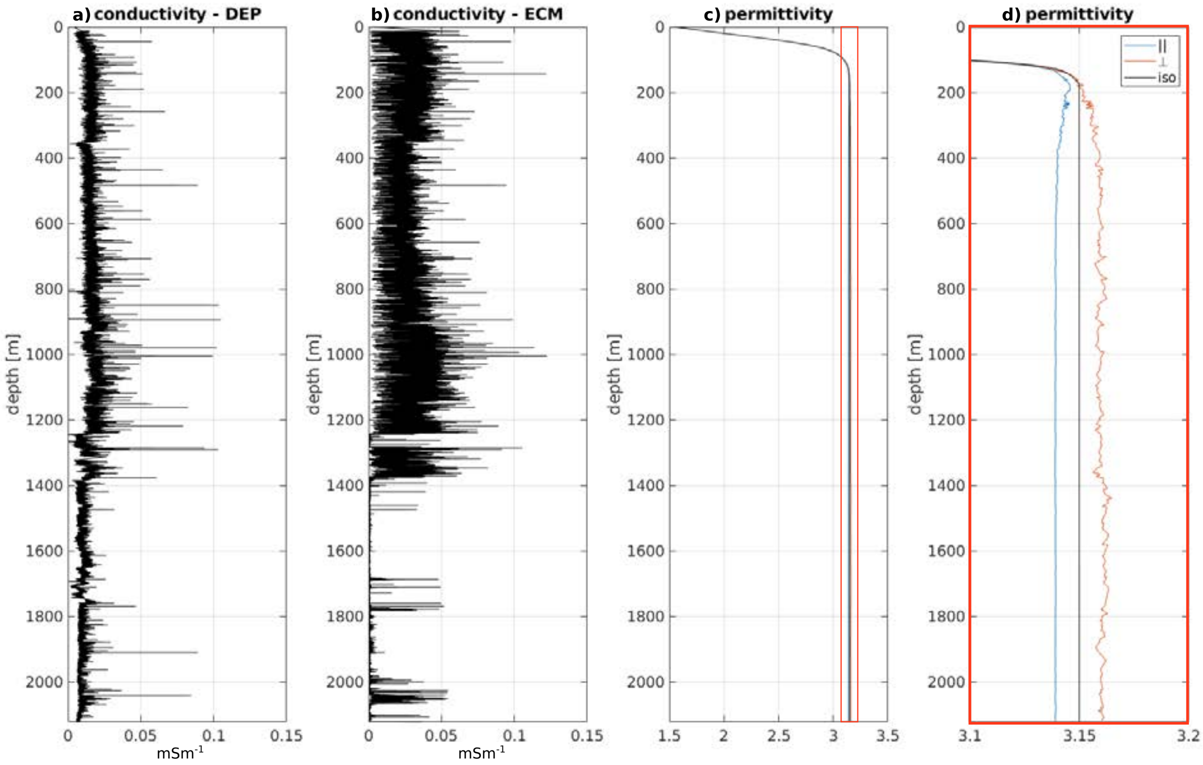

FIGURE 6.1: Model input for simulating the response of the internal stratigraphy: **a)** DEP-inferred conductivity profile, **b)** ECM-inferred conductivity scaled so it matches the average of the DEP profile, **c)** permittivity profiles with the firn-ice transition from the DEP measurements, and **d)** zoom-in to the isotropic permittivity (black) and the flow parallel (blue) and flow-perpendicular (red) permittivities obtained from the fabric eigenvalues.

6.3.2 Layer roughness

2D model simulations

We first investigate the effect of interface roughness in 2D by simulating a radar survey where the transmitter and receiver are moved along a profile (B-Scan, see Fig. 6.2a). The model size is 30 m wide and 50 m deep, at a spatial resolution of 0.02 m. The ice-sheet surface is located 5 m from the upper model boundary and a reflecting interface is positioned at a depth of 40 m. The interface roughness is described using fractal distributions, which have proved to be an accurate representation of natural interfaces (Burrough, 1981). We use the same random seed for all models to ensure comparability. We repeat the same simulation with different roughness amplitudes of 0, 0.2, 1, 2 and 6 m respectively. The material above the reflector has a conductivity of 1×10^{-5} Sm^{-1} and the conductivity below is set to 9×10^{-5} Sm^{-1}. For both materials, the dielectric permittivity is set to 3, the relative permeability is one and the magnetic loss is assumed to be zero. Above the antennas, a layer of free space is introduced with permittivity 1 and conductivity zero. On all sides 40 cells of PML are used to avoid potential side reflections from the model boundary and the layer roughness inside the PML is set to zero. The source and receiver are separated by 1 m and moved at steps of 0.25 m along a profile of 15 m length, starting at 5 m distance from the left model boundary. The source is described as a hertzian dipole polarized in the invariant model direction (y) and emitting a ricker wavelet at a center frequency of 200 MHz.

In addition to the simple case of one interface as illustrated in Fig. 6.2a, we also conduct a number of simulations with two reflectors in order to evaluate the effect of roughness on the ability to distinguish two distinct layers. Hence, we add a third layer below the reflector with a conductivity of 2×10^{-5} Sm^{-1} using the same rough interface as the layer above. The two layers are separated by 2 m and 5 m respectively, and for both cases simulations with all five roughness amplitudes are performed. The simulations were run on the EPCC HPC facilities (https://www.epcc.ed.ac.uk/), using a MPI task farm to simultaneously calculate multiple traces on four nodes. The B-scan was completed in 5 hours, where each A-Scan used ~420MB RAM and a runtime of ~14 minutes.

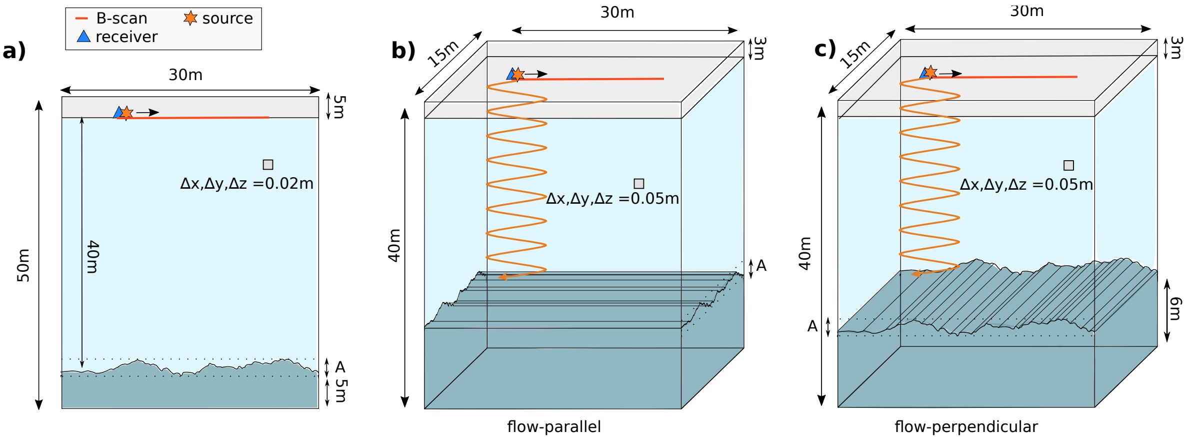

FIGURE 6.2: Model setup for layer-roughness studies: First we perform **a)** 2D simulations of a B-scan of a rough interface at depth of 40m at a high resolution. Then, the effect of folds was simulated with 3D models, imitating a profile recorded **b)** parallel and **c)** perpendicular to the flow direction. All simulations were performed with four different roughness amplitudes A.

3D model simulations

Studying the effects of directional roughness requires a three-dimensional description of the subsurface. 3D models vastly increase the numerical expenses and, therefore, some adjustments of the 2D model size have to be made in order to keep the computational costs as low as possible. The model width is maintained at 30 m length but expanded by 15 m in the invariant direction, and the model depth is decreased by 10 m. The spatial resolution is reduced to a grid spacing of 0.05 m to minimize the number of calculations. While coarser spatial resolution lowers the computational costs, it also increases the risk of numerical instability for high-frequency waves. For this reason, the center frequency of the source waveform is lowered to 150 MHz. The layer of free space above the ice sheet is set to a thickness of 3 m and a boundary layer of 40 PML cells is used at all model boundaries. The material properties are kept the same as in the 2D case, but here we limit the simulations to a single reflecting interface.

The layer roughness is described in the same way as in the 2D model but is kept invariant in one direction (Fig. 6.2b,c). We perform simulations with the same different roughness amplitudes as described for the 2D case above. The radargram is always recorded along a profile of 15 m length in the model x-direction. The source antenna is polarized along-track while the receiver records both polarizations (HH and HV). In a first set of simulations (Fig. 6.2b) we imitate a scenario where the radar profile is recorded parallel to the ice-flow direction, i.e. folding axes are oriented in x-direction parallel to the profile and the source polarization. In a second round we rotate the folds by 90 degrees to simulate a flow-perpendicular scenario where the radar profile is crossing the folding axes (Fig. 6.2c). The simulations were performed on the EPCC HPC facilities using a MPI task farm on four GPUs and each B-scan was solved in ~2 hours, whereby the memory use for the individual A-scans was ~4.34 GB RAM and 8.48 GPU.

6.4 Results

6.4.1 Origin of internal reflections

Before comparing the model output with radar data recorded in the field, we process the simulated trace by taking the envelope and applying a moving average smoothing filter of 0.05 μs window length to mimic the vertical resolution of the airborne survey. For comparison with in-situ data, we use the trace nearest to EastGRIP from the airborne profile 'Data_20180512_01_001' of the EGRIP-NOR-2018 radar survey (Franke et al., 2022b), conducted by the Alfred Wegener Institute, Helmholtz Center for Polar and Marine Sciences (AWI). The profile was recorded parallel to the ice-flow direction with an eight-antenna element system using a linear frequency-modulated chirp signal at the frequency band of 180–210 MHz.

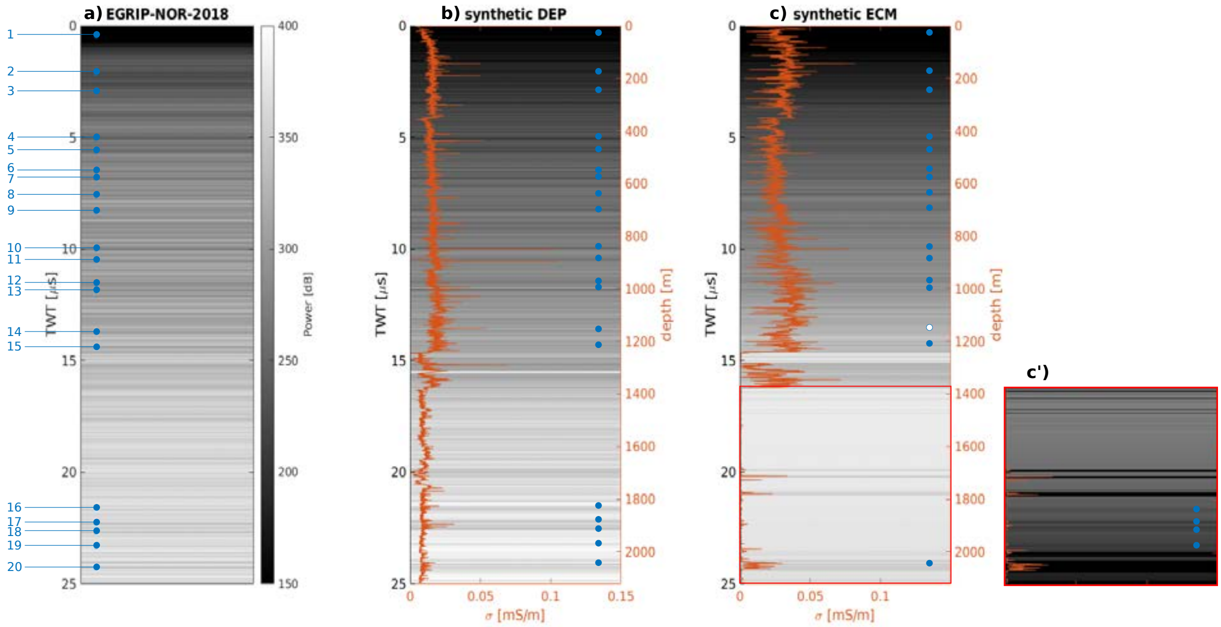

FIGURE 6.3: Comparison between **a)** radargram recorded in the field and synthetic radargrams obtained with **b)** the DEP and **c)** ECM inferred conductivity. In stadial periods (alkaline ice) the ECM signal, and hence the corresponding reflections become very small but can become visible when adjusting the contrast in the radargram **(c′)**. The reference trace in **a)** is taken to be the trace closest to EastGRIP from the Data_20180512_01_001 EGRIP-NOR-2018 radar profile (Franke et al., 2022b).

The upper ∼1200 m of the ice core is covered by ice from the Holocene (Mojtabavi et al., 2020a) where the general agreement between both synthetic radargrams and the reference trace is quite good (Fig. 6.3). Further down, the ice stems from the last glacial period, during which the atmospheric dust levels were higher than in the warmer interglacials. Chemical reactions between the deposited dust particles and the ice lead to the neutralization of acids, so the ice becomes alkaline (Wolff et al., 1995; Rasmussen et al., 2013). Since ECM is mainly sensitive to acidity, the signal level in glacial ice is reduced by around a factor of 100 compared to the Holocene (Hammer, 1980; Taylor et al., 1997). Hence, the small conductivity contrasts of the ECM result in weaker reflections than from the DEP record, which is also responding to the presence of salts (Moore et al., 1989). However, by adjusting the colorscale it can be noticed that some of the reflections observed in the field data can also be reproduced with the ECM profile (Fig. 6.3c′).

We identified 20 prominent reflections observed in the EGRIP-NOR-2018 profile (Fig. 6.3a) and which are reproduced by the simulated traces. To investigate their origin and determine their depth and age, we perform sensitivity studies by muting part of the DEP input signal (see Fig. S6.1–S6.4), following the approach by Mojtabavi et al. (2022). Most of the studied reflections can be connected to single distinct peaks in the ECM and DEP signals. In some cases, however, two or more conductivity peaks close to each other give rise to the same apparent reflection. In that case muting one or the other peak does not cause the synthetic reflection to disappear but makes it slightly weaker. This is for instance the case for reflection number 4 where two conductivity peaks at a distance of 2.4 m interfere, reflector number 9 where three peaks within a distance of 6.4 m occur, leading to a slightly more diffuse reflection (Fig. S6.2), and reflector 16 where the signal of three peaks within 5 m interferes (Fig. S6.4). Darker, 'apparently' thick reflections occur when multiple peaks appear within a short distance like the dark band between reflectors 17 and 18 (Fig. S6.4). Although there are distinct peaks in the DEP record at the upper and lower boundaries of this band, which mark the sharp transition, there are multiple moderate peaks in between which are responsible for the strong signal reflectivity.

TABLE 6.1: Characterization of internal reflections that are reproduced with the DEP-record. The layer numbered layers are shown in Fig. 6.3. The time corresponds to the two-way travel time of the reference radargram, the depth is the mean depth of the muted peak that causes the reflection and the layer age was is obtained from the EastGRIP timescale (Gerber et al., 2021), with the maximum counting error (MCE) indicating the uncertainties.

Layer number	Time [μs]	Depth [m]	Age [yrs b2k]
1	0.47	45.5	216 ± 1
2	2.10	190.1	1,466 ± 2
3	2.97	258.5	2,049 ± 1
4	5.03	437.8	3,654 ± 5
5	5.60	484.1	4,051 ± 6
6	6.50	561.4	4,705 ± 10
7	6.78	587.4	4,931 ± 11
8	7.58	651.6	5,478 ± 13
9	8.27	708.4	5,993 ± 16
10	9.95	850.1	7,250 ± 28
11	10.47	894.4	7,636 ± 35
12	11.49	980.2	8,442 ± 52
13	11.80	1,005.7	8,695 ± 57
14	13.67	1,161.8	10,478 ± 90
15	14.35	1,219.4	11,306 ± 96
16	21.57	1,826.7	34,814 ± 1291
17	22.20	1,878.7	37,133 ± 1417
18	22.57	1,910.2	38,149 ± 1446
19	23.20	1,962.9	41,156 ± 1625
20	24.14	2,042.0	45,560 ± 1848

Table 6.1 shows the relation between the two-way travel time of the reflected signal observed in the EGRIP-NOR-2018 radargram and the (average) depth of the muted DEP peak(s)

which seems to be the cause for the reflection. Knowing the ice-core depth we can also assign an age for the corresponding layer using the GICC05 timescale which was transferred to EastGRIP by Mojtabavi et al. (2020a) and Gerber et al. (2021).

6.4.2 Fabric anisotropy

The simulations with the fabric-corrected permittivity results in travel-time differences between the flow-parallel and flow-perpendicular profiles. The flow-parallel simulation is thereby slightly shifted towards longer travel times (Fig. 6.4a), which can also be observed in the comparison between radargrams recorded in flow-parallel (Data_20180512_01_001) and flow-perpendicular (Data_20180508_06_004) directions in the vicinity of EastGRIP (Fig. 6.4b). Panel c of Fig. 6.4 shows the difference between travel times perpendicular and parallel to ice flow from the GprMax simulation, as well as the travel-time difference from reflections picked in radargrams from six radar intersection points near the EastGRIP drill site (see Chapter 5, Fig. S5.4. In general, the trend of the travel-time anisotropy agrees among different radargrams and the simulations with GprMax, but in the upper half of the ice column, the picked travel time difference seem slightly underestimated.

The comparison of signal amplitudes from reflections in different antenna polarizations can provide information on the degree of anisotropic scattering related to the COF. Panel d) in Fig. 6.4 shows the amplitude difference of the reflections in the simulated and recorded traces, whereby the signal was corrected for the travel time difference. The synthetic radargrams show differences in the return power of up to 20 dB in distinct peaks, particularly pronounced at 17.88 μs and 18.66 μs. The simulated anisotropic scattering occurs where one of the eigenvalues changes rapidly over distances of $\sim$1 m. The anisotropic returns seem superimposed on reflections caused by the conductivity and there is no evidence of reflections which solely occur because of COF changes. The comparison to the amplitude difference in the EGRIP-NOR-2018 data is difficult due to reasons discussed below. Hence, no clear correlation between the synthetic and measured amplitude anisotropy can be observed.

6.4.3 Scattering and depolarization from folded layers

Reflections from interface roughness show clear effects of scattering and appear to be ’thicker’ than the return signal of a smooth layer (Fig. 6.5). Roughness amplitudes of about twice the radar wavelength already make it difficult to recognize the layer, and the strong scattering from roughness amplitudes of 6 m lead to pronounced signal loss, as much power is scattered off-nadir.

The simulations with two interfaces (Fig. 6.6) show, that layer roughness also decreases the ability of distinguishing individual layers located close to each other. For completely flat interfaces, the spacing between the layers must be larger than the range resolution of the radar system in order to resolve as two distinct layers. In the case of rough interfaces, however, two individual layers can appear as one thicker layer, e.g. if the roughness amplitude reaches about half the layer spacing (e.g. Fig. 6.6c,d).

The results from the 3D directional roughness studies (Fig. 6.7) show that the reflections appear perfectly flat in HH-antenna configuration of the flow-parallel simulations (i.e. antenna polarization parallel to folding axes). The reflector strength differs, however, slightly in dependence of the roughness amplitude: The reflection becomes weaker but apparently thicker and almost appears as multiple reflections in the cases where the roughness amplitude A is 2 m or larger (Fig. 6.73b,4b). No depolarization effects, i.e. electrical wave components perpendicular to the transmit polarization could be detected in the HV antenna configuration for the flow-parallel scenario.

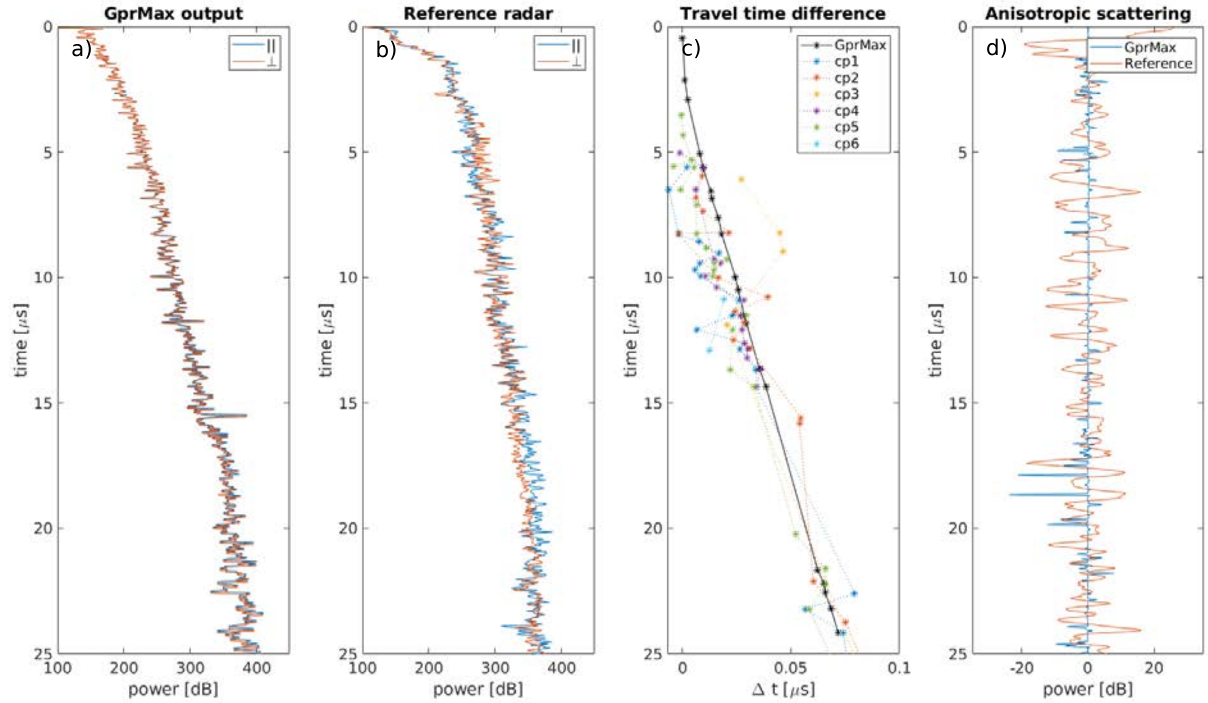

FIGURE 6.4: **a)** Simulated radar traces with permittivities corrected for crystal fabric, **b)** EGRIP-NOR-2018 reference radar traces recorded parallel (blue) and perpendicular (red) to the ice flow, **c)** difference in two-way travel time ($t_{\perp}$-$t_{\|}$) between simulated (black line) and observed reflections (cp1–cp6, equivalent to Fig. S5.4), and **d)** anisotropic scattering of simulated and observed signal, defined as the amplitude differences from the travel-time corrected traces in panel **a)** (blue) and **b)**(red).

The co-polarized (HH) signal for the flow-perpendicular simulations (i.e. antenna polarization perpendicular to folding axes) shows clear signs of scattering in the survey direction (Fig. 6.71–4d). Similar to the 2D case, the reflection thickness tends to increase with increasing roughness amplitude while the reflection simultaneously becomes weaker until it is difficult to recognize for amplitudes of 6m. For all simulations perpendicular to the flow-direction depolarization occurs. The cross-polarized signal shows similar characteristics as the co-polarized one but is roughly two orders of magnitude smaller (Fig. 6.71–4c).

6.5 Discussion

6.5.1 Reflection origin

We successfully produced synthetic radargrams using dielectric properties measured in the EastGRIP ice core and obtained results comparable to a recent study by Mojtabavi et al. (2022). Sensitivity studies show, that all the investigated reflections stem from conductivity contrasts that are measured in the EastGRIP ice core with DEP and ECM. Both of these measurement methods provide good agreement with the field observation in the Holocene ice and in reflections occurring from interstadials. Despite the low signal amplitude of the ECM record in glacial ice, we found that this record can still be used to investigate the reflection origin i.e. in gaps of DEP records.

While most of the investigated reflections can be linked to distinct peaks in the DEP record, in some cases the observed reflections are the result of the superposition of two or more layers close to each other, in which case the reflection appears stronger. The ability of distinguishing closely spaced layers depends on the dynamic range of the radar system but can also be affected

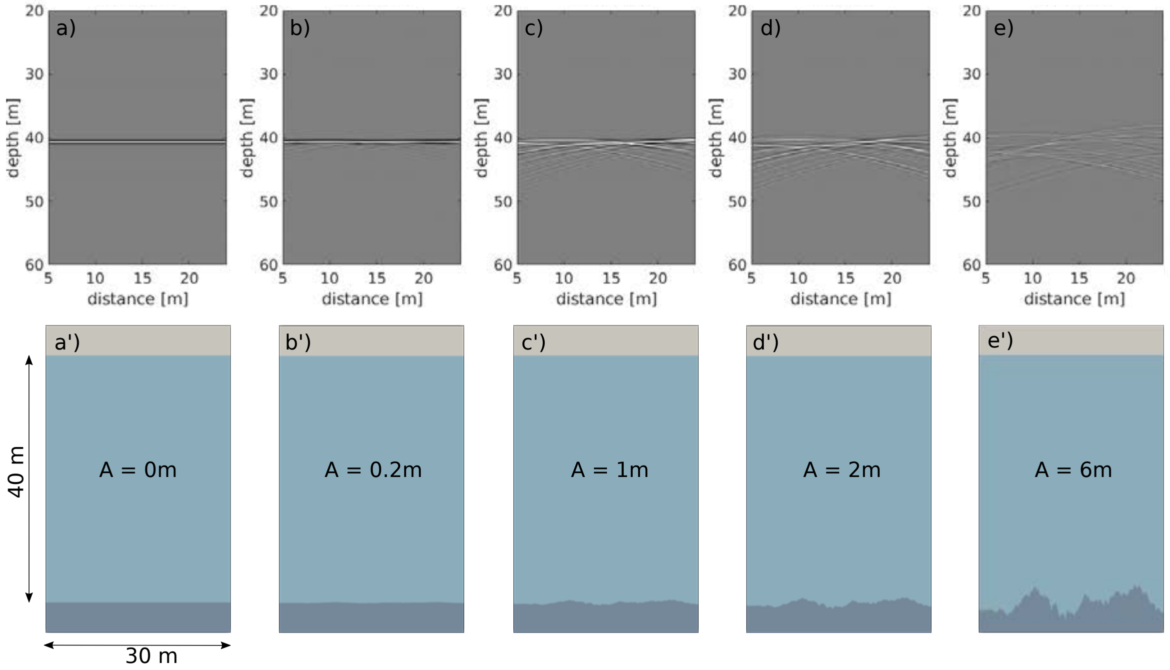

FIGURE 6.5: **a)–e)** RES response from 2D simulations of B-scans over reflectors with increasing roughness amplitudes ranging from 0 to 6 m **(a'–e')**.

by the interface structure. This effect could explain observations during IRH tracing, when a reflector suddenly seems to split up, or two distinct interfaces merge to one.

6.5.2 Anisotropy

The simulations with directional permittivities give insight into the travel-time anisotropy that can be expected at the EastGRIP drill site. The travel-time difference between reflections observed in crossing EGRIP-NOR-2018 profiles parallel and perpendicular to the flow direction show a trend of increasing Δt with depth which agrees with the simulations obtained with GprMax.

The variance of the observed data is rather large and can be associated to the picking uncertainties. The two radar traces from different radar profiles are rarely at the exact same position and while they are close enough that large subsurface changes are unlikely, the signal might still be affected by small-scale differences in e.g. surface topography. Furthermore, the traces are temporally separated, sometimes recorded on different days with different weather conditions which can affect the noise level. The coarse sampling rate makes it difficult to accurately pick the travel time differences, as they are, in particular at shallow depths and for weak fabrics, smaller than the temporal resolution of the data. The apparently underestimated travel-time anisotropy from crosspoint-analysis in the upper part of the ice column could be related to the picking uncertainties due to not high enough range resolution, as the relative error is larger for smaller depths. The grain size could also play a role as larger grains are believed to affect radar signal propagation more. Nonetheless, the fact that a clear trend matching the expected values can be detected shows, that this method works and bears the potential of higher-quality analyses of future data. Ground-based dual-polarized radars, as well as pRES measurements, can drastically reduce these uncertainties, as the different polarization directions are recorded concurrently in space and time and because of a much higher range resolution of cm-scale in pRES measurements.

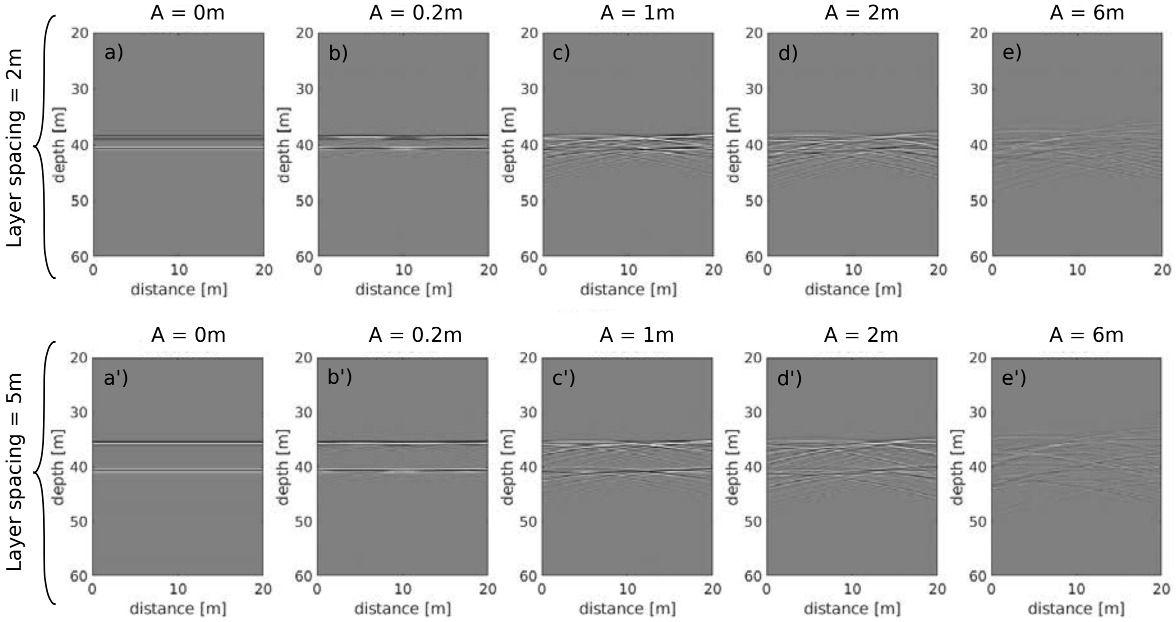

FIGURE 6.6: Effect of layer roughness on the ability to distinguish two layers. The roughness amplitude A increases from left (**a** and **a′** corresponding to A = 0 m) to right (**e** and **e′** corresponding to A = 6 m). In the top panels **(a–e)**, the two reflecting interfaces are separated by 2 m, in the bottom panels **(a′–e′)** the layer spacing is 5 m.

No strong indication of COF-induced reflections or pronounced anisotropic scattering is found by our analysis. Some directional scattering occurs if the COF changes on very short distances of ∼1 m. However, the COF record is not continuous, as samples were taken at intervals of approximately 10 m (Stoll, 2019). More pronounced COF changes could therefore exist but not be captured by the current depth resolution of the COF analyses. There is, however, no indication of strong anisotropic scattering in intersecting radar profiles recorded in the NEGIS, nor is there evidence of a strong reflection which cannot be explained by conductivity contrasts. It has to be kept in mind though, that the comparison to radargrams from the EGRIP-NOR-2018 survey is difficult because of the reasons elaborated on before and that dual-polarized systems would greatly help in reducing the limiting uncertainties. Potential reflections due to strong and abrupt changes in the COF could arise at greater depths e.g. from the transition of a vertical girdle (perpendicular to ice flow) to an often-observed vertical single maximum which could be expected to arise in the basal unit of the NEGIS as a result of strong vertical shear deformation. The ability to detect COF-induced reflections depends on the radar frequency: smoother fabric transitions are more likely to cause reflections for lower radar frequencies, while high-frequency waves require more drastic changes to record reflections.

Directional surface roughness affects the return signal in dependence of the polarization direction. If the radar wave is polarized parallel to the folding axes, little depolarization occurs, but the signal is affected from side reflections which makes the reflection appear thicker, while simultaneously weaker, as part of the energy is scattered sideways and does not return to the receiver. For antenna polarization perpendicular to the folding axes, depolarization effects are clearly notable while the co-polarized return signal shows an ’undulating’ interface due to scattering in the along-track direction.

One important consideration has to be kept in mind when interpreting the results from the layer roughness experiments: Due to the high computation costs, and the relatively high grid resolution required to represent the radar frequencies and dielectric properties that are comparable to field surveys, the model size becomes very large, particularly for 3D studies.

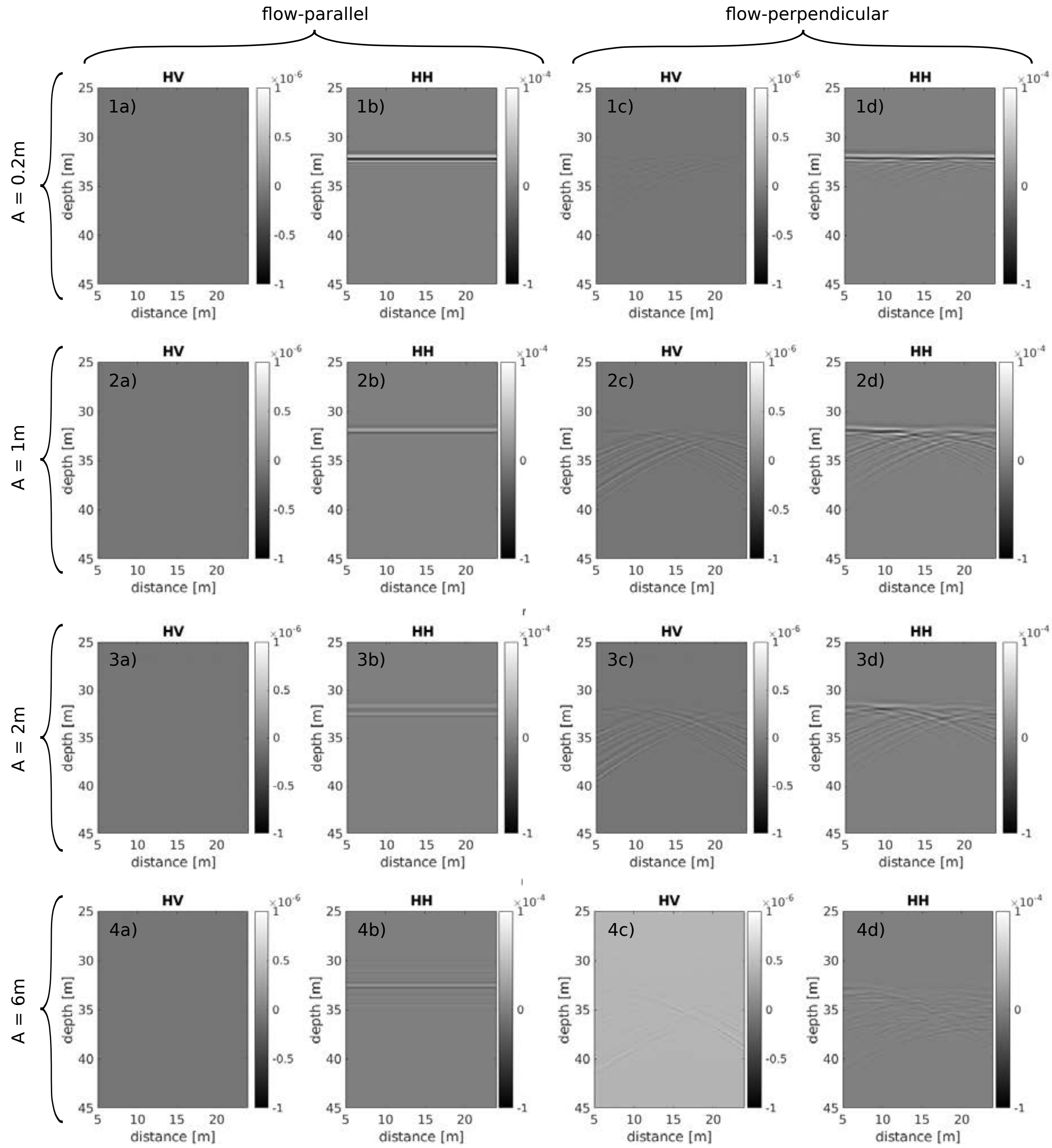

FIGURE 6.7: Results from 3D simulations of reflections from folded layers. The roughness amplitude increases from top to bottom from 0.2 m to 6 m. The left two columns **(a–b)** are the results from a profile parallel to the folding axes (i.e. Fig. 6.2b), the right two columns **(c–d)** are from a profile perpendicular to the folding axes (Fig. 6.2c). HV panels **(a** and **c)** indicate the received signal perpendicular to the polarization of the source signal (cross-polarization) whereas HH panels **(b** and **d)** indicate co-polarized recordings.

We thus had to limit the interface depth to 40 m, while in reality the radar waves are sensing features much further away, and additional spacing between source and target arises from the antennas being mounting on an airplane. Consequently, the modeling results represent a case located much more in the 'close-field' than in reality. While this does not play a significant role in 1D studies or with flat interfaces, it does matter here due to effects related to the radar waveform. Due to geometrical spreading with distance, the wavefront in the modeled scenario is much more curved when hitting the rough interface than it is in a similar setting where the reflector is located much farther away. This affects the amount of signal that returns to the receiver, as that depends on the angle at which an electromagnetic ray is hitting its target. The solution to overcome this issue is the simulation of plane waves, which is however not implemented in the current version of GprMax.

6.5.3 Implications for future radar surveys in the NEGIS

Rough interfaces affect the ability of distinguishing individual layers. 'Thicker' reflections can arise both, from interference of several conductivity peaks close to each other as well as from a single contrast which has a rough interface. Directional roughness causes anisotropic scattering in the direction of the folding axes. Off-nadir scattering leads to decreasing reflection strength and an increasing apparent thickness of the reflection. So far, no evidence of directional roughness and related anisotropic scattering has been observed in radar data recorded in the field. However, the comparison of two traces at radar crosspoints is difficult. Additional radar surveys with ground-based multi-polarized systems (Yan et al., 2020), as well as an extension of the airborne EGRIP-NOR-2018 radar campaign with partially rotated antennas for multi-polarized recordings is planned for the coming field season. Multi-polarimetric radar data can overcome some of the difficulties related to our ability of observing anisotropic signals and might permit to detect variations in reflection thickness or return power related either to directional roughness or anisotropic scattering due changes in the COF. Considering the situation at EastGRIP, where the folding axes and the smaller horizontal eigenvalue point along flow, the two scattering mechanisms would have opposite polarity. The return power from directional roughness tends to be slightly higher for antennas polarized parallel to ice flow. The variations in the smaller horizontal eigenvalue are less pronounced than the eigenvalue-variations perpendicular to ice flow. Hence, COF-induced reflectivity would be expected to be stronger perpendicular to ice flow. This accounts also for a potential reflection occurring at greater depths where a transition from the vertical girdle to a vertical single maximum could be expected. In that case, the permittivity contrast parallel to ice flow would be considerably smaller than the permittivity contrast perpendicular to the flow direction, resulting in a stronger return power perpendicular to the ice stream.

The results obtained in this study are also relevant for future attempts of deriving the COF orientation from pRES measurements and birefringence-induced power modulation, because anisotropic scattering by COF or directional roughness shifts the angle at which power modulation is best visible (e.g. Fujita et al., 2006; Ershadi et al., 2022; Young et al., 2021). The planned dual-polarized radar surveys also holds the potential to decrease the uncertainties with respect to travel-time anisotropy of reflections. The forward simulation with the fabric-corrected permittivities and the agreement with the crosspoint analysis (further described in Chapter 5, Section S5.2.1) highlights the potential of travel-time analysis for determining the horizontal fabric distribution. By reducing the method uncertainties with dual-polarized systems it might even become possible to derive information about depth-dependent fabric variations.

6.5.4 Challenges and potential of simulating glaciological problems with GprMax

Unlike most other geological materials, ice is nearly transparent for radar waves, so signal absorption is very small. While this is a great advantage in 'sensing' deep targets in glaciers and ice sheets, it is a challenge for simulating realistic scenarios with FDTD methods, as it requires very large model domains. The radar response from geometrical effects like layer roughness depends also on the geometry of the waveform. Here, we limited the reflector depth to 40 m due to computational reasons, with the consequence that the wave front hits the target not as 'planar' as it would in reality. Attempts of overcoming this problem by imitating plane waves with multiple sources triggered at the same time (similar to the concept of an exploding reflector, Carcione et al., 2002) failed because of boundary effects which appeared at the transition to the PML layers. Future versions of GprMax will have a plane-wave solution implemented (Craig Warren, pers. communication), which helps to overcome this problem and allows to reduce the model size and computational costs to a minimum.

The boundary conditions implemented in GprMax generally perform well, with a few exceptions which might be relevant for future applications. We observed that the performance of the PML slightly decreases if the model geometry is very long and narrow (as in our simulations with the ice core records and model size 2124.5×2.4m). More concerning, however is the occurrence of boundary reflections if reflecting interfaces consist of inclined layers i.e due to layer roughness or for studying larger-scale folds. The easiest way to improve the performance of absorbing boundary conditions is by increasing the thickness of the PML. This proved to work well for the 2D simulation of the ice-core stratigraphy. However, that also means additional computational costs, especially in 3D simulations. Limiting the layer roughness to the model domain and use flat interfaces within the PML helped to avoid boundary effects in our simulations of layer roughness. However, attempts to simulate larger-scale folds with steeply inclined layers turned out to be more difficult and adding a flat layer in the PML did not avoid the occurrence of reflections from the model boundaries. Technically, GprMax allows the manual adjustment of the PML parameters. In practice however,this turned out to be difficult due to the large number of adjustable parameters which impact the PML performance rather arbitrarily and differently for each individual model setting.

GprMax allows to describe anisotropic materials in 3D models. However, simulating the full ice core COF in 3D turned out to be computationally very expensive and was therefore not attempted here. Furthermore, the antenna polarization and the anisotropy axes can, as for now, only be described in x- or y-direction i.e. polarization parallel to the principal COF axes or other forms of anisotropy (i.e. layer folding axes). It is in theory possible to rotate the model relative to the antenna polarization, that is for example describe folds which run diagonally through the model domain. However, this is in practice quite cumbersome, especially if a small increment in antenna polarization direction are of interest, for instance to simulate the response of pRES measurements. For that reason, matrix-based models e.g. by Fujita et al. (2006) and Rathmann et al. (2022) remain more efficient in studying birefringence effects induced by COF.

6.6 Conclusion

We successfully applied GprMax to study the characteristics of ice internal stratigraphy by using ECM and DEP profiles from the EastGRIP ice core as input. The results obtained from the DEP signal agrees with the findings of a similar previous study by Mojtabavi et al. (2022). Although the results considering the origin of internal reflections are not new, they show the following: 1) GprMax is well suited to conduct forward modeling of internal stratigraphy as was done in earlier approaches, though in contrast to software which has previously been used, GprMax is freely available and well documented. 2) The comparison between ECM- and DEP-induced conductivity shows that despite its small signal amplitude in glacial ice, the ECM record can still provide useful results, particularly if the DEP record is incomplete. 3) By taking into account the directional permittivity from COF information we confirmed the travel time differences observed in (Mojtabavi et al., 2022) and described in Chapter 5, but also found that no reflection seems to occur solely from COF changes down to the current borehole depth at EastGRIP and detectable with radar systems with 195MHz center frequency.

Our investigations further provide information on anisotropic scattering effects resulting from directional layer roughness, which can alter the thickness and amplitude of the recorded reflections. At this point, no direct link to observed signals in RES data recovered in the survey area can be made because of the difficulty in comparing single traces of airborne profiles recorded at slightly different places and times. However, this limitation might soon be overcome with multi-polarized radar surveys planned in the coming field season. The results presented here can therefore be informative for the interpretation of the new generation of radar data.

We also recognize the potential of using GprMax for studying other features observed in glaciological radar data and which are not very well understood yet. For example, it remains unclear what results in the radio-echo-free zone close the bed observed in Antarctica, or why steeply inclined layers sometimes cause almost complete loss of return power, while in other units they can be well mapped. GprMax, in particular the subsequent version with further advances like plane wave solution and subgridding, can potentially help to better understand such features and test hypotheses where direct access through borehole drilling is restricted.

Supplementary Material

Derivation of Eq. (6.5)

The dielectric permittivity tensor of a monocrystal is:

$$\varepsilon' = \begin{pmatrix} \varepsilon_\perp & 0 & 0 \\ 0 & \varepsilon_\perp & 0 \\ 0 & 0 & \varepsilon_\parallel \end{pmatrix}, \tag{6.6}$$

where $\varepsilon_\perp$ is the dielectric permittivity in the basal plane and $\varepsilon_\parallel$ is the permittivity along the c-axis. The average permittivity of a isotropic polycrystal can be regarded as an average of monocrystalline permittivity, i.e.

$$\varepsilon'_{iso} = \frac{1}{3}(2\varepsilon_\perp + \varepsilon_\parallel), \tag{6.7}$$

which can also be written as

$$\varepsilon'_{iso} = \varepsilon_\perp + \frac{\Delta\varepsilon}{3}, \tag{6.8}$$

where $\Delta\varepsilon = \varepsilon_\parallel - \varepsilon_\perp$ is the dielectric anisotropy. Directional dielectric permittivities of polycrystals (ε_i can be described with the fabric eigenvalue as (e.g. Fujita et al., 2006):

$$\varepsilon'_i = \varepsilon_\perp + \lambda_i \Delta\varepsilon, \tag{6.9}$$

where λ_i is the eigenvalue in the corresponding direction i. Combining Eq. (6.9) with Eq. (6.8) for the average polycrystal, we can obtain the directional permittivities from an eigenvalue-corrected isotropic permittivity:

$$\varepsilon'_i = \varepsilon'_{iso} + \Delta\varepsilon(\lambda_i - \frac{1}{3}) \tag{6.10}$$

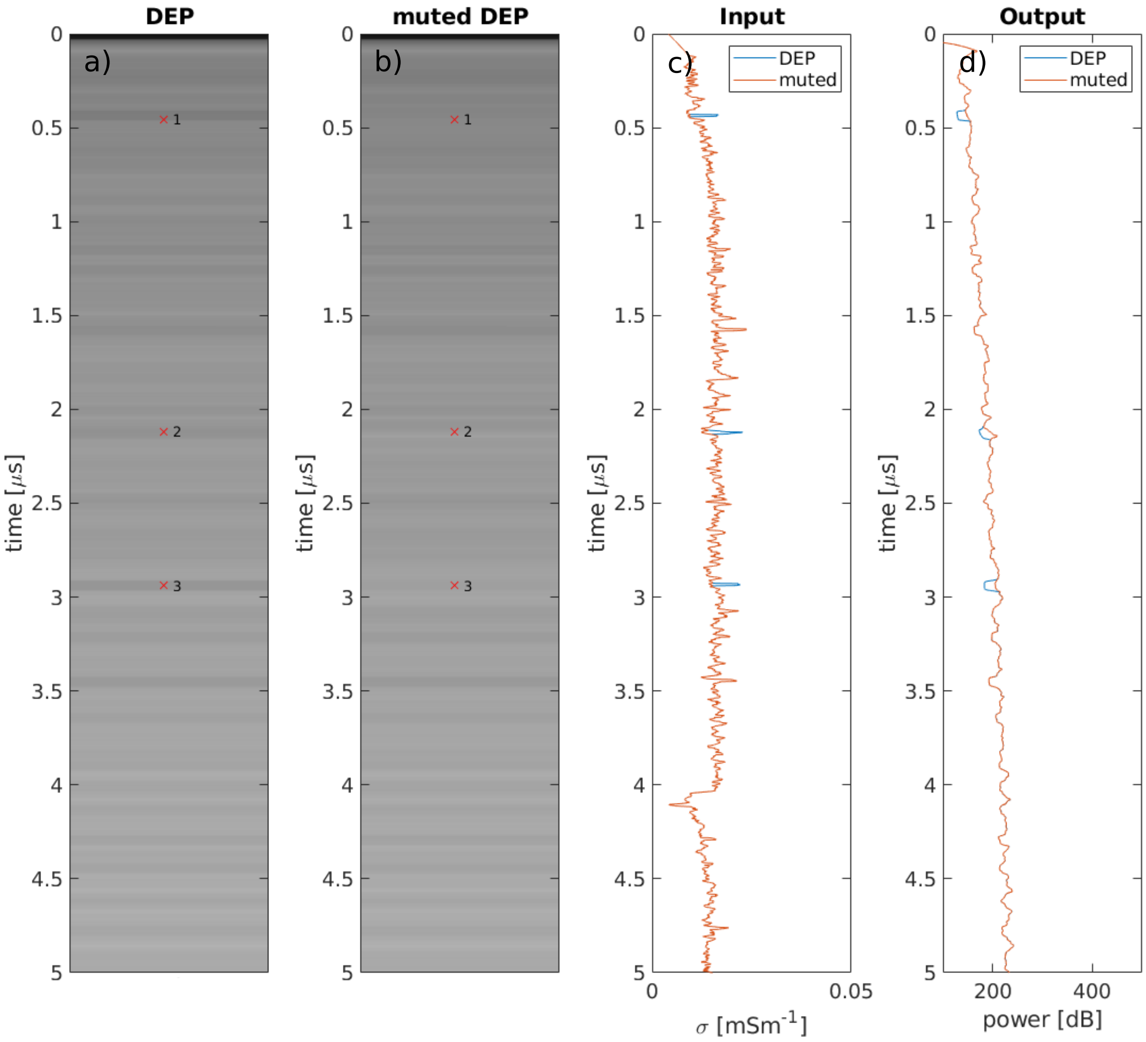

FIGURE S6.1: Sensitivity study for the time window 0–5 μs. **a)** synthetic B-scan obtained from GprMax using DEP as input, **b)** synthetic B-scan with muted DEP signal, **c)** GprMax input of DEP and muted DEP conductivity, and **d)** GprMax output as A-scan.

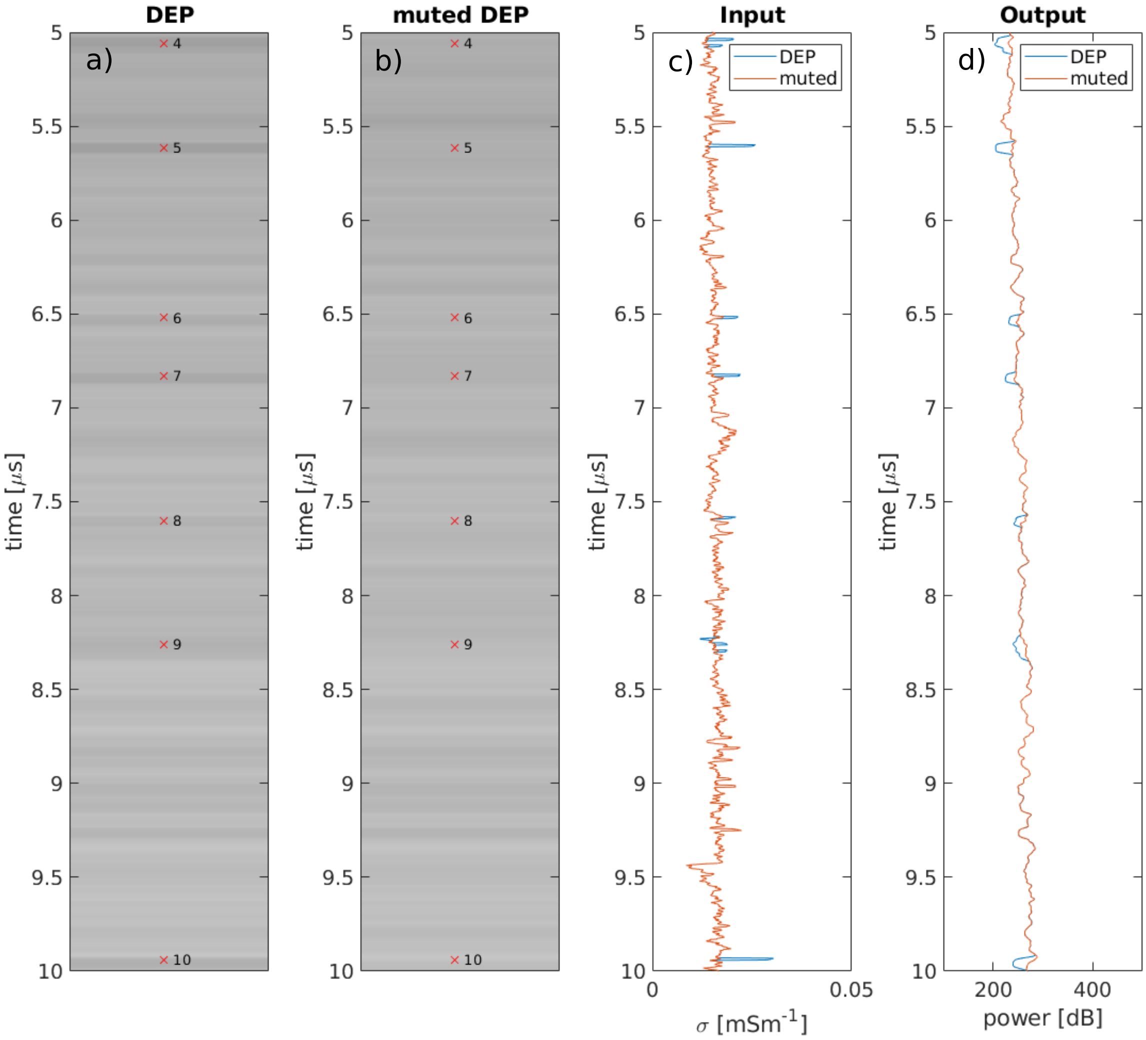

FIGURE S6.2: Sensitivity study for the time window 5–10 μs. **a)** synthetic B-scan obtained from GprMax using DEP as input, **b)** synthetic B-scan with muted DEP signal, **c)** GprMax input of DEP and muted DEP conductivity, and **d)** GprMax output as A-scan.

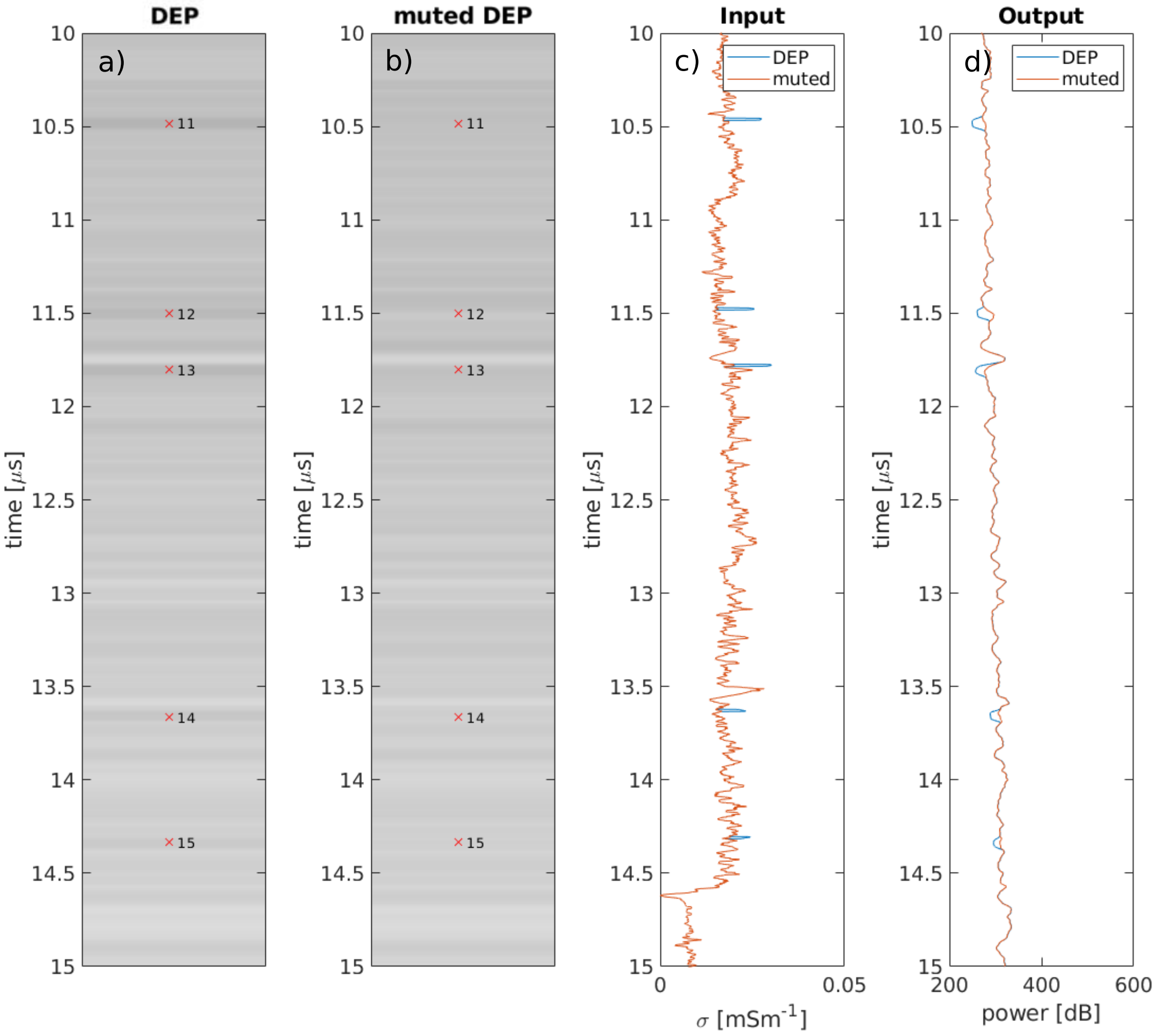

FIGURE S6.3: Sensitivity study for the time window 10–15 μs. **a)** synthetic B-scan obtained from GprMax using DEP as input, **b)** synthetic B-scan with muted DEP signal, **c)** GprMax input of DEP and muted DEP conductivity, and **d)** GprMax output as A-scan.

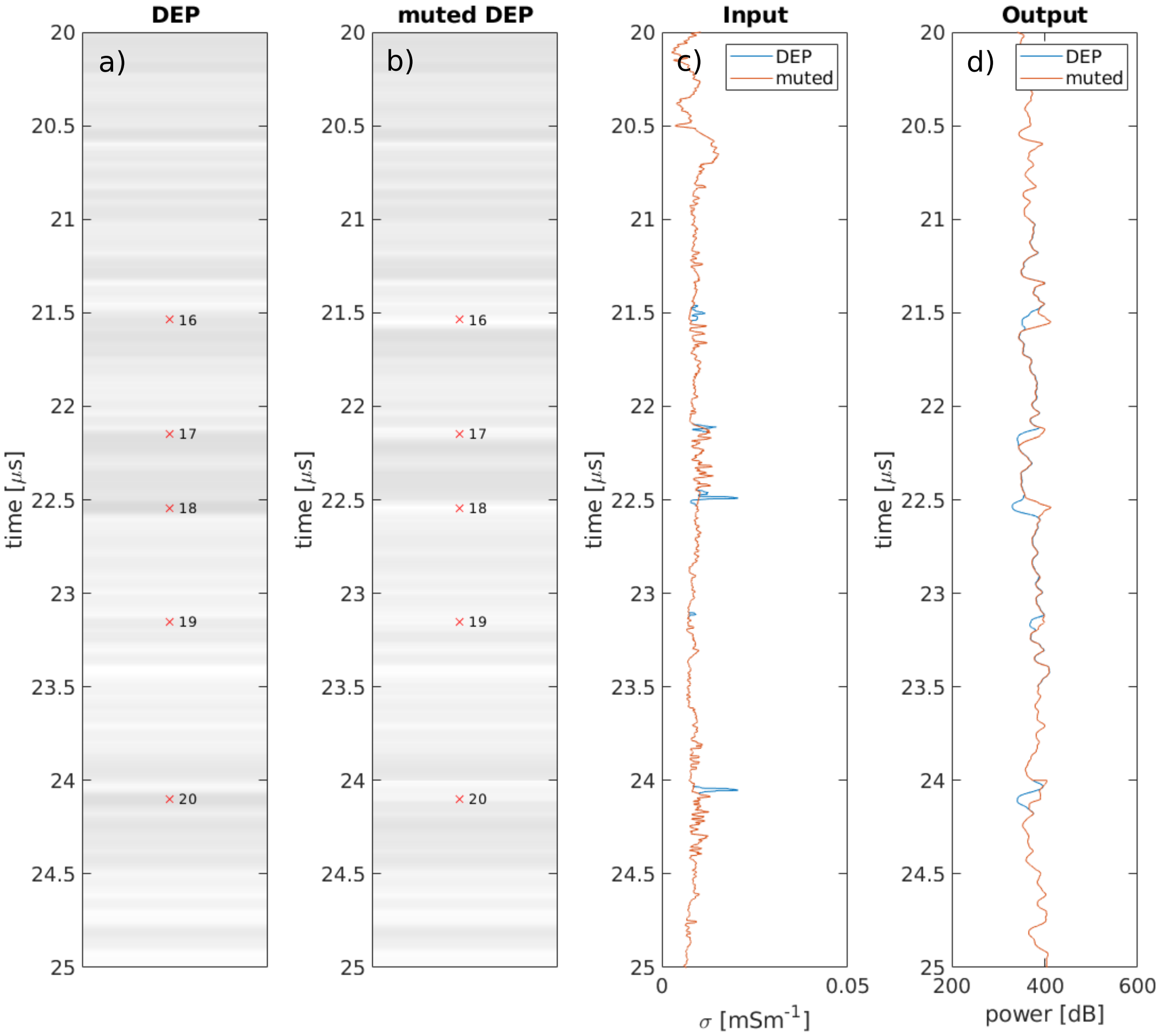

FIGURE S6.4: Sensitivity study for the time window 20–25 μs. **a)** synthetic B-scan obtained from GprMax using DEP as input, **b)** synthetic B-scan with muted DEP signal, **c)** GprMax input of DEP and muted DEP conductivity, and **d)** GprMax output as A-scan.

Author Contributions

TAG designed and carried out the study. TAG wrote the manuscript with input from DDJ and SF.

References

Ackley, S. F. and Keliher, T. E. (1979). “Ice sheet internal radio-echo reflections and associated physical property changes with depth”. In: *Journal of Geophysical Research: Solid Earth* 84.B10, pp. 5675–5680. DOI: `10.1029/JB084iB10p05675`.

Alley, R., Gow, A., Meese, D., Fitzpatrick, J., Waddington, E., and Bolzan, J. (1997). “Grain-scale processes, folding, and stratigraphic disturbance in the GISP2 ice core”. In: *Journal of Geophysical Research: Oceans* 102.C12, pp. 26819–26830. DOI: `10.1029/96JC03836`.

Arcone, S. A., Spikes, V. B., and Hamilton, G. S. (2005). “Stratigraphic variation within polar firn caused by differential accumulation and ice flow: interpretation of a 400 MHz short-pulse radar profile from West Antarctica”. In: *Journal of Glaciology* 51.174, pp. 407–422. DOI: `10.3189/172756505781829151`.

Azuma, N. and Higashi, A. (1985). “Formation processes of ice fabric pattern in ice sheets”. In: *Annals of Glaciology* 6, pp. 130–134. DOI: `10.3189/1985AoG6-1-130-134`.

Bamber, J. L., Griggs, J. A., Hurkmans, R. T. W. L., Dowdeswell, J. A., Gogineni, S. P., Howat, I., Mouginot, J., Paden, J., Palmer, S., Rignot, E., and Steinhage, D. (2013). “A new bed elevation dataset for Greenland”. In: *The Cryosphere* 7.2, pp. 499–510. DOI: `10.5194/tc-7-499-2013`.

Benson, A. K. (1995). “Applications of ground penetrating radar in assessing some geological hazards: examples of groundwater contamination, faults, cavities”. In: *Journal of applied Geophysics* 33.1-3, pp. 177–193. DOI: `10.1016/0926-9851(95)90040-3`.

Brisbourne, A. M., Martín, C., Smith, A. M., Baird, A., Kendall, J., and Kingslake, J. (2019). “Constraining recent ice flow history at Korff Ice Rise, West Antarctica, using radar and seismic measurements of ice fabric”. In: *Journal of Geophysical Research: Earth Surface* 124.1, pp. 175–194. DOI: `10.1029/2018JF004776`.

Burrough, P. A. (1981). “Fractal dimensions of landscapes and other environmental data”. In: *Nature* 294.5838, pp. 240–242. DOI: `10.1038/294240a0`.

Campbell, S., Balco, G., Todd, C., Conway, H., Huybers, K., Simmons, C., and Vermeulen, M. (2013). “Radar-detected englacial stratigraphy in the Pensacola Mountains, Antarctica: implications for recent changes in ice flow and accumulation”. In: *Annals of Glaciology* 54.63, pp. 91–100. DOI: `10.3189/2013AoG63A371`.

Carcione, J. M., Feliciangeli, L. P., and Zamparo, M. (2002). “The exploding-reflector concept for ground-penetrating-radar modeling”. In: *Annals of Geophysics* 45.3-4. DOI: `10.4401/ag-3526`.

Catania, G. A., Neumann, T. A., and Price, S. F. (2008). “Characterizing englacial drainage in the ablation zone of the Greenland ice sheet”. In: *Journal of Glaciology* 54.187, pp. 567–578. DOI: `10.3189/002214308786570854`.

Dall, J., Kristensen, S. S., Krozer, V., Hernández, C. C., Vidkjær, J., Kusk, A., Balling, J., Skou, N., Søbjærg, S. S., and Christensen, E. L. (2010). “ESA’s polarimetric airborne radar ice sounder (POLARIS): Design and first results”. In: *IET Radar, Sonar & Navigation* 4.3, pp. 488–496. DOI: `10.1049/iet-rsn.2009.0035`.

Daniels, J. J., Roberts, R., and Vendl, M. (1995). “Ground penetrating radar for the detection of liquid contaminants”. In: *Journal of Applied Geophysics* 33.1-3, pp. 195–207. DOI: `1-s2.0-0926985195900411-main`.

Davis, J. L. and Annan, A. P. (1989). “Ground-penetrating radar for high-resolution mapping of soil and rock stratigraphy”. In: *Geophysical Prospecting* 37.5, pp. 531–551. DOI: `https://doi.org/10.1111/j.1365-2478.1989.tb02221.x`.

De Moura, C. A. and Kubrusly, C. S. (2013). “The courant–friedrichs–lewy (cfl) condition”. In: *AMC* 10.12.

Doake, C. (1981). “Polarization of radio waves in ice sheets”. In: *Geophysical Journal International* 64.2, pp. 539–558. DOI: `10.1111/j.1365-246X.1981.tb02682.x`.

Drews, R., Eisen, O., Steinhage, D., Weikusat, I., Kipfstuhl, S., and Wilhelms, F. (2012). "Potential mechanisms for anisotropy in ice-penetrating radar data". In: *Journal of Glaciology* 58.209, pp. 613–624. DOI: 10.3189/2012JoG11J114.

Durand, G., Gillet-Chaulet, F., Svensson, A., Gagliardini, O., Kipfstuhl, S., Meyssonnier, J., Parrenin, F., Duval, P., and Dahl-Jensen, D. (2007). "Change in ice rheology during climate variations – implications for ice flow modelling and dating of the EPICA Dome C core". In: *Climate of the Past* 3.1, pp. 155–167. DOI: 10.5194/cp-3-155-2007.

Durand, G., Gagliardini, O., Thorsteinsson, T., Svensson, A., Kipfstuhl, S., and Dahl-Jensen, D. (2006). "Ice microstructure and fabric: an up-to-date approach for measuring textures". In: *Journal of Glaciology* 52.179, pp. 619–630. DOI: 10.3189/172756506781828377.

Eisen, O., Hamann, I., Kipfstuhl, S., Steinhage, D., and Wilhelms, F. (2007). "Direct evidence for continuous radar reflector originating from changes in crystal-orientation fabric". In: *The Cryosphere* 1.1, pp. 1–10. DOI: 10.5194/tc-1-1-2007.

Eisen, O., Nixdorf, U., Wilhelms, F., and Miller, H. (2004). "Age estimates of isochronous reflection horizons by combining ice core, survey, and synthetic radar data". In: *Journal of Geophysical Research: Solid Earth* 109.B4. DOI: 10.1029/2003JB002858.

Eisen, O., Wilhelms, F., Nixdorf, U., and Miller, H. (2003a). "Identifying isochrones in GPR profiles from DEP-based forward modeling". In: *Annals of Glaciology* 37, pp. 344–350. DOI: 10.3189/172756403781816068.

Eisen, O., Wilhelms, F., Nixdorf, U., and Miller, H. (2003b). "Revealing the nature of radar reflections in ice: DEP-based FDTD forward modeling". In: *Geophysical research letters* 30.5. DOI: 10.1029/2002GL016403.

Ershadi, M. R., Drews, R., Martín, C., Eisen, O., Ritz, C., Corr, H., Christmann, J., Zeising, O., Humbert, A., and Mulvaney, R. (2022). "Polarimetric radar reveals the spatial distribution of ice fabric at domes and divides in East Antarctica". In: *The Cryosphere* 16.5, pp. 1719–1739. DOI: 10.5194/tc-16-1719-2022.

Faria, S. H., Freitag, J., and Kipfstuhl, S. (2010). "Polar ice structure and the integrity of ice-core paleoclimate records". In: *Quaternary Science Reviews* 29.1. Climate of the Last Million Years: New Insights from EPICA and Other Records, pp. 338–351. DOI: 10.1016/j.quascirev.2009.10.016.

Fitzpatrick, J. J., Voigt, D. E., Fegyveresi, J. M., Stevens, N. T., Spencer, M. K., Cole-Dai, J., Alley, R. B., Jardine, G. E., Cravens, E. D., Wilen, L. A., Fudge, T., and Mcconnell, J. R. (2014). "Physical properties of the WAIS Divide ice core". In: *Journal of Glaciology* 60.224, pp. 1181–1198. DOI: 10.3189/2014JoG14J100.

Franke, S., Jansen, D., Binder, T., Paden, J. D., Dörr, N., Gerber, T. A., Miller, H., Dahl-Jensen, D., Helm, V., Steinhage, D., Weikusat, I., Wilhelms, F., and Eisen, O. (2022b). "Airborne ultra-wideband radar sounding over the shear margins and along flow lines at the onset region of the Northeast Greenland Ice Stream". In: *Earth System Science Data* 14.2, pp. 763–779. DOI: 10.5194/essd-14-763-2022.

Franke, S., Jansen, D., Binder, T., Dörr, N., Helm, V., Paden, J., Steinhage, D., and Eisen, O. (2020). "Bed topography and subglacial landforms in the onset region of the Northeast Greenland Ice Stream". In: *Annals of Glaciology* 61.81, pp. 143–153. DOI: 10.1017/aog.2020.12.

Fujita, S., Maeno, H., and Matsuoka, K. (2006). "Radio-wave depolarization and scattering within ice sheets: a matrix-based model to link radar and ice-core measurements and its application". In: *Journal of Glaciology* 52.178, pp. 407–424. DOI: 10.3189/172756506781828548.

Fujita, S., Maeno, H., Uratsuka, S., Furukawa, T., Mae, S., Fujii, Y., and Watanabe, O. (1999). "Nature of radio echo layering in the Antarctic ice sheet detected by a two-frequency experiment". In: *Journal of Geophysical Research: Solid Earth* 104.B6, pp. 13013–13024. DOI: 10.1029/1999JB900034.

Fujita, S., Matsuoka, T., Ishida, T., Matsuoka, K., and Mae, S. (2000). "A summary of the complex dielectric permittivity of ice in the megahertz range and its applications for radar sounding of polar ice sheets". In: *Physics of ice core records*. Hokkaido University Press, pp. 185–212.

Gerber, T. A., Hvidberg, C. S., Rasmussen, S. O., Franke, S., Sinnl, G., Grinsted, A., Jansen, D., and Dahl-Jensen, D. (2021). "Upstream flow effects revealed in the EastGRIP ice core using Monte Carlo inversion of a two-dimensional ice-flow model". In: *The Cryosphere* 15.8, pp. 3655–3679. DOI: `10.5194/tc-15-3655-2021`.

Giannakis, I., Giannopoulos, A., and Davidson, N. (2012). "Incorporating dispersive electrical properties in FDTD GPR models using a general Cole-Cole dispersion function". In: *2012 14th International Conference on Ground Penetrating Radar (GPR)*. IEEE, pp. 232–236. DOI: `10.1109/ICGPR.2012.6254866`.

Giannopoulos, A. (1998). "The investigation of transmission-line matrix and finite-difference time-domain methods for the forward problem of ground probing radar." PhD thesis. University of York.

Gogineni, S., Yan, J.-B., Paden, J., Leuschen, C., Li, J., Rodriguez-Morales, F., Braaten, D., Purdon, K., Wang, Z., Liu, W., and Gauch, J. (2014). "Bed topography of Jakobshavn Isbræ, Greenland, and Byrd Glacier, Antarctica". In: *Journal of Glaciology* 60.223, pp. 813–833. DOI: `10.3189/2014JoG14J129`.

Gow, A. J., Ueda, H. T., and Garfield, D. E. (1968). "Antarctic ice sheet: Preliminary results of first core hole to bedrock". In: *Science* 161.3845, pp. 1011–1013. DOI: `10.1126/science.161.3845.1011`.

Hammer, C. U. (1980). "Acidity of polar ice cores in relation to absolute dating, past volcanism, and radio–echoes". In: *Journal of Glaciology* 25.93, pp. 359–372. DOI: `10/hwsm`.

Hargreaves, N. D. (1978). "The Radio-Frequency Birefringence of Polar Ice". In: *Journal of Glaciology* 21.85, pp. 301–313. DOI: `10.3189/S0022143000033499`.

Hillebrand, T. R., Conway, H., Koutnik, M., Martín, C., Paden, J., and Winberry, J. P. (2021). "Radio-echo sounding and waveform modeling reveal abundant marine ice in former rifts and basal crevasses within Crary Ice Rise, Antarctica". In: *Journal of Glaciology* 67.264, pp. 641–652. DOI: `10.1017/jog.2021.17`.

Hong, S., Lai, W.-L., and Helmerich, R. (2015). "Experimental monitoring of chloride-induced reinforcement corrosion and chloride contamination in concrete with ground-penetrating radar". In: *Structure and infrastructure engineering* 11.1, pp. 15–26. DOI: `10.1080/15732479.2013.879321`.

Hvidberg, C. S., Grinsted, A., Dahl-Jensen, D., Khan, S. A., Kusk, A., Andersen, J. K., Neckel, N., Solgaard, A., Karlsson, N. B., Kjær, H. A., and Vallelonga, P. (2020). "Surface velocity of the Northeast Greenland Ice Stream (NEGIS): assessment of interior velocities derived from satellite data by GPS". In: *The Cryosphere* 14.10, pp. 3487–3502. DOI: `10.5194/tc-14-3487-2020`.

Jansen, D., Llorens, M.-G., Westhoff, J., Steinbach, F., Kipfstuhl, S., Bons, P. D., Griera, A., and Weikusat, I. (2016). "Small-scale disturbances in the stratigraphy of the NEEM ice core: observations and numerical model simulations". In: *The Cryosphere* 10.1, pp. 359–370. DOI: `10.5194/tc-10-359-2016`.

Jordan, T. M., Schroeder, D. M., Elsworth, C. W., and Siegfried, M. R. (2020). "Estimation of ice fabric within Whillans Ice Stream using polarimetric phase-sensitive radar sounding". In: *Annals of Glaciology* 61.81, pp. 74–83. DOI: `10.1017/aog.2020.6`.

Knight, R. (2001). "Ground penetrating radar for environmental applications". In: *Annual Review of Earth and Planetary Sciences* 29.1, pp. 229–255. DOI: `10.1146/annurev.earth.29.1.229`.

Kunz, K. S. and Luebbers, R. J. (1993). *The finite difference time domain method for electromagnetics*. CRC press.

Li, J., Paden, J., Leuschen, C., Rodriguez-Morales, F., Hale, R. D., Arnold, E. J., Crowe, R., Gomez-Garcia, D., and Gogineni, P. (2012). “High-altitude radar measurements of ice thickness over the Antarctic and Greenland ice sheets as a part of operation icebridge”. In: *IEEE Transactions on Geoscience and Remote Sensing* 51.2, pp. 742–754. DOI: `10.1109/TGRS.2012.2203822`.

Ludeno, G., Cavalagli, N., Ubertini, F., Soldovieri, F., and Catapano, I. (2020). “On the combined use of ground penetrating radar and crack meter sensors for structural monitoring: Application to the historical Consoli Palace in Gubbio, Italy”. In: *Surveys in Geophysics* 41.3, pp. 647–667. DOI: `10.1007/s10712-019-09526-y`.

MacGregor, J. A., Fahnestock, M. A., Catania, G. A., Paden, J. D., Gogineni, S. P., Young, S. K., Rybarski, S. C., Mabrey, A. N., Wagman, B. M., and Morlighem, M. (2015). “Radiostratigraphy and age structure of the Greenland Ice Sheet”. In: *Journal of Geophysical Research: Earth Surface* 120.2, pp. 212–241. DOI: `10.1002/2014JF003215`.

Matsumoto, M., Yoshimura, M., Naoki, K., Cho, K., and Wakabayashi, H. (2018). “Sea ice thickness measurement by ground penetrating radar for ground truth of microwave remote sensing data”. In: *Int. Arch. Photogramm. Remote Sens. Spat. Inf. Sci* 42.3, pp. 1259–1262. DOI: `10.5194/isprs-archives-XLII-3-1259-2018`.

Matsumoto, M., Yoshimura, M., Naoki, K., Cho, K., and Wakabayashi, H. (2019). “Ground penetrating radar data interpretation using electromagnetic field analysis for sea ice thickness measurement”. In: *The International Archives of Photogrammetry, Remote Sensing and Spatial Information Sciences* 42, pp. 47–50. DOI: `10.5194/isprs-archives-XLII-3-W7-47-2019`.

Matsuoka, T., Fujita, S., Morishima, S., and Mae, S. (1997). “Precise measurement of dielectric anisotropy in ice Ih at 39 GHz”. In: *Journal of Applied Physics* 81.5, pp. 2344–2348. DOI: `10.1063/1.364238`.

Millar, D. (1981). “Radio-echo layering in polar ice sheets and past volcanic activity”. In: *Nature* 292.5822, pp. 441–443. DOI: `10.1038/292441a0`.

Mojtabavi, S., Wilhelms, F., Cook, E., Davies, S. M., Sinnl, G., Skov Jensen, M., Dahl-Jensen, D., Svensson, A., Vinther, B. M., Kipfstuhl, S., Jones, G., Karlsson, N. B., Faria, S. H., Gkinis, V., Kjær, H. A., Erhardt, T., Berben, S. M. P., Nisancioglu, K. H., Koldtoft, I., and Rasmussen, S. O. (2020a). “A first chronology for the East Greenland Ice-core Project (EGRIP) over the Holocene and last glacial termination”. In: *Climate of the Past* 16.6, pp. 2359–2380. DOI: `10.5194/cp-16-2359-2020`.

Mojtabavi, S., Eisen, O., Franke, S., Jansen, D., Steinhage, D., Paden, J., Dahl-Jensen, D., Weikusat, I., Eichler, J., and Wilhelms, F. (2022). “Origin of englacial stratigraphy at three deep ice core sites of the Greenland Ice Sheet by synthetic radar modelling”. In: *Journal of Glaciology*, pp. 1–13. DOI: `10.1017/jog.2021.137`.

Mojtabavi, S., Wilhelms, F., Cook, E., Davies, S. M., Sinnl, G., Skov Jensen, M., Dahl-Jensen, D., Svensson, A. M., Vinther, B. M., Kipfstuhl, S., Karlsson, N. B., Faria, S. H., Gkinis, V., Kjær, H. A., Erhardt, T., Berben, S. M. P., Nisancioglu, K. H., Koldtoft, I., and Rasmussen, S. O. (2020c). “Acidity measured with the Electrical Conductivity Method (ECM) on the EGRIP ice core (down to 1383.84 m depth), converted to hydrogen ion concentration”. In: PANGAEA. DOI: `10.1594/PANGAEA.922199`.

Mojtabavi, S., Wilhelms, F., Cook, E., Davies, S. M., Sinnl, G., Skov Jensen, M., Dahl-Jensen, D., Svensson, A. M., Vinther, B. M., Kipfstuhl, S., Karlsson, N. B., Faria, S. H., Gkinis, V., Kjær, H. A., Erhardt, T., Berben, S. M. P., Nisancioglu, K. H., Koldtoft, I., and Rasmussen, S. O. (2020d). “Permittivity measured with the dielectric profiling (DEP) technique on the EGRIP ice core, 13.77-1383.84 m depth”. In: PANGAEA. DOI: `10.1594/PANGAEA.922138`.

Mojtabavi, S., Wilhelms, F., Cook, E., Davies, S. M., Sinnl, G., Skov Jensen, M., Dahl-Jensen, D., Svensson, A. M., Vinther, B. M., Kipfstuhl, S., Karlsson, N. B., Faria, S. H., Gkinis, V., Kjær, H. A., Erhardt, T., Berben, S. M. P., Nisancioglu, K. H., Koldtoft, I., and Rasmussen, S. O.

(2020e). "Specific conductivity measured with the dielectric profiling (DEP) technique on the EGRIP ice core, 13.77-1383.84 m depth". In: PANGAEA. DOI: `10.1594/PANGAEA.919313`.

Moore, J. (1993). "High-resolution dielectric profiling of ice cores". In: *Journal of Glaciology* 39.132, pp. 245–248. DOI: `10.3189/S0022143000015902`.

Moore, J., Mulvaney, R., and Paren, J. (1989). "Dielectric stratigraphy of ice: A new technique for determining total ionic concentrations in polar ice cores". In: *Geophysical Research Letters* 16.10, pp. 1177–1180. DOI: `10.1029/GL016i010p01177`.

Moore, J. and Paren, J. (1987). "A new technique for dielectric logging of Antarctic ice cores". In: *Le Journal de Physique Colloques* 48.C1, pp. C1–155. DOI: `10.1051/jphyscol:1987123`.

Neal, A. (2004). "Ground-penetrating radar and its use in sedimentology: principles, problems and progress". In: *Earth-science reviews* 66.3-4, pp. 261–330. DOI: `10.1016/j.earscirev.2004.01.004`.

Pälli, A., Kohler, J. C., Isaksson, E., Moore, J. C., Pinglot, J. F., Pohjola, V. A., and Samuelsson, H. (2002). "Spatial and temporal variability of snow accumulation using ground-penetrating radar and ice cores on a Svalbard glacier". In: *Journal of Glaciology* 48.162, pp. 417–424. DOI: `10.3189/172756502781831205`.

Paren, J. and Robin, G. d. Q. (1975). "Internal reflections in polar ice sheets". In: *Journal of Glaciology* 14.71, pp. 251–259. DOI: `10.3189/S0022143000021730`.

Rasmussen, S. O., Abbott, P. M., Blunier, T., Bourne, A. J., Brook, E., Buchardt, S. L., Buizert, C., Chappellaz, J., Clausen, H. B., Cook, E., Dahl-Jensen, D., Davies, S. M., Guillevic, M., Kipfstuhl, S., Laepple, T., Seierstad, I. K., Severinghaus, J. P., Steffensen, J. P., Stowasser, C., Svensson, A., Vallelonga, P., Vinther, B. M., Wilhelms, F., and Winstrup, M. (2013). "A first chronology for the North Greenland Eemian Ice Drilling (NEEM) ice core". In: *Climate of the Past* 9.6, pp. 2713–2730. DOI: `10.5194/cp-9-2713-2013`.

Rathmann, N. M., Lilien, D. A., Grinsted, A., Gerber, T. A., Young, T. J., and Dahl-Jensen, D. (2022). "On the limitations of using polarimetric radar sounding to infer the crystal orientation fabric of ice masses". In: *Geophysical Research Letters*, e2021GL096244. DOI: `10.1029/2021GL096244`.

Robin, G. d. Q., Evans, S., and Bailey, J. T. (1969). "Interpretation of radio echo sounding in polar ice sheets". In: *Philosophical Transactions of the Royal Society of London. Series A, Mathematical and Physical Sciences* 265.1166, pp. 437–505. DOI: `10.1098/rsta.1969.0063`.

Schennen, S., Bricheva, S., and Tronicke, J. (2017). "Potential of ground-penetrating radar for imaging active layer and ice wedges in permafrost areas". In: *23rd European Meeting of Environmental and Engineering Geophysics*. Vol. 2017. 1. European Association of Geoscientists & Engineers, pp. 1–5. DOI: `10.3997/2214-4609.201701988`.

Schroeder, D. M., Bingham, R. G., Blankenship, D. D., Christianson, K., Eisen, O., Flowers, G. E., Karlsson, N. B., Koutnik, M. R., Paden, J. D., and Siegert, M. J. (2020). "Five decades of radioglaciology". In: *Annals of Glaciology* 61.81, pp. 1–13. DOI: `10.1017/aog.2020.11`.

Sokolov, K., Fedorova, L., and Fedorov, M. (2020). "Prospecting and evaluation of underground massive ice by ground-penetrating radar". In: *Geosciences* 10.7, p. 274. DOI: `10/hwsn`.

Solla, M., Lorenzo, H., Rial, F., and Novo, A. (2012). "Ground-penetrating radar for the structural evaluation of masonry bridges: Results and interpretational tools". In: *Construction and Building Materials* 29, pp. 458–465. DOI: `10.1016/j.conbuildmat.2011.10.001`.

Steinhage, D., Nixdorf, U., Meyer, U., and Miller, H. (1999). "New maps of the ice thickness and subglacial topography in Dronning Maud Land, Antarctica, determined by means of airborne radio-echo sounding". In: *Annals of Glaciology* 29, pp. 267–272. DOI: `10.3189/172756499781821409`.

Stoll, N. (2019). *A first glimpse into the EGRIP ice core: An analysis of the influence of deformation and recrystallisation on fabric and microstructures of the Northeast Greenland Ice Stream*. Master thesis, University Bremen FB5.

Svensson, A., Nielsen, S. W., Kipfstuhl, S., Johnsen, S. J., Steffensen, J. P., Bigler, M., Ruth, U., and Röthlisberger, R. (2005). "Visual stratigraphy of the North Greenland Ice Core Project (NorthGRIP) ice core during the last glacial period". In: *Journal of Geophysical Research: Atmospheres* 110.D2. DOI: `10.1029/2004JD005134`.

Taylor, K. C., Alley, R. B., Lamorey, G. W., and Mayewski, P. (1997). "Electrical measurements on the Greenland Ice Sheet Project 2 core". In: *Journal of Geophysical Research: Oceans* 102.C12, pp. 26511–26517. DOI: `10.1029/96JC02500`.

Thorsteinsson, T. (1996). "Textures and fabrics in the GRIP ice core, in relation to climate history and ice deformation". In: *Berichte zur Polarforschung (Reports on Polar Research)* 205.

Thorsteinsson, T., Kipfstuhl, J., and Miller, H. (1997). "Textures and fabrics in the GRIP ice core". In: *Journal of Geophysical Research: Oceans* 102.C12, pp. 26583–26599. DOI: `10.1029/97JC00161`.

Titov, A. and Krylov, S. (2015). "Physical and mathematical modeling approaches for GPR investigation of underground ice in the permafrost zone". In: *Symposium on the Application of Geophysics to Engineering and Environmental Problems 2015*. Society of Exploration Geophysicists, Environment, and Engineering, pp. 374–378. DOI: `10.4133/SAGEEP.28-054`.

Turchetti, S., Dean, K., Naylor, S., and Siegert, M. (2008). "Accidents and opportunities: a history of the radio echo-sounding of Antarctica, 1958–79". In: *The British Journal for the History of Science* 41.3, pp. 417–444. DOI: `10.1017/S0007087408000903`.

Ueltzhöffer, K. J., Bendel, V., Freitag, J., Kipfstuhl, S., Wagenbach, D., Faria, S. H., and Garbe, C. S. (2010). "Distribution of air bubbles in the EDML and EDC (Antarctica) ice cores, using a new method of automatic image analysis". In: *Journal of Glaciology* 56.196, pp. 339–348. DOI: `10.3189/002214310791968511`.

Vaughan, C. J. (1986). "Ground-penetrating radar surveys used in archaeological investigations". In: *GEOPHYSICS* 51.3, pp. 595–604. DOI: `10.1190/1.1442114`.

Waite, A. H. and Schmidt, S. J. (1962). "Gross Errors in Height Indication from Pulsed Radar Altimeters Operating over Thick Ice or Snow". In: *Proceedings of the IRE* 50.6, pp. 1515–1520. DOI: `10.1109/JRPROC.1962.288195`.

Warren, C., Giannopoulos, A., and Giannakis, I. (2016). "gprMax: Open source software to simulate electromagnetic wave propagation for Ground Penetrating Radar". In: *Computer Physics Communications* 209, pp. 163–170. DOI: `10.1016/j.cpc.2016.08.020`.

Westhoff, J., Stoll, N., Franke, S., Weikusat, I., Bons, P., Kerch, J., Jansen, D., Kipfstuhl, S., and Dahl-Jensen, D. (2021). "A stratigraphy-based method for reconstructing ice core orientation". In: *Annals of Glaciology* 62.85-86, pp. 191–202. DOI: `10.1017/aog.2020.76`.

Wilen, L., Diprinzio, C., Alley, R., and Azuma, N. (2003). "Development, principles, and applications of automated ice fabric analyzers". In: *Microscopy research and technique* 62.1, pp. 2–18. DOI: `10.1002/jemt.10380`.

Wilhelms, F., Kipfstuhl, J., Miller, H., Heinloth, K., and Firestone, J. (1998). "Precise dielectric profiling of ice cores: a new device with improved guarding and its theory". In: *Journal of Glaciology* 44.146, pp. 171–174. DOI: `10.3189/S002214300000246X`.

Wilson, C. J., Russell-Head, D. S., and Sim, H. M. (2003). "The application of an automated fabric analyzer system to the textural evolution of folded ice layers in shear zones". In: *Annals of Glaciology* 37, pp. 7–17. DOI: `10.3189/172756403781815401`.

Winter, A., Steinhage, D., Arnold, E. J., Blankenship, D. D., Cavitte, M. G. P., Corr, H. F. J., Paden, J. D., Urbini, S., Young, D. A., and Eisen, O. (2017). "Comparison of measurements from different radio-echo sounding systems and synchronization with the ice core at Dome C, Antarctica". In: *The Cryosphere* 11.1, pp. 653–668. DOI: `10.5194/tc-11-653-2017`.

Winter, K., Woodward, J., Ross, N., Dunning, S. A., Bingham, R. G., Corr, H. F., and Siegert, M. J. (2015). "Airborne radar evidence for tributary flow switching in Institute Ice Stream, West Antarctica: Implications for ice sheet configuration and dynamics". In: *Journal of Geophysical Research: Earth Surface* 120.9, pp. 1611–1625. DOI: `10.1002/2015JF003518`.

Wolff, E. W., Miners, W. D., Moore, J. C., and Paren, J. G. (1997). “Factors controlling the electrical conductivity of ice from the polar regions A summary”. In: *The Journal of Physical Chemistry B* 101.32, pp. 6090–6094. DOI: 10.1021/jp9631543.

Wolff, E. W., Moore, J. C., Clausen, H. B., Hammer, C. U., Kipfstuhl, J., and Fuhrer, K. (1995). “Long-term changes in the acid and salt concentrations of the Greenland Ice Core Project ice core from electrical stratigraphy”. In: *Journal of Geophysical Research: Atmospheres* 100.D8, pp. 16249–16263. DOI: 10.1029/95JD01174.

Xu, X., Xu, Y., and Meng, X. (2022). “SHARAD Observations of Temporal Variations of CO2 Ice Deposits at the South Pole of Mars”. In: *Remote Sensing* 14.3, p. 435. DOI: 10.3390/rs14030435.

Yan, J.-B., Li, L., Nunn, J. A., Dahl-Jensen, D., O’Neill, C., Taylor, R. A., Simpson, C. D., Wattal, S., Steinhage, D., Gogineni, P., Miller, H., and Eisen, O. (2020). “Multiangle, Frequency, and Polarization Radar Measurement of Ice Sheets”. In: *IEEE Journal of Selected Topics in Applied Earth Observations and Remote Sensing* 13, pp. 2070–2080. DOI: 10.1109/JSTARS.2020.2991682.

Yee, K. (1966). “Numerical solution of initial boundary value problems involving Maxwell’s equations in isotropic media”. In: *IEEE Transactions on antennas and propagation* 14.3, pp. 302–307. DOI: 10.1109/TAP.1966.1138693.

Young, T., Schroeder, D. M., Jordan, T. M., Christoffersen, P., Tulaczyk, S. M., Culberg, R., and Bienert, N. L. (2021). “Inferring ice fabric from birefringence loss in airborne radargrams: Application to the eastern shear margin of Thwaites Glacier, West Antarctica”. In: *Journal of Geophysical Research: Earth Surface* 126.5, e2020JF006023. DOI: 10.1029/2020JF006023.

Yu, S.-H., Mehra, R. K., and Witten, T. R. (1999). “Automatic mine detection based on ground-penetrating radar”. In: *Detection and Remediation Technologies for Mines and Minelike Targets IV*. Vol. 3710. International Society for Optics and Photonics, pp. 961–972. DOI: 10.1117/12.357116.

Chapter 7

Co-author publications

7.1 On the limitations of using polarimetric radar sounding to infer the crystal orientation fabric of ice masses

Nicholas M. Rathmann[1] , David A. Lilien[2] , Aslak Grinsted[1] , **Tamara A. Gerber**[1] , Tun Jan Young[3] , Dorthe Dahl-Jensen[1,2]

[1]*Section for the Physics of Ice, Climate and Earth, Niels Bohr Institute, University of Copenhagen, Copenhagen, Denmark*
[2]*Centre for Earth Observation Science, University of Manitoba, Winnipeg, Canada*
[3]*Scott Polar Research Institute, University of Cambridge, Cambridge, UK*

Submitted: 4 October 2021, **Published**: 17 December 2021

Rathmann, N. M., Lilien, D. A., Grinsted, A., Gerber, T. A., Young, T. J., & Dahl-Jensen, D. (2022). On the limitations of using polarimetric radar sounding to infer the crystal orientation fabric of ice masses. Geophysical Research Letters, 49, e2021GL096244.
https://doi.org/10.1029/2021GL096244

Abstract

We introduce a transfer matrix model for radio-wave propagation through layered anisotropic ice that permits an arbitrary dielectric permittivity tensor in each layer. The model is used to investigate how crystal orientation fabrics without a vertical principal direction affect polarimetric radar returns over glaciers and ice sheets. By expanding the c-axis orientation distribution in terms of a spherical harmonic series, we find that radar returns from synthetic fabric profiles are relatively insensitive to the harmonic mode responsible for a nonvertical principal direction; however, only for normally incident waves. Consequently, the strength of this mode might be relatively difficult to infer in glaciers and ice sheets, which in turn has implications for the ability to determine the full second-order structure tensor, needed to infer the local flow regime, flow history, or to represent the directional viscosity structure of glacier ice for ice-flow modeling.

Author contribution

I contributed to the publication of Rathmann et al. (2022) by participating in the discussion about the implications of the results obtained from the developed transfer matrix model with arbitrary fabric orientation, as well as in structuring the manuscript and proofread and commented on the final manuscript.

7.2 Airborne ultra-wideband radar sounding over the shear margins and along flow lines at the onset region of the Northeast Greenland Ice Stream

Steven Franke[1], Daniela Jansen[1], Tobias Binder[1,a], John D. Paden[2], Nils Dörr[3], **Tamara A. Gerber**[4], Heinrich Miller[1], Dorthe Dahl-Jensen[4,5], Veit Helm[1], Daniel Steinhage[1], Ilka Weikusat[1,6], Frank Wilhelms[1,7], and Olaf Eisen[1,8]

[1]*Alfred Wegener Institute, Helmholtz Centre for Polar and Marine Sciences, Bremerhaven, Germany*
[2]*Center for Remote Sensing of Ice Sheets (CReSIS), University of Kansas, Lawrence, KS, USA*
[3]*Institute of Photogrammetry and Remote Sensing, KIT, Karlsruhe, Germany*
[4]*Physics of Ice, Climate, and Earth, Niels Bohr Institute, University of Copenhagen, Denmark*
[5]*Centre for Earth Observation Science, University of Manitoba, Winnipeg, Canada*
[6]*Department of Geosciences, Eberhard Karls University Tübingen, Tübingen, Germany*
[7]*Department of Crystallography, Geoscience Centre, University of Göttingen, Göttingen, Germany*
[8]*Department of Geosciences, University of Bremen, Bremen, Germany*
[a]*now at: Ibeo Automotive Systems, Hamburg, Germany*

Submitted: 17 March 2021 – **Published**: 21 February 2022

Franke, S., Jansen, D., Binder, T., Paden, J. D., Dörr, N., Gerber, T. A., Miller, H., Dahl-Jensen, D., Helm, V., Steinhage, D., Weikusat, I., Wilhelms, F., and Eisen, O.: Airborne ultra-wideband radar sounding over the shear margins and along flow lines at the onset region of the Northeast Greenland Ice Stream, Earth Syst. Sci. Data, 14, 763–779, https://doi.org/10.5194/essd-14-763-2022, 2022.

Abstract

We present a high-resolution airborne radar data set (EGRIP-NOR-2018) for the onset region of the Northeast Greenland Ice Stream (NEGIS). The radar data were acquired in May 2018 with the Alfred Wegener Institute's multichannel ultra-wideband (UWB) radar mounted on the Polar 6 aircraft. Radar profiles cover an area of $\sim$24,000 km^2 and extend over the well-defined shear margins of the NEGIS. The survey area is centered at the location of the drill site of the East Greenland Ice-Core Project (EastGRIP), and several radar lines intersect at this location. The survey layout was designed to (i) map the stratigraphic signature of the shear margins with radar profiles aligned perpendicular to ice flow, (ii) trace the radar stratigraphy along several flow lines, and (iii) provide spatial coverage of ice thickness and basal properties. While we are able to resolve radar reflections in the deep stratigraphy, we cannot fully resolve the steeply inclined reflections at the tightly folded shear margins in the lower part of the ice column. The NEGIS is causing the most significant discrepancies between numerically modeled and observed ice surface velocities. Given the high likelihood of future climate and ocean warming, this extensive data set of new high-resolution radar data in combination with the EastGRIP ice core will be a key contribution to understand the past and future dynamics of the NEGIS. The EGRIP-NOR-2018 radar data products can be obtained from the PANGAEA data publisher (https://doi.pangaea.de/10.1594/PANGAEA.928569; Franke et al., 2021a).

Author contribution

I contributed to the publication of Franke et al. (2022b) in writing the introduction, as well as participating in the discussion of the manuscript structure and in the revision process.

7.3 Accelerating ice flow at the onset of the Northeast Greenland ice stream

Aslak Grinsted[1], Christine S. Hvidberg[1], David A. Lilien[2], Nicholas M. Rathmann[1], Nanna B. Karlsson[3], **Tamara Annina Gerber**[1], Helle Astrid Kjær[1], Paul Vallelonga[4], and Dorthe Dahl-Jensen[1,2]

[1]*Niels Bohr Institute, University of Copenhagen; Copenhagen, Denmark*
[2]*Centre for Earth Observation Science, University of Manitoba, Winnipeg, MB, Canada*
[3]*Geological Survey of Denmark and Greenland; Copenhagen, Denmark*
[4]*Oceans Graduate School, The University of Western Australia; Perth, Australia*

Submitted: 27th April 22, *Nature Communication*

Abstract

Mass loss near the ice-sheet margin is evident from remote sensing as frontal retreat and increases in ice velocities. Velocities in the ice sheet interior are orders of magnitude smaller, making it challenging to detect velocity change. Here, we analyze a 35-year record of remotely sensed velocities, and a 6-year record of repeated GPS observations, at the East Greenland Ice-core Project, located in the middle of the Northeast-Greenland Ice Stream (NEGIS). We find that the shear margins of NEGIS are accelerating, indicating a widening of the ice stream. We demonstrate that the widening of the ice stream is unlikely to be a response to recent changes at the outlets of NEGIS.

Author contribution

I contributed to this work by Grinsted et al. (2022) by adding to the discussion about the NEGIS stability and the implication of the observed shear margin acceleration, as well as the revision of the manuscript.

Chapter 8

Discussion, outlook and conclusion

8.1 Summary

The work presented in this thesis combines information from the EastGRIP ice core and RES data recorded in the onset region of the NEGIS, with the aim of connecting the small scales of direct observations with the large scales accessible by radar surveys.

The chemical and electrical records measured in ice cores show seasonal periodicity and allow the establishment of timescales by means of annual layer counting. The same signals cause englacial reflections which can be traced over long distances (e.g. MacGregor et al., 2015). The study presented in Chapter 4 makes use of IRHs to determine the source area of the ice found in the EastGRIP ice core. Together with others, I transferred the annual layer counted GICC05 chronology to the deeper part of the EastGRIP core by matching ECM and other signals between the EastGRIP, NEEM and NorthGRIP ice-core records, and extended the timescale by Mojtabavi et al. (2020a) to a depth of 2122.45 m. Following this, I dated isochrones observed in radargrams near EastGRIP with the obtained timescale and traced them upstream along three approximated flowlines. By simulating the propagation of the internal stratigraphy over time and adjusting the flow parameters by minimizing the misfit between modeled and observed isochrones, I could estimate the source location of the EastGRIP ice. This is important for a variety of chemical and physical ice-core analyses, as some of the measured quantities are sensitive to spatial variations in e.g. accumulation rate or surface temperature. The inverted flow parameters moreover provide information on the flow dynamics in the upstream part of the NEGIS.

RES images can be further exploited by deriving information about the physical properties of ice. The orientation of ice crystals affects the propagation of radar waves due to their birefringent nature. Crystal orientation fabrics that result in some degree of horizontal anisotropy cause birefringent-induced power extinction, as well as travel time anisotropy of radar reflections. The analysis of these effects in ground-based and airborne radargrams, as well as pRES measurements, allowed me and others to map the distribution of the horizontal fabric anisotropy in the NEGIS onset region (Chapter 5). The good agreement with fabric evolution models and COF observations in ice cores confirms the robustness of the individual methods. By making a few assumptions of the expected fabric type and orientation of the eigenvectors, I estimated the fabric eigenvalues from the horizontal anisotropy by which I could calculate the directional flow enhancement factors to estimate the effect of COF on the ice viscosity. This analysis suggests that ice inside the ice stream can become stiffer for along-flow pure shear deformation by an order of magnitude, which has potential consequences for ice-flow dynamics and the ice stream sensitivity towards disturbances at the bed or at the downstream end of the NEGIS.

Abrupt vertical changes in the crystal orientation fabric can potentially lead to radar reflections which are of anisotropic character. However, other mechanisms of anisotropic scattering exist but are not very well understood yet. The visual stratigraphy of the EastGRIP ice core indicates that the roughness of individual layers depends on the angle at which the cores are cut relative to the ice-flow direction. This directionality of interface roughness is more pronounced at EastGRIP than observed in other ice cores and is interpreted as the result of the prevailing stress regime and ice-flow history. By means of numerical modeling with the open-source software GprMax, I simulated the radar response of the internal stratigraphy in the NEGIS (Chapter 6). Synthetic radargrams with DEP and ECM data enable the accurate determination of the depth and age of internal reflections and in general show a good agreement with radargrams recorded in the field. Sensitivity studies revealed that most reflections can be attributed to single conductivity peaks, although a few reflections arise from interfering signals of two or more conductivity contrasts close to each other. Simulations with directional permittivities obtained from the COF analyses show travel time difference similar to what is observed at radar cross-points, which also confirms the travel-time anisotropy method of deriving the depth-average horizontal fabric anisotropy described in Chapter 5. No evidence of COF induced reflections was found in the ice column down to the current drill depth of ∼2122 m, using a center frequency of 195 MHz. Layer roughness studies showed that rough interfaces can lead to thicker reflections and decrease the ability of distinguishing individual layers. Directional roughness can also cause depolarization effects, in particular if the antenna polarization is perpendicular to the folding axis.

8.2 Discussion

8.2.1 Processes controlling rapid ice flow

Unlike most other ice streams in Greenland, the NEGIS is not confined by basal topography (Joughin et al., 2001; Franke et al., 2020). The high surface velocities observed in its onset region (Hvidberg et al., 2020) can thus not be explained by topographic ice-flow channeling which leads to flow acceleration for reasons of mass conservation and basal hydrology (Bennett, 2003). The NEGIS is also unique because it reaches exceptionally far inland, initiating less than 50 km from Greenland's central ice divide. A much discussed hypothesis for the formation and spatial confinement of the NEGIS is an elevated geothermal heat flux which leads to basal meltwater production and hence facilitates basal sliding (Fahnestock et al., 2001b; Keisling et al., 2014; Smith-Johnsen et al., 2020a). The origin of this high geothermal heat flux is associated with the trail of the Icelandic plume, as the Greenland plate passed the area of mantle upwelling, which underlies Iceland today, around 60 Ma ago (Rogozhina et al., 2016; Martos et al., 2018). A geothermal heat flux as high as 970 $\mathrm{mWm^{-2}}$ was initially suggested by Fahnestock et al. (2001b) to be necessary for explaining the high basal melt rates derived from RES stratigraphy. Fahnestock et al. (2001b) already noted that this number is 17× higher than the continental background. Bons et al. (2021) emphasized that such a high geothermal heat flux is geologically unrealistic, as it exceeds the geothermal heat flux in the Iceland trail by far, as well as that of any other known volcanically active region on Earth.

The in Chapter 4 presented ice-flow parameters along the upstream flowline of EastGRIP indicate considerable amount of basal sliding and the presence of high basal melt rates at distinct locations. This supports the hypothesis that basal melt and sliding is probably an important contributor to the flow dynamics in the NEGIS today, supporting similar conclusions obtained by e.g. Fahnestock et al. (2001b), MacGregor et al. (2016), and Zeising and Humbert (2021). However, the inverted parameters controlling the Dansgaard-Johnsen model are not uncorrelated and their accuracy is limited by several reasons, including the deviation from the real flowline, unknown variations in the past velocity field, and by the simplicity of the 2D model which does not capture the full complexity of the flow dynamics. Furthermore, the flow parameters are averages over time, assuming a steady state of the NEGIS in the past 80,000 years, which might not be the case. Because the flow parameters at one point along the flowline mainly affect the isochrones at that location and further downstream, the parameters around

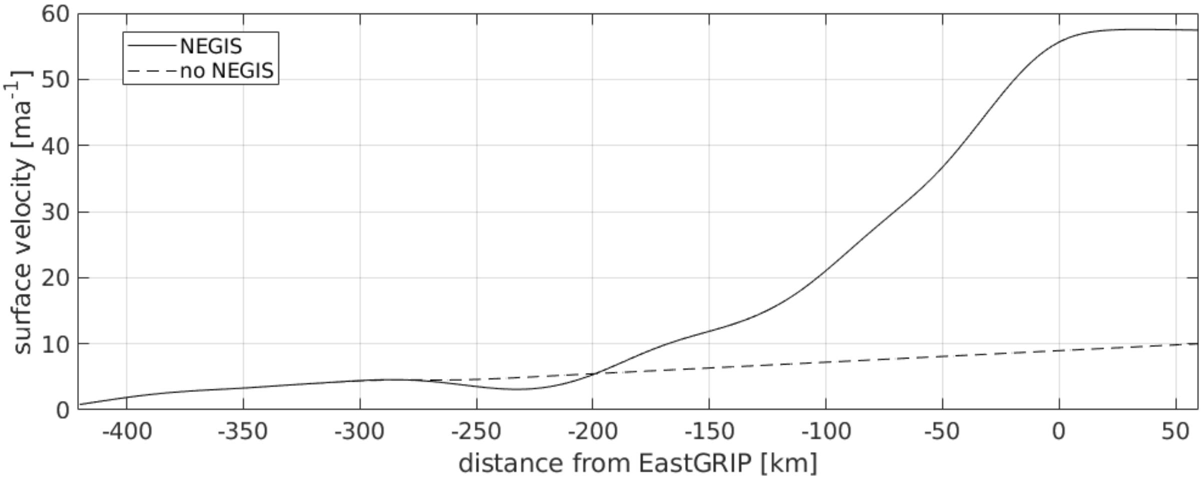

FIGURE 8.1: Surface velocities along a flow line from GRIP to EastGRIP following the ice-stream center (Flow line C in Fig. 4.1). The blue line is the measured present-day surface velocity (Joughin et al., 2018), the red line represents the surface flow in absence of the NEGIS and was obtained via interpolation to 10 ma^{-1} of a typical flank flow outside the NEGIS.

EastGRIP are not very well constrained. Though I can conclude that basal melt and sliding is likely to be important for the high flow velocities of the NEGIS today, I can not draw reliable conclusions about the amount of basal melt and water production from the parameter inversion due to the reasons given above. It therefore remains unclear what kind of basal processes are responsible for how much of the observed surface velocities.

8.2.2 Ice stream age: Long-term stability or recent evolution?

The hypothesis that the NEGIS is initiated and controlled by mantle processes underneath Greenland rises questions about the age and stability of the NEGIS. The passage of Greenland over the mantle plume occurred long before the formation of the Greenland ice sheet, so the geothermal heat prevailed for a long time. The age of the NEGIS, however, is still unclear. The lack of imprint in the upstream basal topography might be an indication of a relatively young age, as basal erosion and the carving of basal troughs takes time. However, Christianson et al. (2014) found evidence of water-saturated till at the ice stream bed, which can shield the underlying bedrock from abrasion (Cuffey and Alley, 1996). The question then remains, if enough unconsolidated sediment exists or is replenished from e.g. melting of dirty ice to sustain the deforming bed for sufficiently long, and inhibit erosion of the underlying bedrock, if the NEGIS would have existed for many thousands of years (Cuffey and Alley, 1996). A recent study by Jansen et al. (2022, in review) suggests that the folds of the internal stratigraphy in the shear margins formed only around 2000 years ago, implying that the present-day form of the NEGIS evolved relatively recently.

The in this thesis presented spatial distribution of the horizontal fabric anisotropy in the NEGIS onset region (Chapter 5) agrees well with the results obtained from a fabric evolution model which assumes a steady state ice stream over 5000 years. Downstream of EastGRIP, the decreasing strength of the horizontal anisotropy is associated with the widening of the ice stream, and is consistent with the current strain-rate regime of the NEGIS. The advection time of the ice at EastGRIP, where a girdle-type fabric prevails until the disappearance of the horizontal anisotropy downstream, is approximately 800 years under present-day surface flow velocities. Assuming that the downstream fabric used to be a girdle when the ice was further upstream, this observation indicates, that fabrics can relatively quickly be overprinted.

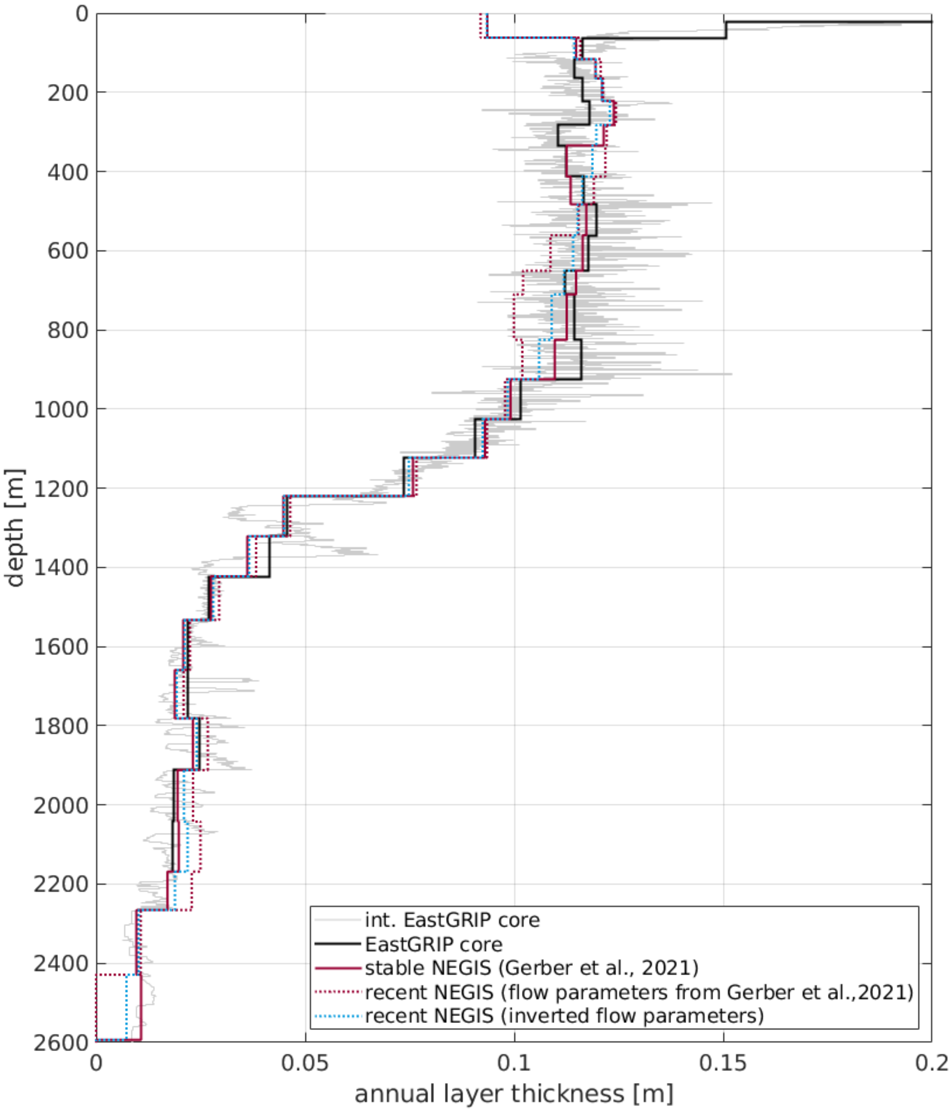

FIGURE 8.2: Annual layer thickness in the EastGRIP ice core. The gray background is a interpolated annual layer thickness as observed from the ice-core timescale. The purple solid line indicates the results obtained from flow line C in Gerber et al. (2021)/Chapter 4, the purple dashed line represents the layer thickness where no ice stream exists before 2ka b2k using the same ice-flow parameters as for the solid purple line. The red dashed line indicates the modeled layer thickness for the NEGIS shutdown scenario where the flow parameters were inverted with a Monte Carlo inversion.

The observed COF anisotropy does therefore not conflict with a possibly young age of the NEGIS, although the absence of disagreement does not necessarily support the hypothesis of a recent evolution of the NEGIS, and no more specific conclusions about the ice-stream age can be drawn from the fabric distribution at this point.

The nearly constant annual layer thickness observed in the upper 900 m of the EastGRIP ice core can be explained by upstream flow effects. As a consequence of increasing accumulation rate with increasing upstream distance, the annual layer thickness becomes larger for older ice deposited farther upstream. This seems to compensate for the vertical thinning due to the overlying pressure, resulting in the constant layer thickness observed in the EastGRIP ice core. In Gerber et al. (2021) (Chapter 4) it was mentioned that the constant annual layer thickness might indicate past ice-stream stability, as past ice-flow velocities must have been high enough to transport ice from upstream areas with sufficiently high accumulation rates to

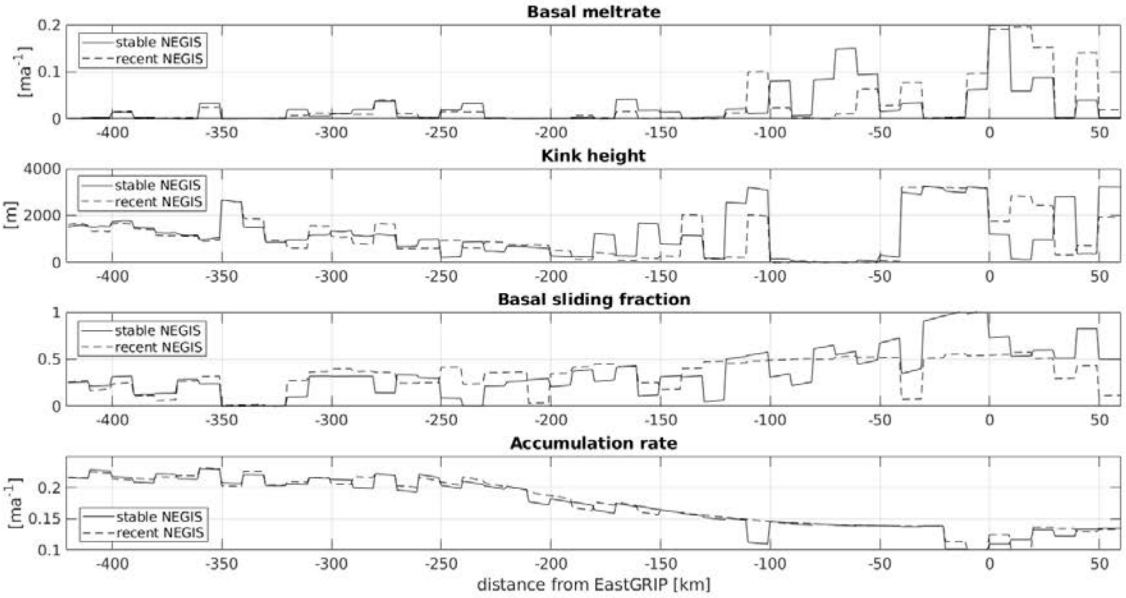

FIGURE 8.3: Comparison of the inverted ice-flow parameters basal meltrate, kink height, basal sliding fraction and accumulation rate. The solid lines are the parameters from Gerber et al. (2021) for a stable NEGIS scenario, the dashed lines represent the scenario of a recent NEGIS evolution from 2000 years ago.

explain the constant layer thickness at EastGRIP. To test the hypothesis of a young ice stream age suggested by Jansen et al. (2022), I repeated the ice-flow simulation (as in Chapter 4) with the flowline from the ice stream center (flowline C, Fig. 4.1), but adjusted the model so that no ice stream existed before 2 ka b2k. For ages older than that I interpolated the surface velocities to a maximum of $\sim$10ma^{-1}, which is comparable to flank flow outside the NEGIS, and used the same present-day surface velocity profile by Gerber et al. (2021) for younger ages (Fig. 8.1). I calculated the annual layer thickness resulting from a 'young' NEGIS with 1) the same flow parameters obtained from the stable ice stream (Gerber et al., 2021), and 2) flow parameters obtained by constraining the Monte-Carlo inversion with the scenario of a recent ice-stream evolution.

Using the same flow parameters as obtained in Gerber et al. (2021), the lower velocities related to the absence of NEGIS before 2000 years unsurprisingly result in an underestimation of the annual layer thickness, in particular between 500 and 1000 m depth (Fig. 8.2). By tuning the ice-flow parameters for the 'recent NEGIS' scenario, however, the annual layer thicknesses are pretty close to the results obtained with a stable ice stream. The inverted flow parameters (Fig. 8.3) of the two scenarios most notably differ in the amount of basal sliding and basal meltrate. In the scenario of a recent evolution of the NEGIS, a larger fraction of the ice flow occurs through internal deformation. As discussed in Chapter 4, high basal sliding and flow-acceleration leads to along-flow extension of the stratigraphy and results in internal layer thinning, while the opposite is true for less slippery beds (Weertman, 1976). The isochrone misfit (Fig. 8.4) is larger for the scenarios with a recent NEGIS development than for the stable ice stream by Gerber et al. (2021), particularly in the downstream end, although the misfit is considerably improved with a parameter inversion adjusted to the new scenario, as can be expected. The large isochrone misfit near EastGRIP in Fig. 8.4d,f can be attributed to an overestimate of basal meltrates in that region. As also discussed in Chapter 4, the large misfit at the downstream end can be explained by the insufficient parameter resolution and extending the flow-line profile farther downstream would help to reduce the inversion ambiguities. The results obtained here imply that the constant annual layer thickness at EastGRIP could also be

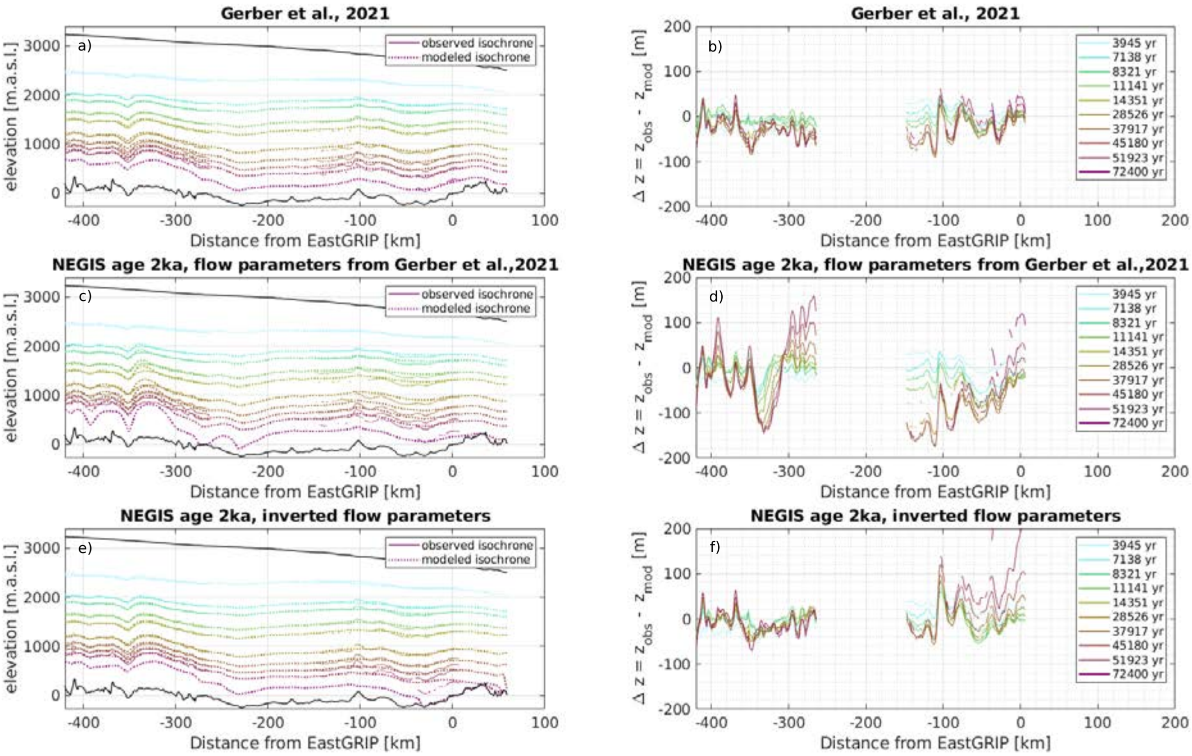

FIGURE 8.4: Modeled and observed isochrones **(a,c,e)** as well as the isochrone misfit **(b,d,f)** for a scenario with a stable ice stream **(a,b)** and a scenario where the ice stream evolved only 2000 years ago **(c-f)**. The middle panels **c** and **d** show the model results using the same flow parameters as in **a,b**. In panel **e** and **f** the flow parameters were inverted for the NEGIS shutdown scenario.

explained by a relatively young age of the NEGIS, if the layer thinning related to along-flow extension is decreased.

Temporal variations in geothermal heat flux are generally small and occur slowly, so a (in geological terms) recent ice stream initiation caused by a geothermal heat anomaly resulting from an event 60 Ma ago seems counter-intuitive. Stevens et al. (2016) discussed processes that can trigger enhanced volcanic activity caused by ice-age cycling. According to their findings, repeated mantle compression and decompression due to variations in the mass load could explain elevated geothermal heat flux and possibly hydrothermal activity, as well as a higher temporal and spatial variability of the geothermal heat flux, although so far no direct observations provide the evidence to confirm that this is the case in central Greenland. Regardless of the ice stream age, a geologically feasible geothermal heat flux alone can not be responsible for the high surface velocities (Smith-Johnsen et al., 2020b; Bons et al., 2021), nor can it explain the narrow geometry of the NEGIS, as evidence of increased basal temperatures cover a spatially more extensive area (MacGregor et al., 2016). While geothermal heat might play a considerable role in facilitating ice flow through meltwater production, it is evident that other processes are important in confining the NEGIS to its current geometry.

8.2.3 Ice stream geometry and role of the shear margins

The ice stream geometry, if not through topography, needs to be confined by other processes. Basal water routing has been proposed to confine the NEGIS by lubricating the bed in a spatially limited zone, causing rapid ice flow inside the NEGIS (e.g. Fahnestock et al., 2001b; Christianson et al., 2014; Keisling et al., 2014). The shear-margin troughs observed in the ice-sheet surface topography (Fahnestock et al., 2001a; Simonsen and Sørensen, 2017) could thereby play an essential role in affecting the hydropotential such that basal water remains inside the ice stream (Christianson et al., 2014). The depression in the surface elevation seems to arise from enhanced firn densification processes related to the high strain-rates within the shear margins (Christianson et al., 2014; Riverman et al., 2019). Furthermore, the internal stratigraphy across the NEGIS indicates enhanced basal melt inside compared to outside the ice stream, which might be attributed to heat generation through basal friction (Keisling et al., 2014). One could thus argue that once shear margins have developed they confine the rapid flow to the ice stream interior by controlling the basal water routing. Moreover, fast ice streaming might support itself through additional frictional heating at the base and supplementary meltwater production. Yet, it remains unclear how the NEGIS shear margins evolved, how actively they contribute to facilitating fast ice flow today and how stable they are in their position.

Shear deformation is likely to produce considerable temperature anomalies through frictional heating which makes ice softer for deformation (Holschuh et al., 2019a). The development of a strong single maximum fabric observed in the S5 shear-margin core in the NEGIS, as well as in other ice streams (e.g. Gerbi et al., 2021; Thomas et al., 2021), is also reproduced by the Elmer/Ice fabric evolution model of the NEGIS onset. The agreement between model and observations implies, that strong horizontal single maximum COF are collective characteristics of shear margins. As discussed in Chapter 5, the horizontal single maximum fabric potentially supports shear-margin softening if the c-axes are predominantly oriented favorably towards shear deformation. However, observations from the available ground-based and airborne radar data do currently not allow us to determine the fabric orientation, and due to the pronounced loss of radar return power in the shear margins, pRES measurements which otherwise have the potential to infer the c-axis orientation are left ineffective.

The fabric, as well as temperature anomalies are advected with ice flow, such that technically, the shear margins should not be fixed in position. Christianson et al. (2014) suggested bands of poorly lubricated bed resulting from water focusing and controlled by the hydropotential to be responsible for a spatial stabilization of the shear margins and for limiting additional inflow of water or ice into the ice stream. They argue that changes at the coastal front which disturb the hydropotential would, however, affect these ’sticky’ bands and, hence, the stability of the shear margin position. Northwest of EastGRIP, the surface strain rates show an ’offset’ of the shear margin, and radargrams crossing that area indicate the downstream advection of folds (Franke et al., 2022a) from the ’inner’ shear margin, while the ’outer’ shear margin is active today. If temperature anomalies and an oriented fabric is important for sustaining shear margins, it is interesting that ice flow seems to favor the evolution of a new ’outer’ shear margin instead of shearing along the already softened margin advected from further upstream. The ’offset’ in the surface strain rates might therefore be an indication of the spatial instability of shear margins and the ice stream geometry in general. Analyses of GPS-measurements and satellite-based velocity maps in the vicinity of EastGRIP in a recent study by Grinsted et al. (2022, in review) indicate ice-flow acceleration in the shear margins, suggesting that the ice stream is currently widening as a result of dynamical instability. However, the observed acceleration is very small, and as the NEGIS was only discovered 30 years ago (Fahnestock et al., 1993), observational data are not long enough to monitor possible shear-margin migration with certainty. Further research is required to fully understand the processes that would trigger ice stream widening as well as the timely evolution of the NEGIS.

8.3 Outlook

The analyses of birefringence-induced beat signatures and travel-time anisotropy from internal reflections allowed me and others to determine the depth-average horizontal fabric anisotropy. However, for a better understanding of its effect on flow dynamics, distinguishing vertically symmetric fabric types and determining the COF orientation, as well as its variation with depth would be highly useful. In our analysis we could not distinguish between vertically symmetric fabrics such as isotropy and vertical single maximum, but the effect of these two options on the ice viscosities are quite different. It is difficult to distinguish these fabrics with radar data, as the wave polarization is perpendicular to the propagation direction, and for nadir-surveys, therefore, inevitably horizontal. Seismic methods could potentially help to distinguish between isotropic ice and vertical single maximum, because seismic p-waves travel faster along the c-axis orientation compared to the basal plane (e.g. Diez et al., 2014; Diez et al., 2015; Brisbourne et al., 2019). Alternatively, borehole-geophysics has been used on alpine glaciers with the attempt of performing travel-time tomography to determine the fabric type (e.g. Holliger et al., 2001). A major challenge in both borehole-seismic and -radar applications is the uncertain position of the hydrophone/shotgun and radar antennas within the boreholes, which introduces large uncertainties in the travel times. If this problem could be overcome by a device that either fixes the antenna within the borehole or determines its position and inclination accurately, borehole methods could be a promising method to reduce ambiguities in vertically symmetric fabrics. Of course, the most direct information could be gained from another ice core further downstream. Shallow cores usually reach depths in the range of 100-200 m. In the EastGRIP ice core the girdle evolves at greater depths, although the rotation is already apparent in the upper 200 m. A shallow core might therefore only provide little information to distinguish vertical symmetry. From a logistical point of view, retrieving a shallow core and/or conducting surface-based seismic surveys would probably be the most efficient methods. Borehole geophysics can be performed in hot-water drilled boreholes which can be more rapidly established than ice-core boreholes, but the depth is limited based on the the hose length. In comparison to the application on temperate glaciers, it would be easier to keep the boreholes dry and reduce noise from running water on the glacier, on the other hand it would be less energy-efficient as snow would first need to be melted to feed the hot-water drill. Of course, drilling another deep ice core would give insight into the fabric without ambiguities, but the expenses related to it would be hard to justify with the purpose of determining the fabric only.

The orientation of the fabric could quite realistically be determined with radar measurements by means of antenna rotation on the spot. This is done with pRES measurements, and while analyses to retrieve the fabric orientation are still ongoing, the good signal quality seems promising. pRES measurements are relatively cumbersome if done by hand and are therefore limited to few locations only. In the coming field season, an autonomous rover is being tested at EastGRIP, which technically can drive for hundreds of kilometers using solar power. If pRES measurements could be automated by programming the rover to rotate on its own and antennas could be mounted on top of the vehicle, it could potentially be a way of determining the fabric distribution at various points more efficiently.

Information on the fabric variation with depth can also be obtained from pRES analyses due to the high vertical resolution, although pRES measurements applied in the NEGIS have so far been limited to a depth of ∼1000 m. Further measurements with more powerful systems provide the possibility of retrieving information from greater depths and are planned for the coming field season. The travel-time anisotropy analysis performed on crosspoints of airborne radar lines in theory also provide information about changes in the horizontal anisotropy with depth. However, the uncertainties in the data used in this thesis were too large to gain reliable results, mostly due to the limited range resolution and the spatial and temporal offsets between the recorded profiles. Dual-polarized ground-based radars would help to reduce these uncertainties, as it can be ensured that the two polarizations are recorded at the same location, and could thus be able to determine the depth-dependent anisotropy and the vertical resolution is higher than in the airborne systems (Yan et al., 2020).

Dual-polarized radars like the EastGRIP UWB radar (Yan et al., 2020) also have the potential to resolve reflections from fabric transitions better. In addition, they bear the potential of retrieving structural information from the interface, such as small-scale folds because of the higher vertical resolution. Based on the modeling studies with GprMax, reflections could appear thicker or thinner, depending on the geometry and the presence of scattering mechanisms. The mapping of the interface roughness could provide additional information on the strain-regime of certain interfaces, if the isochrone folding can be associated with deformation through ice flow, and might thus contribute to our understanding of the past ice flow in the NEGIS and answering the question of the ice-stream age. The presence of folded layers can also cause depolarization effects, which are affecting interpretations of birefringence-induced beat signatures in terms of fabric orientation because anisotropic scattering affects the angle between antenna polarization and fabric axes at which the power extinction nodes are most pronounced (Fujita et al., 2006).

Finally, despite the many obstacles encountered during the EastGRIP project so far, the prospect of reaching the bedrock in the coming years is quite exciting. Unique and important information can be expected from the EastGRIP ice core when getting close to the bed. Information on the basal water pressure, temperatures, basal material and crystal orientation and structure are only a few parameters which will be revealed by extending the current borehole to the bed and are highly important in understanding the ice-flow mechanisms. Some of the important questions discussed above might be partially answered with the insights gained from the deep part of the EastGRIP borehole.

The fabric in the upper 80 % of the EastGRIP ice core is dominated by a vertical girdle (Stoll, 2019), comparable to the observations in e.g. the EDML core. Below ∼1800 m depth of the EDML ice core, Faria et al. (2010) describe the transition from a vertical girdle towards a vertical single maximum due to the horizontal shear deformation related to the bedrock. A similar transition could be expected at EastGRIP because of the rapid flow and presumably strong horizontal shear deformation at the bed. Down to the current borehole depth, however, no indication of fabric rotation has been found. This is not unsurprising, as ice flow in ice streams occurs more as block flow and less due to internal deformation, so that the fabric transition depth is expected to be located deeper than at the EDML site. The fabric transition observed in the EDML core is the cause for a radar reflection of directional strength (Eisen et al., 2007), and a similar reflection might be detectable with ground-based dual-polarized systems near EastGRIP.

8.4 Conclusion

The response of ice sheets to climate change and the complex feedback mechanisms related to their interaction with other components of the Earth system, play a crucial role in defining the kind of challenges that human societies will be facing in the future. Yet, uncertainties in ice-sheet prognoses are still enormous, part of which arise from our incomplete understanding of ice-flow dynamics. In particular the processes that are driving rapid ice flow in ice streams and fast-flowing outlet glaciers, are insufficiently understood. Comprehending the relevant physical mechanisms and implementing them into prognostic ice-sheet models remains one of the biggest challenges in glaciology today.

Ice cores are the only method to retrieve direct information from the depth of ice sheets and continue to be an invaluable tool for glaciological and climatic research. Deep drilling projects are enormous and expensive undertakings, lasting for several years, and typically involve multiple nations and experts from all over the world. Yet, the expenses and logistical efforts of these projects are justified by the large amount of scientific output. Nevertheless, the interpretation of ice-core analyses in terms of flow dynamics is limited due to their confined spatial coverage. Observations in ice cores and their paleoclimatic interpretations are thus not necessarily representative on large spatial scales.

Indirect geophysical methods can partially compensate for this shortcoming through their efficiency in surveying spatially more extensive areas. Radio-echo-sounding specifically, is a powerful tool because it doesn't require ground-coupling and can be conducted from airplanes. Being an indirect sensing method, RES suffers, however, from ambiguities in data analysis and a thorough understanding of ice physics and other factors controlling radar response is necessary for an accurate interpretation of radargrams. The combined analysis of ice cores and RES data can surmount some of these ambiguities and lead to an overall more comprehensive perception of glacial processes.

In this thesis, I presented combined analyses of RES and ice-core data in order to extend the detailed knowledge of the physical and chemical properties of the ice core to the large scales necessary for a thorough understanding of ice flow. The results obtained in my studies help to reduce ambiguities in the interpretation of radargrams and ice-core measurements, and reveal valuable information on the mechanical ice properties relevant for ice-flow models. They thereby promote the ability of ice-sheet models to capture physical processes more accurately and improve their reliability in prognoses of glaciological processes in the future. With this thesis I hope to contribute a small piece of knowledge to the big puzzle of ice dynamics and towards a more thorough understanding of the NEGIS and ice streams in general. Yet, important questions of ice stream evolution, their sensitivity towards perturbations and processes governing the rapid ice flow remain obscured and further research is required to unravel the answers that are hidden somewhere in the ice.

References

Bennett, M. R. (2003). “Ice streams as the arteries of an ice sheet: their mechanics, stability and significance”. In: *Earth-Science Reviews* 61.3-4, pp. 309–339. DOI: `10.1016/S0012-8252(02)00130-7`.

Bons, P. D., Riese, T. de, Franke, S., Llorens, M.-G., Sachau, T., Stoll, N., Weikusat, I., Westhoff, J., and Zhang, Y. (2021). “Comment on “Exceptionally high heat flux needed to sustain the Northeast Greenland Ice Stream” by Smith-Johnsen et al.(2020)”. In: *The Cryosphere* 15.5, pp. 2251–2254. DOI: `10.5194/tc-15-2251-2021`.

Brisbourne, A. M., Martín, C., Smith, A. M., Baird, A., Kendall, J., and Kingslake, J. (2019). “Constraining recent ice flow history at Korff Ice Rise, West Antarctica, using radar and seismic measurements of ice fabric”. In: *Journal of Geophysical Research: Earth Surface* 124.1, pp. 175–194. DOI: `10.1029/2018JF004776`.

Christianson, K., Peters, L. E., Alley, R. B., Anandakrishnan, S., Jacobel, R. W., Riverman, K. L., Muto, A., and Keisling, B. A. (2014). “Dilatant till facilitates ice-stream flow in northeast Greenland”. In: *Earth and Planetary Science Letters* 401, pp. 57–69. DOI: `10.1016/j.epsl.2014.05.060`.

Cuffey, K. and Alley, R. B. (1996). “Is erosion by deforming subglacial sediments significant? (Toward till continuity)”. In: *Annals of Glaciology* 22, pp. 17–24. DOI: `10.3189/1996AoG22-1-17-24`.

Diez, A., Eisen, O., Hofstede, C., Lambrecht, A., Mayer, C., Miller, H., Steinhage, D., Binder, T., and Weikusat, I. (2015). “Seismic wave propagation in anisotropic ice – Part 2: Effects of crystal anisotropy in geophysical data”. In: *The Cryosphere* 9.1, pp. 385–398. DOI: `10.5194/tc-9-385-2015`.

Diez, A., Eisen, O., Weikusat, I., Eichler, J., Hofstede, C., Bohleber, P., Bohlen, T., and Polom, U. (2014). “Influence of ice crystal anisotropy on seismic velocity analysis”. In: *Annals of Glaciology* 55.67, pp. 97–106. DOI: `10.3189/2014AoG67A002`.

Eisen, O., Hamann, I., Kipfstuhl, S., Steinhage, D., and Wilhelms, F. (2007). “Direct evidence for continuous radar reflector originating from changes in crystal-orientation fabric”. In: *The Cryosphere* 1.1, pp. 1–10. DOI: `10.5194/tc-1-1-2007`.

Fahnestock, M., Joughin, I., Scambos, T., Kwok, R., Krabill, W., and Gogineni, S. (2001a). “Ice-stream-related patterns of ice flow in the interior of northeast Greenland”. In: *Journal of Geophysical Research: Atmospheres* 106.D24, pp. 34035–34045. DOI: `10.1029/2001JD900194`.

Fahnestock, M., Abdalati, W., Joughin, I., Brozena, J., and Gogineni, P. (2001b). “High geothermal heat flow, basal melt, and the origin of rapid ice flow in central Greenland”. In: *Science* 294.5550, pp. 2338–2342. DOI: `10.1126/science.1065370`.

Fahnestock, M., Bindschadler, R., Kwok, R., and Jezek, K. (1993). “Greenland Ice Sheet Surface Properties and Ice Dynamics from ERS-1 SAR Imagery”. In: *Science* 262.5139, pp. 1530–1534. DOI: `10.1126/science.262.5139.1530`.

Faria, S. H., Freitag, J., and Kipfstuhl, S. (2010). “Polar ice structure and the integrity of ice-core paleoclimate records”. In: *Quaternary Science Reviews* 29.1. Climate of the Last Million Years: New Insights from EPICA and Other Records, pp. 338–351. DOI: `10.1016/j.quascirev.2009.10.016`.

Franke, S., Jansen, D., Binder, T., Paden, J. D., Dörr, N., Gerber, T. A., Miller, H., Dahl-Jensen, D., Helm, V., Steinhage, D., Weikusat, I., Wilhelms, F., and Eisen, O. (2022a). “Airborne ultra-wideband radar sounding over the shear margins and along flow lines at the onset region of the Northeast Greenland Ice Stream”. In: *Earth System Science Data* 14.2, pp. 763–779. DOI: `10.5194/essd-14-763-2022`.

Franke, S., Jansen, D., Binder, T., Dörr, N., Helm, V., Paden, J., Steinhage, D., and Eisen, O. (2020). “Bed topography and subglacial landforms in the onset region of the Northeast

Greenland Ice Stream". In: *Annals of Glaciology* 61.81, pp. 143–153. DOI: 10.1017/aog.2020.12.

Fujita, S., Maeno, H., and Matsuoka, K. (2006). "Radio-wave depolarization and scattering within ice sheets: a matrix-based model to link radar and ice-core measurements and its application". In: *Journal of Glaciology* 52.178, pp. 407–424. DOI: 10.3189/172756506781828548.

Gerber, T. A., Hvidberg, C. S., Rasmussen, S. O., Franke, S., Sinnl, G., Grinsted, A., Jansen, D., and Dahl-Jensen, D. (2021). "Upstream flow effects revealed in the EastGRIP ice core using Monte Carlo inversion of a two-dimensional ice-flow model". In: *The Cryosphere* 15.8, pp. 3655–3679. DOI: 10.5194/tc-15-3655-2021.

Gerbi, C., Mills, S., Clavette, R., Campbell, S., Bernsen, S., Clemens-Sewall, D., Lee, I., Hawley, R., Kreutz, K., Hruby, K., and al., et (2021). "Microstructures in a shear margin: Jarvis Glacier, Alaska". In: *Journal of Glaciology* 67.266, pp. 1163–1176. DOI: 10.1017/jog.2021.62.

Grinsted, A., Hvidberg Christine S.and Lilien, D. A., Rathmann, N. M., Karlsson, N. B., Gerber, T. A., Kjær, H. A., Vallelonga, P., and Dahl-Jensen, D. (2022). "Accelerating ice flow at the onset of the Northeast Greenland ice stream". In: *Nature Communication*. in review.

Holliger, K., Musil, M., and Maurer, H. (2001). "Ray-based amplitude tomography for crosshole georadar data: a numerical assessment". In: *Journal of Applied Geophysics* 47.3. Ground Penetrating Radar, pp. 285–298. DOI: 10.1016/S0926-9851(01)00072-6.

Holschuh, N., Lilien, D. A., and Christianson, K. (2019a). "Thermal Weakening, Convergent Flow, and Vertical Heat Transport in the Northeast Greenland Ice Stream Shear Margins". In: *Geophysical Research Letters* 46.14, pp. 8184–8193. DOI: 10.1029/2019GL083436.

Hvidberg, C. S., Grinsted, A., Dahl-Jensen, D., Khan, S. A., Kusk, A., Andersen, J. K., Neckel, N., Solgaard, A., Karlsson, N. B., Kjær, H. A., and Vallelonga, P. (2020). "Surface velocity of the Northeast Greenland Ice Stream (NEGIS): assessment of interior velocities derived from satellite data by GPS". In: *The Cryosphere* 14.10, pp. 3487–3502. DOI: 10.5194/tc-14-3487-2020.

Jansen, D., Franke, S., Bauer, C. C., Binder, T., Dahl-Jensen, D., Riese, T. de, Eichler, J., Eisen, O., Llorens, M.-G., Kerch, J., Miller, H., Neckel, N., Paden, J., Sachau, T., Stoll, N., Weikusat, I., Wilhelms, F., Zhang, Y., and Bons, P. D. (2022). "Folded ice reveals: the North East Greenland Ice Stream was formed only 2000 years ago". In: *Nature communication*. in review.

Joughin, I., Fahnestock, M., MacAyeal, D., Bamber, J. L., and Gogineni, P. (2001). "Observation and analysis of ice flow in the largest Greenland ice stream". In: *Journal of Geophysical Research: Atmospheres* 106.D24, pp. 34021–34034. DOI: 10.1029/2001JD900087.

Joughin, I., Smith, B. E., and Howat, I. M. (2018). "A complete map of Greenland ice velocity derived from satellite data collected over 20 years". In: *Journal of Glaciology* 64.243, pp. 1–11. DOI: 10.1017/jog.2017.73.

Keisling, B. A., Christianson, K., Alley, R. B., Peters, L. E., Christian, J. E., Anandakrishnan, S., Riverman, K. L., Muto, A., and Jacobel, R. W. (2014). "Basal conditions and ice dynamics inferred from radar-derived internal stratigraphy of the northeast Greenland ice stream". In: *Annals of Glaciology* 55.67, pp. 127–137. DOI: 10.3189/2014AoG67A090.

MacGregor, J. A., Fahnestock, M. A., Catania, G. A., Paden, J. D., Gogineni, S. P., Young, S. K., Rybarski, S. C., Mabrey, A. N., Wagman, B. M., and Morlighem, M. (2015). "Radiostratigraphy and age structure of the Greenland Ice Sheet". In: *Journal of Geophysical Research: Earth Surface* 120.2, pp. 212–241. DOI: 10.1002/2014JF003215.

MacGregor, J. A., Fahnestock, M. A., Catania, G. A., Aschwanden, A., Clow, G. D., Colgan, W. T., Gogineni, S. P., Morlighem, M., Nowicki, S. M. J., Paden, J. D., Price, S. F., and Seroussi, H. (2016). "A synthesis of the basal thermal state of the Greenland Ice Sheet". In: *Journal of Geophysical Research: Earth Surface* 121.7, pp. 1328–1350. DOI: 10.1002/2015JF003803.

Martos, Y. M., Jordan, T. A., Catalán, M., Jordan, T. M., Bamber, J. L., and Vaughan, D. G. (2018). "Geothermal heat flux reveals the Iceland hotspot track underneath Greenland". In: *Geophysical research letters* 45.16, pp. 8214–8222. DOI: 10.1029/2018GL078289.

Mojtabavi, S., Wilhelms, F., Cook, E., Davies, S. M., Sinnl, G., Skov Jensen, M., Dahl-Jensen, D., Svensson, A., Vinther, B. M., Kipfstuhl, S., Jones, G., Karlsson, N. B., Faria, S. H., Gkinis, V., Kjær, H. A., Erhardt, T., Berben, S. M. P., Nisancioglu, K. H., Koldtoft, I., and Rasmussen, S. O. (2020a). "A first chronology for the East Greenland Ice-core Project (EGRIP) over the Holocene and last glacial termination". In: *Climate of the Past* 16.6, pp. 2359–2380. DOI: `10.5194/cp-16-2359-2020`.

Riverman, K. L., Alley, R. B., Anandakrishnan, S., Christianson, K., Holschuh, N. D., Medley, B., Muto, A., and Peters, L. E. (2019). "Enhanced Firn Densification in High-Accumulation Shear Margins of the NE Greenland Ice Stream". In: *Journal of Geophysical Research: Earth Surface* 124.2, pp. 365–382. DOI: `10.1029/2017JF004604`.

Rogozhina, I., Petrunin, A. G., Vaughan, A. P., Steinberger, B., Johnson, J. V., Kaban, M. K., Calov, R., Rickers, F., Thomas, M., and Koulakov, I. (2016). "Melting at the base of the Greenland ice sheet explained by Iceland hotspot history". In: *Nature Geoscience* 9.5, pp. 366–369. DOI: `10.1038/ngeo2689`.

Simonsen, S. B. and Sørensen, L. S. (2017). "Implications of changing scattering properties on Greenland ice sheet volume change from Cryosat-2 altimetry". In: *Remote Sensing of Environment* 190, pp. 207–216. DOI: `10.1016/j.rse.2016.12.012`.

Smith-Johnsen, S., Schlegel, N. J., Fleurian, B. de, and Nisancioglu, K. H. (2020a). "Sensitivity of the Northeast Greenland Ice Stream to Geothermal Heat". In: *Journal of Geophysical Research: Earth Surface* 125.1, pp. 1–14. DOI: `10.1029/2019JF005252`.

Smith-Johnsen, S., De Fleurian, B., Schlegel, N., Seroussi, H., and Nisancioglu, K. (2020b). "Exceptionally high heat flux needed to sustain the Northeast Greenland Ice Stream". In: *The Cryosphere* 14.3, pp. 841–854. DOI: `10.5194/tc-14-841-2020`.

Stevens, N. T., Parizek, B. R., and Alley, R. B. (2016). "Enhancement of volcanism and geothermal heat flux by ice-age cycling: A stress modeling study of Greenland". In: *Journal of Geophysical Research: Earth Surface* 121.8, pp. 1456–1471. DOI: `10.1002/2016JF003855`.

Stoll, N. (2019). *A first glimpse into the EGRIP ice core: An analysis of the influence of deformation and recrystallisation on fabric and microstructures of the Northeast Greenland Ice Stream*. Master thesis, University Bremen FB5.

Thomas, R. E., Negrini, M., Prior, D. J., Mulvaney, R., Still, H., Bowman, M. H., Craw, L., Fan, S., Hubbard, B., Hulbe, C., Kim, D., and Lutz, F. (2021). "Microstructure and crystallographic preferred orientations of an azimuthally oriented ice core from a lateral shear margin: Priestley Glacier, Antarctica". In: *Frontiers in Earth Science* 9. DOI: `10.3389/feart.2021.702213`.

Weertman, J. (1976). "Sliding–no sliding zone effect and age determination of ice cores". In: *Quaternary Research* 6.2, pp. 203–207. DOI: `10.1016/0033-5894(76)90050-8`.

Yan, J.-B., Li, L., Nunn, J. A., Dahl-Jensen, D., O'Neill, C., Taylor, R. A., Simpson, C. D., Wattal, S., Steinhage, D., Gogineni, P., Miller, H., and Eisen, O. (2020). "Multiangle, Frequency, and Polarization Radar Measurement of Ice Sheets". In: *IEEE Journal of Selected Topics in Applied Earth Observations and Remote Sensing* 13, pp. 2070–2080. DOI: `10.1109/JSTARS.2020.2991682`.

Zeising, O. and Humbert, A. (2021). "Indication of high basal melting at the EastGRIP drill site on the Northeast Greenland Ice Stream". In: *The Cryosphere* 15.7, pp. 3119–3128. DOI: `10.5194/tc-15-3119-2021`.